Estudio sobre el impacto de la geometría de toberas Diesel en el desarrollo del chorro, la formación de la mezcla y la combustión

Tesis Doctoral

Presentada por:
Sr. Enrique Carlos Martínez-Miracle Muñoz

Dirigida por:
Prof. Francisco Javier Salvador Rubio
y
Dr. José Manuel Pastor Enguídanos

Universitat Politècnica de València
Departamento de Máquinas y Motores Térmicos

Febrero 2024, Valencia

Este documento está preparado para ser imprimido a doble cara

Estudio sobre el impacto de la geometría de toberas Diesel en el desarrollo del chorro, la formación de la mezcla y la combustión

Documento que presenta para optar al título de Doctor en Filosofía

Sr. Enrique Carlos Martínez-Miracle Muñoz

Dirigida por

Prof. Francisco Javier Salvador Rubio

y

Dr. José Manuel Pastor Enguídanos

Universitat Politècnica de València

Departamento de Máquinas y Motores Térmicos

Febrero 2024, Valencia

Tesis Doctoral

Estudio sobre el impacto de la geometría de toberas Diesel en el desarrollo del chorro, la formación de la mezcla y la combustión

Escrita por:	Sr. Enrique Carlos Martínez-Miracle Muñoz
Supervisada por:	Prof. Francisco Javier Salvador Rubio Dr. José Manuel Pastor Enguídanos

Comité de tesis:

Presidente:	Prof. Jaime Gimeno García
Secretario:	Dr. Jorge Martínez López
Vocal:	Prof. Adrián Pandal Blanco

Revisores:

Dr. Jorge Martínez López
Prof. Octavio Armas Vergel
Dr. David Jaramillo Císcar

Febrero 2024, Valencia

A mi familia
y
a Lorena

...
Tu bramido resuena como trueno,
En las calles de la ciudad bulliciosa,
Tu fuerza impulsa el carro risueño,
En su veloz y rutilante prosa.
...
ChatGPT 3.5 - Oda al motor de combustión, estilo del siglo XVIII.

Agradecimientos

-Thanks are due to Joe Blotz for assistance with the experiment and to George Frick for valuable discussion... (Blotz did all the work and Frick explained to me what it meant.)

Dictionary of Useful Research Phrases

Es complicado en esta parte de toda tesis hacer justicia a todos aquellos que, de forma directa o indirecta, han contribuido al buen término de la misma. Y de seguro, algunos no serán representados en estos párrafos no por ser menores sino por negligencia de la memoria. Intentando cumplir con todos ellos, quiero agradecer en primer lugar al Instituto CMT de Motores Térmicos su apoyo como institución, y por haber respaldado mis estudios de doctorado. En segundo lugar, quiero agradecer a mis tutores, Javier Salvador y José Manuel Pastor, por su paciencia y experta guía, a la que con mayor o menor éxito consiguieron acercarme. Las investigaciones de esta tesis han sido respaldadas por el Ministerio de Ciencia, Innovación y Universidades el Gobierno de España y mis estudios de doctorado han sido financiados por la Agencia Estatal de Investigación del gobierno de España y el Fondo Social Europeo. Dichas ayudas se concretaron dentro del marco del proyecto "Desarrollo de modelos de combusti ón y emisiones HPC para el análisis de plantas propulsivas de transporte sostenibles" (TRA2017-89139-C2-1-R) a través del "Subprograma Estatal de Formación del Programa Estatal de Promoción del Talento y su Empleabilidad en I+D+i". Sin este apoyo, las investigaciones aquí presentadas no hubieran sido posibles. También quiero dar las gracias a todo el equipo de técnicos, especialmente a José Enrique del Rey y a Omar Huerta, por prestarme sus habilidades experimentales y su tiempo en mediar con mi falta de ellas. Son muchos los compañeros doctorandos que han formado parte de estos años y es difícil mencionarlos a todos. Pese a esto, me gustaría nombrar a Marco Crialesi, por sus consejos en mis inicios de la investigación y a Lucas Antonio González por compartir los primeros proyectos dentro del departamento de inyección. También quiero dar las gracias a Armando Moreno, Mary Y. Alarcon y Alberto Viera por sus pacíficas explicaciones sobre calibración y

procesado. Debo hacer un mención especial a María Martínez por su gran desempeño dentro y fuera del despacho, por su gran uso de la Ley de Murphy, y con la que seguro mantendré una gran y duradera amistad. También nombrar a Vincenzo Pagano por poner el toque italiano y la maraca en el día a día. Y ya, en los últimos pero no menos importantes años, debo mencionar a Javier Marco y a Óscar Bori por las valiosas y amenas charlas y por la filosofía de oficina (nunca se debe infravalorar a la filosofía de oficina). También incluyo con cariño en este grupo a otros muchos compañeros de camino como Mario Belmar, Jesús Peraza, Rami Abboud, Abian Bautista, Tomás Montiel o César Carvallo. Tengo que dar también las gracias al equipo de profesores, en especial a Raúl Payri por su apoyo en la conducción de los proyectos dentro del departamento, y a Jaime Gimeno, Marcos Carreres, Joaquín de la Morena, Josep Gómez y Pedro Martí por su colaboración en las investigaciones. Agradezco en la misma medida a Amparo Cutillas, del equipo de secretaría, por su ayuda en las sombras frente a la tiranía de la burocracia.

Finalmente, agradezco a mi familia, a mis padres Enrique y Matilde, a mi hermana Inés, a mis abuelos Matilde Reviejo y Francisco Muñoz y a mis tíos, Víctor Pedro y Francisco Muñoz, su apoyo incondicional a lo largo de todo el viaje, y por ser uno de los pilares estoicos de este documento. Y a Lorena, mi compañera del alma, por acompañarme durante todo este tiempo, habiendo sido capaz de aguantar todas las manías y problemas, que no son pocos, de un ingeniero.

Resumen

Science is magic that works.
Kurt Vonnegut

El empuje actual de las normativas de emisiones y una conciencia social cada vez más crítica en este aspecto, ha llevado a la industria automotriz a elevar sus estándares en eficiencia a cimas nunca antes vistas. Con el mayor peso de las nuevas normativas puesto sobre los vehículos Diesel, la presión ejercida sobre esta tecnología es, si cabe, aún más crítica. Dada la necesidad de mantener este tipo de plantas propulsivas en determinadas aplicaciones, como son el transporte terrestre pesado, maquinaria o en el transporte marítimo, es también necesario mantener su desarrollo. Como parte fundamental de los motores Diesel, el sistema de inyección interviene directamente en la generación de la energía. La mejora y optimización de su funcionamiento repercute sobre la cadena de eficiencias del sistema. Esta tesis pretende contribuir al desarrollo de las plantas propulsivas Diesel en este aspecto y, concretamente, en el estudio de las geometrías de toberas Diesel de inyección directa. A lo largo del texto, este tipo de geometrías son estudiadas tanto desde la perspectiva del flujo interno como del flujo externo. Los estudios combinan modelos numéricos Eulerianos (para flujo interno o interno-externo acoplado), modelos Lagrangianos discretos (para el estudio del chorro), junto con medidas experimentales diversas que avalan los análisis ejecutados. La exploración de las geometrías propuestas no queda acotada solamente a formas circulares, más convencionales, sino que también se ha extendido a toberas de morfologías más innovadoras como son las elípticas. Las metodologías presentadas demuestran ser eficaces en el estudio de estos sistemas y una herramienta a tener en cuenta en la mejora de su diseño. Los distintos resultados obtenidos defienden, además, como la geometría de la tobera es un condicionante del desarrollo posterior de la mezcla y puede ser utilizada como elemento de optimización de la misma.

Abstract

The current push for emissions regulations and an increasingly critical social awareness in this regard has led the automotive industry to raise its efficiency standards to unprecedented heights. With greater emphasis on new regulations placed on Diesel vehicles, the pressure on this technology is even more critical. Given the need to maintain such propulsion systems in specific applications like heavy land transport, machinery, or maritime transportation, it is also necessary to continue their development. As a fundamental part of Diesel engines, the injection system directly affects energy generation. Improving and optimizing its operation has an impact on the overall efficiency of the system. This thesis aims to contribute to the development of Diesel propulsion systems in this regard, specifically in the study of direct injection Diesel nozzle geometries. Throughout the text, these types of geometries are examined from both internal and external flow perspectives. The studies combine Eulerian numerical models (for internal or coupled internal-external flow), discrete Lagrangian models (for jet analysis), along with various experimental measurements that support the conducted analyses. The exploration of proposed geometries is not limited to conventional circular shapes but has also extended to more innovative morphologies such as elliptical nozzles. The presented methodologies prove to be effective in studying these systems and serve as a valuable tool in improving their design. The different results obtained also argue that nozzle geometry is a determining factor in the subsequent mixture development and can be used as an optimization element for it.

Resum

L'actual impuls de les normatives d'emissions i una consciència social cada vegada més crítica en aquest aspecte ha portat a la indústria automobilística a elevar els seus estàndards d'eficiència a cotes mai vistes abans. Amb el major pes de les noves normatives imposades als vehicles dièsel, la pressió exercida sobre aquesta tecnologia és, si cap, encara més crítica. Donada la necessitat de mantenir aquest tipus de plantes propulsives en determinades aplicacions, com el transport terrestre pesat, maquinària o el transport marítim, és també necessari mantenir el seu desenvolupament. Com a part fonamental dels motors dièsel, el sistema d'injecció intervé directament en la generació d'energia. La millora i optimització del seu funcionament repercuteix en la cadena d'eficiències del sistema. Aquesta tesi pretén contribuir al desenvolupament de les plantes propulsives dièsel en aquest aspecte i, concretament, en l'estudi de les geometries de bussons dièsel d'injecció directa. Al llarg del text, aquest tipus de geometries són estudiades tant des de la perspectiva del flux intern com del flux extern. Els estudis combinen models numèrics Eulerians (per a flux intern o intern-extern acoblat), models Lagrangians discrets (per a l'estudi del corrent), juntament amb mesures experimentals diverses que avalen els anàlisis realitzats. L'exploració de les geometries proposades no queda acotada només a formes circulars, més convencionals, sinó que també s'ha estès a bussons de morfologies més innovadores com les el·líptiques. Les metodologies presentades demostren ser eficaces en l'estudi d'aquests sistemes i una eina a tenir en compte en la millora del seu disseny. Els diferents resultats obtinguts també argumenten que la geometria del busó és un condicionant del desenvolupament posterior de la barreja i pot ser utilitzada com a element d'optimització de la mateixa.

Índice

Índice de figuras

Índice de Tablas

Abreviaturas

1D One-dimensional modelling.

3D Three-dimensional modelling.

ADC Analog to Digital Converter.

AMR Adaptative Mesh Refinement.

BN Base Nozzle.

CAD Computer-Aided Design.

CFD Computational Fluid Dynamics.

DDM Droplet Discrete Modeling.

DPF Diesel Particulate Filter.

ECN Engine Combustion Network.

EGR Exhaust Gas Recirculation.

ELSA Eulerian-Lagrangian Spray Atomization.

ESA Eulerian Spray Atomization.

EVO Exhaust valve closing.

GCI Grid Convergence Indicators.

HEM Homogeneous Equilibrium Model.

HRM Homogeneous Relaxation Model.

IRDCI Injection Discharge Rate Curve Indicator.

IVC Intake valve closing.

KH Kelvin-Helmholtz.

KH-ACT Kelvin Helmholtz-Aerodynamics Cavitation Turbulence.

LES Large Eddy Simulation.

LL Liquid length.

LNT Lean-NOx Trap.

LOL Lift-Off Length.

MCIA Motor de Combustión Interna Alternativo.

OEMs Original Equipment Manufacturers.

OP3 Optimized Nozzle.

PMD Projected Mass Density.

PRF Primary reference fuels.

RANS Reynolds Averaged Navier-Stokes.

RNG Re-Normalisation Group.

ROI Rate of Injection.

RT Rayleigh-Taylor.

SCR Selective Catalytic Reduction.

SEM Scanning electron microscope.

SN Short Nozzle.

SST Shear Stress Tensor.

U-RANS Unsteady Reynolds Averaged Navier-Stokes.

VOF Volume-Of-Fluid.

Símbolos latinos

A_M Thermal conducticity matrix. 53

A_i Coefficient in the heat flow combustion chamber equation. 92

A_o Geometric area of the outlet orifice. 58, 144, 181

$A_{ellipse}$ Ellipse geometric area. 133

A_{geo} Geometric area. 94

B Compressibility modulus. 136

B_i Coefficient in the heat flow combustion chamber equation. 92

C_a Area coefficient. 144, 145, 181

C_d Discharge coefficient. 58, 144, 145, 181

C_p Specific heat. 52

C_v Velocity coefficient. 144, 181

C_Σ Coeffciente in the equilibrium radius equation of Σ. 177

$C_{\epsilon 1}$ C1 constant of the $k-\epsilon$ turbulence closure model. 178, 183

$C_{\epsilon 2}$ C2 constant of the $k-\epsilon$ turbulence closure model. 178

$C_{\epsilon 3}$ C3 constant of the $k-\epsilon$ turbulence closure model. 178

D Diffusion coefficient in the Y transport equation of the $\Sigma - Y$ model. 176

D Specific heat matrix. 52

D Mass diffusion in the energy transport equation of the Σ –Y model. 130

D_i Inlet diameter. 49

D_o Oulet diameter. 49, 82, 97, 147

D_Σ Diffusion coefficient in the surface density area transport equation of the $\Sigma - Y$ model. 131, 177

F HRM condensation parameter. 132, 179

K Thermal conductivity. 130, 178

M_f Steady momentum flux. 96, 149

P Pressure. 97, 130, 144

P_c Critical pressure of the fluid. 132

R Specific gas constant. 93

R_{inf} Lower rounding radius. 82

R_{sup} Superior rounding radius. 82

S Spray penetration. 97, 149

S Wall surface.. 78

S_E Energy source term. 54

S_m Source term in the Y transport equation. 176, 179

$S_{\Sigma_{evap}}$ Vaporization source term in the surface density area transport equation of the $\Sigma - Y$ model. 131

$S_{\Sigma_{init}}$ Initialization value of Σ in the surface density area transport equation of the $\Sigma - Y$ model. 131, 177

Sc Schmidt number. 130

Sc_Σ Schmidt number in the Σ transport equation. 131, 177

T Temperature. 52, 54, 55, 130, 178

T_{gas} Gas temperature in the wall heat losses equation. 78

T_{wall} Surface temperature of the wall in the wall heat losses equation. 78

V Volume. 78, 93

Y Volume fraction of fuel in the surface density area transport equation of the $\Sigma - Y$ model. 131, 132

Y Mass fraction. 179

Y_m Mass fraction in the energy transport equation of the Σ-Y model. 130

$\bar{Y}$ Volume fraction in the liquid transport equation of the Σ-Y model. 129

$\dot{m}_f$ Mass flow. 58, 144

$\dot{q}_m$ Steady-state heat flux density. 92

$\tilde{Y}$ Mean mass averaged volume fraction in the liquid transport equation of the Σ-Y model. 129

$\tilde{u}$ Velocity over the axis in the liquid transport equation of the Σ-Y model. 129

a Ellipse minor radius. 133

a_{ij} Thermal conducticity matrix coefficients. 53

b Heat penetration coefficient in the heat flow combustion chamber equation. 93

b Ellipse major radius. 133

c Linear eccentricity. 133

d_{ij} Specific heat matrix coefficients. 52

e Eccentricity. 133, 146, 148–150

e Specific energy. 130, 178

h Specific enthalpy. 54

h Transfer coefficient in the wall heat losses equation. 78

h_0 Specific stagnation enthalpy. 54

h_m Specific enthalpy in the energy transport equation of the Σ-Y model. 130, 178

k Turbulent kinetic energy. 178

k_t Thermal conductivity. 52–54

l Rod length in the piston acceleration equation. 90

l/d Ratio longitud-diámetro. 11, 22, 215, 220

m Air mass. 93

m_f Steady mass flow. 94, 181

m_g Gas mass. 177

m_l Volumen of the cell element. 135

m_l Liquid mass. 135, 177

m_{th} Theoretical mass flow. 181

n Mesh refinement level. 180

p Pressure. 52–55, 181

p_{cyl} Cylinder pressure. 93

r Crank radius in the piston acceleration equation. 90

r_{eq} Droplet equilibrium radius. 131, 177

t Time. 149

u_{eff} Effective velocity. 96

u_{out} Outlet velocity. 58

u_{th} Bernoulli's theoretical velocity. 94

x Instantanous mass, HRM model. 132

x Axial position in the liquid transport equation of the Σ-Y model. 129

Símbolos griegos

Σ Surface area density. 131, 176, 177

Σ_{eq} Surface area density equilibrium value for a droplet. 177

Υ Liquid volume fraction in the Σ transport equation. 177

α Crankshaft angle in the piston acceleration equation. 90

α Void fraction. 132, 176, 179

α_1 Model parameter of the $\Sigma - Y$ model. 131, 178

α_2 Model parameter of the $\Sigma - Y$ model. 131, 177, 178

$\bar{\rho}$ Density. 129

β Volumetric thermal expansion. 54, 55

δ_{ij} Kronecker delta. 130

ϵ Turbulent kinetic energy dissipation rate. 178

λ Thermal conductivity in the heat flow combustion chamber equation. 92, 93

λ Ratio r/l in the piston acceleration equation. 90

μ Viscosity. 130, 178

μ_0 Dynamic viscosity of the fluid at atmospheric pressure. 52

μ_f Dynamic viscosity. 52

μ_t Turbulent viscosity. 178

ν Kinematic viscosity in the Σ transport equation. 177

ω Angular frecuency. 92

ω Angular velocity. 90

ω Disipation rate of the turbulent kinetic energy. 183

ϕ_{eq} Equivalent diameter. 180

ρ Density. 176

ρ_a Ambient density. 97, 147, 149

ρ_f Density of the fuel. 52, 94, 147, 181

ρ_g Gas density. 130

ρ_l Liquid density. 130, 144

σ_{ij} Stress tensor. 130, 178

θ Spray angle. 149

θ_0 Time scale factor of the HRM model. 132, 179

θ_C Time scale factor of the HRM model for condensation. 132

θ_E Time scale factor of the HRM model for evporation. 132

θ_u Spray angle. 97

φ Non–dimensional pressure ration in the HRM model. 132, 179

Capítulo 1

Planteamiento de la tesis

Instabilitas numeralis similis est karma,
nescis unde veniat, sed semper desinit
venire..

Anónimo

Resumen: Las líneas de esta sección presentan una breve descripción de la evolución histórica de las metodologías aplicadas a los sistemas de inyección y, más concretamente, a las toberas Diesel, hasta culminar con el estado del arte actual. Se pone de manifiesto como este punto ha sido posible gracias a la convergencia de diferentes técnicas y metodologías, a veces provenientes de ramas dispares de la ciencia. Se finaliza el capítulo con la descripción de los objetivos de la tesis y su vinculación con el desarrollo del estado de los sistemas de inyección Diesel actuales.

1.1. Introducción

Desde los años 30 y a lo largo de todo el siglo XX, los vehículos propulsados por un motor de combustión interna alternativo (MCIA) han proliferado enormemente. Con una producción en las primeras décadas de siglo más intensa en Europa y Estados Unidos, su éxito se trasladó rápidamente al resto del mundo. El MCIA ha sido desde entonces uno de los ejes indiscutibles del progreso de la sociedad gracias especialmente a su penetración en lo que al transporte de pasajeros y mercancías se refiere y a otros aspectos no menos importantes como la generación de electricidad. El uso global del motor ha ido acompañado, como no podía ser de otra manera, de un aumento en el consumo de combustibles fósiles y de las emisiones derivadas de la combustión de los mismos. Se puede decir que fue a principios de los años 70 cuando despertó el interés por mitigar los efectos del uso ya mundial de los vehículos siendo en

este periodo, cuando se empezaron a incorporar los primeros elementos especialmente diseñados para este propósito. El ejemplo más representativo es el convertidor catalítico, introducido en Estados Unidos en esta década y cuya función es reducir las emisiones de los gases una vez han abandonado la cámara de combustión durante una etapa de postratamiento con ayuda de ciertos procesos químicos. En Europa, la creciente demanda social de unos motores de combustión sostenibles tanto para las personas como para el medio ambiente se traduciría, a finales de los años 80 y hasta nuestros días, en la creación de las normas de denominación EURO. Dichos textos introducen una serie de regulaciones y limitaciones al valor máximo de las emisiones en escape de los vehículo. El incremento progresivo de las restricciones se ha traducido en un aumento de la presión depositada sobre la ingeniería necesaria para llevarlas a buen término. De esta forma, dentro de los objetivos que forman parte de las nuevas generaciones de motores de combustión deben existir fuertes facetas en términos de eficiencia energética y reducción de emisiones para poder enfrentar dichas restricciones. La necesidad de cumplirlas ha llevado a los investigadores a enfatizar en el diseño de cada una de las partes involucradas en la generación y aprovechamiento de la energía producida y no solo en el tratamiento de los gases de escape. La electrificación de componentes mecánicos, la incorporación de materiales más ligeros, el uso de combustibles alternativos, las nuevas estrategias de inyección, el aprovechamiento de la energía de los gases de escape, los sistemas Exhaust Gas Recirculation (EGR), los filtros antipartículas o la introducción de los catalizadores Selective Catalytic Reduction (SCR), son algunos ejemplos representativos de las mejoras alcanzadas en las nuevas plantas propulsivas. En este sentido, la capacidad de empujar la innovación técnica en ciertos aspectos y procesos del motor se vuelve especialmente compleja debido a las propias características que envuelven sus condiciones de operación. El estudio del proceso de inyección de combustible y generación de la mezcla, condicionante de la eficiencia de la combustión, es, y ha sido durante muchas décadas, un tema difícil de enfrentar por los ingenieros. Las escalas temporales y espaciales en las que dichos procesos se originan y desarrollan, del orden de microsegundos y micrómetros, en condiciones reales de operación, hacen necesaria una ingeniería de detalle de compleja ejecución. La visualización del interior de las toberas de inyección o de la cámara de combustión suele ser prohibitiva debido a las mencionadas escalas y a los materiales metálicos empleados para su fabricación, situación que dificulta el seguimiento de los distintos mecanismos que de desarrollan en su interior. Adicionalmente, en la formación de la mezcla convergen una serie de factores cuyas influencias son difíciles de discernir y cuantificar, por un lado, se dan los efectos de la geometría del inyector, especialmente de la tobera de inyección, sobre el flujo interno. En este aspecto, la morfología de la tobera puede influir en las condiciones del flujo a la salida del orificio y, por tanto, define las condiciones iniciales del chorro. Por otro lado, el estado inicial del chorro a la salida del orificio se superpone a la interacción del combustible con el ambiente de

la cámara provocando un proceso de atomización, mezcla y evaporación. La inyección involucra, por tanto, el estudio de las características de la tobera, el flujo interno y la interacción del chorro con las condiciones en el volumen de descarga. Todos estos retos de conocimiento conforman la fuente primaria de energía en el motor de combustión, el calor liberado y su aprovechamiento dependen directamente de la efectividad de la mezcla, y la capacidad de optimizar este proceso repercutirá directamente sobre la eficiencia de la combustión y sobre el resto de rendimientos. Con la incorporación a la técnica de los métodos computacionales desde principios de los años 70 y la mejora de los modelos numéricos a lo largo de las décadas siguientes, los investigadores han conseguido profundizar en las mecánicas del flujo interno de las toberas y el chorro. La combinación de simulaciones y medidas experimentales ha sido fundamental a la hora de establecer y validar relaciones entre los parámetros geométricos de la tobera y sus efectos sobre el flujo, especialmente dada la capacidad de observar las dinámicas del fluido en cualquier punto del dominio de una simulación. Así, se puede afirmar que los sistemas de inyección modernos difícilmente habrían alcanzado el nivel tecnológico actual sin la aplicación de los métodos computacionales a la mecánica de fluidos y al estudio de estos procesos. Sin embargo, los primeros estudios aplicados a este ámbito se dieron durante las décadas de los años 30 y 40, mucho antes de la computación, con el desarrollo de los sistemas de inyección de combustible dentro de una incipiente industria automovilística, ávida de la incorporación de nuevas tecnologías. Con la intención de cuantificar el efecto de las geometrías de inyección sobre el flujo, algunos de estos estudios, de carácter eminentemente experimentales, aparecen de la mano de pioneros como Gelalles [1], que en 1930 ya relacionó ciertos parámetros de la tobera de inyección de un motor de encendido por compresión, como el diámetro de salida, la longitud de la tobera o el radio de hidroerosión a la entrada de la misma, con el coeficiente de descarga. Gelalles empleó este número adimensional frente a diferentes rangos de presiones para caracterizar diferentes geometrías, lo que le permitió definir ciertas necesidades constructivas de las toberas para mantener un alto flujo de combustible. Otra aportación temprana, ésta vez incluyendo el flujo externo, fue realizada por Lee [2, 3], fotografiando el efecto que distintas geometrías de inyección tenían sobre el chorro bajo diferentes condiciones de descarga. En la Figura 1.1 y Figura 1.2 se pueden observar las capturas obtenidas de la dispersión del chorro.

Aunque los conceptos generales de como la atomización influenciaba a la combustión eran a grandes rasgos conocidos, el creciente interés de los investigadores por la dinámica del chorro favoreció la búsqueda de explicación a los fenómenos más complejos. La problemática de las dinámicas físicas que componen el evento de inyección, desde el paso del flujo por la geometría de la tobera, la dispersión del combustible en cámara, la atomización hasta la combustión llevó a los estudiosos a enfocar el problema desde perspectivas diferentes. A

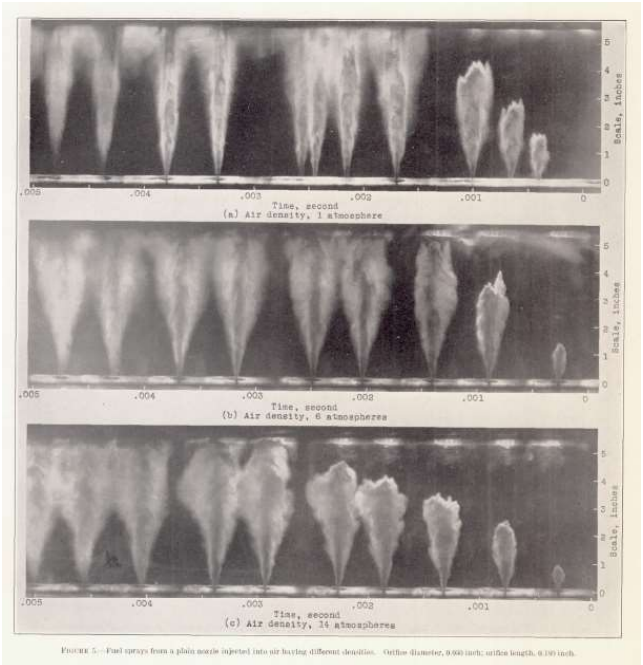

Figura 1.1: Evolución de la penetración un chorro para distintas presiones de descarga, Lee [3].

veces de una forma más general, a partir de parámetros macroscópicos del flujo y el chorro como pueden ser las medidas visuales de penetración o ángulo y otras, a través de las escalas más pequeñas, como el comportamiento de las gotas, la atomización o la concentración de especies. Uno de los primeros trabajos en centrarse en esta relación lo condujo Probert [4] en 1946. En éste, partiendo de distribuciones Rossim-Ramler de gotas y dinámicas de gotas individuales, se relaciona el tamaño y distribución de las mismas con la tasa de evaporación y su influencia sobre la combustión. El estudio de la dinámicas de gotas, a partir de estudios como este, marcaría las aproximaciones al chorro en décadas posteriores donde el chorro, en la zona suficientemente dispersa, se asemeja a un conjunto de gotas gobernado por comportamientos individuales. También son remarcables los estudios tempranos sobre gotas y la vaporización del combustible de El Wakil et al. [5, 6] y de Joyce et al. [7] en años siguientes, donde la atomización del combustible es relacionada con sus propiedades físicas. Desde la perspectiva macroscópica, Forstall y Shapiro [8], utilizando técnicas de mapeado mediante un fluido trazador, estudiaron en el transporte del momento y masa en el chorro gaseoso. Analizaron la dispersión del combustible relacionándola con los números de Schmidt y Prandtl, parámetros fundamentales en el estudio de los chorros. En el aspecto de la trasferencia de velocidad y masa, son interesantes las aportaciones de Sforza y Trentacoste [9, 10] y sus conclusiones sobre la autosimilaridad de chorros frente a

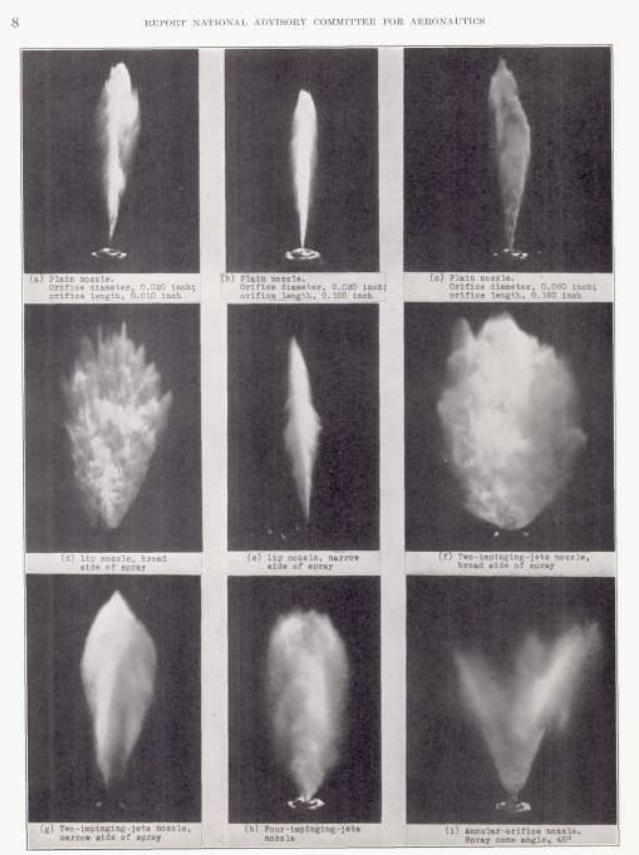

Figura 1.2: Efecto de la geometría en la forma del chorro, Lee et al. [3].

distintos perfiles de velocidad iniciales. De Corso et al. [11, 12], investigó el comportamiento del chorro desde ambas posturas, por un lado, macroscópica, estudiando la influencia de la presión sobre el ángulo y, por otro, microscópica, a través del análisis de imágenes del tamaño resultante de las gotas. Bergwerk [13], de forma similar a los estudios de Gelalles y Lee de principios de siglo, observó el efecto de la morfología de la tobera sobre el flujo interno y sobre el chorro utilizando geometrías transparentes fabricadas en perspex. En sus estudios, se relaciona la presión de inyección y los radios de hidroerosión a la entrada de las toberas, entre otros parámetros, con la cavitación, la atomización, y el número de Reynolds. Aunque las escalas de las geometrías eran mayores que las empleadas en los inyectores reales, los investigadores actuales aún emplean estas ideas en montajes experimentales. Los aportes de Lyn et al. [14, 15] para la visualización de los chorros y la combustión también se siguen aplicando en la caracterización de chorros. En ellos, se utiliza el método de Schlieren para, mediante una cámara rápida, visualizar las variaciones de densidad dentro de la cámara de descarga. Dichos gradientes de densidades diferencian entre la fase gaseosa del chorro y el aire circundante (Figura 1.3) lo

que permitió estudiar la evolución del combustible en condiciones evaporativas e incluso ciertos aspectos de la combustión. Sobre la influencia de las toberas en este proceso, Lyn et al. [16] analizó el efecto de ciertas geometrías principalmente sobre el retraso en la ignición y bajo distintas condiciones de presión y temperatura. Si bien sus resultados al respecto no fueron muy concluyentes, sí detectó un aumento de la tasa de liberación de calor con la reducción del ratio longitud-diámetro de las toberas (l/d). Aunque no fuera el principal objeto de análisis, este artículo contempla el uso de una tobera multi-orificio (9 orificios) taladrada mediante un haz de electrones, del mismo tipo que las toberas modernas. Watts et al. [17] realiza un resumen de algunas de las principales preocupaciones de los ingenieros de la época relativas al desarrollo de los motores de inyección directa. Por una lado, la dificultad en la generación de turbulencia en cámara, debida a su propio diseño y al de los colectores de admisión, que ayude a la mezcla. Y por otro, la interacción entre los chorros y la geometría de ésta y la necesidad de aumentar el número de orificios para disminuir dicho efecto (a costa de poder fabricar orificios más pequeños que pudieran mejorar la distribución del combustible). Watts et al. dejaba dos conclusiones principales, en una primera dudaba, quizás introduciendo cierto pesimismo, de la capacidad de avanzar mucho más en el desarrollo de los motores de inyección directa Diesel, uniéndose de esta forma a otros célebres pronósticos ("El caballo está aquí para quedarse, pero el automóvil es sólo una novedad, una moda pasajera". –El presidente de la Caja de Ahorros de Michigan aconsejando al abogado de Henry Ford no invertir en Ford [18].) Sin embargo, su segunda conclusión fue bastante más acertada. En ella, depositaba el peso de los posibles avances en un mejor entendimiento de los fenómenos turbulentos y en una re-orientación del peso que los sistemas de inyección de combustible tenían en el diseño general del proceso de combustión, hasta la época, más enfocado en la cámara.

Muchos de estos avances llegarían de mano de la tecnología digital, facilitando la incursión por parte de los investigadores en nuevos detalles del funcionamiento y diseño de los motores. Un ejemplo de estas nuevas metodologías de investigación lo da Austen et al. [19] a principios de los 60, empleando un computador digital para obtener la tasa de liberación de calor en función de la tasa de inyección. Sus resultados eran generados a partir de la introducción de 4 parámetros del motor, ángulo del cigüeñal, presión del cilindro, presión en la tobera y la altura de la aguja, en un modelo calibrado. Un computador LEO se encarga del tedioso proceso iterativo de las ecuaciones. Knigh et al. [20] también fue pionero en el modelado computacional del sistema de inyección, donde una serie de ecuaciones acoplaban un modelo de bomba e inyector midiendo el desempeño de la tobera.

En general, se puede afirmar que en los años 50 y 60 ya existía una literatura notable entorno a los procesos internos de los motores de combustión [21-23], que fácilmente podía comenzar a interactuar con toda esta nueva rama

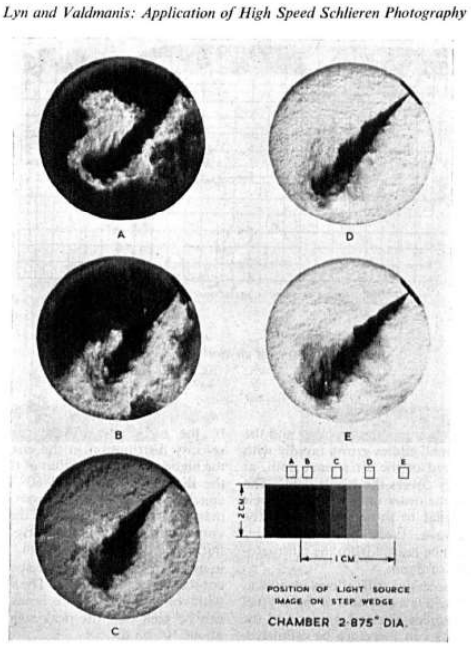

Figura 1.3: Fotografía del chorro empleando el método de Schlieren, Lyn et al. [14].

digital de la ciencia. De la mano de Shockley, Bardeen y Brattain (inventores del transistor en 1947), se cumplía así el vaticinio del famoso matemático L.F. Richardson (1881) ("Quizás algún día en el futuro será posible avanzar en los cálculos más rápido de lo que avanza el clima a un coste menor al de la información ganada. Pero eso es un sueño.") hablando de la que fuese considerada la primera aplicación de la historia de la Mecánica de Fluidos Computacional, o CFD, La Fábrica de Clima de Richardson. Con el avance del hardware informático, la mecánica de los fluidos comienza a ser estudiada desde una nueva perspectiva, donde las ecuaciones, inicialmente difíciles de resolver, ahora pueden ser rápidamente calculadas numéricamente. La convergencia de estas dos ramas de la ciencia dio lugar a lo que hoy se conoce como mecánica de fluidos computacional. Esta unión influyó, como no podía ser de otra forma, en el desarrollo de los motores de combustión interna y poco tardaría en ser usada todos los aspectos de los mismos, desde el diseño de los sistemas de gases y forma de la cámara hasta el estudio del chorro y la combustión. En los años 60 y 70 y paralelamente a los estudios tradicionales experimentales, comienzan a aparecer trabajos basados en modelos computacionales aplicados a la inyección y a la combustión. Estos primeros estudios computacionales eran capaces de presentar problemas complejos en el contexto de la fuerza de cálculo disponible. Y, en comparación con las alternativas manuales de las décadas anteriores, el avance fue nada menos que extraordinario. Como curio-

sidad, Kawaguti et al. [24] (1953), tardó nada menos que un año (20 horas a la semana) en resolver las ecuaciones de Navier-Stokes para un flujo a un régimen de Reynolds de 40 alrededor de un cilindro aplicando una discretización de 232 elementos. Los primeros trabajos con modelado geométrico solían ser bidimensionales, como el presentado por el mismo Kawaguti et al. [25] años más tarde, donde empleaba una malla de 120 elementos para discretizar y resolver una cavidad a distintos números de Reynolds. En este problema, la integración de las ecuaciones fue realizada por un ordenador PC-1 con unos tiempos de cálculo de unos 20 minutos con, como podrá apreciarse, una infinita mejora del aprovechamiento del tiempo personal en comparación con la resolución manual.

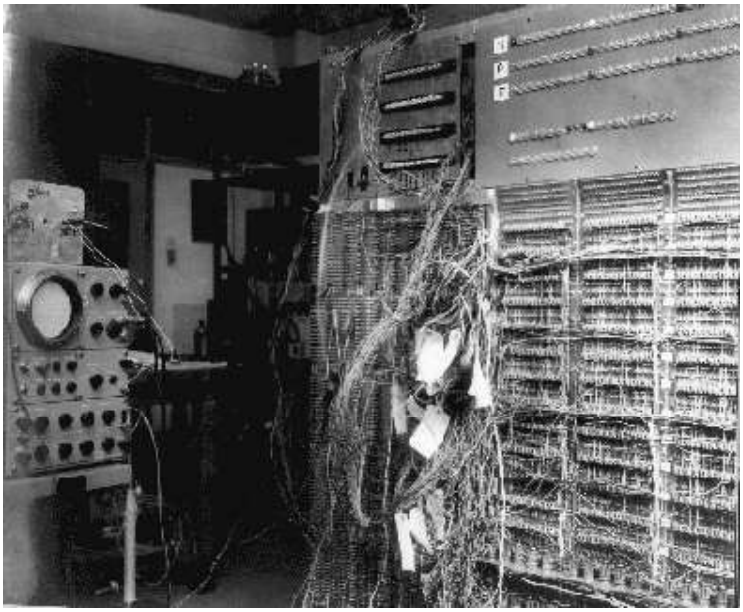

Figura 1.4: Fotografía del ordenador PC-1 de la Universidad de Tokio, Japón. [26].

En este sentido, el número de elementos del que se podía hacer uso para la discretización de los dominios geométricos imponía una importante limitación en la precisión de algunos problemas y a la estabilidad numérica [27, 28]. Fueron considerables los desarrollos de modelos paramétricos calculados por ordenador, por ejemplo, el ya mencionado de Austen et al. [19] o el planteado por Brown et al. [29], donde se modelaba el flujo másico de los conductos de un sistema de inyección incluyendo la generación de vapor por cavitación. Whitehouse y Way [30] también se interesaron por la capacidad de los ordenadores digitales de analizar los procesos en el interior del cilindro. En este caso, y bajo una serie de hipótesis de cálculo y alimentando el modelo con las especificaciones del motor, eran capaces de replicar los diagramas termodinámicos de funcionamiento. Los nuevos trabajos computacionales debían

enfrentar, necesariamente, a los distintos modelos matemáticos con la realidad empírica construida durante los periodos anteriores. A este respecto, era difícil obtener modelos que pudieran emular de forma satisfactoria todos los eventos en el interior del cilindro. Este hecho se acentuaba si se tiene en cuenta que el conocimiento sobre dichos aspectos se encontraba en constante evolución. Ya fuese para mejorar la estabilidad numérica, la eficiencia del cálculo o para adaptarse a comportamientos de flujo específicos, surgieron una gran variedad de nuevos modelos matemáticos aplicados al desarrollo del problema de la turbulencia, nuevas formas de aproximar la mezcla o sobre la química de la combustión, con especial mención a las aportaciones de Bracco et al. [31, 32], y mejoras en aspectos más técnicos, como los algoritmos de resolución o la discretización del dominio. En [32], se analiza una de las primeras simulaciones multifásicas, evaporativas y transitorias de una inyección directa en cámara de combustión (bidimensional), la fase líquida es modelada mediante un marco discreto Lagrangiano y el gas ambiente (inerte) mediante un enfoque continuo Euleriano.

El avance imparable de los recursos a disposición de los investigadores permitía poco a poco el estudio de problemas cada vez más ambiciosos. La capacidad de resolver las ecuaciones de Navier-Stokes en geometrías reales de los sistemas del motor llevó a la necesidad de modelar correctamente flujos cada vez más complejos, donde cambios bruscos de dirección, separación de la capa límite o zonas propensas a fenómenos como la cavitación eran comunes. Ésto llevó a autores como Schlichting [33], Launder et al. [34-37], que popularizaría el conocido modelo $k-\epsilon$ de dos ecuaciones, Spalding et al. [38, 39] o Pope [40, 41], a fijar su atención en el comportamiento turbulento del fluido. El interés por los sistemas de inyección, especialmente en las décadas de los 70 y 80 coincidiendo con las primeras políticas de control de emisiones, propició que muchos investigadores, algunos inicialmente experimentalistas como Spalding [42], incluyeran de forma principal el uso de la computación en el estudio de la inyección y de la combustión [43]. A partir de la década de los 70 y 80, la inyección directa de combustible comienza a generalizarse, volviéndose mucho más relevante para la industria del transporte [1]. Las nuevas motivaciones y técnicas disponibles tuvieron que lidiar con una descripción del chorro y la mezcla que debía hacerse cada vez en condiciones más difíciles, con velocidades del chorro y presiones en cámara mayores que intentaban mejorar los rendimientos del motor.

Son destacados los artículos de Adler et al. [44, 45], sobre la inyección directa del chorro diesel y la generación de modelos en condiciones evaporativas y de *swirl*, y de Gosman et al. [46, 47] sobre el movimiento turbulento de los fluidos, y que en la década de 1980 extendió al comportamiento de la inyección

[1] Aunque la inyección directa se popularizó a partir de la década de los 70, los primeros sistemas se instalaron en algunos modelos de aviones y coches de carreras en la década de los 40 y 50. En general, hasta ese momento la inyección se realizaba en el colector de admisión, en el caso de motores de gasolina o bien en una precámara para el caso de motores Diesel

directa [48] y a la combustión [49, 50]. En sus investigaciones, tanto Lyn et al. como Gosman et al. concentraron sus esfuerzos en acoplar el comportamiento del chorro con la cámara de combustión. En este aspecto, Gosman et al. [48], de forma similar a Bracco et al [32] y sobre los estudios de Haselman y Westbrook [51], emplea un modelo discreto Lagrangiano para aproximar el comportamiento de la atomización, poniendo especial atención al acoplamiento entre la fase continua y discreta. Las gotas eran inyectadas directamente en una posición determinada y con un diámetro específico según una distribución de probabilidad, de forma que se cumpliera la masa total inyectada determinada por una curva de tasa. La aproximación Lagrangiana al modelado del chorro [52-54] se convertiría en la forma más usual de proceder en el análisis numérico de la inyección directa y la combustión [54-56]. Menos costosa en términos computacionales que las aproximaciones continuas, al modelar el combustible mediante partículas discretas, estos enfoques se aprovechaban fácilmente de las teorías desarrolladas anteriormente en torno a la evaporación y comportamiento de gotas individuales. Sin embargo, los modelos de este tipo pecaban de un exceso de parametrización, si bien este defecto se iría reduciendo con la evolución de los mismos. El acople entre la fase líquida Lagrangiana y la fase Euleriana gaseosa de la cámara llevo a Gosman et al.[48] a denotar en sus conclusiones la elevada magnitud de la turbulencia local, generada por el evento de inyección, que superaba a la inducida por el swirl, y resalta el potencial efecto de la turbulencia a la salida del orificio como condicionante del proceso de mezcla.

La geometría interna del sistema de inyección, y más concretamente las toberas de inyección no acapararían el mismo nivel de interés que el estudio del chorro, quizás debido a que los primeros datos sobre el tema no otorgaron un especial peso a este factor en el proceso de atomización. Castleman [57], en 1933, asociaba casi exclusivamente el inicio del proceso de rotura a la diferencia de velocidades entre el aire y el gas circundante de la cámara. Sin embargo, a partir de la década de los 80, las investigaciones se inclinan hacia un claro efecto combinado de la tobera y las condiciones en el volumen de descarga. En estos años, en el marco del estudio del chorro, algunos autores como Hiroyasu et al. [58-62], pusieron especial atención a los condicionantes del comportamiento del chorro en términos de presión de inyección y densidad ambiente para unas condiciones reales de funcionamiento del chorro Diesel de hasta 750 bar de presión de inyección y 20 bar de contrapresión. Entre sus conclusiones más importantes destacan, la independencia del ángulo del chorro frente a la presión de inyección en regímenes de atomización completos, la variación de este con la densidad en cámara y el efecto de la velocidad el chorro sobre la penetración. En sus estudios incluyó el uso de varios tipos de toberas con diferentes ratios de longitud-diámetro (l/d) y diámetros. La forma de la tobera se añadía en la predicción de la penetración a través de un coeficiente específico. Otros investigadores como Arai et al. [63, 64] y Shimizu

et al. [65] contribuyeron de igual forma a estas líneas de investigación obteniendo expresiones para la caracterización del chorro, más o menos similares, donde las principales dependencias de la evolución del combustible en cámara, para una misma tobera, se concentraban en la diferencia entre la presión de inyección y la contrapresión, el diámetro de la tobera, la densidad del gas en cámara, y el tiempo, como bien concluiría Desantes et al. [66]. La creciente influencia del flujo interno en el desarrollo de la inyección y combustión ganaba fuerza entre la literatura, como demostraba la necesidad de incluir parámetros geométricos de la tobera en las ecuaciones de definición de la evolución de la penetración del chorro. Respecto a esta última afirmación, tanto Hiroyasu como Arai enunciaron el efecto de los parámetros diámetro de salida y ratio longitud diámetro (l/d) sobre el chorro. A grandes rasgos, valores l/d menores tendían a reducir la longitud de rotura mientras que valores mayores del diámetro la aumentaban, sin embargo y aunque dejaban resultados interesantes, los parámetros seleccionados no tenían en cuenta elementos más complejos de la geometría. Otros autores, como Reitz et al. [67] estudiaron sus efectos a través de visualización directa con cámaras rápidas de la zona cercana a las toberas. En su estudio, consideró distintos parámetros geométricos de la tobera: ratio l/d, conicidad y redondeo de la sección de entrada y relacionó los valores del ángulo del chorro en condiciones Diesel con los distintos parámetros de las toberas seleccionadas y las condiciones de inyección. Entre sus resultados destaca la importancia de las propiedades del combustible y, concretamente, la viscosidad, obteniendo una variación inversa del valor del ángulo con ésta; la obtención de valores mayores de ángulo al disminuir el ratio l/d; y la obtención también de valores mayores al disminuir el ratio de densidades. Es más, en sus discusiones expone que, dada la existencia de distintos valores en el ángulo para un mismo punto de operación en toberas con un mismo diámetro de salida, las diferencias encontradas deben deberse a las variaciones experimentadas por el flujo interno producidas por las diferencias en la geometría interna. Reitz concluye que, un solo mecanismo, ya sean las fuerzas inerciales, las de interacción aerodinámica o las turbulentas del fluido, no es capaz de explicar por sí mismo el comportamiento de la atomización por completo y, por tanto, todos ellos han de ser tenidos en cuenta en el estudio de la mezcla. Los estudios de Reitz sobre la evolución del proceso de rotura [68-70] darían lugar a los modelos *blob* de rotura en los que, sobre un diámetro inicial de la columna líquida, se aplican sus teorías de la inestabilidad inicial de onda, muy usados actualmente. Otros trabajos continuarían todos estos pensamientos, Wu et al. [71, 72], estudió como la geometría de una tobera podía afectar al desarrollo de la vena líquida y al inicio de la atomización. Aunque los experimentos de su trabajo se realizaron en unas condiciones alejadas de las de funcionamiento de un inyector Diesel, algunas de sus conclusiones pueden ser trasladadas a geometrías de toberas convencionales, como otorgar un peso especial a las condiciones turbulentas a la salida del orificio en la germinación de la rotura de la vena líquida. La relación entre la longitud de la tobera y el

diámetro del orificio también fue objeto de interés en [72]. Wu et al. muestra que una relación l/d elevada puede favorecer que el flujo desarrolle un perfil turbulento completo. Sin embargo, esta condición se relaja en toberas reales de inyección dada la mayor velocidad de los flujos y, las ya de por sí, complejas características geométricas que poseen y que inducen dicho fenómeno. El estudio del flujo interno desde el punto de vista numérico supondría un gran avance en la comprensión de la influencia de la geometría sobre el mismo. Sin embargo, este tipo de trabajos computacionales no llegarían hasta la década de los 90 y principios del siguiente milenio, donde las simulaciones, dotadas de más medios, adquieren la entidad suficiente para replicar las detalladas geometrías de inyección.

La difusión de los métodos computacionales en el estudio de la inyección produjo que durante los años 80 y 90 comenzasen a asentarse ciertos modelos de cálculo, a esto contribuyó en parte el nacimiento de los primeros códigos CFD. La aproximación física de la inyección seguiría siendo eminentemente Euleriana-Lagrangiana hasta los últimos años del pasado siglo y las soluciones más artesanales de los años anteriores se verían normalizadas hacia ciertos estándares junto con las ecuaciones empleadas, especialmente en lo relativo a los modelos turbulentos, y los algoritmos de resolución. Algunos de los modelos de cierre del problema turbulento más empleados en la actualidad vieron la luz en estos años, destacando los modelos Reynolds Averaged Navier-Stokes (RANS) de dos ecuaciones como el $k-\epsilon$ [34], más adecuado para chorro libre y alto número de Reynolds, o el $k-\omega$ desarrollado por Wilcox [73], más enfocado en flujos con una alta importancia de los bajos números de Reynolds o flujos confinados.

Con el comienzo de las restricciones en las emisiones, el estudio de la combustión intentaba ahora replicar los términos de las medidas experimentales tanto en eficiencia como en los residuos generados. Hiroyasu et al. [74, 75] empleó un modelo propio basado en una división por paquetes del chorro, donde el combustible evolucionaba en cámara según una ley de penetración [63]. Al modelo principal de inyección se acoplaron un modelo para el cálculo del calor liberado y otro para las emisiones de hollín y NO. Aunque los cálculos del rendimiento del motor fueron aceptablemente fiables, la precisión de los modelos de emisiones era deficiente, pudiendo predecir tendencias pero no valores absolutos. De forma similar pero empleando el código KIVA [76], uno de los primeros software CFD de carácter más comercial, O'Rourke [77] estudió la inyección directa (n-octano) con combustión mediante un modelo discreto de gotas sobre una geometría de cilindro y pistón móvil. La masa de combustible introducida en el cilindro seguía una ley de inyección experimental que definía la velocidad de inyección mientras que el ángulo de las gotas inyectadas era calculado proporcionalmente al cuadrado de la relación de densidades y un coeficiente de corrección. El tamaño de las gotas de entrada dependía de un coeficiente empírico. Se encontraron fuertes dependencias entre los parámetros

de la inyección (velocidad de inyección, tamaño de las gotas inyectadas...) y las variaciones en cámara, haciéndose patente la importancia de la correcta definición de los parámetros de inyección. En general, el modelo no conseguía comportarse adecuadamente ni en los parámetros de rendimiento ni en las concentraciones resultantes, dándose los mejores resultados en los casos a alta carga mientras que, a baja carga, las discrepancias frente a las medidas experimentales aumentaban considerablemente. Pese a todo, la capacidad de incluir los nuevos métodos de turbulencia, las leyes de pared, geometrías móviles y nuevos modelos de generación de calor y emisiones fue un paso sorprendente en el potencial predictivo de los modelos numéricos aplicados a los sistemas de inyección directa.

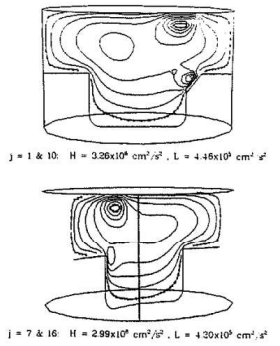

Fig. 23. Contour plots of specific turbulent kinetic energy at 58° BTDC.

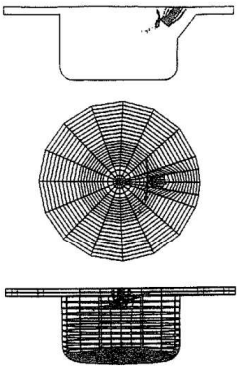

Fig. 24. Spray particle position plots at 13° BTDC.

Figura 1.5: Detalle de algunos de los resultados de O'Rourke [77], distribución de energía cinética turbulenta, mallado y partículas de combustible inyectado.

Zellat et al. [78], como O'Rourke, estudió la combustión en este caso Diesel en precámara empleando también el código KIVA. Para ello se vio obligado a modelar el sistema de precámara acoplado al cilindro junto con un modelo de pistón móvil (Figura: 1.6) para ejecutar la compresión. Con un modelo propio de combustión derivado de sus investigaciones, estudió el efecto del tiempo de inyección y la carga sobre el desarrollo de la inyección y analizó el efecto de la geometría de la precámara y del pistón sobre la mezcla dentro del cilindro. En ausencia de validación de las emisiones generadas, sus resultados numéricos consiguieron acercarse bastante a los experimentales en términos de presión en el cilindro para todos los puntos de operación. La posibilidad de incorporar geometrías realistas junto con la inclusión de nuevos submodelos de cálculo reactivo y de emisiones, entre otros, aunque no fueran validados en todas sus facetas, iba aumentando ese potencial predictivo al que aspiraban este tipo de trabajos.

Hay que mencionar que las técnicas experimentales de medida aplicadas a los sistemas de inyección y combustión evolucionaron a medida que lo hacía la electrónica. Los dispositivos de captación de datos (presión, temperatura,

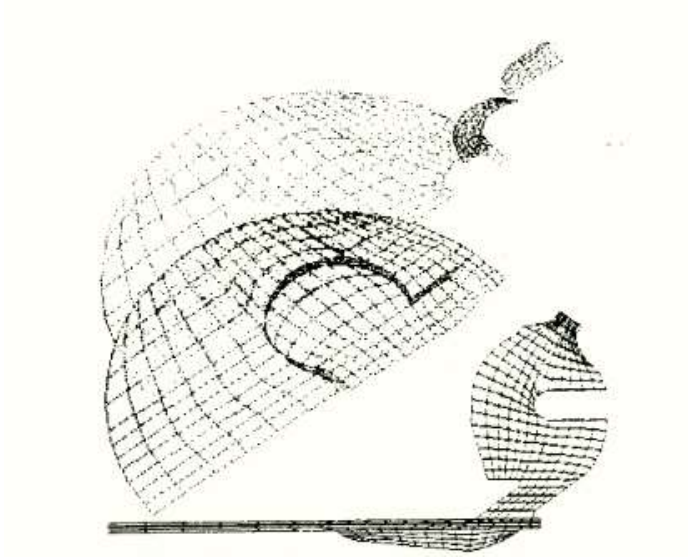

Figura 1.6: Malla empleado por Zellat et al. para modelado de pistón y precámara, de [78].

emisiones...) mejoraron en resolución y precisión y disminuyeron en tamaño. La visualización del chorro, por iluminación directa o la técnica de Schlieren, fue complementada con el uso de las cámaras rápidas digitales. Naber y Siebers [79] siguiendo la obra de autores como Hiroyasu, utilizaron este tipo de dispositivos para visualizar la dependencia de la penetración y el ángulo del chorro de las condiciones de inyección. Sus investigaciones consiguen ampliar y sintentizar las conclusiones de autores anteriores sobre un sistema common-rail de inyección moderno. Conectando el sistema a un inyector mono-orificio, se tomaron medidas en condiciones evaporativas y no evaporativas hasta 1600 bar de presión de inyección y $124\,\mathrm{kg\,m^{-3}}$ de densidad en cámara. Estos autores ejecutaron una extensa matriz de ensayos utilizando diferentes toberas previamente caracterizadas por su conicidad, ratio l/d y comportamiento hidráulico dado por los coeficientes de descarga, área y velocidad. Las imágenes tomadas con las cámaras rápidas empleando la técnica de Schlieren sirvieron para analizar el contorno de los chorros en las diferentes condiciones. Corroboraron el valor del ángulo como un factor independiente de la presión de inyección y como el valor estacionario del mismo determinaba proporcionalmente el aire englobado por el chorro. Al analizar los valores de ángulo frente a los parámetros geométricos de las toberas seleccionadas para el estudio, concluyeron que no se podía establecer una relación directa entre los diámetros de los orificios de salida, sino que había que considerar otros parámetros de la morfología de la tobera. Esta conclusión debe ser resaltada si se tiene en cuenta que los autores [80] solían considerar únicamente el diámetro como medida geométrica relevante. Naber y Siebers, incluyeron los efectos de la geometría a través

de la incorporación no solo del coeficiente de descarga o el diámetro como ya hicieran Dent et al. [81] o Hiroyasu et al. [60] sino a través del coeficiente de velocidad y de área. A parte de los métodos de iluminación ya mencionados, surgieron nuevos sistemas ópticos con la utilización de sistemas de luz láser para medir velocidades y distribuciones de gotas como los PDA (*Phase Doppler Anemometry*) [82, 83] y variantes posteriores. Dentro del cilindro, la comprensión de la combustión mejoró con nuevos montajes, como los empleados por Allen et al. [84] o Schefer et al. [85] entre otros [86, 87], donde un haz pulsado láser configurado en una determinada frecuencia de emisión era utilizado para excitar e iluminar moléculas específicas, y donde un emisor de luz ultra-violeta se empleaba para iluminar el OH resultante de la combustión. Los nuevos datos experimentales, ahora más fiables y detallados repercutían también en los modelos numéricos. Como se ha dicho, el interior de las toberas de inyección recogía cada vez más el interés de los investigadores, situación en parte promovida por una mayor cantidad de datos que abrían el paso a nuevas líneas de investigación. Aunque el modelado de las toberas ya se realizaba con sistemas 0D y 1D como el presentado por Catania et al. [88] o Tokuta et al. [89] para la predicción de señales de tasa entre otros valores, es en estos años (a principios de los 90), cuando aparecen los primeros estudios enfocados en la resolución del flujo interno. Kano et al. [90], resolvió las ecuaciones de Navier-Stokes sobre geometrías bidimensionales de toberas VCO (*Valve Covered Orifice*) Diesel con intención de aportar soluciones que mejoraran la atomización sin necesidad de emplear altas presiones de inyección. En cuanto a estudios tridimensionales, uno de los primeros se puede encontrar en el trabajo de Bruni et al. [91], en el que se analiza una geometría de un inyector de 5 orificios Diesel en un software comercial. Presentando cada orificio una inclinación diferente respecto al plano perpendicular al eje del inyector, la totalidad de la geometría se discretizaba con 48960 elementos. Lo comedido de este refinamiento sugiere una precisión pobre de los resultados, que no se validan experimentalmente, y más teniendo en cuenta la ausencia de modelos de cavitación en una tobera sin ningún tipo de hidroerosión o redondeo a la entrada. Bien es verdad, que las presiones de inyección aplicadas eran moderadamente bajas (400 bar) y que, por tanto, es posible que las imprecisiones por omitir este efecto se vieran minimizadas. Aún así, se efectúa un análisis detallado de los resultados del flujo interno teniendo en cuenta distintas alturas y desviaciones de la aguja de inyección. Entre los valores analizados se encontraban la masa por orificio y la energía del flujo por orificio según la posición de la aguja. Estos parámetros, difícilmente observables experimentalmente, recogen la importancia de estas simulaciones que, previa validación de los modelos, permitirían medir, entre otras cosas, comportamientos individuales de los orificios que pudieran afectar a la mezcla. La simulaciones de flujo interno adquieren una notable sinergia con el resto de medidas experimentales, como demuestra Koo et al. [92], en un artículo que aúna el estudio computacional del flujo interno y la medición del chorro resultante en diferentes toberas. En éste, se estudia el flujo

interno de toberas a escala (x100) junto con simulaciones 3D intentando vincular condiciones especiales del flujo, como la cavitación, con los parámetros adimensionales de la tobera y el comportamiento del chorro. La investigación mostró efectos tan importantes como la reducción brusca del coeficiente de descarga bajo condiciones de *hydraulic-flip* y como la cavitación podía favorecer la atomización. Todas estas conclusiones se vincularon con los diferentes parámetros geométricos y con la turbulencia detectada a la salida de las toberas en las simulaciones de flujo interno. Koo et al. tuvo que emplear geometrías a escala para poder realizar este tipo de estudios manifestando así la dificultad de medir las condiciones directamente en toberas reales. Los efectos de turbulencia y cavitación junto con la problemática de acceder a lo que ocurría en el interior de las toberas llevó a investigadores como Chaves et al. [93, 94] y Soteriou [95] a retomar las ideas de Berwerk et al [13] de mediados del siglo pasado, fabricando toberas transparentes en las que poder observar libremente el flujo interno. Con las nuevas tecnologías de medida y la capacidad de comparar sus resultados con el cálculo del flujo, los datos obtenidos cobraban nueva relevancia. Sobre una tobera mono-orificio sin redondeo a la entrada y de tamaño similar a las toberas Diesel, Chaves [93] analizó la evolución de la cavitación en función de la contrapresión y presión de inyección aplicada hasta los 1000 bar. Observó la relación entre la estabilización del coeficiente de descarga en puntos con cavitación desarrollada y su independencia o ligera disminución frente a aumentos subsecuentes de la presión de inyección. Más tarde, extendería sus estudios al detalle de la geometría, por ejemplo, observando el efecto de diferentes radios de redondeo a la entrada de las toberas [94]. Soteriou [95] por su parte, se enfocó en la variación del área efectiva debido a la cavitación. Numéricamente, Kampmann et al. [96] también se interesó por el efecto de la forma de la geometría a través del radio de entrada. Empleando un número total de elementos cercano al utilizado por Bruni et al. [91], simuló un solo sector de un inyector Diesel aplicando condiciones de simetría a una presión de hasta 400 bar, resultando un dominio mucho más refinado. Estudió el comportamiento del flujo para distintos grados de hidroerosión, aunque sin aplicar ningún modelo de cavitación y, al igual que en el caso de Bruni, esto restaba fiabilidad a los valores finales. Sin embargo, sus conclusiones sobre la influencia de la ausencia de ángulo de redondeo en la turbulencia seguían la línea de autores precedentes. Un paso más allá lo dio Arcoumanis et al. [97] que utilizó un modelo transparente a escala (x20) de los seis orificios de un inyector Diesel y su equivalente en modelo numérico teniendo en cuenta fenómenos de cavitación. Dicha configuración experimental era capaz de medir individualmente el flujo por cada uno de los orificios y de visualizar internamente las toberas. También pudo comprobar las zonas de recirculación a la entrada de las mismas y la desviación en el flujo por orificio producida por la asimetría en la manufactura. A bajo levantamiento de aguja, era posible detectar como la cavitación comenzaba en el asiento de ésta en vez de en la parte superior de la entrada del orificio. La cavitación en toberas Diesel

fue ampliamente discutida por autores como Schmidt et al. [98-102] con una contribución notable al uso y generación de modelos matemáticos. Schmidt [99] consideró fenómenos de compresibilidad tanto para la fase líquida como para la gaseosa derivada de la nucleación y dos modelos para la cavitación, Homogeneous Equilibrium Model (HEM) y Homogeneous Relaxation Model (HRM) [103-105] que mostraron, aunque con diferencias según la condición del problema, buenos comportamientos frente a las validaciones experimentales. En una de sus conclusiones defiende que la aparición de la fase gaseosa generaba un estrechamiento del área efectiva disponible para el trasiego del flujo desplazando ésta hacia el centro de la tobera. La contracción generada repercutía entonces en una aceleración del fluido hacia una velocidad considerablemente mayor que la propuesta por los valores medidos de flujo másico. Los trabajos en este campo de la inyección directa mostrarían la necesidad de incluir los fenómenos de flujo interno, especialmente la cavitación en los modelos de chorro. El efecto de la geometría en el flujo interno sería estudiado también por Arcoumanis et al. [106], Giannadakis et al. [107], Gavaieses et al. [108] y Andriotis et al. [109] con trabajos muy relacionados y sobre las líneas de investigación del primero. Aunque la forma general de aproximar los problemas multifásicos del flujo interno solían ser los marcos Eulerianos, bien con modelos de mezcla o Volume-Of-Fluid (VOF) [110, 111]. Andriotis et al. [109] empleó una aproximación Euleriana-Lagrangiana para modelar este fenómeno con buenos resultados y donde el vapor es tratado como la fase dispersa. Como se puede observar, el interés en la literatura por el flujo interno en las toberas de inyección se disparó en comparación a las décadas anteriores. Los investigadores intentaban ahora aumentar los detalles, ejemplificados en nuevos modelos de cavitación, o con la anexión de otros factores al modelado que pudieran reflejar mejor los comportamientos experimentales. Payri et al. [112-118] y Salvador et al. [119-124] son un buen exponente de este hacer, con una extensa contribución al estudio de la geometría y de los efectos de esta sobre el flujo interno y el chorro.

Sus investigaciones combinan técnicas experimentales y numéricas para estudiar diversos aspectos de la inyección. Salvador et al. [119], estudió la interacción entre cavitación y turbulencia en una tobera Diesel empleando un modelo Large Eddy Simulation (LES) validado experimentalmente. Los resultados numéricos mostraron a un nivel detallado como las zonas origen de la cavitación presentaban una mayor turbulencia y un mayor desarrollo de vórtices siendo la zona entre las fases líquidas y gaseosa, la más crítica en estos términos. Utilizando moldes de silicona [125], Payri et al [112], extrajo la geometría interna de dos toberas, cónica y cilíndrica, obteniendo los valores de radio de entrada y salida de la tobera, radio medio y radios de hidroerosión. Con la información de la geometría presente, estudió el chorro en condiciones controladas de presión de inyección (200-800 bar) y presión en descarga (60 bar). Su investigación demostró como no solo el radio de curvatura a la entrada

afecta a la aparición de cavitación sino el tipo de sección, donde una sección convergente es menos propensa a generarla. En este sentido, la conicidad reveló tener más peso en la generación de velocidad sobre el flujo que el valor del radio de hidroerosión. Los hallazgos respecto al chorro fueron en línea con lo establecido por la literatura, con valores del chorro mayores para la tobera cilíndrica, más cavitante. Payri y sus colaboradores [126] extendieron la influencia de la tobera a la combustión ensayando toberas con diferentes grados de conicidad (alta, media y sin conicidad) y distintos diámetros de salida, y midiendo con técnicas de quimioluminiscencia los radicales CH y OH generados. La importancia de discernir los efectos de la geometría en las variables integrales del flujo llevó a Payri et al [113] a utilizar un montaje experimental dedicado que permitía, mediante un sensor piezo-eléctrico de presión, medir la fuerza de impacto del chorro. Así, junto con los valores de flujo másico era entonces posible calcular las velocidades efectivas del chorro y derivar medidas de área efectiva en la tobera. El avance de los trabajos en la materia llevó a considerar también el comportamiento de las propiedades físicas de los combustibles y como éstas eran afectadas por los efectos termohidráulicos del flujo [127] pudiendo después trasladar los resultados a los modelos numéricos [124]. La expansión de las capacidades de los modelos de cálculo, más fiables y validados por un trasfondo amplio de experiencia y literatura, ha permitido a los investigadores explorar nuevas geometrías de toberas evitando tener que recurrir a una manufactura previa para confiar en los resultados. Molina et al. [128], examinó el efecto de secciones elípticas sobre el flujo interno. Tomando excentricidades de 0.73 y 0.86, comparó estas toberas con variaciones en la disposición del eje mayor, tanto en vertical como en horizontal, con su equivalente circular. Añadiendo a las ecuaciones del flujo un modelo de cavitación barotrópico, las toberas se simularon a presiones de inyección de 1600 y 300 bar y contrapresiones de entre 30 y 90 bar. Basándose en el mayor perímetro de interacción de las toberas elípticas y en las condiciones del flujo interno analizadas, Molina et al. se aventuró a extrapolar un mejor comportamiento de las toberas elípticas en un hipotético proceso de mezcla en comparación con las circulares. Utilizando toberas transparentes, Hong et al. [129], también indagó en este tipo de secciones cavitantes, pudiendo visualizar directamente el flujo a través de la pared de las toberas utilizando agua como fluido de trabajo. Aunque las escalas empleadas en las toberas eran de un orden de magnitud mayor que las empleadas en los orificios de toberas Diesel reales y las condiciones de ensayo distaban mucho de las de un motor, el efecto de la excentricidad alteraba notablemente el chorro, mostrando la tobera de sección elíptica una mejor atomización y un mayor ángulo. Ku et al. [130], desarrolló la investigación de Hong et al. midiendo el tamaño de gotas en este tipo de toberas y analizando numéricamente el flujo interno. Los resultados mostraron que los tamaños de gotas obtenidos en las toberas elípticas fueron menores o iguales a las generadas por la sección circular. Ku también observó como la desintegración de la vena líquida frente al aumento de la presión de

inyección ocurría antes en las toberas elípticas. El efecto de nuevas secciones como éstas también fue puesto a prueba por Yu et al. [131] analizando directamente el efecto de la excentricidad de una tobera real sobre el chorro y donde de igual forma las toberas elípticas mostraron un mejor desempeño con una mayor apertura del chorro. Salvador et al. [122, 132], previa validación de los modelos, estudió geometrías aún más disruptivas, como toberas con secciones convergentes-divergentes. Desde el punto de vista numérico, no era común que los estudios numéricos del flujo interno tuvieran continuidad directa con estudio del chorro o de la combustión. Las aproximaciones para este tipo de estudios numéricos continúan empleando en su mayor parte modelos Eulerianos-Lagrangianos cuyo comportamiento sigue dependiendo de un fuerte factor de calibración. En su evolución, las capacidades de estos modelos se han beneficiado de un mejor modelado de la interacción de las gotas y el gas del volumen de descarga, nuevos modelos de colisión y coalescencia, físicas evaporativas más precisas y de métodos para la representación de la interacción con las paredes de la cámara. De esta forma, las teorías sobre la formación y crecimiento de inestabilidades sobre el chorro se incorporan a través de los modelos de rotura [133], siendo los más comunes el de Kelvin-Helmholtz (KH) [68, 70] como forma de atomización primaria y el de Rayleigh-Taylor (RT) como método de atomización secundaria [77, 134], en lo que respecta a chorros Diesel. Este tipo de modelos dependen principalmente de la cantidad de combustible inyectado y forma de la función de tasa, siendo usual proveer también el ángulo de inyección de las gotas. Las gotas pueden inyectarse según el modelo *blob*, asumiendo un tamaño inicial de gota, o siguiendo una determinada función de probabilidad. Som et al. [135], a través de un modelo discreto de gotas estudió el efecto de geometrías cónicas y cilíndricas sobre algunos de los parámetros de la combustión, Lift-Off Length (LOL), hollín, y óxidos de nitrógeno (NO). Utilizando una tobera cilíndrica como referencia, se estudió y validó primero el flujo interno y posteriormente por separado la combustión. El efecto de la turbulencia derivada de la cavitación se trasladó sobre el diámetro de entrada del *blob* introduciendo el sub-modelo Kelvin Helmholtz-Aerodynamics Cavitation Turbulence (KH-ACT). Para validar el efecto del modelo de atomización por cavitación, entre otras medidas, se contrastaron los resultados numéricos con datos adquiridos por rayos-X en una muestra de lo que sería el estado actual del arte experimental. Som también aplicó esta misma metodología al estudio de la influencia del tipo de combustible sobre el flujo interno y el chorro [136]. A través de la calibración y previa obtención de los datos experimentales requeridos, los modelos Droplet Discrete Modeling (DDM) son capaces de replicar los efectos del flujo interno y, en cierta forma, de la geometría sobre la evolución del chorro. Algunos incluso, los llamados *one-way coupling*, almacenan información de un análisis numérico previo del flujo interno incorporando directamente dicha información en una simulación DDM posterior del flujo externo. Jia et al. [137] utilizó este método para trasladar las características del flujo interno proveniente de toberas elípticas

sobre el chorro. Sin embargo, el modelado discreto en las zonas cercanas a la tobera claramente difiere de la realidad observada, donde la persistencia de una vena de líquido intacta resta validez a los resultados obtenidos por este método. El estado actual del arte en el estudio del chorro, de la mezcla y de la combustión, desde el punto de vista del cálculo numérico, emplea modelos acoplados donde la geometría del flujo interno y la geometría que define el volumen de descarga se simulan solidariamente. Aplicando este sistema, toda la información del flujo interno se traslada íntegramente al chorro sin modelos que hagan de intermediarios. Para este tipo de metodologías es necesario disponer de una información fiable tanto de la geometría en cuestión como de las mecánicas del inyector, en especial del levantamiento de aguja como condicionante de los transitorios del inyector [138, 139]. Actualmente, la extracción de la geometría interna del inyector puede realizarse mediante moldes junto con técnicas de microscopía o mediante tecnologías de rayos-X. Kastengren et al. [140] utilizó y comparó ambos métodos para obtener un representación fiel de la geometría interna de un inyector mono-orificio. Aunque el análisis por moldes es capaz de reflejar con una desviación razonable la geometría, la toma de medidas depende en gran parte de la facilidad de orientar el molde en una posición adecuada según la característica geométrica de interés. Esto puede ser complicado en geometrías multiorificio donde los diferentes orificios pueden interferir entre sí. Por otro lado, las imágenes por contraste de rayos-X no se ven impedidas en este sentido. La capacidad de penetrar a través del material permite también la captación de los transitorio del levantamiento de aguja. Kastengren utilizó la toma de imágenes en diferentes posiciones para reconstruir la geometría 3D por tomografía computerizada. En ausencia de estas tecnologías, un modelo 1D del inyector como el realizado por Salvador et al. y Payri et al. [141, 142] puede servir para replicar su comportamiento hidráulico y con el que obtener, entre otros parámetros, las leyes de levantamiento. Kastengren et al. [143, 144] y Picket el al. [145] también utilizaron rayos-X para estudiar la atomización, obteniendo valores de densidad proyectada del combustible, tamaño de gotas y densidad de área superficial, ángulo o incluso fracción volumétrica de líquido. Tekawade et al. [146] exploró el uso de estas metodologías para analizar el flujo del interior de toberas cavitantes. Utilizando los mismos principios, obtuvo una reconstrucción tanto de la geometría de una tobera cavitante como del flujo en el interior de la misma. Mediante este sistema mostró que es posible distinguir la localización espacial de la fase vapor generada por cavitación y el subsecuente desplazamiento de la fase líquida pudiendo visualizar el estrechamiento del área efectiva. Este tipo de medidas se encuentran limitadas por el carácter repetitivo e integral de las mismas, lo que dificulta su uso en el estudio de los procesos transitorios. Sin embargo, la información que proveen es muy valiosa, no solo para aumentar el conocimiento sobre el comportamiento de toberas reales sino de cara a validar los modelos numéricos. Xue et al. [147] utilizó medidas provenientes en parte de los experimentos de Kastengren, para validar un modelo

acoplado de tobera monorificio y cámara de descarga. Utilizando un modelo VOF junto con un sistema de cierre $k - \epsilon$ de dos ecuaciones, se configuró la aguja móvil sobre la geometría reconstruida por escaneado de rayos-X. El modelo se validó en términos de densidad proyectada, flujo másico y velocidad relativa, donde el refinamiento, especialmente en las zonas cercanas al orificio donde el flujo abandona el confinamiento de la tobera, fue determinante para obtener buenos resultados. Desantes et al. [148, 149], exploró las diferencias entre un modelo $\Sigma - Y$ acoplado y un modelo DDM. Aunque ambos modelos se comportaron bien para un punto de referencia escogido y para el que tuvo lugar la calibración de las constantes de rotura del modelo discreto, la variación de las condiciones de contorno con el correspondiente desplazamiento del punto de referencia perjudicó el desempeño del modelo discreto. Por el contrario, el modelo acoplado consiguió una mejor aproximación al variar el punto de funcionamiento y especialmente en el campo cercano a la tobera al eliminar la dependencia de la calibración. El modelado de la zona dispersa del chorro, cuando la vena líquida ha quedado desintegrada, puede realizarse entonces utilizando modelos Eulerianos, y dentro de estos con modelos de mezcla o de interfase [150], o transicionando a un modelo Lagrangiano [151, 152] pudiendo aplicar entonces las mecánicas tradicionales de los modelos de rotura prescindiendo de la condición inicial de gota y atomización primaria.

Los modelos acoplados introducen una nuevo grado de predicción al sustituir gran parte de las calibraciones tradicionales por aproximaciones más físicas, mucho menos dependientes de parámetros específicos. Como bien mencionaba Desantes [148, 149], este hecho cobra mayor relevancia a efectos de la atomización primaria donde el chorro hereda las variables generadas en el flujo interno consiguiendo así acercarse al comportamiento real del inyector. Sin embargo, la aplicación de estos modelos no está exenta de inconvenientes desde el punto de vista numérico. El modelar el flujo interno junto con los procesos en cámara obliga a introducir una densidad de elementos mucho mayor en la zona de la tobera y en ciertas partes de la cámara adyacentes al orificio. Esta disposición aumenta considerablemente la carga computacional pudiendo ralentizar el cálculo en dominios grandes o en modelos con gran número de ecuaciones. Al mismo tiempo, es innegable que la difusión de este tipo de simulaciones junto con los nuevos datos experimentales abren todo un campo de posibilidades, especialmente en lo que al estudio de los efectos de la geometría sobre el chorro y la combustión se refiere. Retomando los temas planteados al comienzo de esta introducción, los avances desarrollados en los nuevos modelos numéricos permiten estudiar de un modo mucho más profundo toda esta serie de procesos, desde el flujo interno, hasta la distribución del combustible y la combustión posterior de una forma mucho más interrelacionada y acoplada que con los modelos tradicionales. Y dentro de dichas mecánicas, definir el papel que puede jugar la geometría de las toberas de inyección en el balance final. La difusión de estas nuevas metodologías puede permitir el estudio de

nuevas geometrías como forma eficaz de enfrentar las necesidades de reducción de emisiones y como forma de aumentar la eficiencia actuando directamente sobre la fuente de la generación de energía de los motores de combustión.

1.2. Objetivos y estructura de la tesis

Tomando como referencia los párrafos de la introducción anterior, se puede afirmar que existe relación entre la forma de las toberas de inyección y el desarrollo del chorro Diesel. Bajo esta afirmación, esta tesis busca profundizar en este aspecto de los sistemas de inyección mediante una combinación de técnicas numéricas de simulación y experimentales que permitirán el estudio en profundidad del flujo interno, el chorro y la combustión bajo una sólida validación de los resultados numéricos. El objetivo fundamental es, por tanto, el estudio de la influencia de la geometría de las toberas de inyección en el proceso de formación de la mezcla y combustión. El planteamiento de esta meta conlleva el previo desarrollo de metodologías computacionales robustas, donde las tendencias capturadas y resultados otorguen fiabilidad a las conclusiones. De esta forma, el objetivo primario primordial depende, en su base, del cumplimiento de ciertas necesidades entorno al cálculo y a la toma de medidas. Algunas de las más elementales serían: la adopción de los modelos matemáticos más adecuados, la correcta definición de las propiedades de los fluidos de trabajo o la capacidad de definir correctamente las características geométricas de las toberas. Todas estas metas serán extendidas alrededor del objetivo principal a lo largo de cada uno de los capítulos. Este desarrollo es conducido a través de un compendio de artículos que abarcan desde el estudio de la influencia de la geometría en el flujo interno, bajo un importante nivel de detalle termohidráulico, pasando por su influencia sobre el chorro y la combustión empleando toberas comerciales convencionales, y finalizando con el estudio del comportamiento del chorro bajo geometrías más innovadoras de sección elíptica. La forma de esta tesis queda estructurada partiendo de un primer capítulo introductorio (capítulo actual), seguido por el Capítulo 2, centrado en el efecto de la geometría sobre el flujo en la tobera desde una perspectiva termo-hidráulica, y donde se prestará especial atención al modelado de las propiedades del combustible. Mediante el cálculo computacional, en esta parte se observarán los efectos sobre el flujo de una tobera cónica donde los cambios térmicos debidos a la compresibilidad y a la conicidad son relevantes. En el Capítulo 3, se analizan los efectos de la geometría sobre el proceso global de inyección y combustión utilizando dos toberas cónicas multiorificio de diferente ratio longitud diámetro. En esta investigación, materializada a través de un proyecto de cooperación, se han empleado modelos Eulerian-Lagrangian Spray Atomization (ELSA) (híbridos Euleriano-Lagrangiano) y DDM (Lagrangiano) como dos formas distintas de trasladar el efecto de la geometría al chorro y, finalmente, a la combustión. Los resultados de las simu-

laciones se han validado frente a una extensa matriz de ensayos en términos de caracterización hidráulica, penetración y ángulo del chorro en maqueta, y ensayos de combustión en motor. La influencia de la geometría se traslada finalmente al cálculo de los balances de energía en el motor y la mezcla. En el Capítulo 4, se exploran nuevas geometrías susceptibles de mejorar el proceso de mezcla a través del modelo acoplado flujo interno-externo Eulerian Spray Atomization (ESA). Utilizando formas elípticas en la sección de la tobera, se han analizado diferentes grados de excentricidad para medir la influencia de dichas secciones sobre los parámetros de dispersión del chorro. En el Capítulo 5, se enfatiza sobre el efecto de la geometría de sección elíptica distinguiendo entre toberas de sección constante, propensas a la aparición de la cavitación, y toberas de sección cónica. Se han estudiado las variaciones en el comportamiento del flujo interno así como la repercusión en la variación del ángulo y otros parámetros de mezcla. El Capítulo 6 queda dedicado a un comentario final de los resultados obtenidos a lo largo de las diferentes investigaciones resumiendo y resaltando los más importantes. Finalmente, el Capítulo 7 recoge las conclusiones obtenidas y los trabajos futuros.

Bibliografía

[1] A. G. Gelalles. "Coefficients of discharge of fuel-injection nozzles for compression-ignition engines". En: *NACA-TR-373* (sep. de 1932).

[2] Dana W. Lee. "The effect of nozzle design and operating conditions on the atomization and distribution of fuel sprays". En: *NACA Technical Reports* NACA TR 520 (feb. de 1932).

[3] D W Lee. "A Comparison of Fuel Sprays from Several Types of Injection Nozzles". En: *NACA TR 520* (1936).

[4] R.P. Probert. "XV. The influence of spray particle size and distribution in the combustion of oil droplets". En: *The London, Edinburgh, and Dublin Philosophical Magazine and Journal of Science* 37.265 (1946), págs. 94-105. DOI: 10.1080/14786444608561330. eprint: https://doi.org/10.1080/14786444608561330. URL: https://doi.org/10.1080/14786444608561330.

[5] M. M. El Wakil, O. A. Uyehara y P. S. Myers. "A theoretical investigation of the heating-up period of injected fuel droplets vaporizing in air". En: *NACA-TN-3179* (1954).

[6] M. M. El Wakil, P. S. Myers y O. A. Uyehara. "Fuel Vaporization and Ignition Lag in Diesel Combustion". En: *SAE Transactions* 64 (1956), págs. 712-729. ISSN: 0096736X. URL: http://www.jstor.org/stable/44468675 (visitado 15-06-2022).

[7] J R Joyce. "The atomization of liquid fuels for combustion". En: *Journal of the American Society for Naval Engineers* 61.3 (abr. de 1949), págs. 650-663. DOI: 10.1111/j.1559-3584.1949.tb02817.x.

[8] Jr. Forstall Walton y Ascher H. Shapiro. "Momentum and Mass Transfer in Coaxial Gas Jets". En: *Journal of Applied Mechanics* 17.4 (dic. de 1950), págs. 399-408. ISSN: 0021-8936. DOI: 10.1115/1.4010167. eprint: https://asmedigitalcollection.asme.org/appliedmechanics/article-pdf/17/4/399/6746717/399_1.pdf. URL: https://doi.org/10.1115/1.4010167.

[9] P. M. Sforza, M. H. Steiger y N. Trentacoste. "Studies on three-dimensional viscous jets". En: *AIAA Journal* 4.5 (1966), págs. 800-806. ISSN: 00011452. DOI: 10.2514/3.3549.

[10] Nicholas Trentacoste y Pasquale Sforza. "Further experimental results for threedimensional free jets". En: *AIAA Journal* 5.5 (1967), págs. 885-891. ISSN: 00011452. DOI: 10.2514/3.4096.

[11] S. M. DeCorso. "Efect of Ambient and Fuel Pressure on Spray Drop Size". En: *Journal of Engineering for Power* 82.1 (ene. de 1960), págs. 10-18. ISSN: 0022-0825. DOI: 10.1115/1.3672710. URL: https://doi.org/10.1115/1.3672710.

[12] S. M. De Corso y G. A. Kemeny. "Effect of Ambient and Fuel Pressure on Nozzle Spray Angle". En: *Transactions of the American Society of Mechanical Engineers* 79.3 (feb. de 1957), págs. 607-614. ISSN: 0097-6822. DOI: 10.1115/1.4013107. URL: https://doi.org/10.1115/1.4013107.

[13] W. Bergwerk. "Flow Pattern in Diesel Nozzle Spray Holes". En: 1959.

[14] W. T. Lyn y E. Valdmanis. "The Application of High Speed Schlieren PhotographY to Diesel Combustion Research". En: *The Journal of Photographic Science* 10.2 (1962), págs. 74-82. DOI: 10.1080/00223638.1962.11736841. URL: https://doi.org/10.1080/00223638.1962.11736841.

[15] W. T. Lyn. "Study of burning rate and nature of combustion in diesel engines". En: *Symposium (International) on Combustion* 9.1 (1963), págs. 1069-1082. ISSN: 0082-0784. DOI: 10.1016/S0082-0784(63)80112-5. URL: https://www.sciencedirect.com/science/article/pii/S0082078463801125.

[16] W-T. Lyn y E. Valdmanis. "Second Paper: The Effects of Physical Factors on Ignition Delay". En: *Proceedings of the Institution of Mechanical Engineers: Automobile Division* 181.1 (1966), págs. 34-59. DOI: 10.1243/PIME_AUTO_1966_181_011_02. eprint: https://doi.org/10.1243/PIME_AUTO_1966_181_011_02. URL: https://doi.org/10.1243/PIME_AUTO_1966_181_011_02.

[17] R. Watts y W. M. Scott. "Air Motion and Fuel Distribution Requirements in High-Speed Direct Injection Diesel Engines". En: *Proceedings of the Institution of Mechanical Engineers, Conference Proceedings* 184.10 (1969), págs. 181-191. DOI: 10.1243/PIME_CONF_1969_184_331_02. eprint: https://doi.org/10.1243/PIME_CONF_1969_184_331_02. URL: https://doi.org/10.1243/PIME_CONF_1969_184_331_02.

[18] Sarah T. Bushnell. *The truth about Henry Ford*. 1922.

[19] A. E. W. Austen y W.-T. Lyn. "Relation between Fuel Injection and Heat Release in a Direct-Injection Engine and the Nature of the Combustion Processes". En: *Proceedings of the Institution of Mechanical Engineers: Automobile Division* 14.1 (1960), págs. 47-62. DOI: 10.1243/PIME_AUTO_1960_000_011_02. eprint: https://doi.org/10.1243/PIME_AUTO_1960_000_011_02. URL: https://doi.org/10.1243/PIME_AUTO_1960_000_011_02.

[20] B. E. Knight. "Fuel-Injection System Calculations". En: *Proceedings of the Institution of Mechanical Engineers: Automobile Division* 14.1 (1960), págs. 25-33. DOI: 10.1243/PIME_AUTO_1960_000_009\

_02. eprint: https://doi.org/10.1243/PIME_AUTO_1960_000_009_02. URL: https://doi.org/10.1243/PIME_AUTO_1960_000_009_02.

[21] E. Giffen y A. Muraszew. *The Atomisation of Liquid Fuels*. Chapman & Hall, University of Michigan, 1953.

[22] F. A. Williams. "Spray Combustion and Atomization". En: *The Physics of Fluids* 1.6 (1958), págs. 541-545. DOI: 10.1063/1.1724379. eprint: https://aip.scitation.org/doi/pdf/10.1063/1.1724379. URL: https://aip.scitation.org/doi/abs/10.1063/1.1724379.

[23] G Sitkei. *Contribution to the theory of jet atomization*. 1-2. 1959, págs. 474-480.

[24] Mitutosi Kawaguti. "Numerical Solution of the Navier-Stokes Equations for the Flow around a Circular Cylinder at Reynolds Number 40". En: *Journal of the Physical Society of Japan* 8 (1953), págs. 747-757.

[25] Mitutosi Kawaguti. "Numerical Solution of the Navier-Stokes Equations for the Flow in a Two-Dimensional Cavity". En: *Journal of the Physical Society of Japan* 16.11 (1961), págs. 2307-2315. DOI: 10.1143/JPSJ.16.2307.

[26] Information Processing Society of Japan. *PC1, operation panel and indicators*. 1958. URL: http://museum.ipsj.or.jp/en/computer/dawn/0016.html.

[27] Alexandre Joel Chorin. "A numerical method for solving incompressible viscous flow problems". En: *Journal of Computational Physics* 2.1 (1967), págs. 12-26. ISSN: 0021-9991. DOI: https://doi.org/10.1016/0021-9991(67)90037-X. URL: https://www.sciencedirect.com/science/article/pii/002199916790037X.

[28] Alexandre Joel Chorin. "Numerical Solution of the Navier-Stokes Equations". En: *Mathematics of Computation* 22.104 (1968), págs. 745-762. ISSN: 00255718, 10886842. URL: http://www.jstor.org/stable/2004575 (visitado 13-06-2022).

[29] G. W. Brown y H. McCallion. "Simulation of an Injection System with Delivery Pipe Cavitation Using a Digital Computer". En: *Proceedings of the Institution of Mechanical Engineers, Conference Proceedings* 182.12 (1967), págs. 206-216. DOI: 10.1243/PIME_CONF_1967_182_374_02. eprint: https://doi.org/10.1243/PIME_CONF_1967_182_374_02. URL: https://doi.org/10.1243/PIME_CONF_1967_182_374_02.

[30] N. D. Whitehouse y R. Way. "Rate of Heat Release in Diesel Engines and Its Correlation with Fuel Injection Data". En: *Proceedings of the Institution of Mechanical Engineers, Conference Proceedings* 184.10 (1969), págs. 17-27. DOI: 10.1243/PIME_CONF_1969_184_315_02. eprint: https://doi.org/10.1243/PIME_CONF_1969_184_315_02. URL: https://doi.org/10.1243/PIME_CONF_1969_184_315_02.

[31] Frediano V. Bracco. "Introducing a New Generation of More Detailed and Informative Combustion Models". En: *1975 Automotive Engineering Congress and Exposition*. SAE International, feb. de 1975. DOI: https://doi.org/10.4271/751187. URL: https://doi.org/10.4271/751187.

[32] F. V. Bracco et al. "Two-Phase, Two-Dimensional, Unsteady Combustion in internal Combustion Engines; Theoretical-Experimental Results". En: *1976 Automotive Engineering Congress and Exposition*. SAE International, feb. de 1976. DOI: https://doi.org/10.4271/760114. URL: https://doi.org/10.4271/760114.

[33] Herman Schlichting. *Boundary-layer theory*. McGraw-Hill Book Co., 1969.

[34] B. E. Launder y D. B. Spalding. "Mathematical Models of Turbulence". En: *Academic Press, London* ().

[35] B. E. Launder y D. B. Spalding. "The numerical computation of turbulent flows". En: *Computer Methods in Applied Mechanics and Engineering* 3.2 (1974), págs. 269-289. ISSN: 00457825. DOI: 10.1016/0045-7825(74)90029-2. arXiv: 1204.1280v1.

[36] B.E. Launder y B.I. Sharma. "Application of the energy-dissipation model of turbulence to the calculation of flow near a spinning disc". En: *Letters in Heat and Mass Transfer* 1.2 (nov. de 1974), págs. 131-137. ISSN: 00944548. DOI: 10.1016/0094-4548(74)90150-7. URL: https://linkinghub.elsevier.com/retrieve/pii/0094454874901507.

[37] W.P Jones y B.E Launder. "The prediction of laminarization with a two-equation model of turbulence". En: *International Journal of Heat and Mass Transfer* 15.2 (1972), págs. 301-314. ISSN: 0017-9310. DOI: https://doi.org/10.1016/0017-9310(72)90076-2. URL: https://www.sciencedirect.com/science/article/pii/0017931072900762.

[38] D. B. Spalding. "Predicting the Performance of Diesel Engine Combustion Chambers". En: *Proceedings of the Institution of Mechanical Engineers, Conference Proceedings* 184.10 (1969), págs. 241-299. DOI: 10.1243/PIME_CONF_1969_184_336_02. eprint: https://doi.org/10.1243/PIME_CONF_1969_184_336_02. URL: https://doi.org/10.1243/PIME_CONF_1969_184_336_02.

[39] K. H. Ng y D. B. Spalding. "Turbulence Model for Boundary Layers near Walls". En: *The Physics of Fluids* 15.1 (1972), págs. 20-30. DOI: 10.1063/1.1693739. URL: https://aip.scitation.org/doi/abs/10.1063/1.1693739.

[40] S. B. Pope. "An explanation of the turbulent round-jet/plane-jet anomaly". En: *AIAA Journal* 16.3 (1978), págs. 279-281. ISSN: 00011452. DOI: 10.2514/3.7521.

[41] S.B Pope. "The calculation of turbulent recirculating flows in general orthogonal coordinates". En: *Journal of Computational Physics* 26.2 (1978), págs. 197-217. ISSN: 0021-9991. DOI: https://doi.org/10.1016/0021-9991(78)90091-8. URL: https://www.sciencedirect.com/science/article/pii/0021999178900918.

[42] D. B. Spalding. "Theory of Particle Combustion at High Pressures". En: *ARS Journal* 29.11 (1959), págs. 828-835. DOI: 10.2514/8.4918. eprint: https://doi.org/10.2514/8.4918. URL: https://doi.org/10.2514/8.4918.

[43] D. B. Spalding. "Computational fluid dynamics and its application to liquid-atomisation and spray systems". En: *IN: ICLASS-85; Proceedings of the Third International Conference on Liquid Atomisation and Spray Systems* 2 (ene. de 1986).

[44] D. Adler y W-T. Lyn. "The Evaporation and Mixing of a Liquid Fuel Spray in a Diesel Air Swirl". En: *Proceedings of the Institution of Mechanical Engineers, Conference Proceedings* 184.10 (1969), págs. 171-180. DOI: 10.1243/PIME_CONF_1969_184_330_02. eprint: https://doi.org/10.1243/PIME_CONF_1969_184_330_02. URL: https://doi.org/10.1243/PIME_CONF_1969_184_330_02.

[45] D Adler y W.T Lyn. "The steady evaporation and mixing of a spray in a gaseous swirl". En: *International Journal of Heat and Mass Transfer* 14.6 (1971), págs. 793-812. ISSN: 0017-9310. DOI: https://doi.org/10.1016/0017-9310(71)90108-6. URL: https://www.sciencedirect.com/science/article/pii/0017931071901086.

[46] A. D. Gosman et al. *Heat and Mass Transfer in Recirculating Flows*. Academic Press, London. Illustrated., 1969.

[47] L. Caretto, A. Gosman, S. Patankar y D. Spalding. "Two Calculation Procedures for Steady, Three-Dimensional Flows With Recirculation". En: vol. 2. 1972, págs. 60-68. ISBN: 978-3-540-06171-7. DOI: 10.1007/BFb0112677.

[48] A. D. Gosman y R. J. R. Johns. "Computer Analysis of Fuel-Air Mixing in Direct-Injection Engines". En: feb. de 1980. DOI: 10.4271/800091. URL: https://www.sae.org/content/800091/.

[49] A. D. Gosman y E. loannides. "Aspects of Computer Simulation of Liquid-Fueled Combustors". En: *Journal of Energy* 7.6 (1983), págs. 482-490. DOI: 10.2514/3.62687. eprint: https://doi.org/10.2514/3.62687. URL: https://doi.org/10.2514/3.62687.

[50] A. D. Gosman. "Aspects of the simulation of combustion in reciprocating engines". En: *Lecture Notes in Physics, Berlin Springer Verlag*. Ed. por Roland Glowinski, Bernard Larrouturou y Roger Temam. Vol. 241. 1985, págs. 46-73. DOI: 10.1007/BFb0008652.

[51] L. C. Haselman y C. K. Westbrook. "A Theoretical Model for Two-Phase Fuel Injection in Stratified Charge Engines". En: *1978 Automotive Engineering Congress and Exposition*. SAE International, feb. de 1978. DOI: https://doi.org/10.4271/780318. URL: https://doi.org/10.4271/780318.

[52] Anthony A. Amsden y Cyril W. Hirt. "YAQUI: an arbitrary Lagrangian–Eulerian computer program for fluid flow at all speeds". En: 1973.

[53] C. T. Crowe, M. P. Sharma y D. E. Stock. "The Particle-Source-In Cell (PSI-CELL) Model for Gas-Droplet Flows". En: *Journal of Fluids Engineering* 99.2 (jun. de 1977), págs. 325-332. ISSN: 0098-2202. DOI: 10.1115/1.3448756. eprint: https://asmedigitalcollection.asme.org/fluidsengineering/article-pdf/99/2/325/5899536/325_1.pdf. URL: https://doi.org/10.1115/1.3448756.

[54] John K. Dukowicz. "A particle-fluid numerical model for liquid sprays". En: *Journal of Computational Physics* 35.2 (1980), págs. 229-253. ISSN: 0021-9991. DOI: https://doi.org/10.1016/0021-9991(80)90087-X. URL: https://www.sciencedirect.com/science/article/pii/002199918090087X.

[55] W. A. Sirignano. "The Formulation of Spray Combustion Models: Resolution Compared to Droplet Spacing". En: *Journal of Heat Transfer* 108.3 (ago. de 1986), págs. 633-639. ISSN: 0022-1481. DOI: 10.1115/1.3246983. eprint: https://asmedigitalcollection.asme.org/heattransfer/article-pdf/108/3/633/5745395/633_1.pdf. URL: https://doi.org/10.1115/1.3246983.

[56] A. P. Watkins, A. D. Gosman y B. S. Tabrizi. "Calculation of Three Dimensional Spray Motion in Engines". En: *SAE International Congress and Exposition*. SAE International, abr. de 1986. DOI: https://doi.org/10.4271/860468. URL: https://doi.org/10.4271/860468.

[57] R. A. Castleman. "The Mechanism of Atomization Accompanying Solid Injection". En: 1933.

[58] H. Hiroyasu y T. Kadota. "Fuel droplet size distribution in diesel combustion chamber". En: *SAE International* (1974). DOI: https://doi.org/10.4271/740715.

[59] H. Hiroyasu, M. Shimizu y M. Arai. "The Breakup of a High Speed Jet in a High Pressure Gaseous Atmosphere". En: *Proceedings of the International Conference of Liquid Atomization and Spray Systems (ICLASS-82)* (1982), págs. 69-74.

[60] Hiro Hiroyasu y Masataka Arai. "Structures of Fuel Sprays in Diesel Engines". En: 2002.724 (feb. de 1990). DOI: 10.4271/900475. URL: https://www.sae.org/content/900475/.

[61] Hiroyuki Hiroyasu. "Spray Breakup Mechanism from the Hole-type Nozzle and its Applications". En: *Automization and Sprays: Journal of the International Institutions for Liquid Atomization and Spray Systems* 10 (mayo de 2000), págs. 511-527. DOI: 10.1615/AtomizSpr.v10.i3-5.130.

[62] Hiro Hiroyasu y Haiyan Miao. "Measurement and Calculation of Diesel Spray Penetration". En: *Proceedings of ICLASS Conference* October (2003). URL: http://www.ilasseurope.org/ICLASS/iclass2003/fullpapers/1413.pdf.

[63] M Arai, M Tabata, H Hiroyasu y M. Shimizu. "Disintegrating Process and Spray Characterization of Fuel Jet Injected by a Diesel Nozzle". En: *SAE Technical Paper* 840275 (1984), pág. 16. DOI: 10.4271/840275. URL: https://www.sae.org/content/840275/.

[64] Hiro Hiroyasu ;Masataka Arai. "Structures of Fuel Sprays in Diesel Engines". En: *SAE Technical Paper* (1990).

[65] Masanori SHIMIZU, Masataka ARAI e Hiroyuki HIROYASU. "Measurements of Breakup Length in High Speed Jet". En: *Bulletin of JSME* 27.230 (1984), págs. 1709-1715. DOI: 10.1299/jsme1958.27.1709.

[66] Jose Maria Desantes, Raul Payri, Francisco Javier Salvador y Jaime Gimeno. "Different Measurement Techniques To Determine Hole To Hole dispersion in a real diesel injector". En: *Proceedings of the FEDSM2006* February 2015 (2006), págs. 1-8. DOI: 10.1115/FEDSM2006-98212.

[67] Rolf D. Reitz y Frediano V. Bracco. "On the dependence of spray angle and other spray parameters on nozzle design and operating conditions". En: *SAE Paper 790494* (1979). DOI: 10.4271/790494.

[68] R. D. Reitz y F. V. Bracco. "Mechanism of atomization of a liquid jet". En: *Physics of Fluids* 25.10 (1982), págs. 1730-1742. ISSN: 10706631. DOI: 10.1063/1.863650.

[69] R. D. Reitz y R. Diwakar. "Effect of drop breakup on fuel sprays". En: *SAE Technical Papers* (1986). ISSN: 26883627. DOI: 10.4271/860469.

[70] R D Reitz. "Mechanisms of atomization processes in high-pressure vaporizing sprays". En: *Atomization and Spray Technology* 3 (1987), págs. 309-337.

[71] P.-K. Wu, L.-K. Tseng y G. M. Faeth. "Primary Breakup in Gas/Liquid Mixing Layers for Turbulent Liquids". En: *Atomization and Sprays* 2.3 (1992), págs. 295-317. ISSN: 1044-5110.

[72] P.-K. Wu, R. F. Miranda y G. M. Faeth. "EFFECTS OF INITIAL FLOW CONDITIONS ON PRIMARY BREAKUP OF NONTURBULENT AND TURBULENT ROUND LIQUID JETS". En: *Atomization and Sprays* 5.2 (1995), págs. 175-196. ISSN: 1044-5110.

[73] David C. Wilcox. "Reassessment of the scale-determining equation for advanced turbulence models". En: *AIAA Journal* 26.11 (1988), págs. 1299-1310. ISSN: 00011452. DOI: 10.2514/3.10041.

[74] Hiroyuki HIROYASU, Toshikazu KADOTA y Masataka ARAI. "Development and Use of a Spray Combustion Modeling to Predict Diesel Engine Efficiency and Pollutant Emissions : Part 1 Combustion Modeling". En: *Bulletin of JSME* 26.214 (1983), págs. 569-575. DOI: 10.1299/jsme1958.26.569.

[75] Hiroyuki Hiroyasu, Toshikazu Kadota y Masataka Arai. "Development and Use of a Spray Combustion Modeling to Predict Diesel Engine Efficiency and Pollutant Emissions : Part 2 Computational Procedure and Parametric Study". En: *Bulletin of JSME* 26.214 (1983), págs. 576-583. DOI: 10.1299/jsme1958.26.576.

[76] A. A. Amsden, T. D. Butler, P. J. O'Rourke y J. D. Ramshaw. "KIVA-A Comprehensive Model for 2-D and 3-D Engine Simulations". En: SAE International Congress y Exposition, mar. de 1985. DOI: https://doi.org/10.4271/850554. URL: https://doi.org/10.4271/850554.

[77] Peter J. O'Rourke y Anthony A. Amsden. "Three Dimensional Numerical Simulations of the UPS-292 Stratified Charge Engine". En: *SAE International Congress and Exposition*. SAE International, feb. de 1987. DOI: https://doi.org/10.4271/870597. URL: https://doi.org/10.4271/870597.

[78] M. Zellat, Th. Rolland y F. Poplow. "Three Dimensional Modeling of Combustion and Soot Formation in an Indirect Injection Diesel Engine". En: *International Congress & Exposition*. SAE International, feb. de 1990. DOI: https://doi.org/10.4271/900254. URL: https://doi.org/10.4271/900254.

[79] Jeffrey Naber y L. Dennis. "Effects of Gas Density and Vaporization on Penetration and Dispersion of Diesel Sprays". En: (1996), pág. 960034. ISSN: 0148-7191. DOI: 10.4271/960034. URL: http://papers.sae.org/960034/.

[80] N. Hay y P. L. Jones. "Comparison of the Various Correlations for Spray Penetration". En: *National Farm, Construction, Industrial Machinery, Powerplant Meeting*. SAE International, feb. de 1972. DOI: https://doi.org/10.4271/720776. URL: https://doi.org/10.4271/720776.

[81] J. C. Dent. "A Basis for the Comparison of Various Experimental Methods for Studying Spray Penetration". En: *International Mid-Year Meeting*. SAE International, feb. de 1971. DOI: https://doi.org/10.4271/710571. URL: https://doi.org/10.4271/710571.

[82] C. Presser, A. K. Gupta, R. J. Santoro y H. G. Semerjian. "Laser diagnostics for characterization of fuel sprays". En: *International Congress on Applications of Lasers & Electro-Optics* 1986.2 (1986), págs. 160-167. DOI: 10.2351/1.5057799. eprint: https://lia.scitation.org/doi/pdf/10.2351/1.5057799. URL: https://lia.scitation.org/doi/abs/10.2351/1.5057799.

[83] W. BACHALO y M. HOUSER. "Development of the phase/Doppler spray analyzer for liquid drop sizeand velocity characterizations". En: (). DOI: 10.2514/6.1984-1199. eprint: https://arc.aiaa.org/doi/pdf/10.2514/6.1984-1199. URL: https://arc.aiaa.org/doi/abs/10.2514/6.1984-1199.

[84] M.G. Allen y R.K. Hanson. "Digital imaging of species concentration fields in spray flames". En: *Symposium (International) on Combustion* 21.1 (1988). Twenty-First Symposuim (International on Combustion), págs. 1755-1762. ISSN: 0082-0784. DOI: https://doi.org/10.1016/S0082-0784(88)80409-0. URL: https://www.sciencedirect.com/science/article/pii/S0082078488804090.

[85] R W Schefer, M Namazian y J Kelly. "CH, OH and CH4 concentration measurements in a lifted turbulent-jet flame". En: *Symposium (International) on Combustion* 23.1 (1991), págs. 669-676. ISSN: 0082-0784. DOI: https://doi.org/10.1016/S0082-0784(06)80315-2. URL: https://www.sciencedirect.com/science/article/pii/S0082078406803152.

[86] Hidenori Kosaka et al. "Simultaneous 2D Imaging of OH Radicals and Soot in a Diesel Flame by Laser Sheet Techniques". En: *International Congress & Exposition*. SAE International, feb. de 1996. DOI: https://doi.org/10.4271/960834. URL: https://doi.org/10.4271/960834.

[87] John E. Dec y Edward B. Coy. "OH Radical Imaging in a DI Diesel Engine and the Structure of the Early Diffusion Flame". En: *International Congress & Exposition*. SAE International, feb. de 1996. DOI: https://doi.org/10.4271/960831. URL: https://doi.org/10.4271/960831.

[88] A. E. Catania et al. "Numerical Analysis Versus Experimental Investigation of a Distributor-Type Diesel Fuel-Injection System". En: *Journal of Engineering for Gas Turbines and Power* 116.4 (oct. de 1994), págs. 814-830. ISSN: 0742-4795. DOI: 10.1115/1.2906890. eprint: https://asmedigitalcollection.asme.org/gasturbinespower/article-pdf/116/4/814/5702204/814_1.pdf. URL: https://doi.org/10.1115/1.2906890.

[89] Tokuta Inoue et al. "A Simulation Of Diesel Injection System Using A Hybrid Computer". En: *20th FISITA Congress (1984), Vienna, Austria.* SAE International, ene. de 1984. DOI: https://doi.org/10.4271/845035. URL: https://doi.org/10.4271/845035.

[90] Hiroyuki Kano, Masaaki Kato, Terutada Kojima y Makoto Katagiri. "Contribution of Optimum Design for Nozzle Configuration to Spray Formation". En: *International Congress & Exposition.* SAE International, feb. de 1990. DOI: https://doi.org/10.4271/900824. URL: https://doi.org/10.4271/900824.

[91] Giovanni Bruni, Angelo Fiore, Domenico Laforgia y Luigi Fiorentino. "3-D Analysis of the Flow Through a Multihole V.C.O. Nozzle for D.I. Diesel Engine". En: *International Congress & Exposition.* SAE International, feb. de 1995. DOI: https://doi.org/10.4271/950085. URL: https://doi.org/10.4271/950085.

[92] Ja Ye Koo, Seung Tae Hong, Joseph S. Shakal y Shinichi Goto. "Influence of Fuel Injector Nozzle Geometry on Internal and External Flow Characteristics". En: *International Congress & Exposition.* SAE International, feb. de 1997. DOI: https://doi.org/10.4271/970354. URL: https://doi.org/10.4271/970354.

[93] H. Chaves et al. "Experimental study of cavitation in the nozzle hole of diesel injectors using transparent nozzles". En: *SAE Technical Papers* 412 (1995). ISSN: 2688-3627. DOI: 10.4271/950290.

[94] H Chaves y Ch Ludwig. "Characterization of cavitation in transparent nozzles depending on the nozzle geometry". En: *Proceedings of the 20th ILASS - Europe Meeting 2005* August (2005).

[95] Celia Soteriou, Richard Andrews y Mark Smith. "Direct Injection Diesel Sprays and the Effect of Cavitation and Hydraulic Flip on Atomization". En: *SAE Technical Paper Series.* Vol. 1. 412. Feb. de 1995. DOI: 10.4271/950080. URL: https://www.sae.org/content/950080/.

[96] S. Kampmann, B. Dittus, P. Mattes y M. Kirner. "The influence of hydro grinding at VCO nozzles on the mixture preparation in a di diesel engine". En: *SAE Technical Papers* 412 (1996). ISSN: 26883627. DOI: 10.4271/960867.

[97] C. Arcoumanis et al. "Analysis of the flow in the nozzle of a vertical multi-hole diesel engine injector". En: *SAE Technical Papers* 724 (1998). ISSN: 26883627. DOI: 10.4271/980811.

[98] David P. Schmidt, Christopher J. Rutland y M. L. Corradini. "A numerical study of cavitating flow through various nozzle shapes". En: *SAE Technical Papers* 412 (1997). ISSN: 26883627. DOI: 10.4271/971597.

[99] David P. Schmidt. "Cavitation in Diesel Fuel Injector Nozzles". Tesis doct. Wisconsin: University of Wisconsin - Madison, 1997.

[100] David P. Schmidt et al. "Cavitation in two-dimensional asymmetric nozzles". En: *SAE Technical Papers* 724 (1999). ISSN: 26883627. DOI: 10.4271/1999-01-0518.

[101] D. P. Schmidt. "The internal flow of diesel fuel injector nozzles: A review". En: *International Journal of Engine Research* 2.1 (2001), págs. 1-22. ISSN: 20413149. DOI: 10.1243/1468087011545316.

[102] David P. Schmidt, Suresh Gopalakrishnan y H. Jasak. "Multi-dimensional simulation of thermal non-equilibrium channel flow". En: *International Journal of Multiphase Flow* 36.4 (abr. de 2010), págs. 284-292. ISSN: 03019322. DOI: 10.1016/j.ijmultiphaseflow.2009.11.012. URL: http://linkinghub.elsevier.com/retrieve/pii/S030193220900192X.

[103] Z. Bilicki y J. Kestin. "Physical Aspects of the Relaxation Model in Two-Phase Flow". En: *Proceedings of the Royal Society A: Mathematical, Physical and Engineering Sciences* 428.1875 (abr. de 1990), págs. 379-397. ISSN: 1364-5021. DOI: 10.1098/rspa.1990.0040. URL: http://dx.doi.org/10.1098/rspa.1990.0040%20http://rspa.royalsocietypublishing.org/cgi/doi/10.1098/rspa.1990.0040.

[104] P. Downar-Zapolski, Z. Bilicki, L. Bolle y J. Franco. "The non-equilibrium relaxation model for one-dimensional flashing liquid flow". En: *International Journal of Multiphase Flow* 22.3 (1996), págs. 473-483. ISSN: 03019322. DOI: 10.1016/0301-9322(95)00078-X.

[105] E W Bilicki, Salim Ali, Fluid Flow Machinery y Polish Academy. "Evaluation of the relaxation time of heat and mass exchange in the liquid-vapour bubble flow". En: 39.4 (1996).

[106] C. Arcoumanis, H. Flora, M. Gavaises y M. Badami. "Cavitation in Real-Size Multi-Hole Diesel Injector Nozzles". En: *SAE Technical Paper Series* 1.724 (2010). DOI: 10.4271/2000-01-1249.

[107] E. Giannadakis, M. Gavaises y C. Arcoumanis. "Modelling of cavitation in diesel injector nozzles". En: *Journal of Fluid Mechanics* 616 (2008), págs. 153-193. ISSN: 00221120. DOI: 10.1017/S0022112008003777.

[108] Manolis Gavaises y C Arcoumanis. "LINKING NOZZLE FLOW WITH SPRAY CHARACTERISTICS IN A DIESEL FUEL INJECTION SYSTEM". En: *Atomization and Sprays* 8.3 (1998), págs. 307-347. ISSN: 1044-5110.

[109] A. Andriotis, M. Gavaises y C. Arcoumanis. "Vortex flow and cavitation in diesel injector nozzles". En: *Journal of Fluid Mechanics* 610 (2008), págs. 195-215. ISSN: 14697645. DOI: 10.1017/S0022112008002668.

[110] C.W Hirt y B.D Nichols. "Volume of fluid (VOF) method for the dynamics of free boundaries". En: *Journal of Computational Physics* 39.1 (1981), págs. 201-225. ISSN: 0021-9991. DOI: https://doi.org/10.1016/0021-9991(81)90145-5. URL: https://www.sciencedirect.com/science/article/pii/0021999181901455.

[111] E. Giannadakis et al. "Evaluation of the predictive capability of diesel nozzle cavitation models". En: *SAE Technical Papers* 2007.724 (2007), págs. 776-790. ISSN: 26883627. DOI: 10.4271/2007-01-0245.

[112] F. Payri, V. Bermúdez, R. Payri y F. J. Salvador. "The influence of cavitation on the internal flow and the spray characteristics in diesel injection nozzles". En: *Fuel* 83.4-5 (2004), págs. 419-431. ISSN: 00162361. DOI: 10.1016/j.fuel.2003.09.010.

[113] R. Payri, J. M. García, F. J. Salvador y J. Gimeno. "Using spray momentum flux measurements to understand the influence of diesel nozzle geometry on spray characteristics". En: *Fuel* 84.5 (2005), págs. 551-561. ISSN: 00162361. DOI: 10.1016/j.fuel.2004.10.009.

[114] Raul Payri, Bernardo Tormos, Francisco Javier Salvador y Lucio Araneo. "Spray droplet velocity characterization for convergent nozzles with three different diameters". En: *Fuel* 87.15-16 (2008), págs. 3176-3182. ISSN: 00162361. DOI: 10.1016/j.fuel.2008.05.028. URL: http://www.sciencedirect.com/science/article/pii/S0016236108002275.

[115] R. Payri, F. J. Salvador, J. Gimeno y R. Novella. "Flow regime effects on non-cavitating injection nozzles over spray behavior". En: *International Journal of Heat and Fluid Flow* 32.1 (2011), págs. 273-284. ISSN: 0142727X. DOI: 10.1016/j.ijheatfluidflow.2010.10.001. URL: http://dx.doi.org/10.1016/j.ijheatfluidflow.2010.10.001.

[116] R. Payri, F.J. Salvador, J. Gimeno y R. Novella. "Flow regime effects on non-cavitating injection nozzles over spray behavior". En: *International Journal of Heat and Fluid Flow* 32.1 (2011), págs. 273-284. ISSN: 0142-727X. DOI: https://doi.org/10.1016/j.ijheatfluidflow.2010.10.001. URL: https://www.sciencedirect.com/science/article/pii/S0142727X10001633.

[117] F. Payri, R. Payri, F. J. Salvador y J. Martínez-López. "A contribution to the understanding of cavitation effects in Diesel injector nozzles through a combined experimental and computational investigation". En: *Computers and Fluids* 58.April (2012), págs. 88-101. ISSN: 00457930. DOI: 10.1016/j.compfluid.2012.01.005.

[118] R. Payri, F. J. Salvador, M. Carreres y J. De La Morena. " Fuel temperature influence on the performance of a last generation common-rail diesel ballistic injector. Part II: 1D model development, validation and analysis ". En: *Energy Conversion and Management* 114.May (2016),

págs. 376-391. ISSN: 01968904. DOI: 10.1016/j.enconman.2016.02.043.

[119] F. J. Salvador, S. Hoyas, R. Novella y J. Martinez-Lopez. "Numerical simulation and extended validation of two-phase compressible flow in diesel injector nozzles". En: *Proceedings of the Institution of Mechanical Engineers, Part D: Journal of Automobile Engineering* 225.4 (2011), págs. 545-563. ISSN: 09544070. DOI: 10.1177/09544070JAUTO1569.

[120] Francisco Javier Salvador, Jorge Martínez-López, J. V. Romero y M. D. Roselló. "Computational study of the cavitation phenomenon and its interaction with the turbulence developed in diesel injector nozzles by Large Eddy Simulation (LES)". En: *Mathematical and Computer Modelling* 57.7-8 (2013), págs. 1656-1662. ISSN: 08957177. DOI: 10.1016/j.mcm.2011.10.050. URL: http://dx.doi.org/10.1016/j.mcm.2011.10.050.

[121] Francisco Javier Salvador, Santiago Ruiz, José Miguel Salavert y Joaquin De la Morena. "Consequences of using biodiesel on the injection and air-fuel mixing processes in diesel engines". En: *Proceedings of the Institution of Mechanical Engineers, Part D: Journal of Automobile Engineering* 227.8 (2013), págs. 1130-1141. ISSN: 09544070. DOI: 10.1177/0954407012463667.

[122] Francisco Javier Salvador, David Jaramillo, J. V. Romero y M. D. Roselló. "Using a homogeneous equilibrium model for the study of the inner nozzle flow and cavitation pattern in convergent-divergent nozzles of diesel injectors". En: *Journal of Computational and Applied Mathematics* 309 (2015), págs. 630-641. ISSN: 03770427. DOI: 10.1016/j.cam.2016.04.010. URL: http://dx.doi.org/10.1016/j.cam.2016.04.010.

[123] F.J. Salvador, Marcos Carreres, Debanhi Jaramillo y J. Martínez-López. "Comparison of microsac and VCO diesel injector nozzles in terms of internal nozzle flow characteristics". En: *Energy Conversion and Management* 103 (oct. de 2015). DOI: 10.1016/j.enconman.2015.05.062.

[124] F. J. Salvador, J. De la Morena, J. Martínez-López y D. Jaramillo. "Assessment of compressibility effects on internal nozzle flow in diesel injectors at very high injection pressures". En: *Energy Conversion and Management* 132 (2017), págs. 221-230. ISSN: 01968904. DOI: 10.1016/j.enconman.2016.11.032. URL: http://dx.doi.org/10.1016/j.enconman.2016.11.032.

[125] V. Macian, V. Bermudez, R. Payri y J. Gimeno. "New Technique for Determination of Internal Geometry of a Diesel Nozzle With the Use of Silicone Methodology". En: *Experimental Techniques* 27.2 (2003), págs. 39-43. ISSN: 0732-8818. DOI: 10.1111/j.1747-1567.2003.

tb00107.x. URL: http://doi.wiley.com/10.1111/j.1747-1567.2003.tb00107.x.

[126] R. Payri, F. J. Salvador, J. Gimeno y J. de la Morena. "Effects of nozzle geometry on direct injection diesel engine combustion process". En: *Applied Thermal Engineering* 29.10 (2009), págs. 2051-2060. ISSN: 13594311. DOI: 10.1016/j.applthermaleng.2008.10.009. URL: http://dx.doi.org/10.1016/j.applthermaleng.2008.10.009.

[127] R. Payri, F. J. Salvador, J. Gimeno y G. Bracho. "Effect of fuel properties on diesel spray development in extreme cold conditions". En: *Proceedings of the Institution of Mechanical Engineers, Part D: Journal of Automobile Engineering* 222.9 (2008), págs. 1743-1753. ISSN: 09544070. DOI: 10.1243/09544070JAUTO844.

[128] S. Molina, F. J. Salvador, M. Carreres y D. Jaramillo. " A computational investigation on the influence of the use of elliptical orifices on the inner nozzle flow and cavitation development in diesel injector nozzles ". En: *Energy Conversion and Management* 79 (2014), págs. 114-127. ISSN: 01968904. DOI: 10.1016/j.enconman.2013.12.015. URL: http://dx.doi.org/10.1016/j.enconman.2013.12.015.

[129] Jung Goo Hong, Kun Woo Ku, Sung Ryoul Kim y Choong Won Lee. "Effect of cavitation in circular nozzle and elliptical nozzles on the spray characteristic". En: *Atomization and Sprays* 20.10 (2010), págs. 877-886. ISSN: 10445110. DOI: 10.1615/AtomizSpr.v20.i10.40. URL: http://www.scopus.com/inward/record.url?eid=2-s2.0-79955791257&partnerID=tZOtx3y1.

[130] Kun Woo Ku, Jung Goo Hong y Choong Won Lee. "Effect of internal flow structure in circular and elliptical nozzles on spray characteristics". En: *Atomization and Sprays* 21.8 (2011), págs. 655-672. ISSN: 10445110. DOI: 10.1615/AtomizSpr.2012004192.

[131] Shenghao Yu et al. "Experimental study on the spray characteristics discharging from elliptical diesel nozzle at typical diesel engine conditions". En: *Fuel* 221.February (2018), págs. 28-34. ISSN: 00162361. DOI: 10.1016/j.fuel.2018.02.090.

[132] Francisco J. Salvador, Joaquin de la Morena, Marcos Carreres y David Jaramillo. "Numerical analysis of flow characteristics in diesel injector nozzles with convergent-divergent orifices". En: *Proceedings of the Institution of Mechanical Engineers, Part D: Journal of Automobile Engineering* 231.14 (2017), págs. 1935-1944. ISSN: 09544070. DOI: 10.1177/0954407017692220.

[133] F. dos Santos y L. le Moyne. "Spray atomization models in engine applications, from correlations to direct numerical simulations". En: *Oil and Gas Science and Technology* 66.5 (2011), págs. 801-822. ISSN: 12944475. DOI: 10.2516/ogst/2011116.

[134] Jennifer C. Beale y Rolf D. Reitz. "Modeling spray atomization with the Kelvin-Helmholtz/Rayleigh-Taylor hybrid model". En: *Atomization and Sprays* 9.6 (1999), págs. 623-650. ISSN: 10445110. DOI: 10.1615/atomizspr.v9.i6.40.

[135] Sibendu Som, Anita I. Ramirez, Douglas E. Longman y Suresh K. Aggarwal. "Effect of nozzle orifice geometry on spray, combustion, and emission characteristics under diesel engine conditions". En: *Fuel* 90.3 (2011), págs. 1267-1276. ISSN: 00162361. DOI: 10.1016/j.fuel.2010.10.048. URL: http://dx.doi.org/10.1016/j.fuel.2010.10.048.

[136] Sibendu Som y Douglas E. Longman. "Nozzle flow characteristics of alternate fuels for compression ignition engine applications". En: *Proceedings of the Spring Technical Conference of the ASME Internal Combustion Engine Division* April 2016 (2012), págs. 703-714. ISSN: 15296598. DOI: 10.1115/ICES2012-81078.

[137] Hekun Jia, Zhuangbang Wei, Bifeng Yin y Zhiyuan Liu. "Analysis of elliptical diesel nozzle spray dynamics using a one-way coupled spray model". En: *International Journal of Engine Research* (2021), págs. 755-766. ISSN: 1468-0874. DOI: 10.1177/14680874211063352.

[138] Xandra Margot, Antonio Garcia, Pablo Fajardo y Stavroula Patouna. "Analysis of the Cavitating Flow in Real Size Diesel Injectors With Fixed and Moving Needle Lift Simulations". En: *V European Conference on Computational Fluid Dynamics* June (2010), págs. 14-17.

[139] Pedro Marti-Aldaravi, Kaushik Saha, Jaime Gimeno y Sibendu Som. "Numerical Simulation of a Direct-Acting Piezoelectric Prototype Injector Nozzle Flow for Partial Needle Lifts". En: *SAE Technical Papers* 2017-24-01 (2017). ISSN: 01487191. DOI: 10.4271/2017-24-0101.

[140] Alan L Kastengren et al. "Engine Combustion Network (ECN): Measurements of Nozzle Geometry and Hydraulic Behavior". En: *Atomization and Sprays* 22.12 (2012), págs. 1011-1052. ISSN: 1044-5110. DOI: 10.1615/AtomizSpr.2013006309.

[141] F. J. Salvador, J. Gimeno, J. Martín y M. Carreres. "Thermal effects on the diesel injector performance through adiabatic 1D modelling. Part I: Model description and assessment of the adiabatic flow hypothesis". En: *Fuel* 260.May (2020). ISSN: 00162361. DOI: 10.1016/j.fuel.2019.116348.

[142] R. Payri, F. J. Salvador, M. Carreres y M. Belmar-Gil. "Thermal effects on the diesel injector performance through adiabatic 1D modelling. Part II: Model validation, results of the simulations and discussion". En: *Fuel* 260.May 2020 (2020). ISSN: 00162361. DOI: 10.1016/j.fuel.2019.115663.

[143] A. L. Kastengren et al. "Time-resolved X-ray radiography of sprays from Engine Combustion Network spray a diesel injectors". En: *Atomization and Sprays* 24.3 (2014), págs. 251-272. ISSN: 10445110. DOI: 10.1615/AtomizSpr.2013008642.

[144] A. Kastengren et al. "Measurements of droplet size in shear-driven atomization using ultra-small angle x-ray scattering". En: *International Journal of Multiphase Flow* 92 (2017), págs. 131-139. ISSN: 03019322. DOI: 10.1016/j.ijmultiphaseflow.2017.03.005. URL: http://dx.doi.org/10.1016/j.ijmultiphaseflow.2017.03.005.

[145] Lyle M. Pickett, Julien Manin, Alan Kastengren y Christopher Powell. "Comparison of Near-Field Structure and Growth of a Diesel Spray Using Light-Based Optical Microscopy and X-Ray Radiography". En: *SAE International Journal of Engines* 7.2 (abr. de 2014), págs. 1044-1053. ISSN: 1946-3936. DOI: https://doi.org/10.4271/2014-01-1412. URL: https://doi.org/10.4271/2014-01-1412.

[146] Aniket Tekawade et al. "Time-resolved 3D imaging of two-phase fluid flow inside a steel fuel injector using synchrotron X-ray tomography". En: *Scientific Reports* 10.1 (2020), págs. 1-9. ISSN: 20452322. DOI: 10.1038/s41598-020-65701-x.

[147] Q. Xue et al. "An Eulerian CFD model and X-ray radiography for coupled nozzle flow and spray in internal combustion engines". En: *International Journal of Multiphase Flow* 70.December (2015), págs. 77-88. ISSN: 03019322. DOI: 10.1016/j.ijmultiphaseflow.2014.11.012.

[148] Jose Maria Desantes et al. "Coupled/decoupled spray simulation comparison of the ECN spray a condition with the Σ-Y Eulerian atomization model". En: *International Journal of Multiphase Flow* 80 (2016), págs. 89-99. ISSN: 03019322. DOI: 10.1016/j.ijmultiphaseflow.2015.12.002.

[149] J. M. Desantes, J. M. García-Oliver, J. M. Pastor y A. Pandal. "A comparison of diesel sprays CFD modeling approaches: DDM versus σ-γ Eulerian atomization model". En: *Atomization and Sprays* 26.7 (2016), págs. 713-737. ISSN: 10445110. DOI: 10.1615/AtomizSpr.2015013285.

[150] J. Anez et al. "Eulerian-Lagrangian spray atomization model coupled with interface capturing method for diesel injectors". En: *International Journal of Multiphase Flow* 113 (2018), págs. 325-342. ISSN: 03019322.

DOI: 10.1016/j.ijmultiphaseflow.2018.10.009. URL: https://doi.org/10.1016/j.ijmultiphaseflow.2018.10.009.

[151] M Zellat, G Desoutter, Y Liang y F Ravet. "Application of the Eulerian-Lagrangian spray atomization (ELSA) model for the Diesel injection simulation". En: (2010), págs. 1-12.

[152] Yue Wang, Won Geun Lee, Rolf Reitz y Ramachandra Diwakar. "Numerical simulation of diesel sprays using an Eulerian-Lagrangian Spray and Atomization (ELSA) model coupled with nozzle flow". En: *SAE 2011 World Congress and Exhibition*. Abr. de 2011. DOI: 10.4271/2011-01-0386. URL: https://www.sae.org/content/2011-01-0386/.

Capítulo 2

Influencia de la geometría en el flujo interno: efectos termo-hidráulicos

Perhaps some day in the dim future it will be possible to advance the computations faster than the weather advances and at a cost less than the saving to mankind due to the information gained. But that is a dream.

Lewis Fry Richardson, 1922

Resumen: En este capítulo se analiza el efecto de la geometría desde la perspectiva del flujo interno. A través de una caracterización detallada de las propiedades del combustible y de distintas hipótesis sobre las transmisión de calor, se ha analizado el efecto de la geometría sobre la propia variación de las propiedades físicas del líquido y sobre los principales parámetros e indicadores del flujo interno.

Computational assessment of temperature variations through calibrated orifices subjected to high pressure drops: application to diesel injection nozzles.

Referencia: F.J. Salvador, M. Carreres, J. De la Morena, E. Martínez-Miracle, Computational assessment of temperature variations through calibrated orifices subjected to high pressure drops: Application to diesel injection nozzles, Energy Conversion and Management, Volume 171, 2018, Pages 438-451, ISSN 0196-8904, https://doi.org/10.1016/j.enconman.2018.05.102.

Abstract: *This paper conducts an investigation on the temperature variations experienced by the fuel when it expands through the calibrated orifices of a commercial diesel injector. Experimental results of the temperature change across a calibrated orifice upon expansion, extracted from a previous work, are compared to the temperature predicted by computational fluid dynamic simulations under the assumption of adiabatic flow, with no heat transfer to the surroundings. The comparison points out that the simulations are able to predict the thermal effects taking place inside the orifice. Once the model is validated, the flow morphology is analyzed to explain the trends observed in the fuel temperature change across the orifice depending on the operating conditions. Two opposed effects take place inside the orifice: on the one hand, the flow is cooled in the orifice core due to depressurization; on the other hand, the fuel is importantly heated near the walls due to viscous friction. As expected, the net effect on the outlet temperature mainly depends on the orifice discharge coefficient, governed by the orifice geometry and the flow regime (Reynolds number) induced by the injection conditions. Next, the analysis is extended to a diesel nozzle, considering that the higher pressure drops achieved in it are expected to induce even more important thermal effects. The two opposed effects also take place inside the orifice. Even though their net effect is similar, the*

separate effect of each phenomenon is greater, leading to differences that could be relevant for the atomization and spray formation processes. Additionally, the flow pattern shows a non-uniform distribution of the flow inside the nozzle influencing the results from the thermal point of view.

2.1. Introduction

In diesel engines, the fuel-air mixing process dominates the combustion process and emissions formation. This mixing process is directly linked to the interaction between the in-cylinder air motion, driving the design of the intake ports and valve profiles as investigated by Nigro et al. [1], and the fuel injection system, as thoroughly reviewed by Mohan et al. [2]. For this reason, research has been recently focused on the influence of both the injector geometry and the injection conditions on the atomization and mixing processes. From the point of view of the geometry, Som et al. [3] computationally analyzed the effect of the nozzle orifice diameters, conicity and inlet radii on the spray features, linking them to combustion and emission characteristics. Sayin et al. [4] investigated the influence of the injector hole number on the engine performance and emissions, whereas Gavaises [5] and the authors [6] tried to gain insight on the role of cavitation on the fuel spray mixing capabilities through an analysis of the effect of the hydroerosion. As a result, for instance, new nozzle concepts have been suggested by the authors in the form of elliptical orifices [7] or convergent-divergent orifices [8], whereas other researchers analyzed the possibility of including twin-hole nozzles in diesel injection systems [9], reporting their lower penetration when compared to the equivalent single hole nozzles. As far as the injection conditions are concerned, Wang et al. [10] analyzed the effect of increasing the injection pressure on the soot formation, whereas Gumus et al. [11] linked this property to the engine emissions. As a result, the injection pressures used by OEMs have been progressively growing up to even 300 MPa. The flow within diesel injectors has traditionally been regarded to as isothermal. Giannadakis et al. [12] studied the flow patterns through a cylindrical hole and a tapered hole nozzle with this approach, comparing simulations with constant fuel properties with simulations that considered variations in the fuel properties with the local pressure. They observed a gain in accuracy in the latter case, but omitted the effect of the temperature variations in the simulations. Som et al. also conducted numerical investigations with the isothermal flow assumption [13], reporting the influence of the fuel properties on the diesel. They compared the internal flow and spray features when injecting fluids with the reference properties of both diesel and biodiesel, reporting that biodiesel would need to be injected at a higher temperature than diesel in order to exhibit similar atomization characteristics. More recently, Sun et al. [14] investigated the effects of nozzle

geometry and injection pressure on the cavitation formation and spray characteristics, but also neglected the effect of the fuel temperature changes in the problem. Nevertheless, as a result of the progressive growth in the fuel injection pressures, some thermal effects inside the injector that were not especially relevant in the past are now gaining importance. This is the case of the flow along the injector control orifices or the nozzle, where the strong pressure gradients driving the flow result in important temperature changes due to two main effects: on the one hand, the rapid depressurization of the fuel, which may significantly reduce the fuel temperature in the orifice core; on the other hand, an important viscous heating at the wall of the orifices induced by friction due to the high velocity gradients. This behavior drives for the need to introduce also the pressure and temperature dependence of the fluid properties into the solver, due to their impact on the fluid-dynamic field [15]. Therefore, some works started treating the flow inside the injector as adiabatic. In the 1D modelling field, Catania et al. [16] were the first authors to introduce this assumption. Later on, the authors incorporated it to their models of complete diesel injectors [17]. As far as CFD modelling is concerned, Shi et al. [18] included the effect of the strong pressure gradients through the nozzle on fuel temperature and consequently fuel density and viscosity, coupling the CFD code to a 1D injector model. They compared the accuracy of this approach with the constant properties one for a honed and an unhoned nozzle. Theodorakakos et al. [19] also investigated the thermal effects in nozzle holes subjected to high pressure drops, paying more attention to the temperature field along the nozzle. Analyzing the two aforementioned effects on the flow, they reported that, depending on the nozzle discharge coefficient and the injection conditions, the flow in average could be heated at the outlet or even subcooled. Next, Strotos et al. [20] extended this work by analyzing the transient stages of the injection through the inclusion of the needle movement. However, even though this work offers a comparison of computational results against 0D theoretical models with the adiabatic flow assumption, none of them were compared with experimental results. Later, the authors [21] tried to assess the hypothesis of adiabatic flow in diesel injectors by experimentally measuring the temperature change across calibrated orifices subjected to an isenthalpic expansion in different conditions and comparing it to the theoretical one. In the present paper, an investigation of the thermal effects found in different characteristic orifices of a diesel injector subjected to significant expansions is carried out. First, the dimensions of the orifices and the physical properties of the fuel used are determined experimentally, allowing to introduce pressure and temperature dependent properties in the CFD solver. Later on, the results obtained by simulations are validated (both in terms of mass flow rate and predicted temperature change) against experimental measurements, previously performed on one of the calibrated orifices inside the injector control volume, as described in [21]. Results for the OZ calibrated orifice are analyzed by determining the conditions that lead to either heating or sub-

cooling the flow. Also, special attention is given to the flow morphology in order to justify the reasons for the reported trends and evaluate the impact of the observed temperature distribution on the fuel properties. Finally, once the methodology is validated on the calibrated orifice, it is applied also to the orifices of a diesel injector nozzle. Although the results in this case cannot be validated against experimental temperature values, due to the high difficulty to measure the temperature upstream and downstream of the nozzle orifices in an accurate way, there are two reasons why exploring such a geometry can be of interest. First, the orifices of the diesel nozzle are subjected to a larger pressure drop than the calibrated orifices (in the range of up to 250 MPa for current production injectors), so the thermal effects inside these orifices can be more relevant. Additionally, changes in the temperature characteristics inside the nozzle orifices can significantly affect the spray atomization and evaporation characteristics, with a direct impact on the combustion process. Thus, providing a reasonable estimation of the fuel temperature at the nozzle outlet, which is the aim of the current investigation, can be of great relevance for other works in fuel injection and combustion simulations. The paper is divided in 6 sections. Section 2.2 deals with the experimental techniques used for the study, including the geometrical characterization of the orifices used for the CFD study and the fuel properties determination. Next, Section 2.3 describes the computational model and the setup used for the simulations performed on the basis of Ansys CFX with a customized fuel. The used mesh and the simulation cases are also dealt with in this section. Section 2.4 shows the validation of the model against the experimental results from a previous work by the authors [21] and a discussion of the relevance of the thermal effects depending on the studied condition. Section 2.5 analyzes the potential temperature effects appearing inside the nozzle orifices, by means of a simulation campaign on a realistic nozzle geometry. Finally, Section 2.6 gathers the main conclusions of the study.

2.2. Experimental facilities

Next section briefly describes the techniques and resources that have been used in order to perform the experimental measurements.

Geometric characterization of the calibrated orifice

The calculation of the modelled temperature due to viscous effects or the cooling caused by decompression is highly influenced and highly dependent on the involved geometry. Determining the geometry of the injector control volume with precision is of key importance to obtain results and validate the theoretical CFD model correctly. The chosen geometry for the thermal experimental characterization and modelling corresponds to the calibrated

inlet orifice (OZ) of a control volume from a commercial Bosch CRI 2.20 injector. In Figure 2.1, the piece containing the control volume and the OZ orifice is depicted at the right hand side. The control volume assembled on the injector is plotted at the left hand side. The role of this orifice in the way the injector works does not fall within the scope of this work and further explanations on this regard are given in [22].

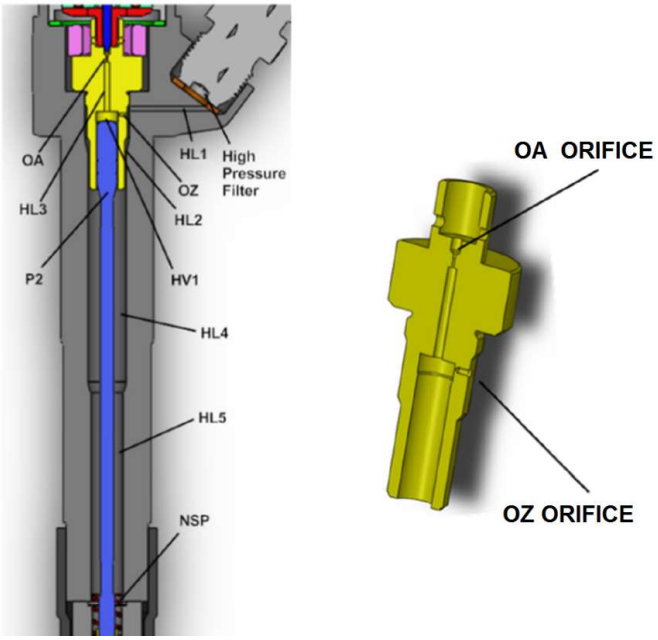

Figure 2.1: Control volume piece containing the calibrated orifice (OZ) in Bosch 2.20 injector.

In order to fully describe its volume, a silicone mold from the interior cavity has been obtained and visualized in a scanning electronic microscope SEM. This methodology is thoroughly described in [23]. This technique provides a high resolution picture of the topography of the injectors inlet orifice. The dimensions based on this image are measured by an auxiliary CAD software. The deviation over the mean value has been reported to be below 2% [24]. The most critical part of the whole orifice is the throat, where pressure and velocity gradients are significantly strong. Taking this into account, several measurements of the radius of this section have been gauged over three points along its length (inlet point, middle point and outlet point). In Figure 2.2, some pictures of the silicone molds obtained with the SEM to define the OZ orifice geometry are shown. Additionally, Figure 2.3 depicts the geometry of the orifice obtained through the metrology analysis from the silicone molds. All sections inside the OZ orifice are assumed to be circular.

As it can be noted, the most restrictive part of the OZ orifice from the point of view of the flow (where the diameter is smallest) has a conical shape:

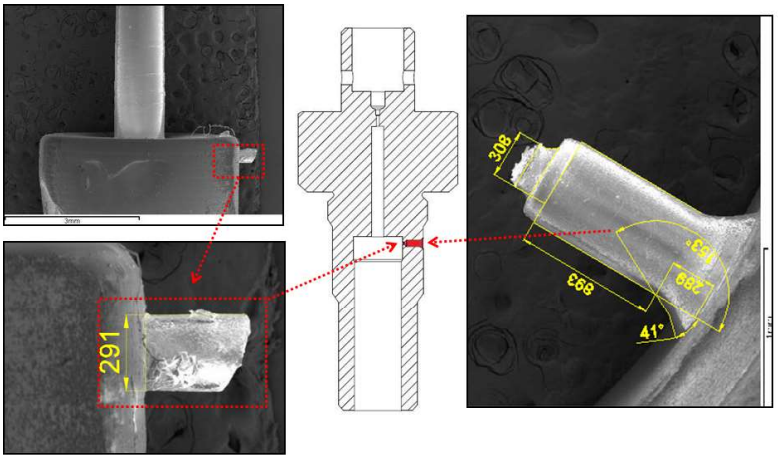

Figure 2.2: Geometrical characterization of the calibrated orifice (OZ) with silicone molds and SEM visualization.

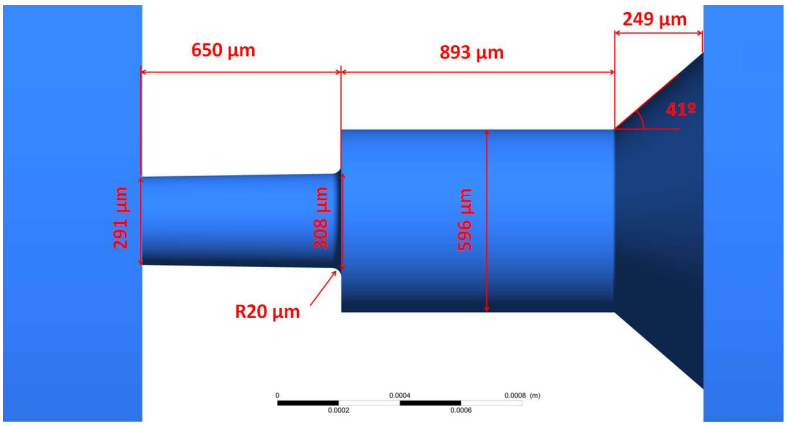

Figure 2.3: Dimensional characteristics of the calibrated orifice (OZ).

308 µm at the inlet vs 291 µm at the outlet. In this part of the orifice, a conicity factor (k-factor), can be defined to quantify the level of conicity. Using the Bosch definition, it may be calculated by means of Equation 2.1:

$$k - factor = \frac{D_i[\mu m] - D_0[\mu m]}{10} \tag{2.1}$$

where D_i and D_o are, in the current case, 308 µm and 291 µm, respectively. With these values, the k-factor equals 1.7. Considering this value, and according to previous results reported by the authors, cavitation phenomenon inside the orifice is not expected [25–28]. This result will be confirmed later by the experimental and computational results.

Geometric characterization for the nozzle orifices

As stated in the introduction, the current paper will explore not only the previously presented OZ calibrated orifice in the control volume, but also the orifices of a diesel injector nozzle. For this purpose, the geometry of a 7-holes nozzle extracted from a commercial common-rail Bosch solenoid injector has been characterized using the previously cited silicone molds technique. Figure 2.4 shows a schematic of the nozzle geometry, together with some sample images obtained from the post-processing of the silicone molds for some of the key orifice dimensions. For the subsequent 3D modeling of the injector flow, the orifice is constructed using the average values from the seven holes. This represents an inlet diameter of 0.143 mm, an outlet diameter of 0.124 mm, an inlet rounding radius of 0.029 mm and a total length of 0.715 mm. Again, the shape of the difference sections inside the nozzle orifices is assumed to be circular.

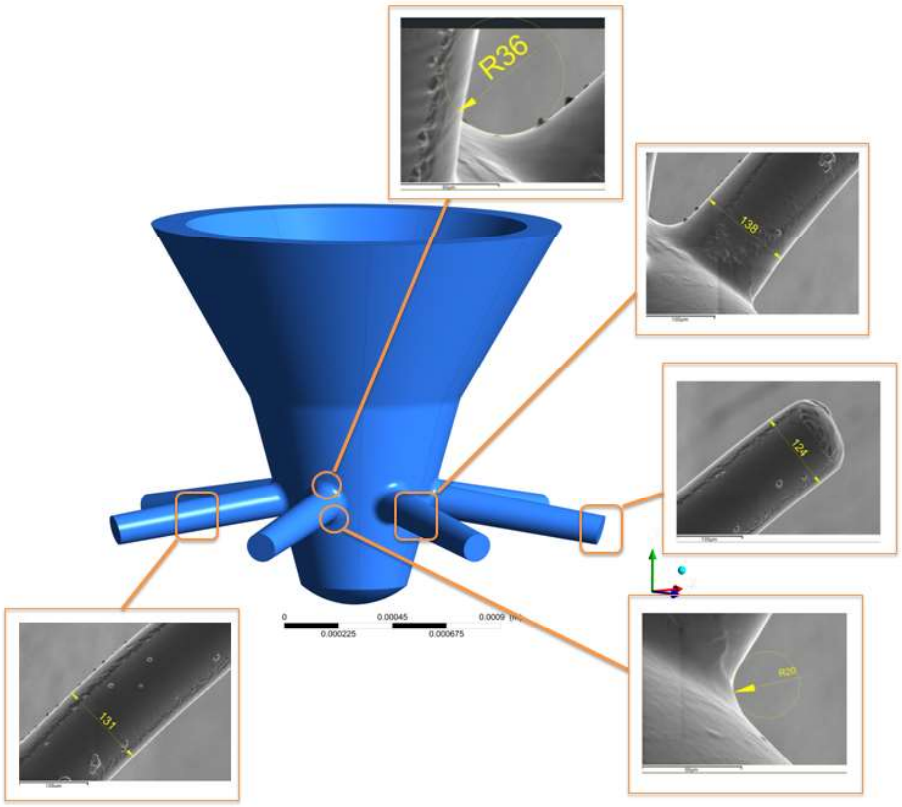

Figure 2.4: Dimensional characterization of the nozzle orifices.

Fuel properties determination

From the point of view of the CFD modelling, the correct definition of the functions that govern the behavior of the fuel with respect to the principal thermodynamic variables, namely pressure and temperature, will affect the result of the CFD simulation ([29]). These functions will also determine the range of conditions in which the code can be validated according to the experimental data. In an attempt to be as accurate as possible, fuel density, viscosity, specific heat and thermal conductivity have been set as variable properties of pressure and temperature. The numerical adjustment of these features follows empirical data and the methods employed to define them are described below. Therefore, as a first step, the main properties of the fuel have been measured under a wide range of pressure and temperature conditions. The considered fluid consists of a European standard winter diesel fuel. The density was characterized by the authors at atmospheric pressure as a function of temperature (ranging from 273 K to 373 K) using a standard hydrometer, taking into account the considerations stated by the ASTMD1298 procedure [30] (including those corresponding to the calibration procedure [31]). The accuracy of the hydrometer was determined to be $\pm\ 5 \times 10^{-4}\,\mathrm{kg\,m^{-3}}$. In order to establish the variations of the fuel density with the pressure, speed of sound measurements were also performed at different pressures (up to 20 MPa) and temperatures (from 300 K to 353 K) following the methodology established in [31]. The maximum deviations reported during the calibration of the facility were 1.24% over the expected values. The kinematic viscosity of the fuel was determined at atmospheric pressure for a wide range of temperatures (from 263 K to 373 K) by means of a commercial Cannon-Fenske viscometer. This device, a type of capillary viscometer, was used following the procedure specified in the ASTMD445 standard [32] in order to obtain an empirical expression for the viscosity as a function of temperature at atmospheric pressure. In accordance to this standard, the tolerance of this device was determined to be ±0.36% with 95% certainty. A comparison of the measured values for reference substances during the calibration led to deviations lower than 3% in all cases. The viscosity values at high pressure were estimated from the expression introduced by Kouzel [33]. In order to quantify these trends and dispose of suitable data for the computational model implementation, the experimental data coming from the density and viscosity characterization tests have been fitted to mathematical expressions as a function of temperature and pressure. These expressions showed a high coefficient of determination (R^2=0.99) in all cases [31]. In the case of the density, the expression obtained was:

$$\begin{aligned}\rho_f = 826.5 - 1.0217(T-298) + 1.251\cdot 10^{-3}(T-298)^2 \\ +0.6035(p-0.1) - 8.265\cdot 10^{-4}(p-0.1)^2 \\ +1.441\cdot 10^{-3}(T-298)(p-0.1)\end{aligned} \tag{2.2}$$

where ρ_f is the density (in kg/m^3) whereas p and T are the fuel pressure and temperature (in MPa and K), respectively. On the other hand, the viscosity approach leads to an exponential expression as derived from the Kouzel expression [33]:

$$\mu_f = 10^{-3}\mu_0 \cdot 10^{\left[(-1.48 + 5.86\cdot \mu_0^{0.181})\left(\frac{p-0.1013}{1000}\right)\right]} \tag{2.3}$$

Where μ_f is the dynamic viscosity at a given pressure and temperature, whereas μ_0 is the dynamic viscosity of the fluid at atmospheric pressure (0.1 MPa) and at a given temperature:

$$\mu_0 = 3.2158 \cdot \exp\left[(-0.0263(T-298)\right] \tag{2.4}$$

This dynamic viscosity is obtained by multiplying the measured density and the corresponding kinematic viscosity. Both μ_f and μ_0 have units of Pa $\cdot$ s. As in Equation 2.2, p and T are the fuel pressure and temperature (in MPa and K), respectively.

The resulting values of density and dynamic viscosity as a function of pressure and temperature are plotted in Figure 2.5 for the winter Diesel fuel used both for the experiments and the calculations.

Additional fuel properties related to heat transfer effects, such as thermal conductivity (k_t) and specific heat (C_p) have been obtained from Kolev [34] for a similar diesel fuel. As in the case of the fuel density, experimental results have been fitted to polynomial expressions. In this case, their coefficients have been compiled on a matrix. As it happened for the density and viscosity, the characterization of these properties is valid over a wide range of pressures and temperatures, ranging from 0 to 250 MPa in the case of the pressure and 273 K to 393 K in the case of temperature. Equation 2.5 deals with the specific heat polynomial expression as a function of pressure and temperature:

$$C_p = \sum_{i=1}^{5}\left(\sum_{j=1}^{3} d_{ij}\cdot T^{j-1}\left(\frac{p}{10^5}\right)^{i-1}\right) \tag{2.5}$$

where p is in Pa and the d_{ij} coefficients are the elements of a matrix (D) defined as:

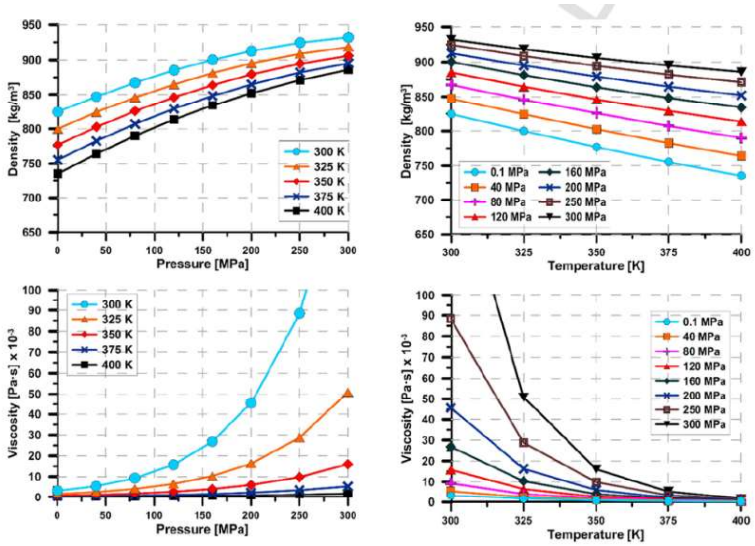

Figure 2.5: Winter diesel density and viscosity as a function of pressure and temperature.

$$D_{5x3} = \begin{pmatrix} -977.16186 & 14.025100 & -0.01374 \\ 2.22361e-4 & -1.62143e-4 & 2.23214e-9 \\ -1.96181e-9 & 2.03748e-7 & -1.78571e-14 \\ 4.15000e-14 & -7.54100e-11 & 4.03897e-28 \\ -3.48714e-18 & 1.00688e-14 & -1.47911e-31 \end{pmatrix} \tag{2.6}$$

As far as the thermal conductivity (k_t) is concerned, as in the case of the specific heat, it is defined by the following polynomial expression:

$$k_t = \sum_{i=1}^{3} \left(\sum_{j=1}^{3} a_{ij} \cdot T^{j-1} \right) (p)^{i-1} \tag{2.7}$$

where p is in Pa and the coefficients a_{ij} are the elements of a matrix (A_M) defined as:

$$A_{3x3} = \begin{pmatrix} 0.13924 & 3.78253e-5 & -2.89732e-7 \\ 6.27425e-11 & 6.08052e-13 & 3.64777e-16 \\ -1.38756e-19 & -2.57608e-22 & -2.70893e-24 \end{pmatrix} \tag{2.8}$$

All the polynomial fits reported in this section correspond to measurements for a Diesel fuel that are experimentally verified for pressures between 0.1 MPa and 250 MPa and temperatures between 273 K and 393 K. Even though the speed of sound measurements used as a basis for the determination of the fuel density at high pressure were only performed from 300 to 353 K, the known linear behavior of the density of the diesel fuels with the temperature does not compromise the validity of these fits in the aforementioned range.

2.3. Numerical approach

The main aspects related to the modeling work performed are described next.

Computational model and governing equations

CFD simulations have been performed using the CFX commercial software developed by ANSYS Inc v17.0, which has been customized using appropriate user functions related to the thermodynamic fuel properties introduced in section 2.3. The software solves the conservation equations based on a Finite Volume Methodology, which has proven to be optimal for similar CFD applications [35]. The k-epsilon model for turbulence flow in his RNG form ([36, 37]) was used because of the better results it has provided for similar studies compared to those found by the authors with its standard version [6, 7, 38]. The near-wall approach function has been defined using scalable-wall functions [39]. The common Navier-Stokes equations are numerically solved, including the continuity, momentum and energy equations. The energy equation is of particular interest and is described as:

$$\frac{\partial(\rho h_0)}{\partial t} - \frac{\partial p}{\partial t} + \nabla \cdot (\rho \vec{u} h_0) = \nabla \cdot (k_t \nabla T) + \nabla \cdot (\vec{u} \cdot \tau) + \vec{u} \cdot \vec{S}_M + S_E \quad (2.9)$$

where S_E is the energy source term, k_t is the thermal conductivity and h_0 is the stagnation enthalpy, related to the specific enthalpy $h(T, p)$ through:

$$h_0 = h + \frac{1}{2}u^2 \quad (2.10)$$

The general formulation for the specific entalphy h as a function of T and p is:

$$dh = \left(\frac{\partial h}{\partial T}\right)_p dT + \left(\frac{\partial h}{\partial p}\right)_T dp \quad (2.11)$$

Using the heat capacity under constant pressure (C_p), Eq. 13 can be rewritten as:

$$dh = C_p \cdot dT + \frac{1}{\rho}\left[1 + \frac{T}{\rho}\left(\frac{\partial \rho}{\partial T}\right)_p\right] dp \quad (2.12)$$

which can also be written as a function of the volumetric thermal expansion (β):

$$dh = C_p \cdot dT + \frac{1 - \beta \cdot T}{\rho} dp \quad (2.13)$$

where β is defined as:

$$\beta = -\frac{1}{\rho}\left(\frac{\partial \rho}{\partial T}\right)_p \tag{2.14}$$

Note that the second term of the right hand side of Eqs. 2.12 and 2.13 would be null for an ideal gas (for which $\beta \cdot T = 1$), but cannot be neglected for a liquid. In each calculation, values of $\rho(p,T)$, $\mu(p,T)$, $k_t(p,T)$ and $C_p(p,T)$ are updated using the available polynomial fits (recall Section 2.2) with the latest calculated values of p and T after each iteration.

Mesh description, simulation cases and model setup

In the case of the calibrated OZ orifice, due to the symmetry of the domain, axisymmetric simulations have been performed using a wedge geometry of 5°. The orifice dimensions included in Figure 2.3 have been used in order to build the mesh. Figure 2.6 shows the complete 3D computational domain with a detail of the mesh structure in the orifice. Constant pressure boundary conditions are selected for both the inlet and the outlet boundary conditions. The particular values of these boundary conditions come from the experimental campaign performed for this same orifice in a previous publication by the authors [21]. The fuel inlet temperature is set as 293 K for all cases. Fuel mass flow and the mean temperature at the orifice outlet are the most important results predicted by the simulations and they have been compared to the experimental values and analyzed in the next section. A non-slip boundary condition is used for the walls.

For the nozzle and OZ orifice meshes, similar meshing strategy and characteristic cell sizes to those employed in previous 3D-CFD nozzle flow simulations [28] have been used. A mesh sensitivity study including grid convergence indicators (GCI) calculations and Richardson extrapolation [40, 41] was performed in order to ensure a small numerical error due to the meshes. From a practical point of view and aiming to future applications, the nozzle is the most interesting case and given the complexity of the geometry, its meshing process must be carefully carried out. Figure 2.7 shows the convergence of the nozzle mass flow rate as a function of the number of cells for the nozzle mesh in the case of 130 MPa of injection pressure.

It can be seen how the mass flow rate asymptotically tends to a maximum value ($\sim$31.4 g s^{-1}). The grid convergence indicators (GCI) [40] for the three finest meshes result in GCI_{21}=0.15% and GCI_{32}=0.65% while the Richardson extrapolation is computed with a value of 31.38 g s^{-1}. Thus, a small discretization error is expected. Respecting both the computational cost and the quality criterion a committed mesh of 238567 cells inside the asymptotic solution range has been chosen for the nozzle. In the case of the calibrated OZ orifice a total of 162846 elements generate the wedge geometry (5°) and, therefore, 4.48 Mcells for the whole 3D geometry (360°). A high resolution scheme

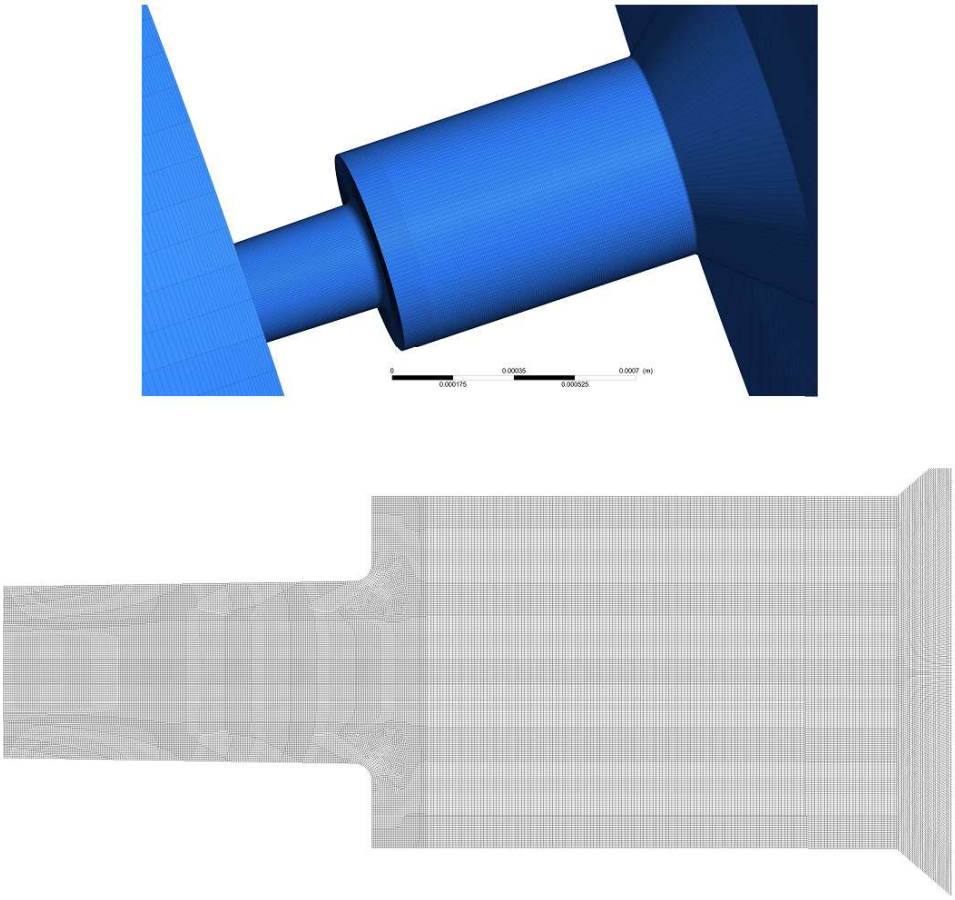

Figure 2.6: Mesh used for the simulations.

has been used in order to solve the discretized equations. Using the previously determined mesh characteristics, all cases have been run on six cores of an Intel Core i7-4700HQ 2.40GHz eight-core processor. A steady-state solver was selected, using two main convergence criteria: first, all the residuals must be below 1×10^{-5}; additionally, the average velocity and temperature must reach steady conditions. Regarding the nozzle orifices, the main difference is related to the fact that the nozzle geometry is not axisymmetric. Consequently, the simulations have been performed for a 51.43° sector representing one of the seven orifices included in the nozzle. This allows to achieve a reasonably consistent prediction of the main flow features at a reduced computational cost compared to a calculation of the complete 360° geometry. Nevertheless, when comparing to the experiments it has to be considered that, in reality, some orifice-to-orifice dispersion is always present due to small geometrical differences linked to the manufacturing tolerances. This fact may influence the injection characteristics to some extent, as explored by the authors by

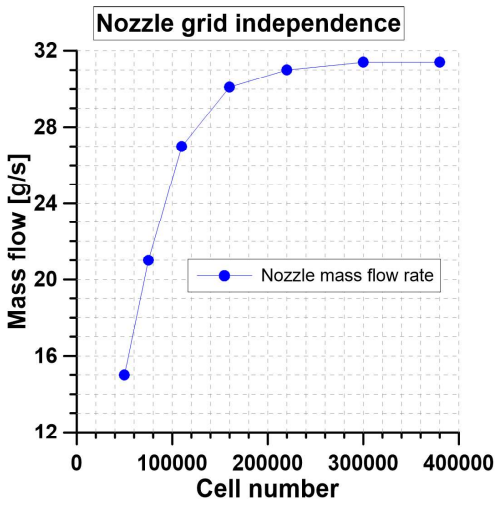

Figure 2.7: Mass flow rate versus number of cells for the mesh sensitivity study.

means of 1D modelling [42] in the case of the orifice diameter and discharge coefficient, among other parameters. Some potential non-uniformities in the needle position and the nozzle flow pattern, including those due to the needle eccentricity, have also been reported in the literature [43]. In any case, symmetry is considered as a reference in this study in order to make this study independent from the influence of the aforementioned manufacturing tolerances on the analyzed thermal effects. The same modeling methodology and boundary conditions previously explained for the calibrated orifice simulation have been also considered for the nozzle orifice.

2.4. Calibrated OZ orifice calculation

In a previous publication by the authors [21], as previously stated, the temperature variation across a calibrated orifice was measured for a set of boundary conditions in terms of upstream and downstream conditions. These results are used in this section to validate the CFD methodology described in Section 2.3. Figure 2.8 shows the simulation results in terms of the mass flow through the orifice. On the left hand side, this mass flow is plotted against the square root of the pressure drop, defined as the difference between the upstream and downstream pressures (p_{up} and p_{dw}). Observing the curves, the mass flow rate increases linearly with the square root of the pressure drop. This means that no cavitation appears inside the orifice, as it was expected considering the high conicity factor present in the orifice [8]. Under these

conditions, the mass flow inside the orifice is ruled by the following equation:

$$\dot{m}_f = C_d \cdot \rho_f \cdot A_0 \cdot u_{out} = C_d \cdot A_0 \cdot \sqrt{2(p_{up} - p_{dw})\rho_f} \tag{2.15}$$

where C_d is the orifice discharge coefficient, A_o the geometrical outlet section of the orifice and u_{out} the outlet velocity, calculated from Bernoulli's equation. The graph in the right hand side of Figure 2.8 represents the relative error committed with the numerical approach, defined as the difference among the computed and experimental values divided by the experimental mass flow. It can be observed that below a value of $2\,\mathrm{MPa}^{0.5}$ the relative error is very low, confirming the capability of the current simulation approach to reproduce the main flow characteristics.

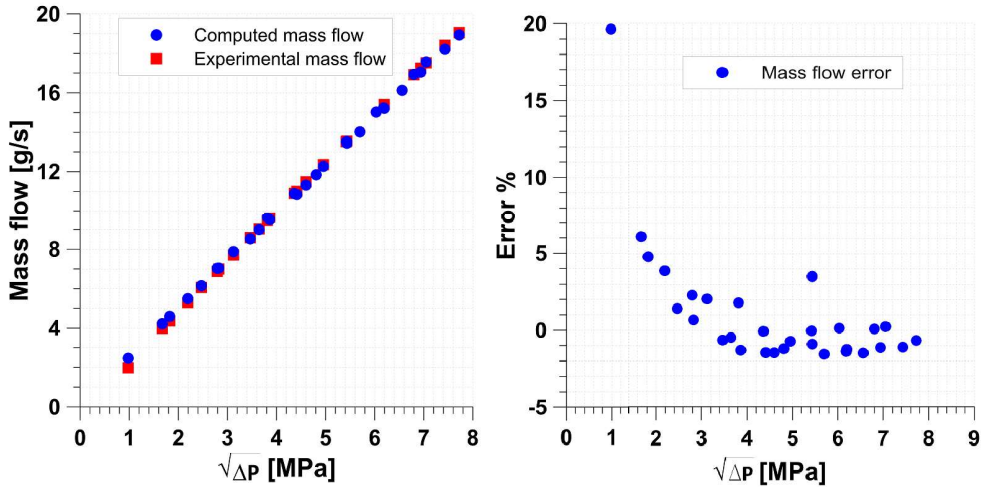

Figure 2.8: Experimental (from [21]) and computed mass flow (calibrated OZ orifice) as a function of pressure drop from experiments and computed (left). Deviation between experiments and simulations results (right).

Figure 2.9 shows the results in terms of the outlet temperature. In the left hand side, the outlet temperature is represented as a function of the pressure drop. The experimental results (squares) show the temperature measured by a thermocouple placed downstream of the orifice, according to the experimental arrangement described in [21]. The computational values (circles) show the numerical results of the average temperature in the section where the thermocouple is located. The data show that the outlet temperature tends to increase linearly with the pressure drop, mainly as a consequence of the heating effect produced by the relative friction between the fluid and the orifice walls. Computational results are well aligned with the experiments, with a maximum under-prediction of up to approximately 3 K for the 60 MPa case. The accuracy of the predictions can be better seen in the chart present in the right hand side of that figure, where the relative error associated to the

simulation approach in the outlet temperature is depicted, with a maximum value of approximately 0.9%.

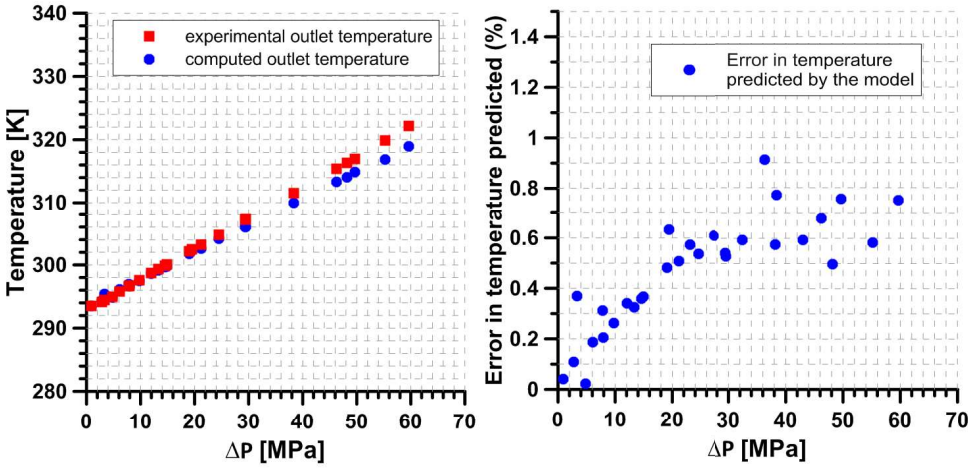

Figure 2.9: Experimental (from [21]) and computed values of temperature increase as a function of the pressure drop for the calibrated OZ orifice tested (left). Deviation between experiments and simulations (right).

The previous results can also be directly related to the temperature increase along the domain, considering that in all cases the inlet temperature was fixed at 293 K (equal to the ambient temperature). Thus, the maximum heating produced inside the orifice on the experimental results is approximately 30 K for an upstream pressure of 60 MPa. It has to be noted that this temperature increase could be even more significant when looking at the nozzle orifices of a diesel injector, which are subjected to a much higher pressure drops (and consequently higher velocities). For example, for a 200 MPa injection pressure case (typical for commercial diesel injector nozzles), if the linear trend previously observed were maintained, it would lead to an overall temperature increase of approximately 80 K. This increase can affect the fuel properties at the nozzle outlet, influencing the spray formation processes, so it may need to be considered for spray simulation activities. The heating effects on the nozzle orifices will be further analyzed in Section 2.5 for a specific diesel nozzle geometry. While the average value of the temperature tends to increase, the computational results show that the depressurization in the core of the flow induces a local cooling effect in this region. This behavior can be better seen in Figure 2.10, where the minimum local temperature in the domain is represented against the pressure drop. For low pressure values, the effect of this depressurization is negligible and the minimum temperature in the domain is approximately equal to the inlet temperature. Starting from approximately a pressure drop value of 10 MPa, the minimum temperature starts to drop, reaching a value of approximately 280 K for the 60 MPa condition,

which is in contrast with the average temperature value of 319 K computed in the outlet section for this particular condition. The non-uniform distribution of the temperature achieved inside the injector orifices may be of relevance for spray atomization simulations, for instance, especially due to the fact that the fuel viscosity is very sensitive to the temperature in this particular range of temperatures. In addition, the cooling effect may be more significant for the diesel nozzle orifices, since a stronger depressurization would be achieved. This fact will also be analyzed in Section 2.5.

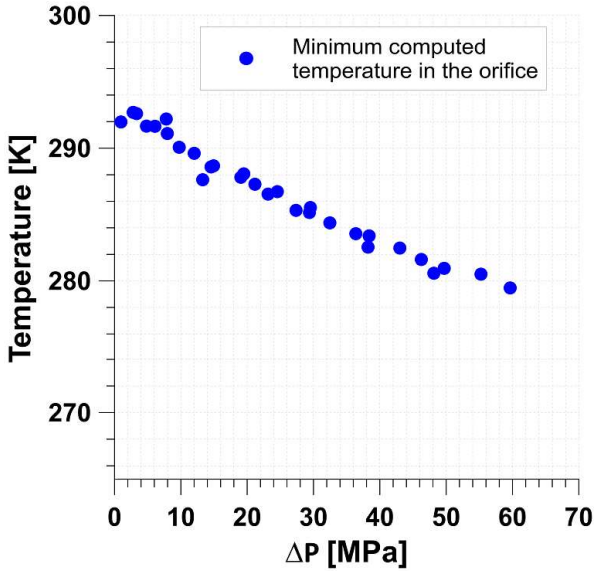

Figure 2.10: Minimum temperature computed in the whole domain.

A detail of the temperature distribution inside the orifice is provided in Figure 2.11 for a 60 MPa upstream pressure and 5 MPa downstream pressure case. In this figure, the flow would go from right (upstream pressure) to left (orifice outlet). Two different behaviors can be observed. On the one hand, the core of the flow suffers a decrease in temperature from 293 K to approximately 280.5 K. This decrease, as previously mentioned, is related to the transition from high pressure (60 MPa) to low pressure (5 MPa) along the orifice length, coupled to a local increase of the velocity. On the other hand, it can be seen how the temperature tends to increase when moving from the axis to the orifice walls, due to the friction-induced heating effect. Consequently, maximum temperatures of around 315 K are reached inside the orifice for this particular condition. The final value of outlet temperature previously seen in Figure 2.9 is a consequence of the combined influence of both effects: cooling in the core flow and heating around the walls. In the case of the geometry studied, the impact of the wall heating is more significant than the one of the core flow cooling, leading to an overall temperature increase. Nevertheless, it has to be noted that a different geometry characterized by a different discharge

coefficient (and consequently different amount of friction losses) could vary the balance between the two terms, and thus the outlet temperature behavior.

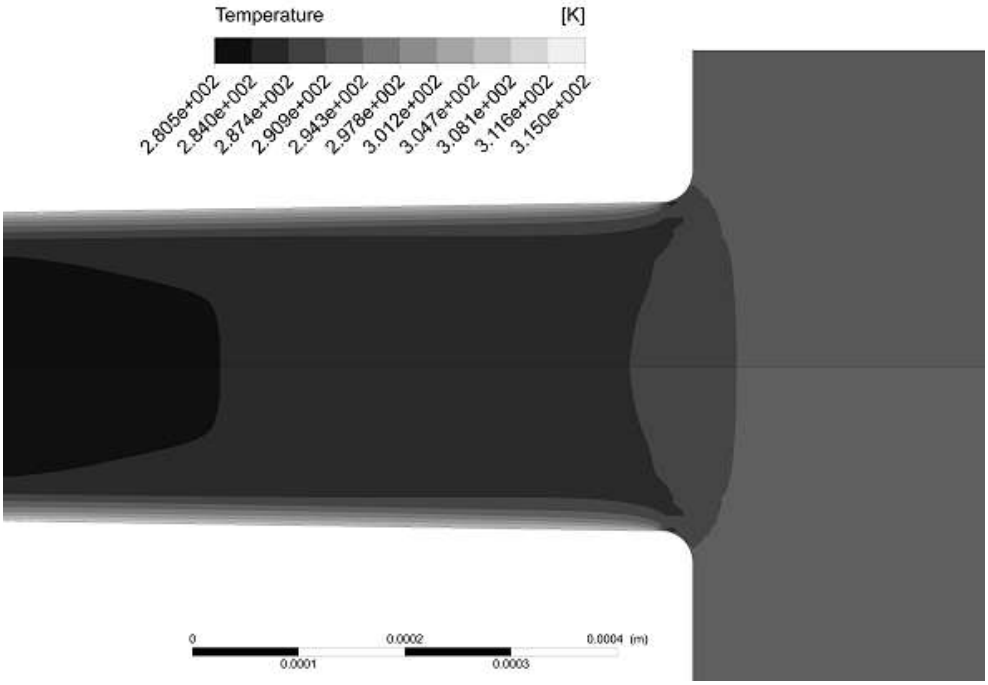

Figure 2.11: Contour of temperature variations in the calibrated orifice (OZ) for the pressure drop 60 MPa - 5 MPa.

Figure 2.12 shows a detail of the temperature distribution at the orifice outlet section for the same case presented in Figure 10. Since the flow is fully axisymmetric, this temperature distribution appears as a set of concentric rings. It can also be easily seen how most of the temperature gradient is observed close to the orifice walls, while up to approximately two thirds of the orifice radius the temperature ranges from 287.5 to 280.5 K.

Figure 2.13 shows a detail of the distributions of density, pressure, velocity and viscosity around the orifice section. As it can be seen, when the flow enters the orifice (moving from right to left) a small recirculation zone associated to a low pressure region is created around the orifice walls. Nevertheless, the extension of this region is reduced thanks to the combination of the inlet rounding radii and the tapered shape. In the core of the flow, the pressure transitions rapidly from the upstream (60 MPa) to the downstream pressure (5 MPa). Associated to the pressure decrease, the flow velocity also increases in the core flow. Nevertheless, the effect of the friction creates a layer of relatively low velocity around the orifice walls. In the case of the density distribution, two different phenomena can be observed. On the one hand, there is a trend to reduce the fuel density when passing through the

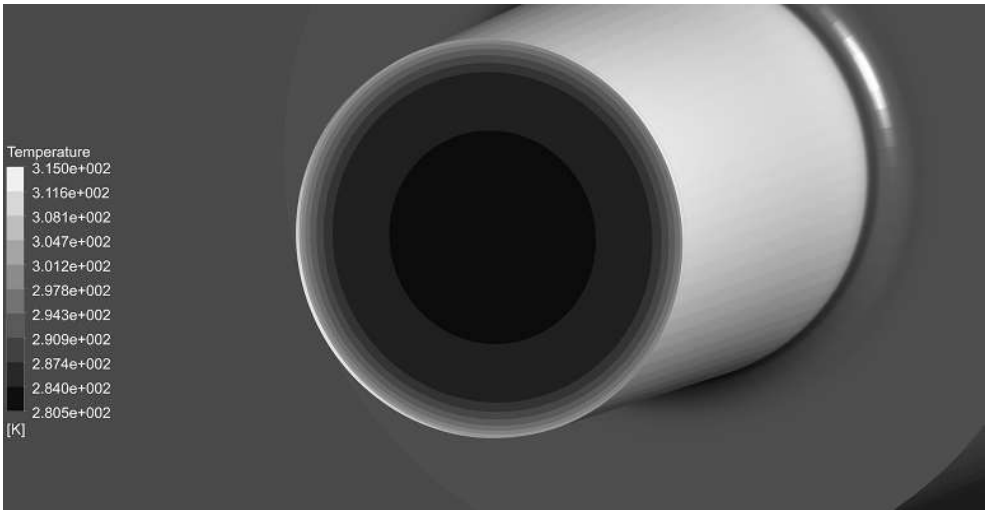

Figure 2.12: Detail of temperature distribution in the calibrated orifice (OZ) outlet section for the pressure drop 60 MPa-5 MPa.

orifice, which is especially visible when comparing the density upstream and inside the orifice. This is associated to the higher-pressure values previously observed upstream the orifice. On the other hand, it can be observed that inside the orifice lower density values are achieved around the walls compared to the center of the flow. This is associated to the non-uniform temperature distribution previously commented, which tends to produce higher temperature values around the walls (due to friction-induced heating) and lower values in the core (induced by the depressurization). Regarding the fuel dynamic viscosity, the influence of the fuel pressure in the range 0-60 MPa is low, so only the temperature influence can be noticed.

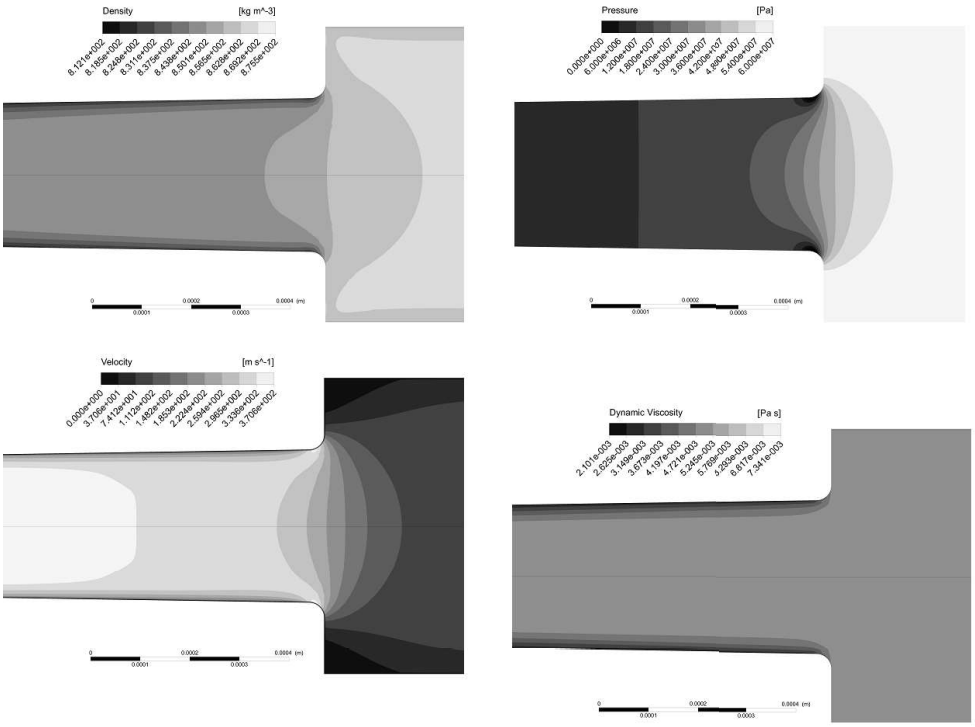

Figure 2.13: Contours of density, pressure, velocity and dynamic viscosity variations in the calibrated orifice (OZ) for the pressure drop 60 MPa-5 MPa.

2.5. Nozzle orifice calculation

Figure 13 shows the validation of the nozzle flow simulations in terms of outlet mass flow. The experimental values had been previously obtained using a rate of injection meter, with the methodology described in previous publications by the authors [44]. As it is appreciable, the computational results follow the linear trend of mass flow with respect to the square root of the pressure drop along the nozzle that appears in the experiments. Nevertheless, some overprediction is observed in the computations. On the one hand, it has to be considered that the simulations have been performed introducing an inlet pressure boundary condition in the needle seat region with a pressure value equal to the common-rail pressure, while in reality some pressure drop would occur between these two sections. On the other hand, in reality there is some non-uniformity in the flow produced by each nozzle orifice, which is not captured with the current setup. Additionally, there are some uncertainties in geometrical parameters such as the inlet rounding radii or the orifice surface finish, which could impact in some way the nozzle outlet velocity and mass flow estimations [45]. In any case, differences between experimental and computational mass flow values are within typical ranges in the literature for

this kind of simulations.

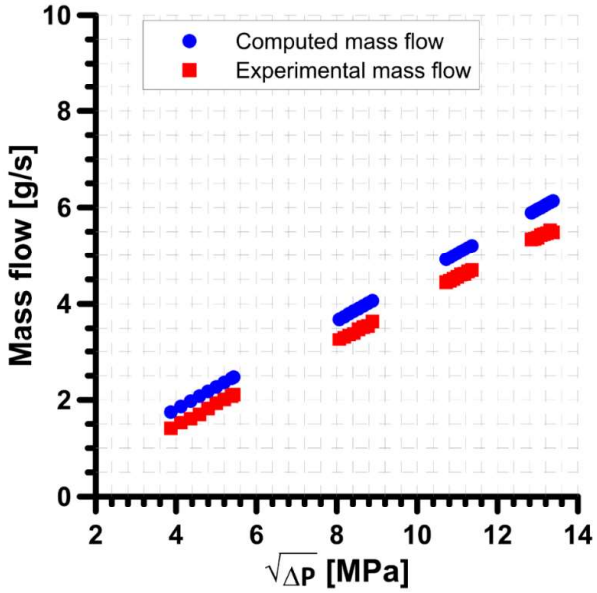

Figure 2.14: Mass flow validation for nozzle orifice simulations.

Figure 2.15 shows some figures of the thermal behavior inside the orifice as a function of the pressure drop along the nozzle. The "x" symbols represent the maximum local temperature values at the nozzle orifice outlet, which correspond to the area near the orifice walls. As it can be seen, the high pressure drop characteristic of the nozzle orifice leads to a strong friction-induced heating effect in this region (up to 50 K in the most extreme pressure drop case). On the contrary, the triangles show the minimum temperature values in this same outlet section, linked to the subcooling effect in the core flow. In this area, the temperature can go as low as 260 K, representing approximately a 33 K temperature decrease. As a consequence, for the 200 MPa injection conditions, there are local differences inside the nozzle outlet section of up to 85 K, which can significantly affect the fuel properties and the spray characteristics. Finally, the circles show the average temperature at the nozzle outlet. While in the OZ calibrated orifice it could be seen that the heating effect in the walls was more significant than the subcooling in the core, always leading to a temperature increase along the domain, in the case of the nozzle orifice the opposite trend is found. This is probably linked to the high discharge coefficient of the particular nozzle geometry used for this study, characterized by a combination of high degree of conicity and high inlet rounding radii. As a consequence, the average temperature drops up to a value of 275 K for the 200 MPa injection pressure conditions.

Figure 2.16 represents the contours of the temperature distribution inside the orifice. On the left hand side, the temperature contour in the middle plane

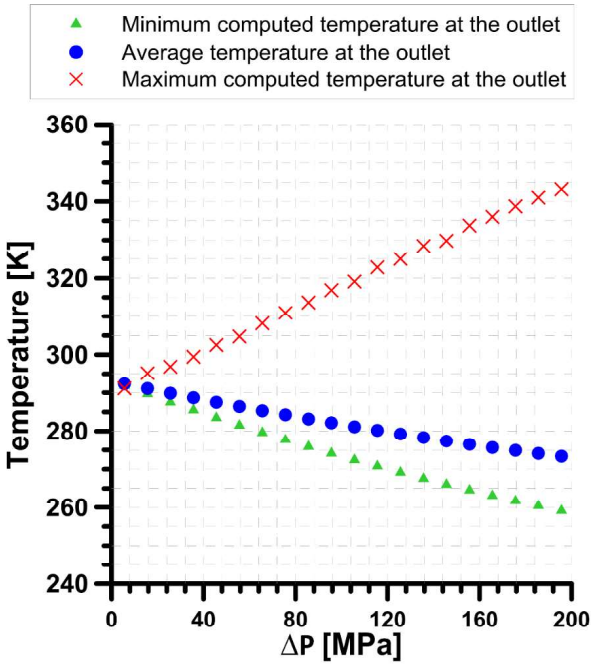

Figure 2.15: Computed maximum, minimum and average temperatures in the nozzle outlet section as a function of the pressure drop.

of the computational domain is depicted. In the inlet part of the orifice (corresponding to the rounding radii region), it can be seen how the temperature drops in the upper side as a consequence of the flow detachment and local low pressure values achieved. Once the flow starts to reorganize, the behavior becomes more similar to what was previously observed for the OZ orifice: a high temperature area appears near the walls due to the friction-heating effect, while the core flow reaches low temperature values due to the depressurization. Nevertheless, it can be noticed that the high temperature area is wider in the upper side. Consequently, the temperature distribution in the outlet section (seen in the right hand side of the figure) shows a deformation for the isotemperature curves in this upper side, inducing most of the low-temperature area to be located near the lateral walls. As it can also be seen in this figure, a similar behavior is also achieved in the bottom side of the orifice, but to a much lower extent.

This non-symmetric distribution of temperature can be better understood looking at the information depicted in Figure 2.17. In this figure, the local temperature contours are superimposed with streamlines reproducing the direction of the flow path. As it can be seen, most of the streamlines reaching the orifice are originated in the needle seat region. Thus, higher local velocities are reached in this region, producing a stronger friction-heating effect and higher local temperatures compared to the lateral sides. Something similar appears

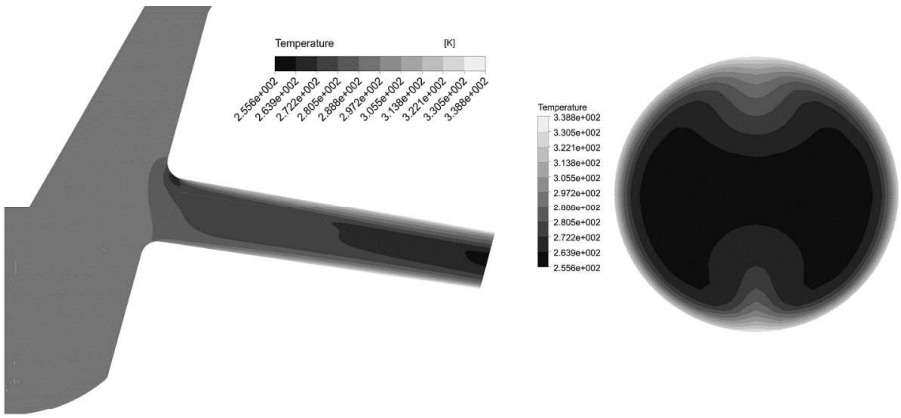

Figure 2.16: Temperature distribution contours inside the nozzle geometry, for a middle plane of the domain (left) and the outlet section (right).

in the bottom side of the orifice, where some of the streamlines appear from the lowest portion of the sac volume, inducing also an extension of the high temperature zone.

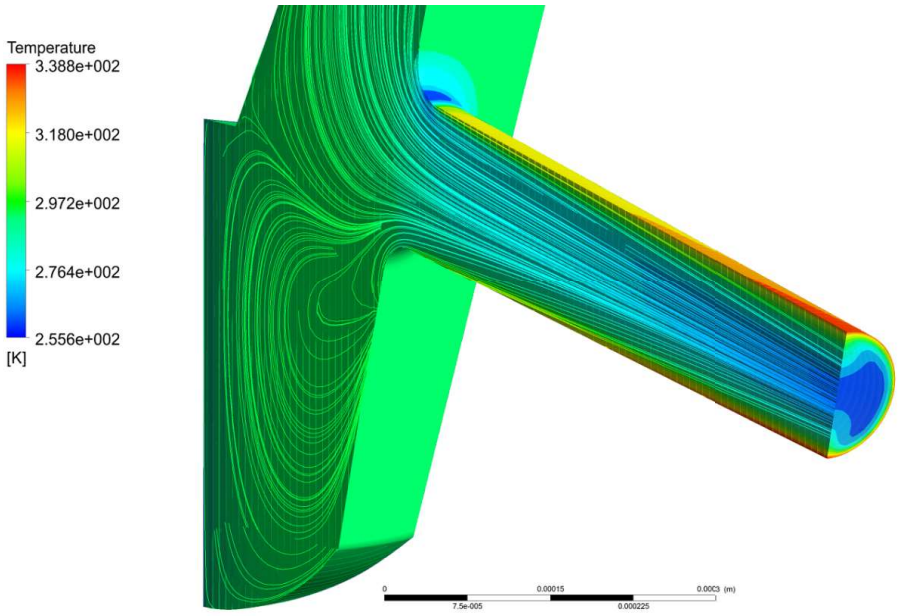

Figure 2.17: Combination of flow streamlines and temperature contours for the nozzle orifice.

2.6. Conclusions

In the current paper, a modeling methodology has been proposed in order to evaluate the thermal aspects involved inside diesel injectors through CFD simulations. This methodology is based on an adiabatic flow condition, which is considered reasonable due to the high flow velocities characteristic of the diesel injection process. Additionally, the dependencies of the most important fuel properties (density, viscosity, thermal conductivity and heat capacity) as a function of pressure and temperature have been incorporated into the CFD code by means of user-defined functions. This methodology has shown a very good capability to reproduce the experimental outlet temperature on a calibrated orifice, with a maximum deviation of approximately 0.9% with respect to the experimental tests. Additionally, the CFD approach has been validated also in terms of the mass flow behavior. Nevertheless, it has to be noted that no experimental validation of the temperature spatial distribution could be performed, given the small dimensions characterizing the orifices of study. A detailed analysis of this temperature distribution in the orifice has shown that in reality there are two counter-acting phenomena occurring inside the orifice. On the one hand, there is a friction-induced heating near the walls, as previously anticipated. On the other hand, the core flow is generally subjected to a depressurization, associated to a decrease in the local temperature. In the case of the control volume calibrated orifice, this second effect is less significant compared to the friction-induced heating, producing a net temperature increase. Once the modeling methodology has been validated for the calibrated orifice, the same kind of analysis has been extended for a diesel nozzle orifice. The interest of this orifice is linked to its much higher pressure drop, which is expected to induce stronger thermal effects, and the impact that this different temperature behavior could have on the atomization and spray formation processes. For this purpose, a commercial 7-holes solenoid injector has been geometrically characterized in order to obtain information to construct the 3D model for the internal flow simulations. The results for the nozzle orifices show again a separated behavior between the walls and the core of the flow. For an injection pressure of 200 MPa, the difference between the local maximum and minimum temperatures in the outlet section is around 83 K, which would induce significant differences in terms of the fuel physical properties, which in turn may be relevant for atomization and spray formation processes. Additionally, it can be seen how the non-uniform distribution of the flow inside the nozzle, induced mostly by the flow bending from the needle seat region to the orifice, produces also a non-symmetric temperature distribution in the outlet orifice.

References

[1] Alessandra Nigro, Angelo Algieri, Carmine De Bartolo and Sergio Bova. "Fluid dynamic investigation of innovative intake strategies for multi-valve internal combustion engines". In: *International Journal of Mechanical Sciences* 123 (2017), pp. 297–310. ISSN: 0020-7403. DOI: https://doi.org/10.1016/j.ijmecsci.2017.02.018. URL: https://www.sciencedirect.com/science/article/pii/S0020740317304411.

[2] Balaji Mohan, Wenming Yang and Siaw kiang Chou. "Fuel injection strategies for performance improvement and emissions reduction in compression ignition engines-A review". In: *Renewable and Sustainable Energy Reviews* 28 (2013), pp. 664–676. ISSN: 1364-0321. DOI: https://doi.org/10.1016/j.rser.2013.08.051. URL: https://www.sciencedirect.com/science/article/pii/S1364032113005911.

[3] Sibendu Som, Anita I. Ramirez, Douglas E. Longman and Suresh K. Aggarwal. "Effect of nozzle orifice geometry on spray, combustion, and emission characteristics under diesel engine conditions". In: *Fuel* 90.3 (2011), pp. 1267–1276. ISSN: 00162361. DOI: 10.1016/j.fuel.2010.10.048. URL: http://dx.doi.org/10.1016/j.fuel.2010.10.048.

[4] Cenk Sayin, Metin Gumus and Mustafa Canakci. "Influence of injector hole number on the performance and emissions of a di diesel engine fueled with biodiesel-diesel fuel blends". In: *Applied Thermal Engineering* 61.2 (2013), pp. 121–128. ISSN: 13594311. DOI: 10.1016/j.applthermaleng.2013.07.038. URL: http://dx.doi.org/10.1016/j.applthermaleng.2013.07.038.

[5] Manolis Gavaises. " Flow in valve covered orifice nozzles with cylindrical and tapered holes and link to cavitation erosion and engine exhaust emissions ". In: *International Journal of Engine Research* 9.6 (2008), pp. 435–447.

[6] Francisco Javier Salvador, Marcos Carreres, David Jaramillo and Jorge Martínez-lópez. "Analysis of the combined effect of hydrogrinding process and inclination angle on hydraulic performance of diesel injection nozzles". In: *Energy Conversion and Management* 105 (2015), pp. 1352–1365. ISSN: 0196-8904. DOI: 10.1016/j.enconman.2015.08.035.

[7] S. Molina, F. J. Salvador, M. Carreres and D. Jaramillo. " A computational investigation on the influence of the use of elliptical orifices on the inner nozzle flow and cavitation development in diesel injector nozzles ". In: *Energy Conversion and Management* 79 (2014), pp. 114–127. ISSN: 01968904. DOI: 10.1016/j.enconman.2013.12.015. URL: http://dx.doi.org/10.1016/j.enconman.2013.12.015.

[8] Francisco J. Salvador, Joaquin de la Morena, Marcos Carreres and David Jaramillo. "Numerical analysis of flow characteristics in diesel injector nozzles with convergent-divergent orifices". In: *Proceedings of the Institution of Mechanical Engineers, Part D: Journal of Automobile Engineering* 231.14 (2017), pp. 1935–1944. ISSN: 09544070. DOI: 10.1177/0954407017692220.

[9] D Nguyen et al. " Spray flow structure from twin-hole diesel injector nozzles ". In: *Experimental Thermal and Fluid Science* 86 (2017), pp. 235–247. ISSN: 08941777. DOI: 10.1016/j.expthermflusci.2017.04.020. URL: http://linkinghub.elsevier.com/retrieve/pii/S0894177717301231.

[10] Xiangang Wang et al. "Effects of ultra-high injection pressure and micro-hole nozzle on flame structure and soot formation of impinging diesel spray". In: *Applied Energy* 88.5 (2011), pp. 1620–1628. ISSN: 0306-2619. DOI: https://doi.org/10.1016/j.apenergy.2010.11.035. URL: https://www.sciencedirect.com/science/article/pii/S0306261910004988.

[11] Metin Gumus, Cenk Sayin and Mustafa Canakci. "The impact of fuel injection pressure on the exhaust emissions of a direct injection diesel engine fueled with biodiesel-diesel fuel blends". In: *Fuel* 95 (2012), pp. 486–494. ISSN: 0016-2361. DOI: https://doi.org/10.1016/j.fuel.2011.11.020. URL: https://www.sciencedirect.com/science/article/pii/S0016236111007149.

[12] Manolis Gavaises, Emmanouil Giannadakis and Andreas Theodorakakos. "The Influence of Variable Fuel Properties in High-Pressure Diesel Injectors". In: Apr. 2009. DOI: 10.4271/2009-01-0832.

[13] S. Som, D.E. Longman, A.I. RamÃrez and S.K. Aggarwal. "A comparison of injector flow and spray characteristics of biodiesel with petrodiesel". In: *Fuel* 89.12 (2010), pp. 4014–4024. ISSN: 0016-2361. DOI: https://doi.org/10.1016/j.fuel.2010.05.004. URL: https://www.sciencedirect.com/science/article/pii/S0016236110002139.

[14] Zuo Yu Sun et al. " Numerical investigation on effects of nozzle's geometric parameters on the flow and the cavitation characteristics within injector's nozzle for a high-pressure common-rail di diesel engine ". In: *Energy Conversion and Management* 89 (2015), pp. 843–861. ISSN: 01968904. DOI: 10.1016/j.enconman.2014.10.047. URL: http://dx.doi.org/10.1016/j.enconman.2014.10.047.

[15] M.S. Alam, M. Asiya Khatun, M.M. Rahman and K. Vajravelu. "Effects of variable fluid properties and thermophoresis on unsteady forced convective boundary layer flow along a permeable stretching/shrinking wedge with variable Prandtl and Schmidt numbers". In: *International*

Journal of Mechanical Sciences 105 (2016), pp. 191–205. ISSN: 0020-7403. DOI: https://doi.org/10.1016/j.ijmecsci.2015.11.018. URL: https://www.sciencedirect.com/science/article/pii/S0020740315003951.

[16] Andrea Emilio Catania, Alessandro Ferrari and Ezio Spessa. " Temperature variations in the simulation of high-pressure injection-system transient flows under cavitation ". In: *International Journal of Heat and Mass Transfer* 51 (2008), pp. 2090–2107. ISSN: 00179310. DOI: 10.1016/j.ijheatmasstransfer.2007.11.032.

[17] R. Payri, F. J. Salvador, M. Carreres and J. De La Morena. " Fuel temperature influence on the performance of a last generation common-rail diesel ballistic injector. Part II: 1D model development, validation and analysis ". In: *Energy Conversion and Management* 114.May (2016), pp. 376–391. ISSN: 01968904. DOI: 10.1016/j.enconman.2016.02.043.

[18] Gavin Dober et al. "Complex physics modelling of diesel injector nozzle flow and spray supported by new experiments". In: *Proc. Conference on thermo and fluid dynamic processes in direct injection engines, Thiesel 2014*. Jan. 2014.

[19] Andreas Theodorakakos et al. " Friction-induced heating in nozzle hole micro-channels under extreme fuel pressurisation ". In: *Fuel* 123.x (2014), pp. 143–150. ISSN: 00162361. DOI: 10.1016/j.fuel.2014.01.050. URL: http://dx.doi.org/10.1016/j.fuel.2014.01.050.

[20] George Strotos et al. "Transient heating effects in high pressure Diesel injector nozzles". In: *International Journal of Heat and Fluid Flow* 51 (2015). Theme special issue celebrating the 75th birthdays of Brian Launder and Kemo Hanjalic, pp. 257–267. ISSN: 0142-727X. DOI: https://doi.org/10.1016/j.ijheatfluidflow.2014.10.010. URL: https://www.sciencedirect.com/science/article/pii/S0142727X14001350.

[21] F.J. Salvador, J. Gimeno, M. Carreres and M. Crialesi-Esposito. "Experimental assessment of the fuel heating and the validity of the assumption of adiabatic flow through the internal orifices of a diesel injector". In: *Fuel* 188 (2017), pp. 442–451. ISSN: 0016-2361. DOI: https://doi.org/10.1016/j.fuel.2016.10.061. URL: https://www.sciencedirect.com/science/article/pii/S0016236116310237.

[22] F. J. Salvador, J. Gimeno, J. De La Morena and M. Carreres. " Using one-dimensional modeling to analyze the influence of the use of biodiesels on the dynamic behavior of solenoid-operated injectors in common rail systems: Results of the simulations and discussion ". In: *Energy Conversion and Management* 54.1 (2012), pp. 122–132. ISSN: 01968904. DOI: 10.1016/j.enconman.2011.10.007. URL: http://dx.doi.org/10.1016/j.enconman.2011.10.007.

[23] V. Macian, V. Bermudez, R. Payri and J. Gimeno. "New Technique for Determination of Internal Geometry of a Diesel Nozzle With the Use of Silicone Methodology". In: *Experimental Techniques* 27.2 (2003), pp. 39–43. ISSN: 0732-8818. DOI: 10.1111/j.1747-1567.2003.tb00107.x. URL: http://doi.wiley.com/10.1111/j.1747-1567.2003.tb00107.x.

[24] F.J. Salvador, Jaime Gimeno, Joaquin De la Morena and Marcos Carreres. "Comparison of Different Techniques for Characterizing the Diesel Injector Internal Dimensions". In: *Experimental Techniques* 42 (Apr. 2018), pp. 1–6. DOI: 10.1007/s40799-018-0246-1.

[25] R. Payri, F.J. Salvador, J. Gimeno and R. Novella. "Flow regime effects on non-cavitating injection nozzles over spray behavior". In: *International Journal of Heat and Fluid Flow* 32.1 (2011), pp. 273–284. ISSN: 0142-727X. DOI: https://doi.org/10.1016/j.ijheatfluidflow.2010.10.001. URL: https://www.sciencedirect.com/science/article/pii/S0142727X10001633.

[26] F. Payri, V. Bermúdez, R. Payri and F. J. Salvador. "The influence of cavitation on the internal flow and the spray characteristics in diesel injection nozzles". In: *Fuel* 83.4-5 (2004), pp. 419–431. ISSN: 00162361. DOI: 10.1016/j.fuel.2003.09.010.

[27] F. J. Salvador, S. Hoyas, R. Novella and J. Martinez-Lopez. "Numerical simulation and extended validation of two-phase compressible flow in diesel injector nozzles". In: *Proceedings of the Institution of Mechanical Engineers, Part D: Journal of Automobile Engineering* 225.4 (2011), pp. 545–563. ISSN: 09544070. DOI: 10.1177/0954407OJAUTO1569.

[28] Francisco Javier Salvador, Jorge Martínez-López, J. V. Romero and M. D. Roselló. "Computational study of the cavitation phenomenon and its interaction with the turbulence developed in diesel injector nozzles by Large Eddy Simulation (LES)". In: *Mathematical and Computer Modelling* 57.7-8 (2013), pp. 1656–1662. ISSN: 08957177. DOI: 10.1016/j.mcm.2011.10.050. URL: http://dx.doi.org/10.1016/j.mcm.2011.10.050.

[29] F. J. Salvador, J. De la Morena, J. Martínez-López and D. Jaramillo. "Assessment of compressibility effects on internal nozzle flow in diesel injectors at very high injection pressures". In: *Energy Conversion and Management* 132 (2017), pp. 221–230. ISSN: 01968904. DOI: 10.1016/j.enconman.2016.11.032. URL: http://dx.doi.org/10.1016/j.enconman.2016.11.032.

[30] American Society for Testing and Materials. "Standard Test Method for Density, Relative Density, or API Gravity of Crude Petroleum and Liquid Petroleum Products by Hydrometer Method". In: *ASTM International* 05.01 (2005). DOI: 10.1520/D1298-12B.

[31] J M Desantes, F J Salvador, M Carreres and D Jaramillo. " Experimental Characterization of the Thermodynamic Properties of Diesel Fuels Over a Wide Range of Pressures and Temperatures ". In: *SAE International Journal of Fuels and Lubricants* 8.1 (2015), pp. 951–2015. ISSN: 1946-3960. DOI: 10.4271/2015-01-0951. URL: http://papers.sae.org/2015-01-0951/.

[32] ASTM D445. "ASTM D445: Standard test method for viscosity of transparent and opaque liquids (Kinematic and dynamic viscosities)". In: *American National Standard Institute, American Society for Testing and Materials* 552.37 (2001), pp. 184–189. DOI: 10.1520/G0154-12A.

[33] B. Kouzel. "How pressure affects liquid viscosity". In: *Hydrocarbon Proc. Pet. Refin* (1965), 44(3):120.

[34] Nikolay Ivanov Kolev. "Thermodynamic and transport properties of diesel fuel". In: *Multiphase Flow Dynamics 4: Turbulence, Gas Adsorption and Release, Diesel Fuel Properties*. Berlin, Heidelberg: Springer Berlin Heidelberg, 2012, pp. 293–327. ISBN: 978-3-642-20749-5. DOI: 10.1007/978-3-642-20749-5_13. URL: https://doi.org/10.1007/978-3-642-20749-5_13.

[35] Woowon Jeong and Jaehoon Seong. "Comparison of effects on technical variances of computational fluid dynamics (CFD) software based on finite element and finite volume methods". In: *International Journal of Mechanical Sciences* 78 (2014), pp. 19–26. ISSN: 0020-7403. DOI: https://doi.org/10.1016/j.ijmecsci.2013.10.017. URL: https://www.sciencedirect.com/science/article/pii/S002074031300297X.

[36] Victor Yakhot and Leslie M. Smith. "The renormalization group, the eps-expansion and derivation of turbulence models". In: *Journal of Scientific Computing* 7.1 (1992), pp. 35–61. ISSN: 0885-7474. DOI: 10.1007/BF01060210.

[37] Robert Castilla et al. "Numerical simulation of turbulent flow in the suction chamber of a gearpump using deforming mesh and mesh replacement". In: *International Journal of Mechanical Sciences* 52 (Oct. 2010), pp. 1334–1342. DOI: 10.1016/j.ijmecsci.2010.06.009.

[38] F.J. Salvador, Marcos Carreres, Debanhi Jaramillo and J. Martínez-López. "Comparison of microsac and VCO diesel injector nozzles in terms of internal nozzle flow characteristics". In: *Energy Conversion and Management* 103 (Oct. 2015). DOI: 10.1016/j.enconman.2015.05.062.

[39] *Ansys-CFX-solver theory guide, release 15.0.* 2013.

[40] P J Roache. " Perspective: A Method for Uniform Reporting of Grid Refinement Studies ". In: *Journal of Fluids Engineering* 116.3 (1994), p. 405. ISSN: 00982202. DOI: 10.1115/1.2910291. URL: http://fluidsengineering.asmedigitalcollection.asme.org/article.aspx?articleid=1427780.

[41] Pengfei Li et al. "Premixed Moderate or Intense Low-Oxygen Dilution (MILD) Combustion from a Single Jet Burner in a Laboratory-Scale Furnace". In: *Energy & Fuels* 25 (May 2011). DOI: 10.1021/ef200208d.

[42] F.J. Salvador, Marcos Carreres, Marco Crialesi Esposito and Alejandro H Plazas. "Determination of critical operating and geometrical parameters in diesel injectors through one dimensional modelling, design of experiments and an analysis of variance". In: *Proceedings of the Institution of Mechanical Engineers, Part D: Journal of Automobile Engineering* 232 (Nov. 2017), p. 095440701773526. DOI: 10.1177/0954407017735262.

[43] F. J. Salvador, J. Martínez-López, J.-V. Romero and M.-D. Roselló. "Study of the influence of the needle eccentricity on the internal flow in diesel injector nozzles by computational fluid dynamics calculations". In: *International Journal of Computer Mathematics* 91.1 (2014), pp. 24–31. DOI: 10.1080/00207160.2013.770483.

[44] R. Payri, F. J. Salvador, J. Gimeno and G. Bracho. "A new methodology for correcting the signal cumulative phenomenon on injection rate measurements". In: *Experimental Techniques* 32.1 (2008), pp. 46–49. ISSN: 07328818. DOI: 10.1111/j.1747-1567.2007.00188.x.

[45] Yukui Cai et al. "Fluid mechanics of internal flow with friction and cutting strategies for micronozzles". In: *International Journal of Mechanical Sciences* 100 (2015), pp. 41–49. ISSN: 0020-7403. DOI: https://doi.org/10.1016/j.ijmecsci.2015.06.011. URL: https://www.sciencedirect.com/science/article/pii/S0020740315002222.

Capítulo 3

Influencia de la geometría en los procesos de inyección-combustión

En teoría, no hay diferencia entre la teoría y la práctica. En la práctica, sí la hay.

Científico de computación anónimo

Resumen: Este capítulo analiza el efecto de geometrías de morfología cónica convergente sobre el proceso de mezcla y combustión. Se han escogido dos geometrías con distinto ratio l/d sobre las que se han ejecutado diversas campañas experimentales con las correspondientes simulaciones. Sobre los resultados producidos se han estudiado las diferencias en términos de flujo interno, penetración y ángulo en condiciones maqueta, y desarrollo de la mezcla y balances energéticos en condiciones motor.

Efficiency increase by means of air insulation through targeted spray and combustion chamber design and reduction of combustion duration in diesel engines

Referencia: J. Benajes, J. M. Pastor, F. J. Salvador, E. C. Martínez-Miracle, U. Wagner, C. Böhmeke, Air Insulation Diesel Engine, FVV Transfer+Networking Event Germany, 30 March 2023.

Abstract: *The aim of this project was to improve the Diesel high-pressure cycle efficiency by mean of a reduction of the heat wall losses in the combustion chamber and an acceleration of the end of combustion thanks to advanced injector nozzle design. In parallel, a "reverse engineering" methodology has been proposed and tested to numerically define an optimized nozzle geometry. Numerical and experimental tools have been used in parallel to precisely characterize the injector nozzles provided by Robert Bosch GmbH and to evaluate the impact of their design on the combustion and particularly on the wall temperature and heat flux in the cylinder. To achieve the first item, CMT used two approaches implemented in the software CONVERGE CFD: the internal nozzle flow and the prediction of the spray trends have been studied using an ELSA (Eulerian-Lagrangian Spray Atomization) [1–4] model as, for the study of the spray and combustion, a DDM (Droplet Discrete Model) approach has been employed. Combustion system simulations relied on the same spray and turbulence modelling approach but, in addition, a finite-rate chemistry solver [5] was used to account for ignition and combustion development. Concerning the wall heat-fluxes, law-of-the-wall temperature boundary condition proposed by O'Rourke and Amsden [6] has been used. A single cylinder engine based on a heavy duty powertrain has been used at IFKM for implementing time resolved advanced temperature and heat flux measurement techniques; a radio frequency system avoiding any electric link between moving and static parts has been implemented at IFKM and successfully tested, providing experimental data to*

CMT. Two injector nozzles with different hole geometries, have been characterized on the bench; the choice of the different spray model parameters has been shown to be robust w/o any necessity to adapt it while changing the nozzle. On the two mid and high load operating points, CFD has shown quite close results in terms of combustion and wall losses but some differences have anyway been highlighted, allowing a possible slight engine efficiency improvement of the order of 1% thanks to both the cycle efficiency and to the heat exchanges. Based on these results, an "optimized" nozzle has been defined and evaluated by simulation. The project has demonstrated the robustness of the spray modelling with the ability to simulate different nozzle geometries with the same model coefficients. The association with combustion models has been successful, paving the way to a "reverse engineering" methodology, defining the nozzle by CFD before any prototype. In terms of experiments, FVV partners can now have access to a cycle resolved piston head temperature measurement at different engine speeds thanks to a radio frequency transmission between moving and static engine parts. Due to a lack of time and prototypes, the nozzle optimization and the final in situ tests of the new defined parts could not be achieved within the frame of the project. The sensitivity to the nozzle hole length to diameter ratio versus the wall losses has nevertheless been highlighted by CFD and the associated physical mechanism explained.

3.1. Acknowledgement

This report is the scientific result of a research project undertaken by the FVV eV and performed by CMT-Motores Térmicos (CMT) at University Politècnica de València under the direction of Prof. Dr.-Ing. Jesús Benajes and by Institute of Internal Combustion Engines (IFKM) of the Karlsruhe Institute of Technology (KIT) under the direction of Prof. Dr. sc. techn. Thomas Koch. The FVV would like to thank the professors Benajes and Koch and their scientific research assistants Dr.-Ing. José Manuel Pastor (CMT), Prof. Dr.-Ing. F. Javier Salvador (CMT), Enrique Carlos Martínez-Miracle, M.Sc. (CMT) and Christian Böhmeke, M.Sc. (IFKM) for the implementation of the project. The project was conducted by a working group led by Dr. habil. Patrick Gastaldi (Aramco Fuel Research Center (AFRC)). We gratefully acknowledge the support received from the project coordination and from all members of the project user committee. In addition, we would like to thank Robert Bosch GmbH for the provision of the injectors and the technical support. The research project was self-financed (funding no. 601318) by the FVV eV.

3.2. Introduction

State of the art

In the field of road transportation, the Diesel engine still presents one of the best solutions to achieve a fair trade-off between cost and CO2 contribution. Nevertheless, the continuous need for reducing the earth global warming leads to one time again improve its efficiency and, with other words, to reduce losses. Among them, the heat transfer to the walls (cylinder head, cylinder liner and piston) plays a significant role in the indicated split-off (Figure 3.1).

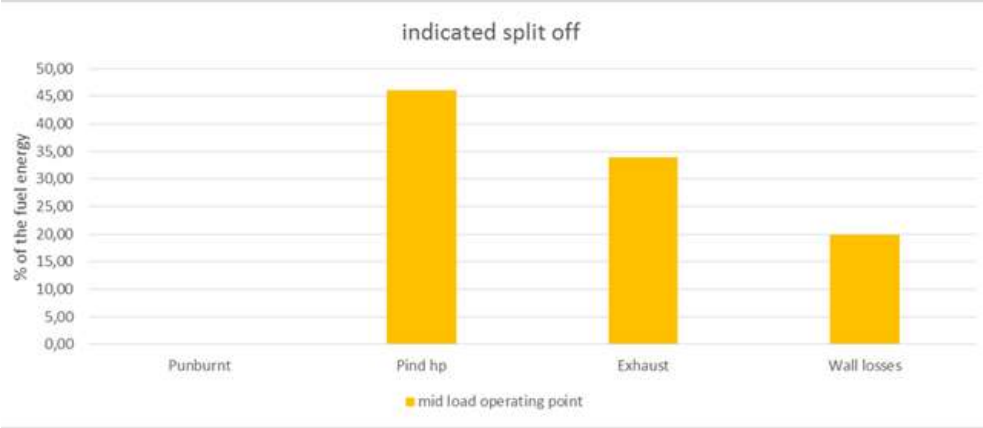

Figure 3.1: Energy balance in a Diesel engine operating at mid-load.

These wall losses are generally described by the following equation:

$$\frac{Q_{wall}}{Q_{fuel}} \propto \frac{S}{V}(T_{gas} - T_{wall})h \tag{3.1}$$

where S is the wall surface, V the chamber volume, T_{gas}, the gas temperature in the vicinity of the wall (more or less in the thermal boundary layer), T_{wall} the surface temperature of the wall and h the transfer coefficient. A great effort is therefore generally achieved to design compact combustion chambers with a low S/V ratio. Nevertheless, this criteria is not sufficient for reducing heat losses and the local aerodynamics (via h) takes also a significant importance; it is admitted that "quiescent" chambers, for instance like those used on industrial engines, with a very low or no swirl provides good benefits despite some drawbacks concerning emissions. Another way is to increase Twall, that is, to insulate the chamber or at least a part of the chamber (Figure 3.2) and especially the piston [7]. This strategy is currently investigated with the FVV M0416 program proposal.

Investigations on T_{gas} have been mainly focused on reducing the bulk temperature, for instance by mean of high levels of Exhaust Gas Recirculation (EGR) or Homogeneous Combustion, in order to decrease the NOx emissions.

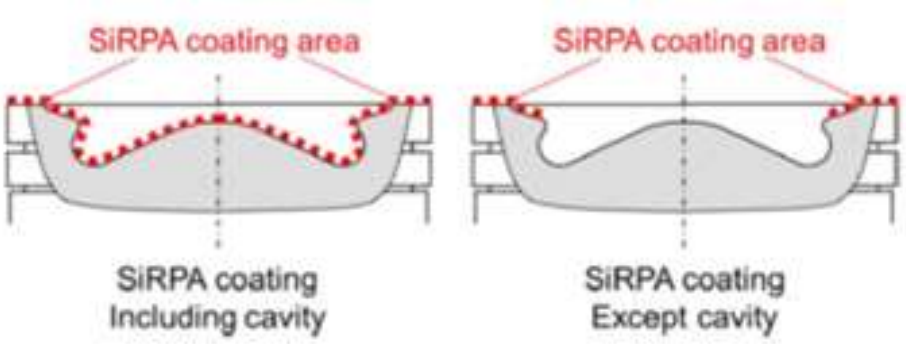

Figure 3.2: Examples of SIPRA Coating.

The piston, the cylinder head or the liner vicinities have not been intensively investigated even if they govern the wall losses. That is to say that the location of the flame in the chamber, and, before, the location of the spray plume, is a major parameter. As spray angle and penetration temporal developments are highly defined by rail pressure and nozzle geometry, the focus has to be shift to injection and mixture preparation topics. As described in Figure 3.3, small bore engines are particularly concerned by this question, but the reduction of heat losses is nevertheless important for all displacements. Improvements in

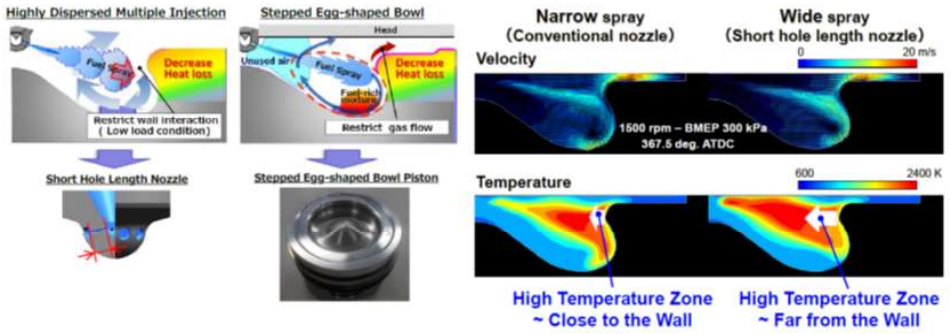

Figure 3.3: The new small Diesel engine Mazda SkyD 1.5l from [8].

the field of the injection system, not only but also by increasing the rail pressure up to 2500 bars and more, and by developing the capacity to produce sophisticated nozzles with high number of holes, complex geometries of the orifices have been up to now mainly used to improve the NOx/soot trade-off but the optimization of their impact on wall losses or end of combustion has been more or less neglected.

Scope, objectives and benefits

The scope of this program is to both obtain a better understanding of the impact of mixture formation and combustion on wall losses in a Diesel

combustion chamber, and to propose a new methodology to reduce them by optimizing the injector nozzle geometry. For these purposes, advanced numerical tools are necessary but not sufficient; significant improvements have to be made to couple experimental measurements like wall temperatures, heat flux, spray behaviour in conditions close to the engine in order to optimize the model calibration. The different tools and techniques are more precisely described by IFKM and CMT in the following sections. Four kinds of deliverables were targeted for FVV members: Guidelines for improving the high-pressure cycle efficiency by a reduction of the thermal losses thanks to new nozzle hole design, order of magnitude of the achieved improvements. Improved methodologies to associate experimental data to 3D simulation for the evaluation of thermal losses and for the spray simulation, linked to the nozzle design. Improved measurement techniques allowing in situ temperature and heat flux measurements in actual operating conditions. A kind of "reverse engineering" methodology, starting with the identification of the origin of the losses and coming up to a nozzle design proposal.

Methodology and program architecture

The methodology followed in this research program is based on the following two main steps. As it is explained below, the second step contains the core of the research, and is divided in two important phases.

- **Step 1: Experimental and computational characterization of the standard combustion system and methodology setup.**
  The main objective of this step was to set up the tools and methodologies that are required for the characterization and analysis of the combustion process in real engine operating conditions. For this step, a real single-cylinder engine in its basic configuration has been used, and a baseline standard nozzle has been tested to avoid any uncertainty that could arise from using innovative nozzles. One first important objective was the set-up and calibration of the CFD modelling tools able to describe the spray evolution and the combustion in the chamber, including the evaluation of the heat losses. The origin of the thermal losses (temporal, spatial) has been identified. Similarly, a second milestone concerned the adaptation of a specific thermometry system for measuring heat flux across the combustion chamber walls of the operating single-cylinder engine. The data obtained from the use of this system has been used for evaluating and eventually calibrating the CFD heat transfer models. For achieving the described objectives, Step 1 is organized combining the experimental and modelling tasks illustrated in Figure 3.4 (left side) and described in Section 3.4.

- **Step 2: Phase 1. Experimental and computational characterization of the prototype nozzle (phase 1) and CFD design of new optimized geo-**

metry (phase 2)
There were two main objectives in Step 2. The first objective was to apply the methodology developed in the previous Step1 to a new prototype injector nozzle to check the ability of the models to reflect a significant change in the hole design. The second was to design a new nozzle geometry, that should be able to improve the heat losses and the combustion rate. For this purpose, Step 2 was divided into two consecutive phases described following.

- Phase 1. Detailed analysis of the behavior of a nozzle prototype:
  In this phase, the same procedure as in Step1 has been applied to a prototype nozzle, again combining experiments in injection test rigs and in engine with CFD modelling, as illustrated in Figure 4: Work flow of Step 1 (left side) and Step 2-Phase 1 (right side). On one hand, this procedure has allowed to check the ability of the models to reflect a significant change in the hole design.

- Phase 2: Proposal of new improved nozzle variation:
  The main purpose was to propose some spay patterns able to reduce losses and to improve the efficiency, with some adaptation to the injection strategy and the piston bowl design, and second to define the corresponding nozzle geometry by the help of the flow simulation.

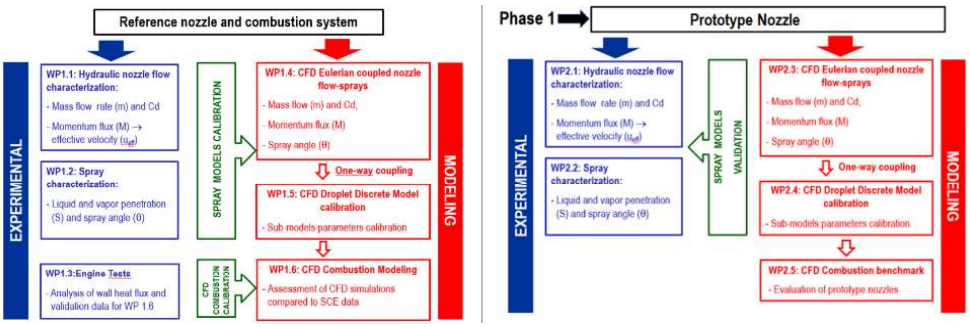

Figure 3.4: Work flow of Step 1 (left side) and Step 2-Phase 1 (right side).

3.3. Experimental facilities and experimental and computational techniques

In this section, the different experimental and computational tools used in the project are described.

Nozzles description and Hydraulic characterization: mass flow rate and momentum flux test rigs

Two different nozzles were used for the study, the first one, so-called the baseline nozzle, used for the Step 1, and the second one for the Step 2- Phase 1. A scheme of them and their main characteristics are depicted in Figure 3.5.

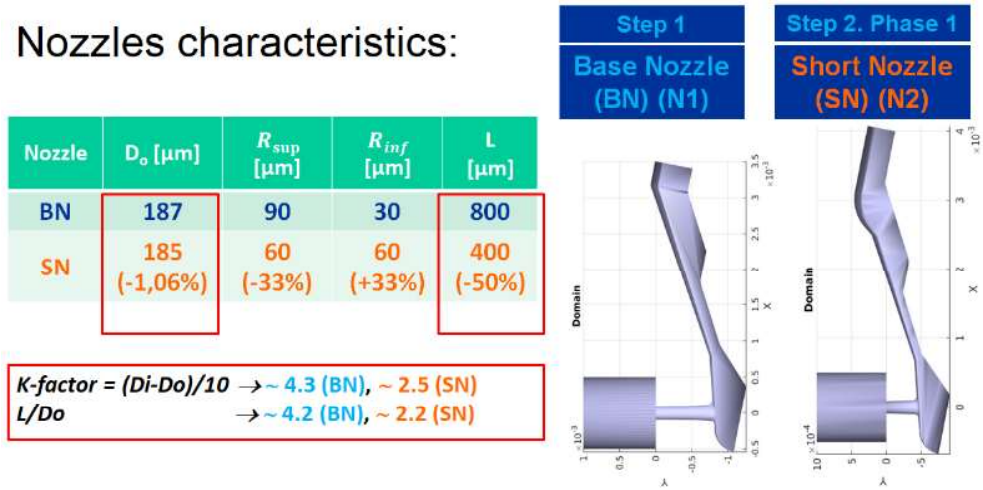

Figure 3.5: Characteristics of nozzles used for Step 1 and Step 2 (Phase 1).

As it can be seen in this figure, both nozzles are conical with different degrees of conicity quantified by the k-factor (definition in Figure 3.5). The basis nozzle presents the highest conicity value with a value of 4.3 vs 2.5 of the second nozzle. In both cases, the high value of conicity factor preserves nozzles from cavitation [9], as it will be shown in the results section. Aside the conicity value, among other factors, the main difference between the nozzles lies in the different length of the holes being the half in the case of the second nozzle. For this reason, this second nozzle was normally called "short nozzle" throughout the investigation and this paper in results section. Since both nozzles has similar outlet diameter, D_o (187 µm vs 185 µm) the reduction in the length is, in turn, in the L/Do value (4.2 vs 2.2, respectively). In Figure 3.5, R_{sup} and R_{inf} refers to rounding radius in the upper part and lower part of the orifice inlet due to hydro-grinding process [10]. Both nozzles have 9 orifices with the same inclination angle. For the development of work packages WP1.1 and WP2.1 (see Figure 3.4), it was necessary to measure the instantaneous mass flow rate and the momentum flux for the baseline nozzle and the prototype nozzle. Measurements of injection rate were carried out with an Injection Discharge Rate Curve Indicator (IRDCI) commercial system from the company IAV [11, 12]. The measurements were of the spray momentum flux were carried out in a dedicated test rig, where the force of the impinging spray on a pressure sensor is recorded [13]. This force is equivalent

to the spray momentum flux. Sprays are injected into a chamber that can be pressurized with nitrogen up to 10 MPa, to simulate pressure discharge conditions that are representative of real pressure conditions inside the engine combustion chamber during the injection process. The combination of mass flow rate measurements and momentum flux measurements make it possible to obtain the effective velocity at the nozzle outlet. This parameter, jointly with the discharge coefficient are of special relevance for the validation of Eulerian coupled nozzle flow simulations, as will be seen in results section.

Spray characterization test rig. Mie-scattering and Schlieren techniques

In work packages WP1.2 and WP2.2, it is necessary to visualize the spray evolution for detecting the instantaneous evolution of the spray liquid and vapor phases. For both objectives, a high-pressure and high-temperature test rig will be used [14]. The liquid phase penetration was visualized by the means of Mie scattering technique [15]. A schematic example of the Mie scattering setup is presented on the left side of Figure 3.6. For the detection of the vapour phase penetration, a double pass Schlieren arrangement was implemented [16], as seen in the right side of this Figure.

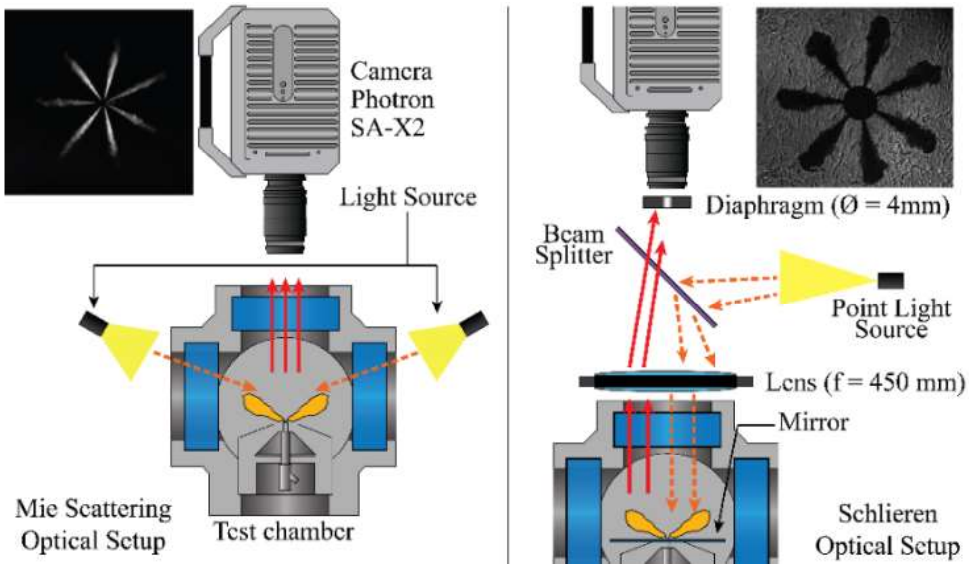

Figure 3.6: Schematics of the optical arrangements used for liquid phase characterization by means of Mie Scattering technique (left side) and vapor phase characterization by means of Schlieren technique (right side).

Internal nozzle flow and spray modelling: Eulerian and discrete droplet model approaches

In this study, two approaches implemented in the software CONVERGE CFD have been followed. The internal nozzle flow and the prediction of the spray trends have been studied using an ELSA (Eulerian-Lagrangian Spray Atomization [1–4] model that allows the transition from an initial Eulerian field to a Lagrangian one. Also, for the study of the spray and combustion, a DDM (Droplet Discrete Model) approach has been employed [17]. The ELSA model can couple the internal flow behaviour thanks to its initial Eulerian framework and the behaviour of the spray. However, it may require a minimal calibration and the computational cost limits its use. On the other hand, the un-expensive DDM model allows good agreement in spray and combustion modelling in exchange of a need of constants calibration. This calibration was performed feeding the model with ROI (Rate of Injection), spray angle, geometrical values of the nozzle and rates of injection. Constants were varied accordingly to match the spray penetration of liquid and vapour phases [18]. In Figure 3.7 basic schemes of two approaches are shown.

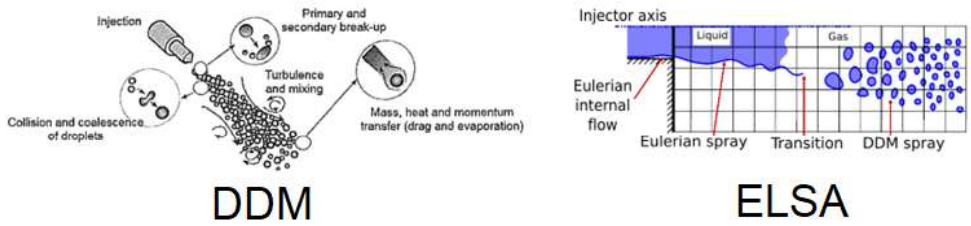

Figure 3.7: Schemes of DDM (left side) and ELSA (right side) approaches.

As there was no information about the needle lift motion of the studied injectors for the eulerian simulations, in order to emulate the injector behaviour, the internal geometry of the nozzle was replaced by its outlet orifice. In this new inlet boundary, the characteristics of the internal flow simulations were mapped in order to match the rate of injection of each nozzle through the variations of the velocity profiles values. The resulting droplets of both ELSA and DDM model are subjected to break-up according to a KH-RT model [19]. A Re-Normalisation Group (RNG) [20] model was used for the Eulerian turbulent frame. The Frossling model was selected as evaporation approach [6, 21]. In Figure 3.8, a scheme of the methodology used is shown.

Simulations were performed using a characterized diesel fuel in terms of density, viscosity, enthalpy and surface tension [22] and diesel vapour was approached by n-heptane. Geometry for the base nozzle internal flow simulations was reconstructed from the SEM (Scanning Electronic Microscopic) visualization using a CAD software [23]. The 3D geometry for the nozzle prototype was provided by the manufacturer. CFD evaluations of the spray penetration

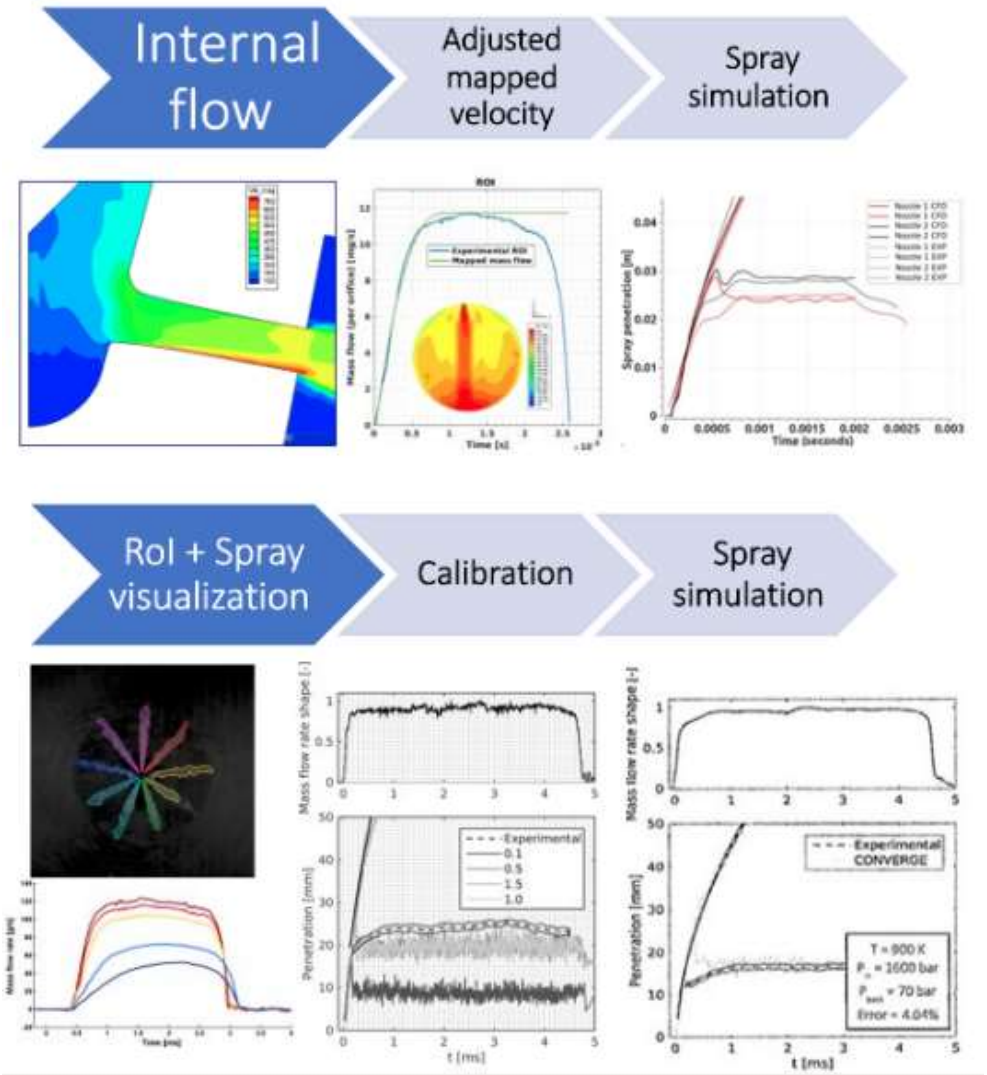

Figure 3.8: Example of methodology schemes.

were performed using a 99% criteria of the total spray mass [24]. All mesh configurations were accompanied by grid independence studies.

Engine combustion modelling

Combustion system simulations rely on the same spray and turbulence modelling approach described in Section 3.3. In addition, a finite-rate chemistry solver [5] is used to account for ignition and combustion development. Diesel fuel chemistry is represented by a surrogate PRF mechanism with 70-species and 192-reactions [25]. Concerning the wall heat-fluxes, law-of-the-wall temperature boundary condition proposed by O'Rourke and Amsden [6] Com-

putational domain comprises 1/9th sector of the combustion chamber, taking benefit from the equally space 9-hole nozzle and piston bowl axi-symmetry. The calculations were run from IVC to EVO, i.e. during the closed thermodynamic cycle. The initial (pressure, temperature, composition) and boundary (surface temperatures) conditions were estimated based on the combustion diagnostics in-house code CALMEC [26].

Single cylinder engine test bench and set-up

This chapter describes the experimental setup, the development of the telemetry system, the setup of the thermocouple in the piston and in the cylinder head as well as the operating conditions.

Engine setup

The experimental engine investigations of the project were performed on a single-cylinder MTU BR2000 research engine. Key engine and testbed data are given in Table 3.1. An overview of the setup is provided in Figure 3.9.

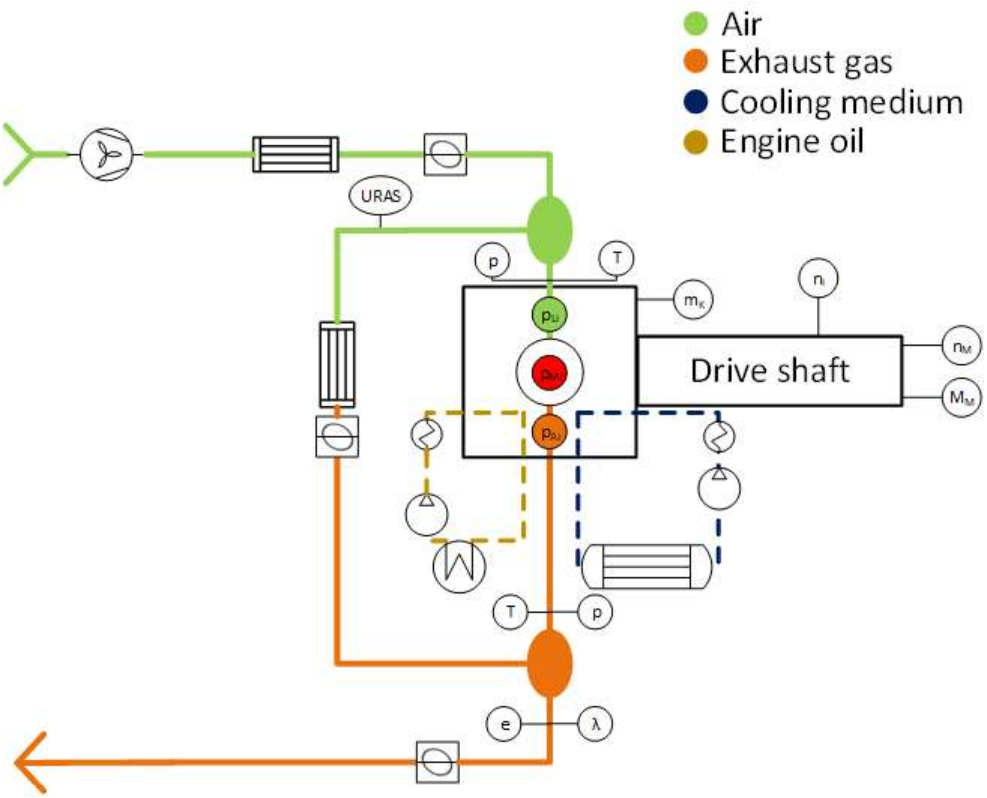

Figure 3.9: Sketch test bench.

Engine data	
Engine type	One-cylinder research engine
Compression ratio	13.3:1
Displacement	1.99 dm3
Injector	Bosch CRIN-3 (9 Hole)
Emission measurement systems	
Gaseous emissions	AVL AMA4000
CO2 for EGR-rate calculation	URAS
Soot	AVL Smoke Meter
Testbed Systems	
Engine oil	Temperature and pressure controlled.
Engine coolant	Temperature und volume flow controlled.
Cooled EGR	EGR rate controlled.
Charged Air	Pressure and temperature controlled, rotary gas meter for volume and mass flow.
Exhaust pressure	Controlled by back pressure valve depending on boost pressure level.
Fuel supply	External fuel pressure supply; volumetric fuel consumption measurement and density correction by AVL PLU/KMA-unit.
Indication system	Cylinder pressure, Exhaust pressure, Inlet pressure, dynamic rail pressure, surface temperatures.

Table 3.1: Engine data and testbed setup of the one-cylinder research engine.

Operating points

A broad experimental matrix was established within the project, which is shown in Table 3.2. Two different speeds were selected as well as 3 different loads. Within these operating points, variations with different mean indicated pressure/constant fuel mass, rail pressures, SOI variations and EGR rates were chosen. A backpressure of 200 mbar above boost pressure was set at each operating point, as well as a pre-injection with a constant energizing timing of 10 °CA before the main injection. Furthermore, an inlet temperature of 40 °C was controlled.

Thermocouples of the piston and the cylinder head

In order to measure the temperatures and local heat flux of the piston and cylinder head on the combustion chamber side, the cylinder head was fitted

	A25	**A50**	**A100**	**B100**
n [rpm]	1200	1200	1200	1500
IMEP [bar]	5.5	10.5	21.0	21.0
p_2 [mbar]	1300 - 1700	2000 - 2400	3000 - 3400	3000 - 3400
p_Rail [bar]	800 - 1200	1000 - 1400	1400 - 1600	1400 - 1600
CA50 [°CA]	6 - 8 - 12	6 - 8 - 12	11 - 13 - 15	12 - 13 - 15
EGR [%]	0 - 15 - 30	0 - 15 -30	0 - 15	0 - 15

Table 3.2: Operating points.

with eight and the piston with six surface thermocouples. For this purpose, corresponding holes were drilled in the cylinder head and in the piston. Type K thermocouples were then inserted through these holes and bonded gas tight using a temperature resistant epoxy adhesive. Since the temporal measurement resolution of the thermocouples is too low to obtain crank angle resolved measurements, the top end is milled off and then the thermo-wires are reconnected with a chromium layer. To protect the connection, a gold layer is also applied [27]. This is shown as an example in Figure 3.10.

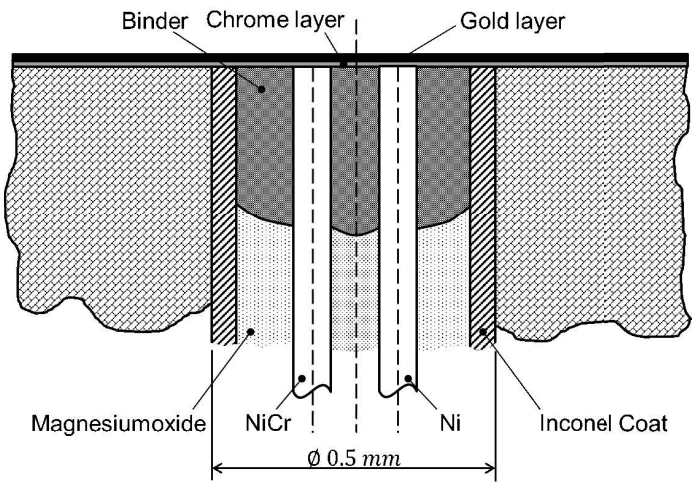

Figure 3.10: Installation of surface thermocouple [28].

In order to obtain the influence of the position of the thermocouples in addition to the temporal course of the surface temperatures, the thermocouples were distributed throughout the cylinder head. Furthermore, the thermocouples were distributed in the piston along the x-axis from inlet to outlet. The respective positions are shown in Figure 3.11.

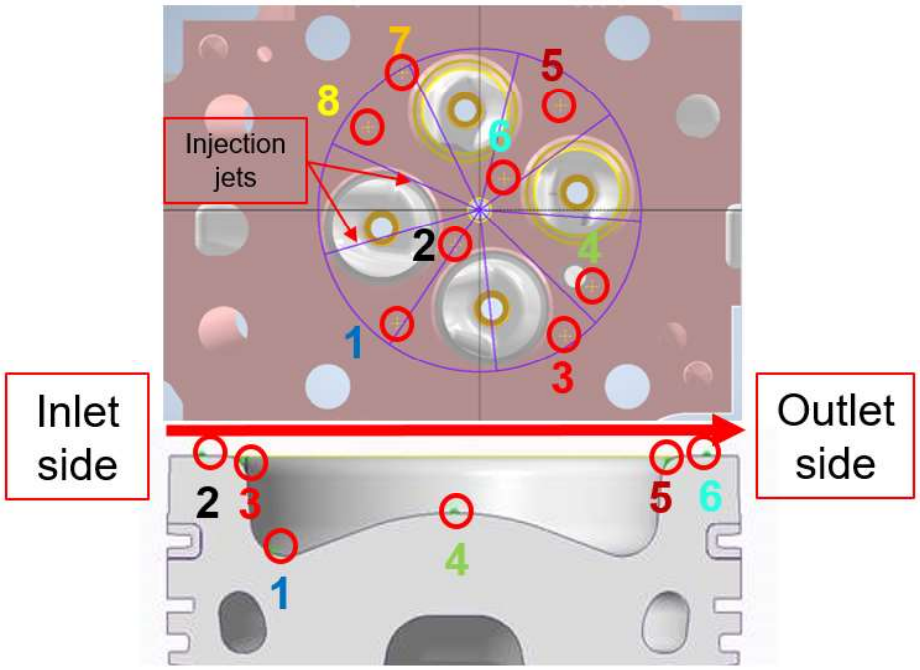

Figure 3.11: Positions of the surface thermocouples in the piston and cylinder head.

Telemetry system

During the project, a self-developed telemetry system was used to measure various surface temperatures of the piston used in this case and transfer the measurement values wirelessly to a data sampling device. The principle of operation is shown in Figure 3.12. The thermocouple, which measures only a few millivolts, is connected to a voltage amplifier, which in turn is connected to an analog to digital converter (ADC) to convert the voltage into a digital signal. The digital signal is used as input for the microcontroller (ESP8266), which can transmit the measured signal via WLAN. These shown components are placed inside the piston. Inside the crankcase a receiver is installed, which is connected to the indication system to record the measured data via a USB interface. This system allows the measurement of seven individual temperatures, a reference temperature directly on the system and the piston acceleration. Depending on the speed, a temporal resolution of about 1 °CA is possible. The reference temperature, which is available as an absolute temperature, is required because the temperatures at the surface thermocouples are only measured as relative temperatures and thus the actual temperatures at the piston surface can be inferred.

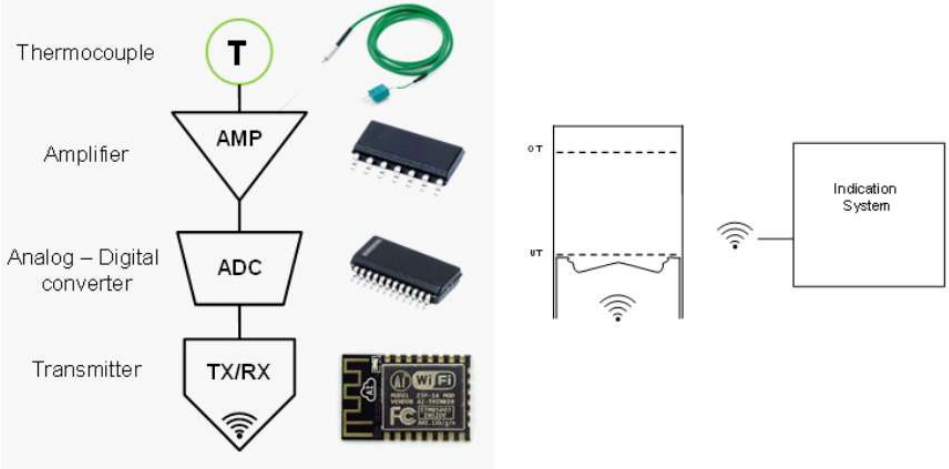

Figure 3.12: Functionality telemetry system.

Since no temporal allocation to the crank angle is directly available for the respective measured temperatures, the acceleration of the piston is required, which on the one hand is measured with the installed acceleration sensor and on the other hand can be determined according to Equation 3.2 via the position of the crankshaft, the speed and the geometric data of the engine.

$$a_{Piston} = r \cdot \omega \cdot \left[\cos\alpha + \left(\lambda \cdot \frac{\cos 2\alpha + \lambda^2 \cdot \sin^4 \alpha}{\sqrt{(1 - \lambda^2 \cdot \sin^2 \alpha)^3}} \right) \right] \tag{3.2}$$

with $\lambda = r/l$ By calculating the two accelerations, the signals can be synchronized. This is shown in Figure 3.13. Furthermore, the receiver outputs a voltage signal as a trigger as soon as it receives data from the transmitter and stops again as soon as the transmission is completed. This trigger is needed so that the indication system measures at the same time as the telemetry system. Since signal delays cause an offset of the measurements, a synchronization must be performed.

By synchronization, the measured surface temperatures can now be assigned to a crank angle and subsequently averaged over the measured cycles. Furthermore, it must be noted that the temperatures of the surfaces are sampled one after the other, so that the respective temperature signal must be additionally shifted afterwards on the basis of the sampling sequence. An averaged measurement including time allocation is shown as an example in Figure 3.14.

Power supply

A central challenge is to supply the system used with sufficient power, as it is exposed to extreme conditions and no wiring for external power supply

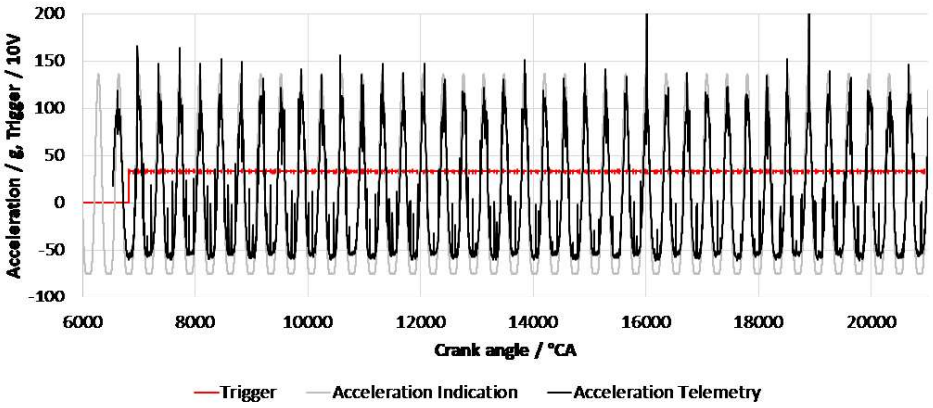

Figure 3.13: Synchronisation telemetry system and indication system.

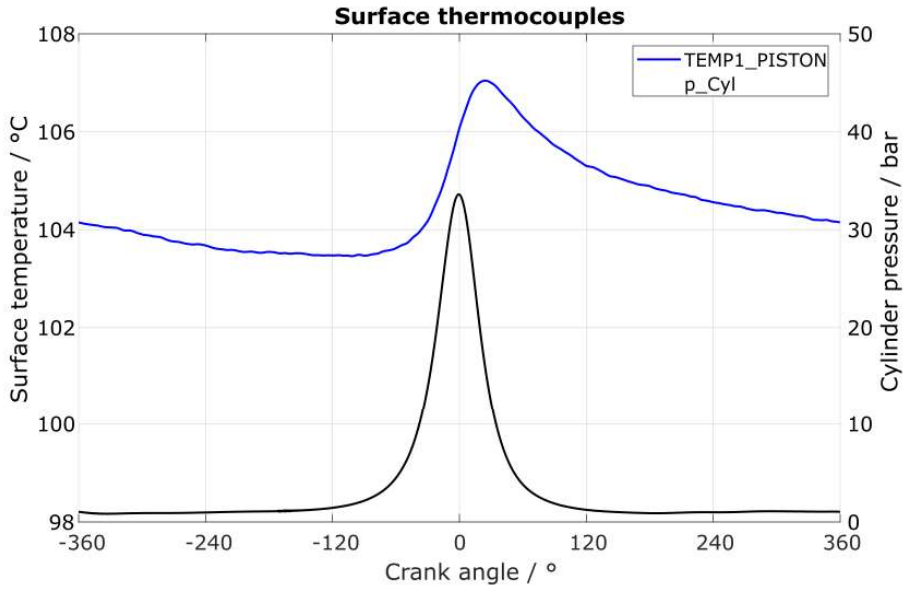

Figure 3.14: Finalized synchronisation surface temperature.

should be used. On the one hand, high acceleration occurs inside the piston and on the other hand, high temperatures are reached. To ensure a continuous power supply, a battery solution was chosen. At this point, it must be noted that the batteries used have shown only limited durability. The reason for this lies in the extreme accelerations of the piston. Since the batteries in our case were installed vertically in the piston (see Figure 3.15), the vertical acceleration also increased with increasing speed. This repeatedly led to the interior of the batteries being destroyed and thus a sufficient power supply could not be guaranteed.

Figure 3.15: Piston with installed battery case.

Heat flux calculation

As already described in chapter 3.3, the surface temperatures of the piston were measured and transmitted by means of a telemetry system due to its mobility. To determine the surface temperatures of the cylinder head, on the other hand, the thermocouples were connected directly to the indication system. This enables the various temperatures to be measured with crank angle resolution. The temperatures determined by the telemetry system and the indication system can then be used to calculate the local heat flux with a temporal resolution. The surface temperature method was used to determine the wall heat losses. This is explained in the following section.

Surface temperature method

The periodic sequence of compression, combustion, expansion and charge exchange, temperature oscillations occur at the combustion chamber surface. temperature oscillations, which can be recorded by measuring the temperature curves in the area of the combustion chamber surface. The temperature curve on the combustion chamber wall can be divided into a stationary and a dynamic part. The assumptions are made that it is a one-dimensional, one-sided infinite extended temperature field, so that the heat flow can be described by means of Fourier's differential equation [29, 30]. The following equation is used to evaluate the heat flow at the combustion chamber surface [31, 32]

$$\dot{q}(t) = \dot{q}_m + \lambda \sum_{i=1}^{\inf} [(A_i - B_i)\cos(i\omega t) + (B_i - A_i) \cdot \sin(i\omega t)] \qquad (3.3)$$

Here $\dot{q}_m$ is the steady-state heat flux density, λ the thermal conductivity and ω the angular frequency. The coefficients A_i and B_i can be determined

by Fourier analysis from the time course of the measured temperatures. Furthermore, the thermal conductivity λ and the thermal diffusivity a can be replaced by the heat penetration coefficient b according to Equation 3.4.

$$b = \frac{\lambda}{\sqrt{a}} \tag{3.4}$$

The heat penetration coefficient can be determined experimentally as well as mathematically [33]. Within this project, the heat penetration coefficient for the piston and cylinder head was determined by calculation on the basis of the material properties. A heat penetration coefficient of 5500 $\mathrm{W\,s^{0.5}/(m^2\,K)}$ was determined for the cylinder head and 11 595 $\mathrm{W\,s^{0.5}/(m^2\,K)}$ for the piston. The zero-crossing method was used within the project to determine the stationary part. In addition to the determination of the surface temperatures, the gas temperature within a cycle is required for this. This is calculated using the cylinder pressure and the measured fuel and air mass calculated according to Equation 3.5 [34].

$$T_{gas} = (p_{cyl} \cdot V)/(m \cdot R) \tag{3.5}$$

Here, p_{cyl} represents the crank angle resolved measured cylinder pressure, V the actual volume in the combustion chamber, m the total mass of air and fuel within the cycle, and R the specific gas constant. It is assumed that using this method the heat flux is zero when wall temperature and gas temperature are equal [34]. The stationary heat flux qm can then be calculated according to Equation 3.3. This principle is illustrated in Figure 3.16.

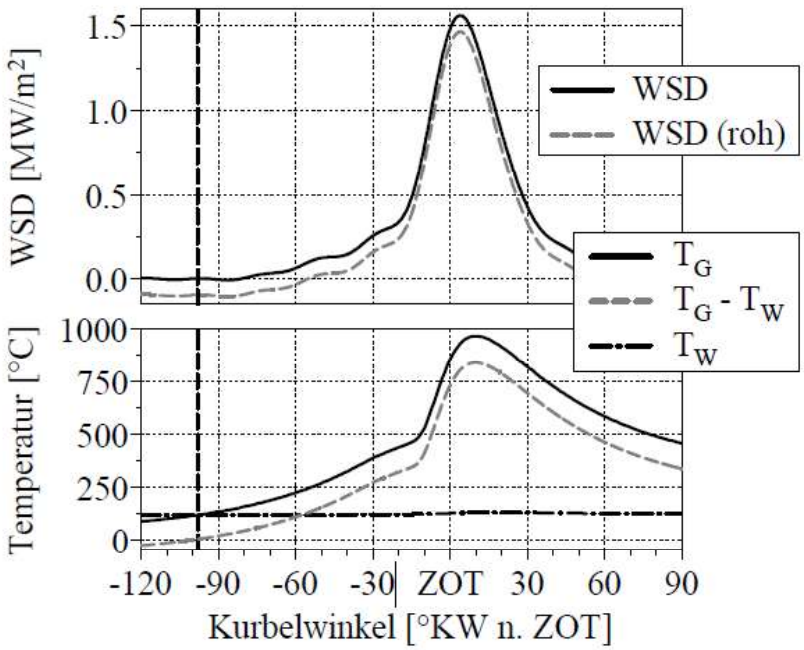

Figure 3.16: Principle of the zero crossing method [35].

3.4. Results and analysis

Step 1: characterization of the reference combustion system

In this section, experimental and computational results concerning the reference combustion system are shown and analysed. Mass flow rate and momentum results Following the methodology presented in section 3.3, mass flow rate and momentum flux were measured for several test points at low, medium and high injection pressures ranging from 500 to 2000 bar, different back-pressures and several energizing times. As a sample, in Figure 3.17, the mass flow rates for different injection pressures and backpressures and an energizing time of 1.5 ms are depicted. Considering the steady part of the mass flow rate signal, the average steady mass flow can be plotted as a function of the squared root of the pressure drop (difference between injection pressure and backpressure) as plotted in Figure 3.18 (left side). In this figure the stabilized mass flow per orifice is shown. Taking into account the orifice diameter, the discharge coefficient can be calculated as:

$$C_d = \frac{m_f}{A_{geo} \cdot \rho_f u_{th}} \tag{3.6}$$

Being m_f, the steady mass flow, A_{geo} the geometric outlet section, ρ_f the fuel density and u_{th}, the Bernoulli´s theoretical velocity. The discharge coefficient

has been plotted in Figure 3.18 (right side) considering all the tested points. Discharge coefficient shows a typical asymptotic behaviour of a convergent (non-cavitating) nozzle which is compatible with the linear trend observed in previous graph (absence of mass flow choking) [14]. Maximum discharge coefficient is around 0.91.

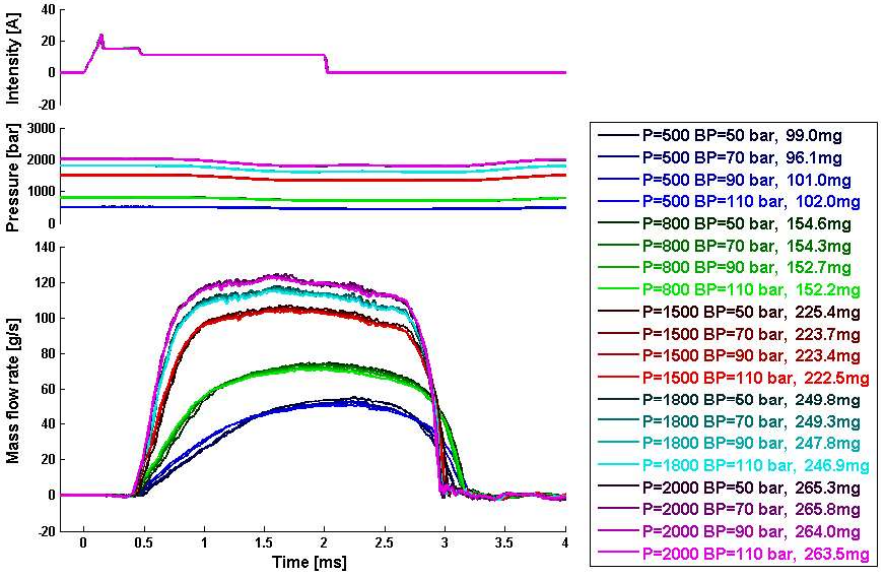

Figure 3.17: Mass flow rate measurements for different injection and back pressures at the same energizing time.

Figure 3.18: Steady mass flow as a function of the pressure drop (left side) and discharge coefficient as a function of pressure drop (right side).

As far as momentum flux measurements are concerned, they were carried out by following the aforementioned methodology (section 3.3). Momentum flux signal are quite like those obtained from mass flow rate. Proceeding in the same way as for mass flow rates, in Figure 19 (left side), the steady momentum flux in N is plotted against the squared pressure drop for all the

injection conditions. Nevertheless, the main utility of this signal is obtained when combined with previous steady mass flow measurements, since this combination, according to Equation 3.7, provides the effective injection velocity, calculated as :

$$u_{eff} = \frac{M_f}{m_f} \tag{3.7}$$

being M_f the steady momentum flux. The effective velocity for all the characterized injection conditions is plotted in Figure 3.19 (right side). This effective velocity varies from around 300 m s^{-1} for 500 bar to around 600 m s^{-1} at 2000 bar.

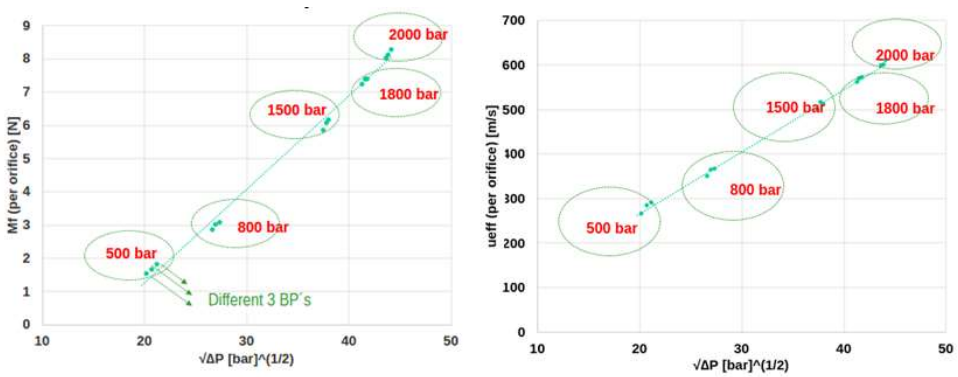

Figure 3.19: Steady momentum flux as a function of the pressure drop (left side) and discharge coefficient as a function of pressure drop (right side).

Experimental spray characterization results

The basis' nozzle sprays were characterized following the methodology explained in Section 3.3. The characterization was made in terms of macroscopic spray parameters: spray tip penetration and spreading angle in both, non-evaporative and evaporative inert conditions. The selected injection pressures were 500, 800, 1500, 1800 and 2000 bar while the back pressures were 50, 70 and 90 bar over an energizing time of 2 ms at 400 (non-evaporating condition) and 900 K (evaporating condition). The resulting ambient density values for both temperatures were respectively: 41.4, 57.6 and 73.4 kg/m^3 at 400 K and 18.4, 25.5, 32.6 kg/m^3 at 900 K. The ambient chamber gas was N2 (inert conditions). As a sample of the measurements performed, in Figure 20 (left side), the liquid and vapor penetration as function of time is are depicted for an injection pressure of 150 bar and three different densities in chamber: 18, 25.5 and 32.6 kg/m^3 at 900 K. In continuous line, the liquid spray penetrations obtained by means of Mie-scattering technique are plotted and, dotted lines refers to vapor penetration obtained by means of double pass Schlieren technique. The coloured shadow that accompanies the different signals represents

the standard deviation of the ten repetitions performed for each point. As far as liquid penetration is concerned, as can be seen liquid penetration stabilizes at different liquid lengths (LL) depending on the chamber density, ρ_a. In fact, according to Equation 3.8, liquid length inversely depends on chamber density, therefore, the higher the density, the shorter the liquid length experimentally observed. In this Equation 3.8, $\tan(\theta_u/2)$ is the tangent of the spray semi-angle which has also been measured for all the tested points and plotted in the right side of Figure 3.20. As it can be noted, the higher the chamber density, the wider the spray cone angle.

$$LL \propto \frac{D_o}{\rho_a^{0.5} \tan(\theta_u/2)} \tag{3.8}$$

As far as the vapor penetration is concerned, as it can be seen in the left-hand side of Figure 20 (dotted points), the lower the density, the higher the spray penetration. This result agrees with Equation 3.9 which is a well-known penetration law as a function of time and other injection and chamber conditions [36, 37].

$$S = cte \cdot \Delta P^{1/4} \cdot D_o^{1/2} \cdot \tan^{-1/2}(\theta_u/2) \tag{3.9}$$

It is worth noting that both techniques (Mie and Schlieren) provide the same results for liquid penetrations shorter than the liquid length for which evaporation has not yet taken place.

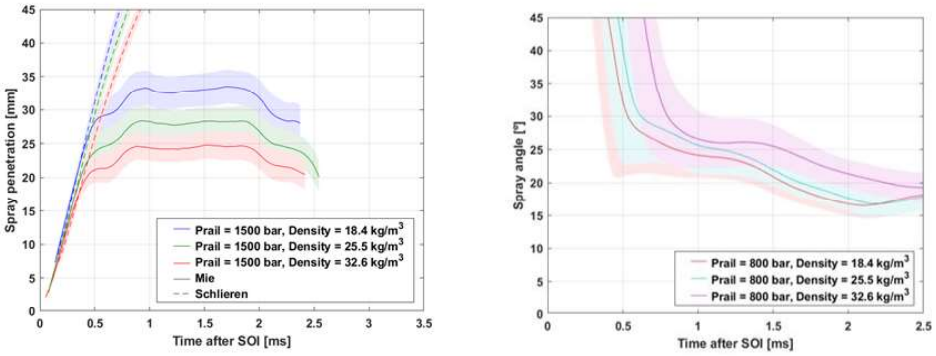

Figure 3.20: Liquid and vapor spray penetration (left side) and spray cone angle (right side) for different chamber values.

Internal nozzle flow and Spray Modelling

The simulations for the internal flow study were carried out in the same injection conditions using the geometry of the base nozzle. The nozzle geometry is attached to a small chamber domain where the back pressure of each point

is reproduced. The mesh configuration for the internal flow is shown in Figure 21 (left side) where the mesh characteristics are also provided. From an initial refinement of 48 µm in the needle section and 12 µm in the nozzle section an AMR is activated along the injector body up to 12 µm. After the nozzle outlet orifice, a fixed embedding of 24 µm is applied following the injection direction.

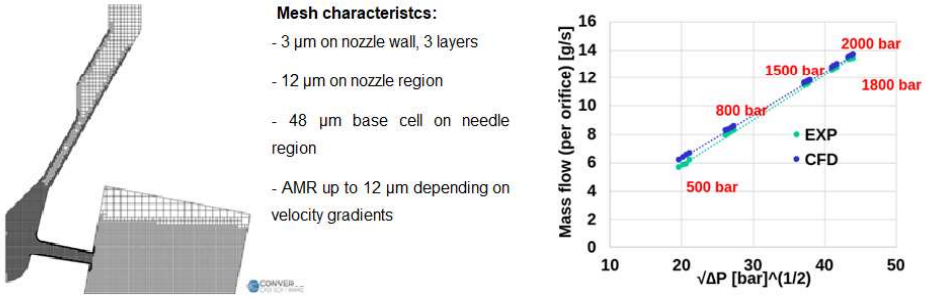

Figure 3.21: Internal nozzle flow mesh characteristics (left side) and computational results compared to experimental ones (right side).

In Figure 3.21 (right side), the comparison between computational results and experimental results in terms of steady mass flow rate as a function of pressure drop is shown for all the tested points. In overall terms, computational results show small deviation from the experimental ones, with bounded errors around 3%. Higher deviation is found for small pressure drops. The main reasons of this deviation could be the uncertainties in geometry determination, needle deformation, etc. In any case, the code is able to predict the experimental results with high level of confidence. On the other hand, the simulations of the spray covered the same conditions as the experiments. Using the rate of injection, the geometrical parameters of the nozzle, and the experimental spray angle, the DDM constants were calibrated to have an error on spray penetration below 7% for all the tested points. In Figure 3.22 it is shown as an example the comparison between the computational DDM model results and experiments for two different points in non-evaporative (at 400 K) and evaporative conditions (at 900 K), on the left and right side, respectively. Injection conditions can be read under the different graphs. As it can be seen, results show a good agreement in terms of liquid and vapor penetration. Regarding the ELSA model, in this case, inlet velocity conditions are directly mapped from internal nozzle flow calculations. As an example, in Figure 3.23, experimental and computational vapor and liquid penetrations from an evaporative point are compared. The point corresponds to 1500 bar of injection pressure and 70 bar of backpressure. Temperature in the chamber was 900 K. As it can be observed, ELSA model slightly underpredicts the experimental measurements, especially in liquid length estimation, but in any case, with an uncertainty level lower than 10%. In the same Figure (right side), the exper-

imental and ELSA model spray angle are compared for the same operating point. As it is shown, although there is a high deviation during the transient period, the difference in stabilized spray angle gets smaller with an estimation error around 6.8% ($+1.4^{o}$). It must be highlighted here that, unlike the DDM model, results are not subjected by any calibration process and so, they mainly depend on the reliability of the inlet mapped boundary conditions, apart from, obviously, on mesh quality, turbulence model, among others.

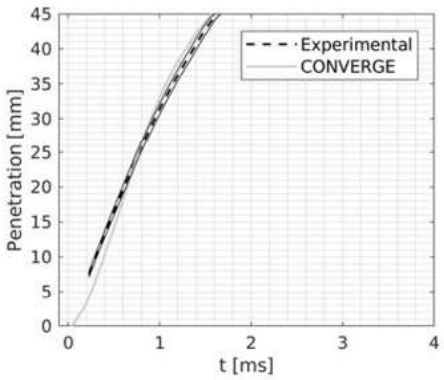

Pinj = 800bar , Pback = 70 bar

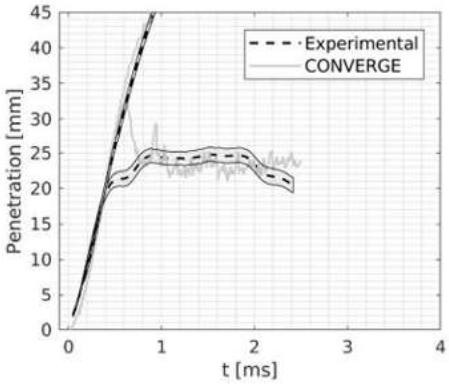

Pinj = 1500bar , Pback = 90 bar

Figure 3.22: Some results of the spray DDM numerical modelling in non-evaporative and evaporative conditions.

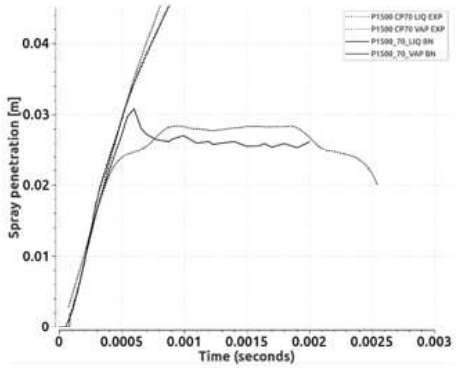

Pinj = 1500 bar, Pback = 70 bar

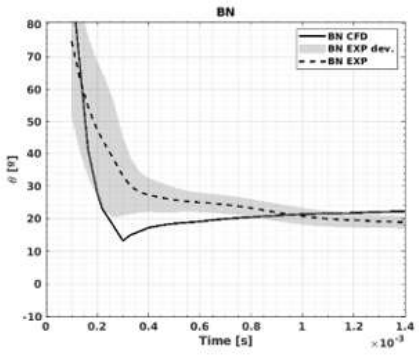

Pinj = 1500 bar , Pback = 70 bar

Figure 3.23: Some results of the spray ELSA numerical modelling in evaporative conditions.

Combustion modelling

SCE combustion system simulations were performed according to the methodology previously described. Different operating conditions were simulated to set-up and assess the computational model. Figure 3.24 shows that the model is able to properly predict the in-cylinder pressure both at medium (A50) and high-load (B100) conditions. The heat-release rate (HRR), derived from the experimental data by the thermodynamic diagnostics tool, is also well captured in the simulations.

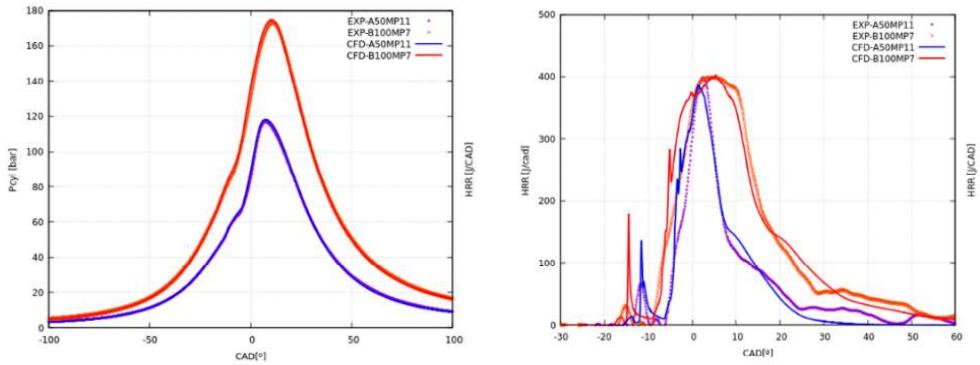

Figure 3.24: In-cylinder pressure (left side) and heat-release rate (right side) for CFD and SCE experiments.

In addition, heat transfer model was evaluated and calibrated by comparing heat-fluxes obtained from the thermocouples. The temperature wall-function was modified (heat flux was scaled by a constant factor) in order to improve the agreement on local heat-fluxes, while keeping the accuracy on in-cylinder pressure trace predictions, as shown in Figure 3.25.

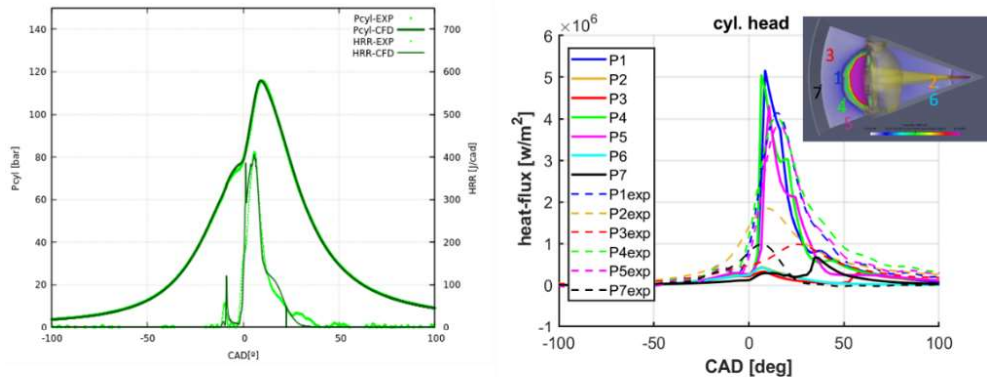

Figure 3.25: In-cylinder pressured and heat-release rate (left side) and heat-flux at cylinder head thermocouple locations for CFD and SCE experiments.

The combustion system CFD model was then used to evaluate the heat

losses spatial and temporal evolution. Figure 3.26 (left) presents the heat transfer rate over combustion chamber surfaces, showing that spray-flame interaction noticeably increases heat flux. The accumulated values over piston, cylinder-head and liner surfaces are plotted in Figure 3.26 (right) during the combustion development, indicated by the HRR.

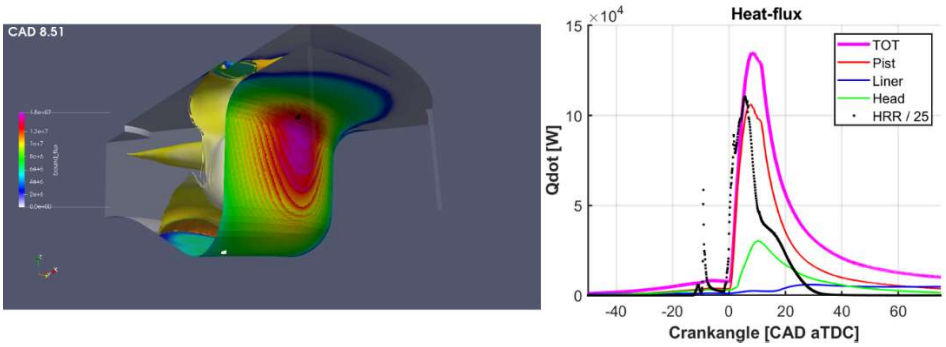

Figure 3.26: Heat flux through chamber surfaces spatial distribution (right) and temporal evolution. The stoichiometric isosurface represents the flame location in right picture.

Step 2. Second nozzle characterization and Optimization

In this section, the results concerning the second nozzle are presented and analysed. In order to evaluate the potential of this nozzle in comparison to the basis one, the most interesting results from the point of view of the internal nozzle flow, spray behaviour, fuel-air mixing process, combustion, heat transfer and combustion efficiency are compared to those of the first nozzle. From now on, basis nozzle and second nozzle will be referred in the paper as BN and SN, respectively.

Mass flow rate and momentum results

For the second nozzle (SN), mass flow rate measurements at the same injection conditions as for the first one were carried out. In Figure 3.27 (left side) the steady mass flow at maximum needle lift of the SN is plotted against the squared-root of pressure drop and compared to the same results of the first nozzle (BN). As depicted in the Figure, the steady mass flow rate from the SN is slightly higher than that of the BN. This is mainly due to the slightly smaller diameter of SN vs BN (185 vs 187 µm) and small differences in the discharge coefficient. In any case, differences in mass flow rates are only around 1.5%. When comparing the same parameter but coming from calculations differences were a little bit higher in favour of the BN (-3.5%). The same Figure 3.27 (right side) compares the effective injection velocity between both nozzles as a function of the pressure drop for all the tested cases. As can be seen from

this graph, the SN nozzle presents higher velocity than BN. Differences are around 3.8%. This is mainly due the reduction of the orifices length which contributes to a reduction of friction losses, which, in turn, highly increases the velocity despite having less conicity factor than BN.

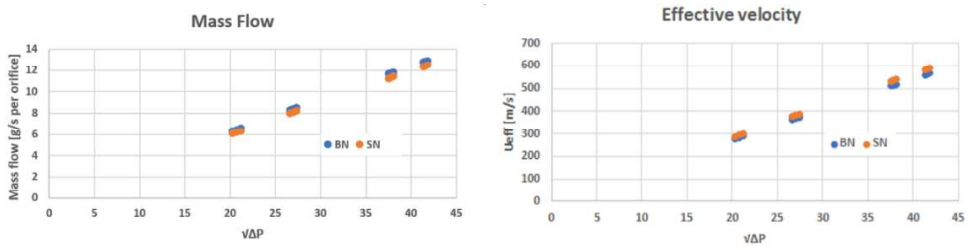

Figure 3.27: Mass flow rates for the SN nozzle (left side) and comparison of stabilized mass flow between nozzles (right side).

Experimental spray characterization

As in the case of BN, the SN sprays were characterized using the same methodologies. This nozzle was only evaluated in the most interesting points from the point of view of engine tests, including only evaporative conditions. The proposed test matrix covered three injection pressures (800, 1500 and 1800 bar) and three back pressures (50, 70 and 90 bar). The ambient temperature was kept at 900 K. In Figure 3.28, vapor and liquid penetration of SN are compared to those of BN for three different injections pressures and two different backpressures. In the same graph, the cone spray angle of both nozzles is compared for three different chamber densities (bottom, right side). Results for BN are plotted in dotted line while those for SN are depicted in continuous line. As far as the liquid penetration is concerned, SN presented lower values for all conditions. This result is completely in line with Equation 3.8 since the orifice diameter is smaller than for the BN case, and also, the spray cone angle, is too much wider in the case of SN. Differences in angle are about 14%. The reason of this last evidence was justified by means of CFD calculations of the inner nozzle flow that shown higher turbulence and vorticity levels at the orifice outlet that directly affect atomization and so, air-fuel interaction. As for what concerns the vapor penetration, BN exhibits slightly higher values. In this case and according to Equation 3.9, this result is justified by its fairly smaller spray angle despite having a slightly larger diameter.

Internal nozzle flow and Spray Modelling

As in the case of BN, internal nozzle flow and spray simulations were also done for the SN. The DDM model approach for the SN uses the same

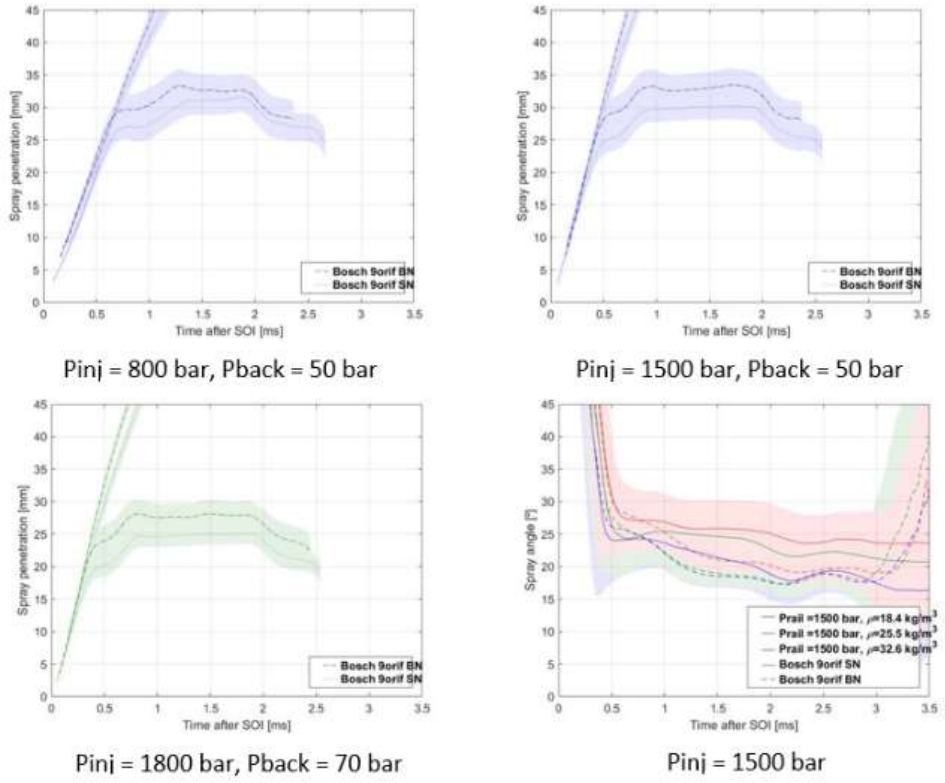

Figure 3.28: Comparison of liquid and vapor penetration and spray cone angle for BN and SN.

calibration of BN, but, obviously, considering the new input parameters. This approach makes sense if we consider that the injector model is the same in both cases, and, therefore, it is assumed that the differences in the model´s input parameters are exclusively due to nozzles geometrical differences. In overall terms, the DDM model of SN performs quite well when comparing with experimental results providing pretty accurate results with similar deviation from experiments and same level of reliability than the DDM model applied to the BN case. As a sample, for instance, in Figure 3.29, DDM results of SN are plotted for a couple of evaporative points (see injection conditions at the bottom of the figure). As far as the ELSA model is concerned, just like it was done with BN, the model capabilities were proved by comparing its results against experimental data under a wide range of operating conditions. As a sample, in Figure 3.29 (left side), the ELSA model liquid and vapor penetration predictions are compared with experimental results for a given operating point (see bottom of the figure). Additionally, previous BN ELSA experimental and model results have been added. As it can be seen, this figure highlights again the ability of the model to reproduce the experimental results. In particular, liquid length is as well predicted as in the previous BN

case. However, the vapour penetration is even better predicted for the SN case than BN. In the same Figure 3.30 (right side) the spray angle from ELSA model is compared to the experimental one, including also previous BN ELSA numerical and experimental results. In this case, as it was also the case for the BN nozzle, SN ELSA results shows a deviation of around 15% with respect to the experimental stabilized spray angle. It is very important to highlight here that, although the angle proved by ELSA model is slightly higher for the SN than that of the BN, these differences are not of the same order than those observed experimentally.

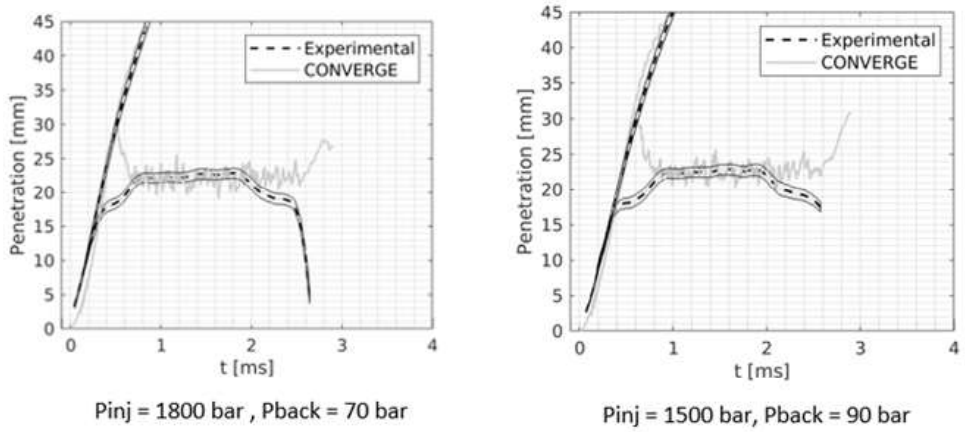

Figure 3.29: Some results of the DDM spray approach for the SN nozzle versus experimental.

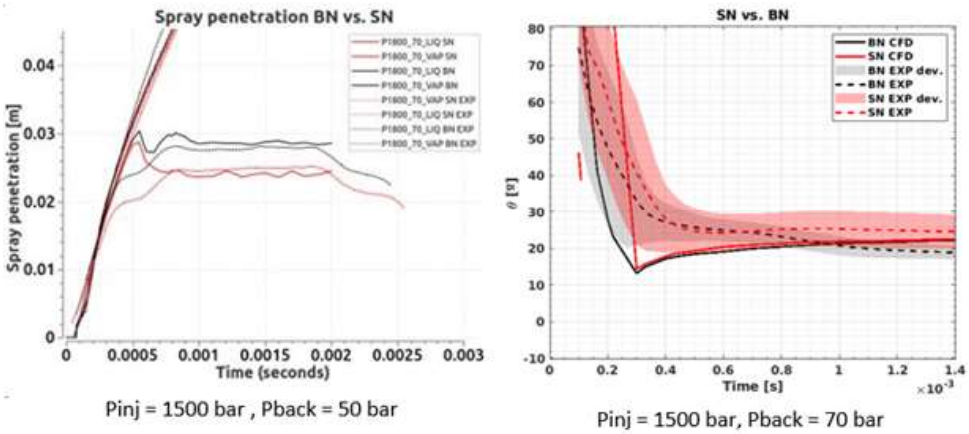

Figure 3.30: Some results of the ELSA model spray approach versus experimental for the BN and SN nozzles.

Combustion modelling

Using the same validated model of Section 3.4, and the new characterized spray of the SN nozzle, both injectors have been compared in terms of combustion and cycle efficiency. The SN model respects the injection duration and total injected mass used for the BN. Figure 3.31 shows the in-cylinder pressure (left side) and heat release rate (right side).

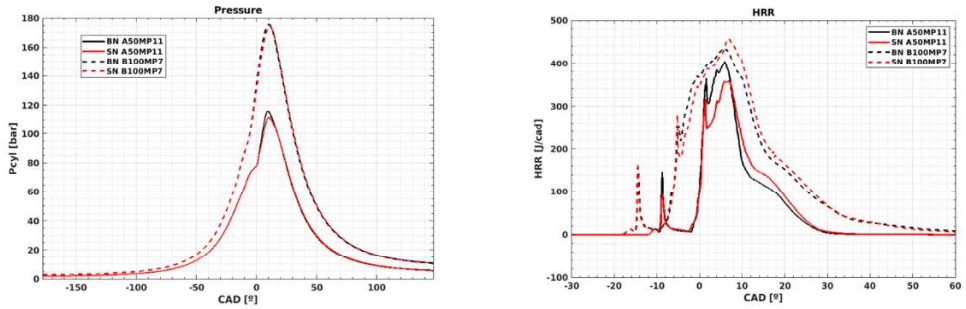

Figure 3.31: In-cylinder pressure and heat release for CFD BN and SN simulations.

At a mid-load condition (continuous line), the SN nozzle shows an initial lower heat release that leads to slightly lower in-cylinder peak pressure. However, the later combustion is more intense as shown in the accumulated heat release of Figure 3.31 (left side). Something similar occurs at high load, in this case the maximum peak is almost the same and the SN nozzle, even if its heat release is delayed, improves the heat release beyond the BN nozzle. These trends were confirmed by ELSA combustion simulations at mid load as shown in Figure 3.32.

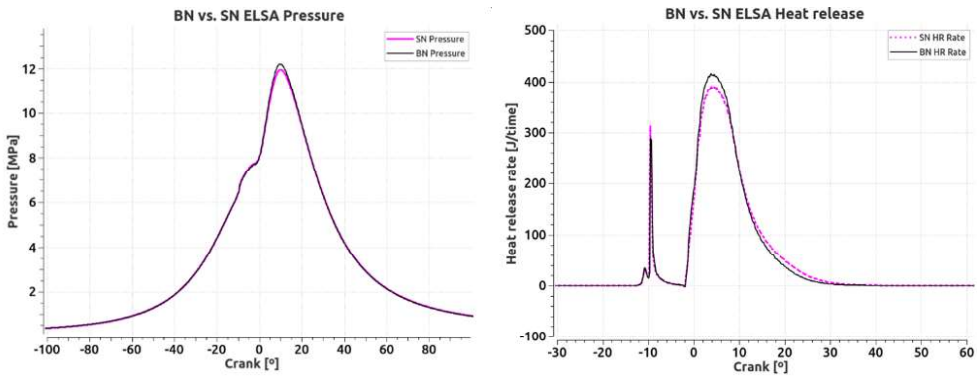

Figure 3.32: ELSA combustion approach, pressure and heat release.

The impact of the nozzle design on the wall heat transfer is presented in Figure 3.33 (right side) and Figure 3.34. Here, for the mid-load point a reduction in the heat transfer through the piston can be observed. At high

load condition, despite the higher cumulative heat release for the SN nozzle, the heat losses remain almost the same. Again, the ELSA simulation confirms the trends (Figure 3.34 right side) but with an overprediction of the transfer heat compared to DDM values (Figure 3.34 left side). This leads us to think that, although the ELSA model can predict the trends, also requires a more in-depth study.

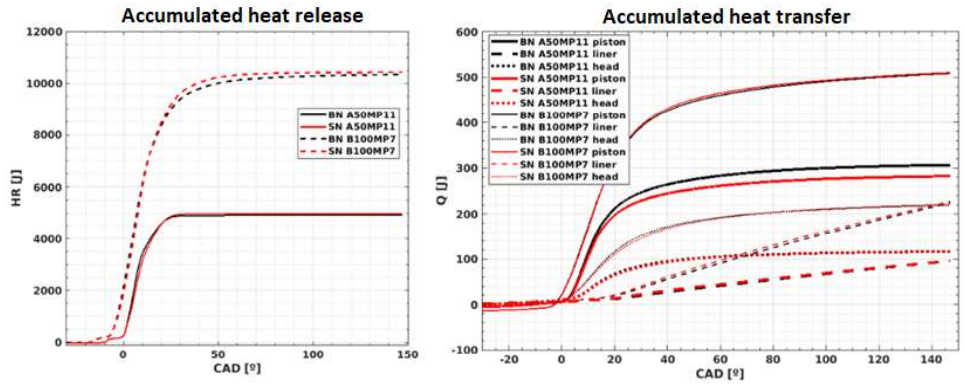

Figure 3.33: Accumulated heat release and heat transfer of the DDM model, BN and SN nozzles.

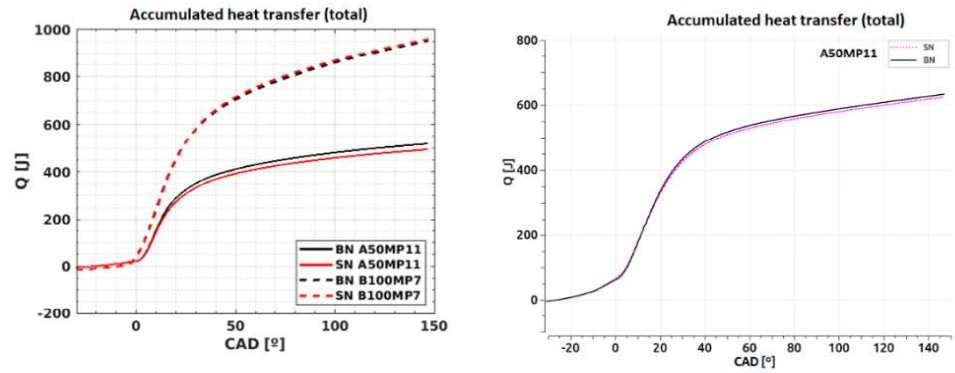

Figure 3.34: Total heat transfer DDM (left side) and ELSA (right side) of BN and SN.

The mixing behaviour represented in Figure 3.35 helps in the understanding of the heat release results. In this figure is presented the amount on in-cylinder mass with equivalence ratio (ϕ) higher than 1 and 2. It is shown that rich regions mass ($\phi > 1$) is lower for SN during late combustion, indicating more efficient mixing process that allows faster burning rates. This

difference is more noticeable under high-load conditions, also supported by heat release results.

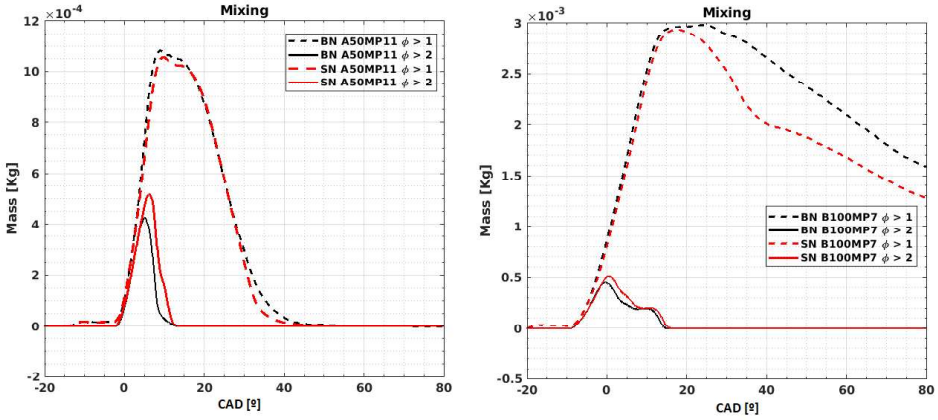

Figure 3.35: Mixture for the BN and SN nozzle at mid-load point (left) and high-load point (right).

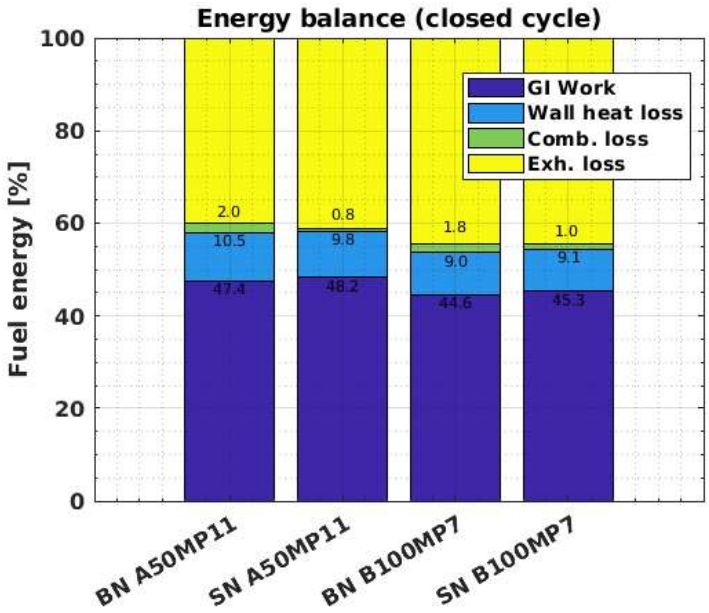

Figure 3.36: Energy balance for BN and SN nozzle.

The closed thermodynamic cycle is evaluated in terms of the energy usage balance of Figure 3.36. The energy balance for the mid-load point (A50MP11) shows how part of the increased SN combustion efficiency (-1.2% combustion loss) together with lower heat transfer losses (-0.7%) derives in a net increase of cycle work (+0.8%). For the high-load point (B100MP7), there is a minor

increase in the heat losses (+0.1%), as the combustion efficiency (-0.8% of combustion losses) also increases, there is also an increment in the cycle work (+0.7%).

Results of step 2 (phase 2): Optimized geometry

In view of the previous results related to the SN and BN comparison in terms of fuel-air mixing and combustion, with this new proposed geometry, the pursued objective was to improve even more the air-fuel mixing process by trying to further increase the injection velocity and the spray angle while keeping the same mass flow rate as the SN. With this goal in mind, the same (short) orifice length (equal than SN) has been employed but with a high level of conicity (same value as BN) and increased inlet rounding radius. Since this geometry is expected to have better discharge coefficient than SN, it has been necessary to reduce the outlet diameter to keep the same mass flow rate. With these modifications a higher injection velocity would be expected which, in turn, due to the greater turbulence level reached, should lead to a wider spray angle (higher atomization). This decrease in outlet diameter with respect to SN together with the higher spray angle should have consequently a smaller liquid length, according to Equation 3.8, and so, a better mixing fuel-air process. Figure 3.37 summarizes the new geometrical parameters compared to those of SN. This nozzle will be referenced for now on as OP3.

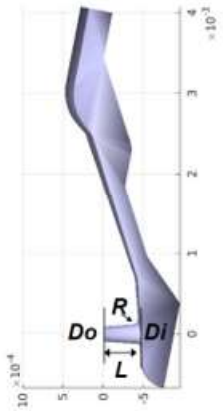

OP3 Nozzle, 3D geometry.

New OP3 geometry characteristics:

Parameter	SN	OP3
L [μm]	400	400
D_0 [μm]	185	180
L/D_0	2,2	2,22
R [μm]	60	90
K-factor	2,5	4

Internal flow CFD results (Pinj:1500 bar, Pback: 70 bar):

	SN	OP3
Mass flow [g/s]	11.3	11.3
Momentum flux [N]	6,05	6,12
Cd	0.88	0.91
Eff. Velocity [m/s]	534	545

Figure 3.37: New OP3 geometry and internal flow results for a given injection condition.

CFD Internal nozzle flow results for a reference point (1500 bar-70 bar)

are depicted in the bottom of the same 3.37. As it can be seen, OP3 nozzle showed a similar mass flow, a slightly higher momentum (+1.15%) and only an increase of 2% in effective injection velocity. The characterization of the spray was studied by means of ELSA model at the same injection and back pressure in evaporative conditions (900 K). Obviously, no experimental data is available for this virtual nozzle. Results of the simulation are shown in Figure 3.38. In this Figure, the vapor and liquid penetration are depicted in the left side while spray cone angle is depicted in the right side. In both graphs, a comparison between SN and OP3 nozzles are shown. As it can be seen, both nozzles shown practically the same spray angle, with negligible differences. This is mainly due to the small differences found in terms of injection velocity. The same spray angle together the smaller diameter of OP3 vs SN (180 vs 185 µm) is at the origin of the small difference found in the liquid length plotted in Figure 3.38 (left), being slightly shorter for OP3 proportional to its diameter reduction according to Equation 3.8. OP3 nozzle also shows a slightly greater vapor penetration which may be attributed to its higher momentum and same spray cone angle than SN.

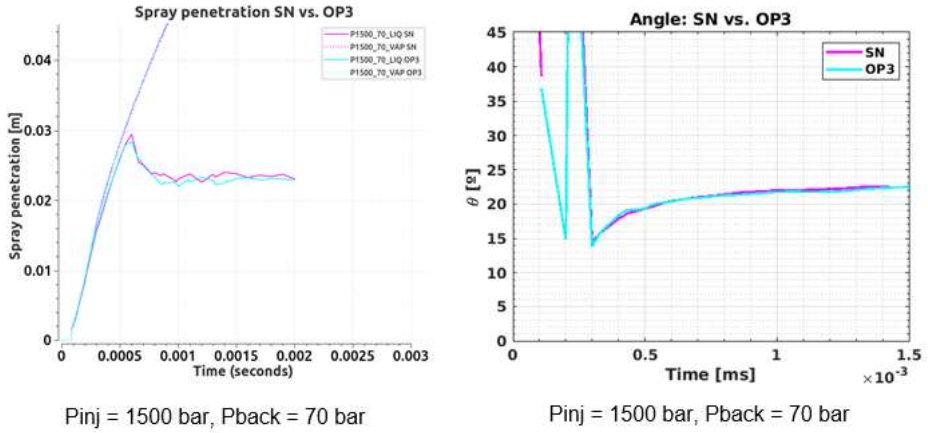

Figure 3.38: OP3 geometry spray behaviour predicted by the ELSA approach compared with the SN nozzle.

For the DDM approach, the same model as for the BN and SN nozzles was used. The input parameters varied according to the new geometry. The ROI obtained from the SN nozzle was used for the OP3 nozzle since there is no experimental data and injector technology is the same. Without any experimental data available for this new nozzle, the trends predicted by the ELSA simulations (Figure 3.38) were used to complete the rest of parameters. The DDM model was fed by the same angle than the SN nozzle (according to the ELSA prediction), the new geometrical parameters and the same mass flow rate. Figure 3.39 shows the results for the same operating point with the DDM approach.

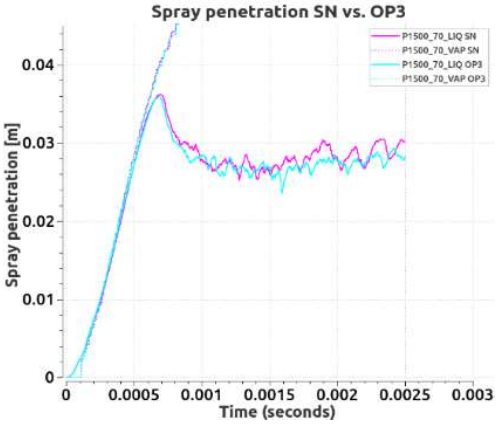

Figure 3.39: DDM spray penetration, SN and OP3 nozzles.

For both ELSA and DDM approaches trends are consistent. A slightly higher momentum leads to a slightly faster spray penetration while the liquid length is reduced in a proportion (in average) according to the reduction of the new OP3 nozzle diameter ($\sim$ -2.65%). In summary, the new nozzle main differences rely on a smaller liquid length. Combustion simulations of the new nozzle uses the same model as previous ones. In this case, only DDM simulations have been performed. Figure 3.40 shows the pressure and heat release rate evolution for the SN and OP3 nozzle, as it can be seen, the new nozzle geometry only causes minor differences.

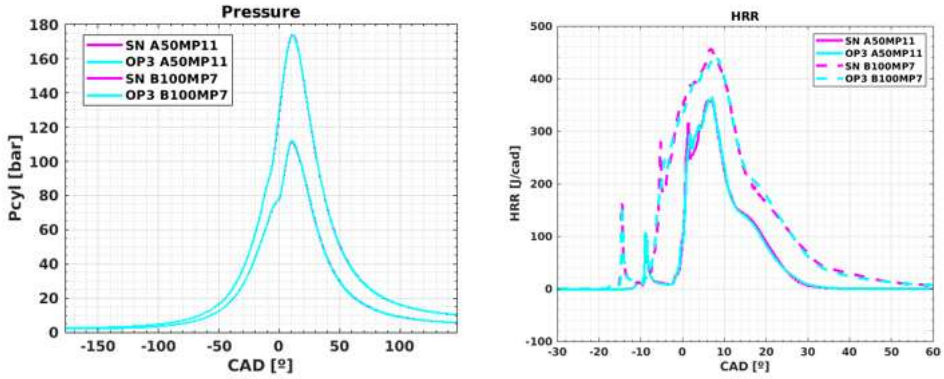

Figure 3.40: Pressure and heat release comparison for the SN and OP3 nozzle simulations.

The accumulated heat release in Figure 3.42, in consonance with the HRR, also shows minor changes. Heat transfer is also almost unaffected, with slight improvement for OP3 at high-load but opposite result at mid-load. The mixing results (Figure 3.41, left side) also are consistent with previous results.

Finally, the energy balance of Figure 3.43 (right side) shows no noticeable

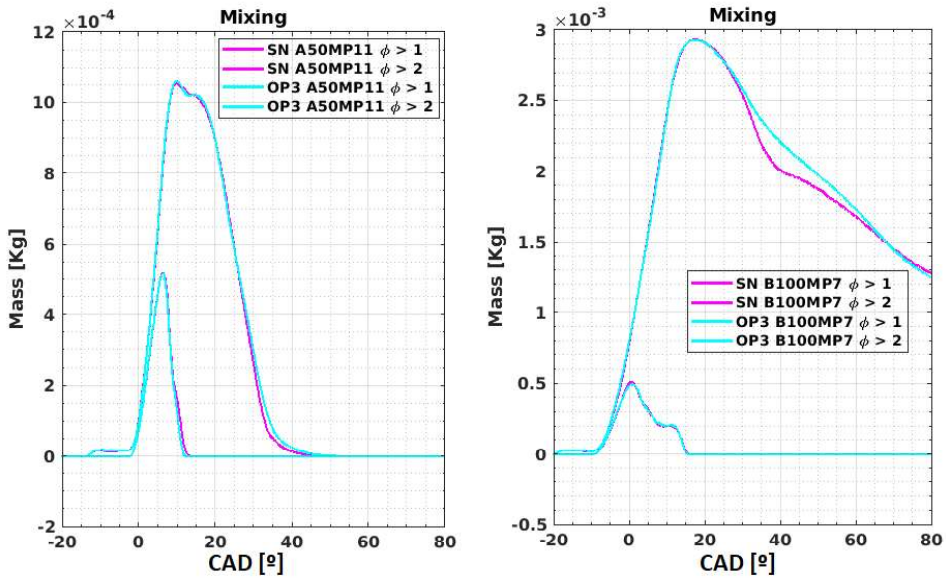

Figure 3.41: Mixture for SN and OP3 nozzles.

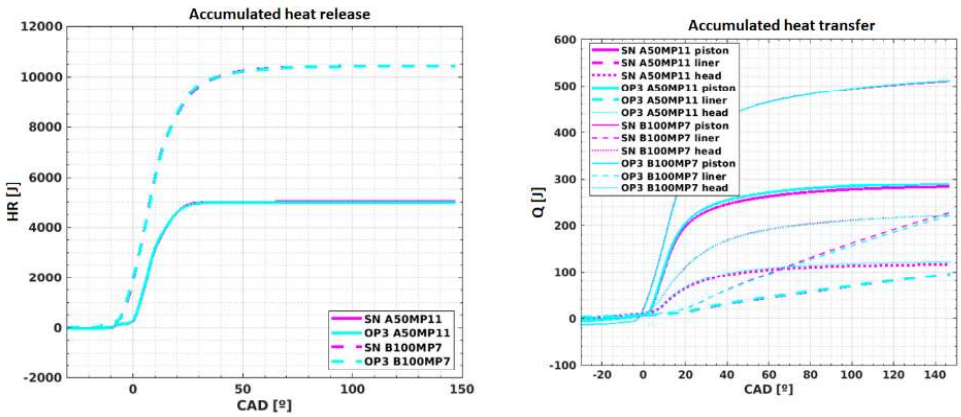

Figure 3.42: Accumulated heat release and integrated heat transfer for the numerical SN and OP3 simulations.

differences in the cycle work, due to similar combustion and heat transfer performance.

Single cylinder engine tests

This chapter describes the experimental results on the engine test bench with regard to emissions, temperatures and heat flows of the base nozzle as well as the short nozzle.

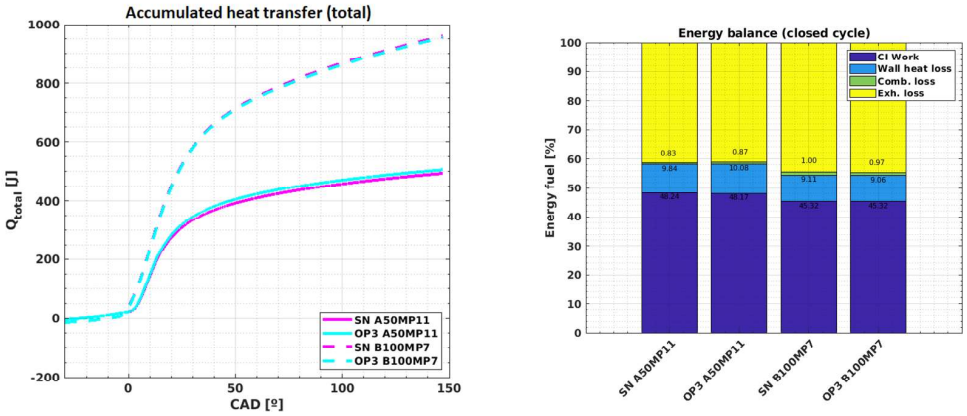

Figure 3.43: Total heat transfer and energy balance for SN and OP3 nozzle.

Emissions

In this section, the emission results of the two nozzles are contrasted and compared (see Figure 3.44 and Figure 3.45). The solid and dashed lines represent the results of the base nozzle with a rail pressure of 1200 bar and 1000 bar and the dotted and dash-dotted lines represent this for the short nozzle. This is shown once for different center of combustion positions and for different EGR rates. It can be clearly seen that the second nozzle measurements show significantly more HC, CO and soot, but also significantly less NOx. Since the HC and CO values are rather negligible, special attention must be paid to soot values. These are roughly 4 to 5 times higher regardless of the respective engine load.

Temperature measurements

In this section, the temperatures of the various positions in the cylinder head and piston are compared. This is shown as an example for a quarter load point with the base nozzle in Figure 3.46. Here, it can basically be stated that the temperatures in the piston are higher on average than at the cylinder head. The dashed lines represent the temperatures in the piston and the solid lines the temperatures in the cylinder head. For the cylinder head, it can be said that thermocouples positioned closer to the center measure significantly higher temperatures than thermocouples positioned further out. For the thermocouples in the piston, it can be observed that the temperature is lowest in the center of the piston, since the flame does not cover the surface here, the temperature in the piston bowl is slightly higher than that in the center of the piston. Significantly higher temperatures are detected at the edge of the piston and at the rim of the piston. The highest temperature can be detected in the direction of the outlet side at the piston bowl, since on the

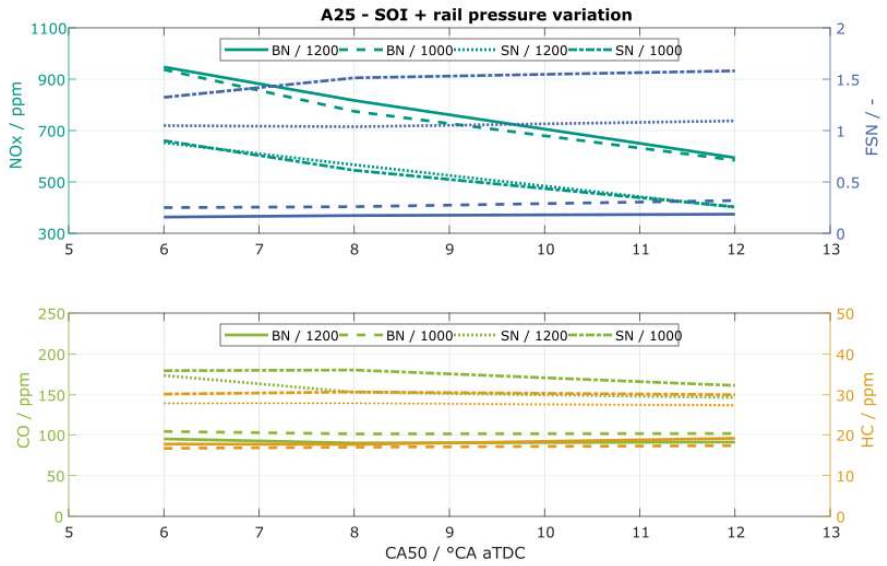

Figure 3.44: Emission behavior A25 / SOI + rail pressure variation.

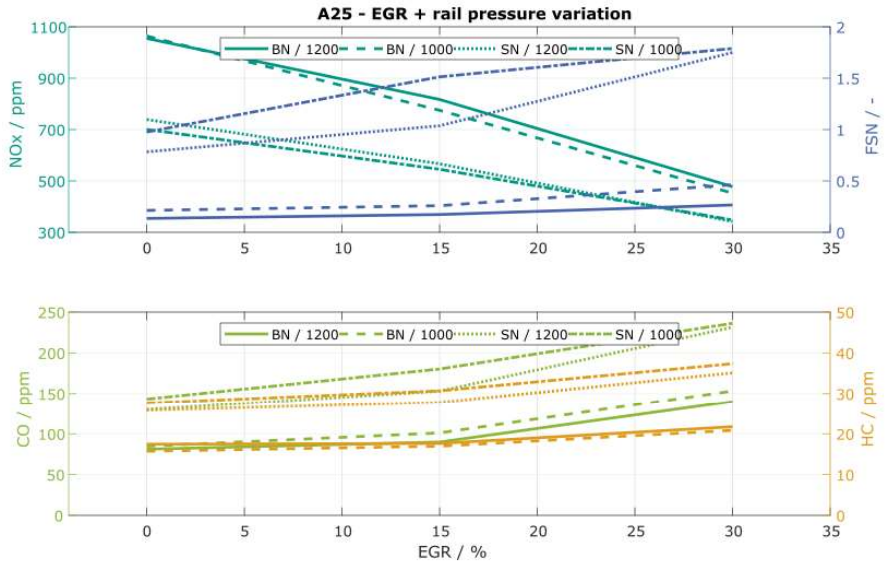

Figure 3.45: Emission behavior A25 / EGR + rail pressure variation.

one hand the flame front generally points in this direction and on the other hand the distance to the jet plumes is smallest here.

In Figure 3.47 a comparison of the peak temperatures of the respective positions of the thermocouples in the cylinder head and piston for all 25% load points with the base nozzle is shown. This once again confirms the statements

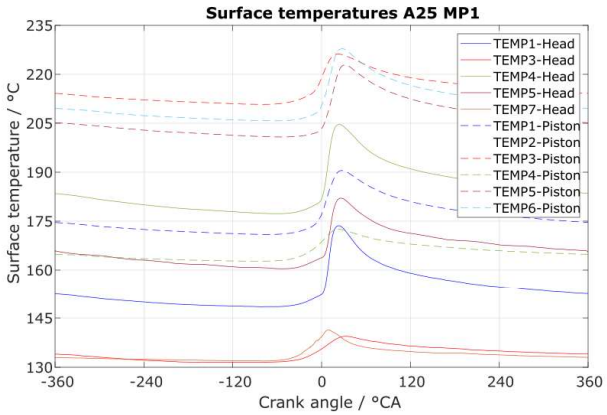

Figure 3.46: Temperature curve of the different thermocouples.

made above, irrespective of variations. The highest temperatures occur in the middle of the cylinder head, and the temperatures drop towards the outside. On the piston, the lowest temperature is in the center and in the bowl. The highest temperatures occur at the piston edge and at the piston rim.

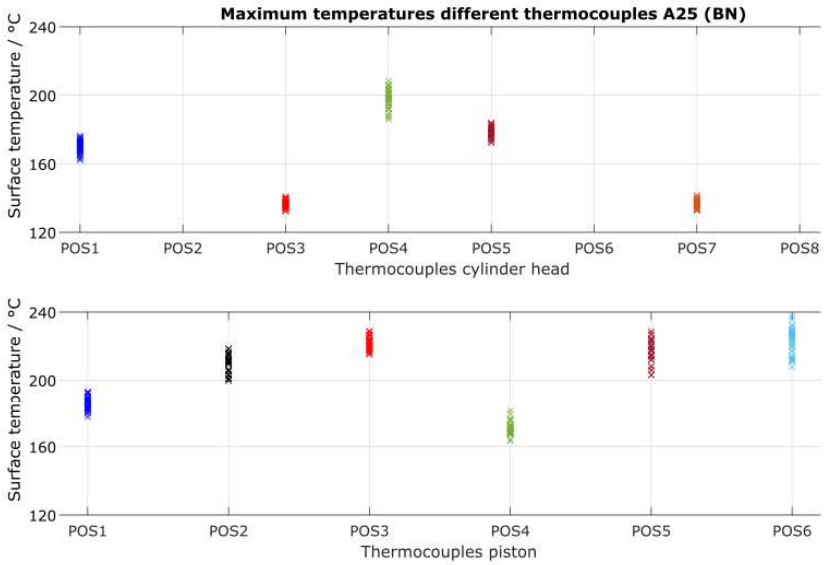

Figure 3.47: Maximum temperatures of the different thermocouples A25 (BN).

Figure 3.48 and Figure 3.49 show the direct comparison for all quarter-load and half-load points in terms of the maximum temperature of the respective operating points and variations between the base nozzle and the short nozzle. Since only two thermocouples in the piston and four thermocouples in the cylinder head were still functional at this point, due to the low durability

of the surface thermocouples, only the peak temperatures of still operational thermocouples are compared. It can be seen that at both the quarter-load points and the half-load points, the peak temperatures in the cylinder head do not differ, so that no influence of the nozzle geometry can be detected with respect to temperatures. With the thermocouples operational in the piston, no difference can be detected between the peak temperatures at position 2 either. However, at both load points it can be seen that the peak temperature has dropped by about 10 °C on average at position 1 in the piston bowl from the base nozzle to the short nozzle. This shows that the penetration depth of the injection jets or flame plumes must be reduced here, resulting in a lower peak temperature. Conversely, this then leads to a lower wall heat loss, which is explained in Section 3.4

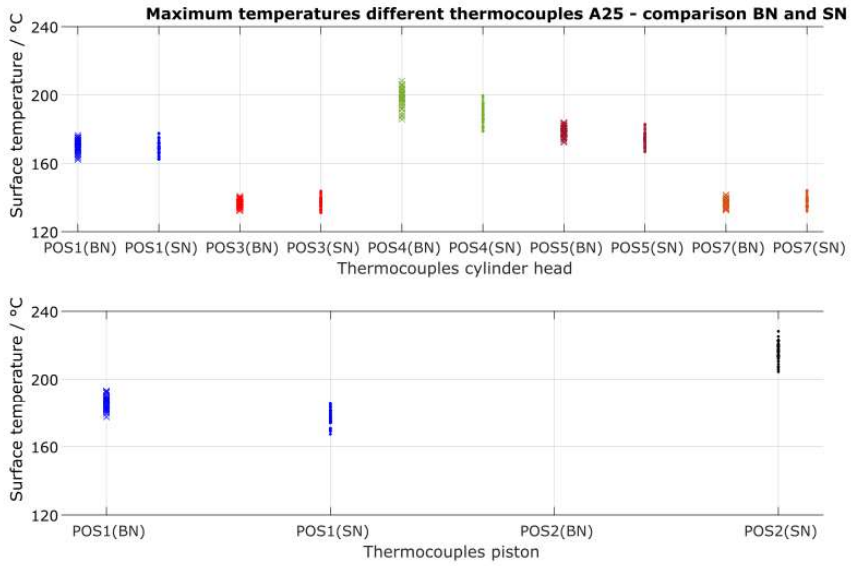

Figure 3.48: Maximum temperatures A25 - comparison between base nozzle and short nozzle.

Heat flux calculations

Using the method described in Section 3.3, all heat flows of the respective thermocouple positions are calculated in this chapter. This is shown as an example in Figure 3.50 for a quarter load point with the base nozzle. Here it can be seen clearly that the heat flows of the piston are above the heat flows in the cylinder head. Normally, due to the smaller difference between gas temperature and wall temperature, the heat flows in the piston should be significantly lower, but due to the different material properties and the twice as high heat penetration number at the piston, the reverse effect can be seen.

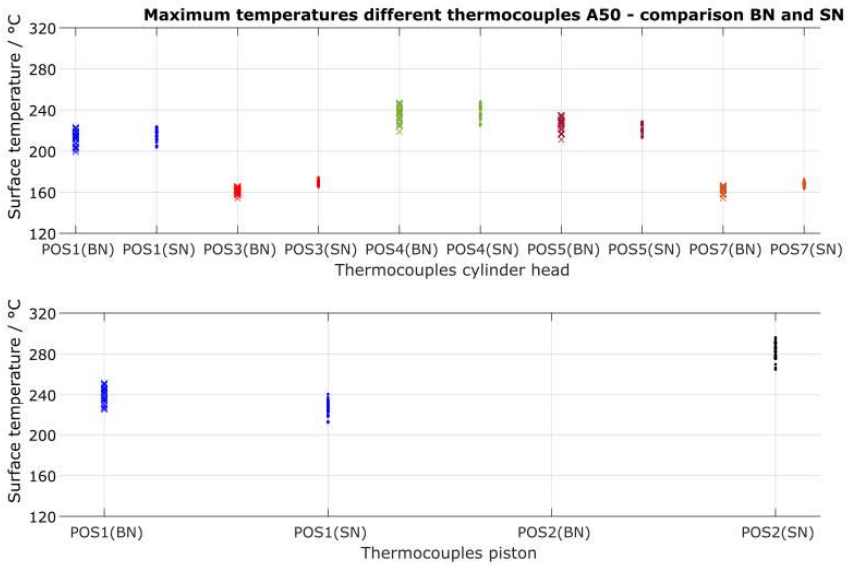

Figure 3.49: Maximum temperatures A50 - comparison between base nozzle and short nozzle.

As with the temperatures, it can be seen that the highest temperatures at positions 5 and 6 in the piston also result in the highest heat flows, and the lowest at position 4 in the center of the piston.

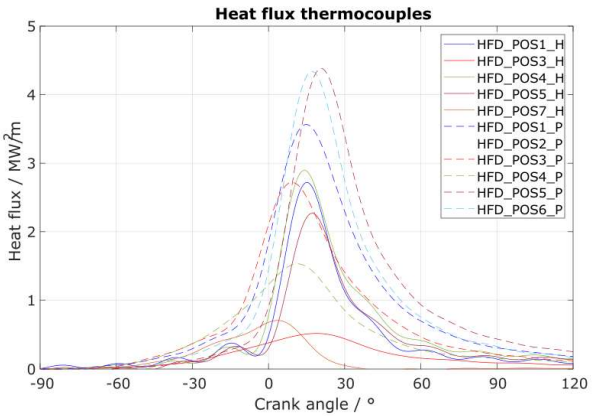

Figure 3.50: Heat flux densities A25 MP1.

The area fraction of the total cylinder wall area which is attributed to a certain thermocouple position can be used to determine an average heat flow for the entire combustion chamber as well as for the cylinder head and piston, so that these can be compared using different models. Table 3.3 shows the area share attributed to the respective thermocouple position. The piston surface

takes up 57% of the total area of the combustion chamber and the cylinder head area 43%, the cylinder liner is neglected.

Thermocouple shared area							
Position Head	1	2	3	4	5	6	7
Share [%])	25	10	25	20	20		
Position Piston	1	2	3	4	5	6	
Share [%]	35	10	15	15	10	15	

Table 3.3: Shares of the surfaces.

Figure 3.51 shows the average heat flow based on the listed proportions for piston and cylinder head for the same operating point. Furthermore, the wall heat transfer models according to Woschni, Woschni-Huber and Hohenberg have been calculated and also shown. It can be seen that the values of the average total heat flux is between that of the piston and the cylinder head due to similar surface weighting. The real calculated heat flux matches the Hohenberg model in course and maximum peak, only the Hohenberg model shows a faster heat release before top dead center, since the maximum peak in the real measured course occurs later. This behavior can also be seen in unfired operation. The models of Woschni and Woschni-Huber overestimate the heat flux, so that they are not suitable for modeling. On the basis of these comparisons, the Hohenberg model could be modified accordingly to reflect the measured heat flow.

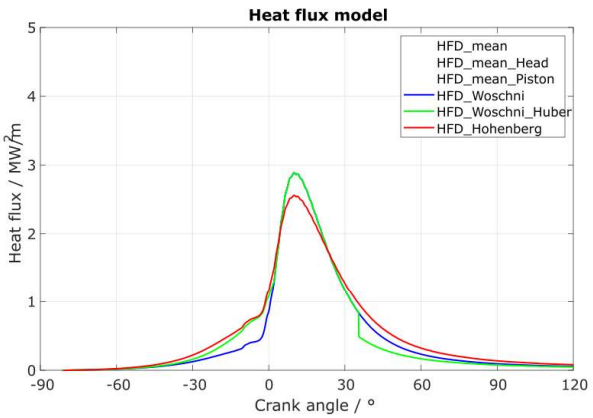

Figure 3.51: Heat flux densities A25 MP1 (comparison to model).

Based on these calculations, the total wall heat losses were calculated for all quarter load points of the base nozzle and put in relation to the total energy introduced via the fuel. This is shown in Figure 3.52 for both the measured and the Hohenberg modelled heat flux. It can be seen that the wall heat loss after Hohenberg is below the measured wall heat loss for each operating point,

resulting in an average difference of about 2.6%. This can be explained by the faster wall heat transfer. The determined wall heat losses are between 13.2% and 15.0%. Furthermore, it can be noted here that the wall heat losses drop with a later center of combustion. This is due to the lower peak temperature in the combustion chamber. Since sufficient temperatures could only be recorded for the quarter load points with the base nozzle, the total heat losses were only determined for these.

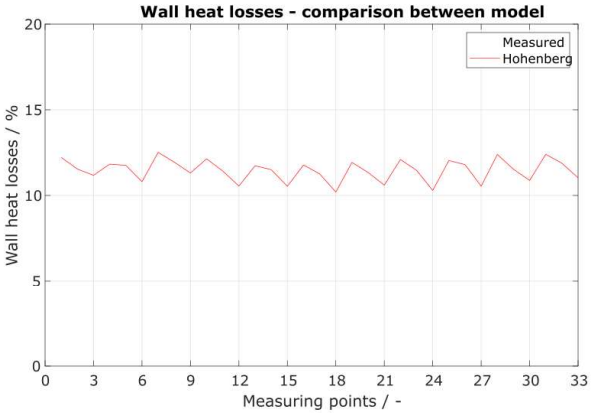

Figure 3.52: Wall heat losses A25 (Hohenberg).

As mentioned before, no complete wall heat losses of the combustion chamber can be made for the different nozzles due to missing data. Furthermore, no real differences between the nozzles could be detected between the wall temperatures of the operational thermocouples, only at position 1 of the piston the wall temperature was lower than for the base nozzle during tests with the short nozzle. Figure 3.53 shows for a half-load point the direct comparison in terms of heat flows for two temperatures from the cylinder head and for the, at time, still operational two thermocouples in the piston.

As expected, the heat flows of the two thermocouples from the cylinder head differ only slightly due to approximately equal wall temperatures, and no major difference can be detected at position 2 of the piston either. In contrast, a clear influence of the nozzle geometry can be observed for the heat flows at position 1 of the piston. The wall heat flux peak is about 28% lower with the second nozzle compared to the base nozzle. This effect is the same for all measuring points examined. It shows that it is possible to reduce the wall heat transfer with appropriate adjustment of the nozzle geometry. Unfortunately, however, it is not possible to say whether the total wall heat transfer can also be reduced as a result, since the temperatures in the piston could also have risen equivalently elsewhere. In the overall efficiency results, no striking differences can be quantified.

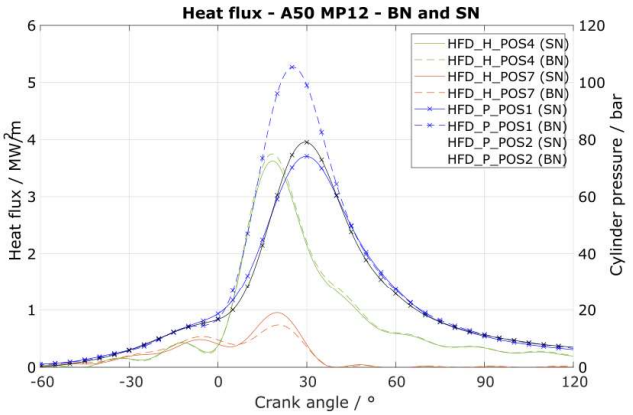

Figure 3.53: Comparison between BN and SN (A50 MP12).

3.5. Summary and conclusions

The project has demonstrated the robustness of the spray modelling with the ability to simulate different nozzle geometries with the same model coefficients. The association with combustion models has been successful, paving the way to a "reverse engineering" methodology, defining the nozzle by CFD before any prototype. In terms of experiments, FVV partners can now have access to a cycle resolved piston head temperature measurement at different engine speeds thanks to a radio frequency transmission between moving and static engine parts. Due to a lack of time and prototypes, the nozzle optimization and the final in situ tests of the new defined parts could not be achieved within the frame of the project. The sensitivity to the nozzle hole length to diameter ratio versus the wall losses has nevertheless been highlighted by CFD and the associated physical mechanism explained.

References

[1] Jose Maria Desantes et al. “Coupled/decoupled spray simulation comparison of the ECN spray a condition with the Σ-Y Eulerian atomization model”. In: *International Journal of Multiphase Flow* 80 (2016), pp. 89–99. ISSN: 03019322. DOI: 10.1016/j.ijmultiphaseflow.2015.12.002.

[2] Jose Maria Garcia-Oliver et al. “ Diesel Spray Cfd Simulations Based on the Σ-ϒ Eulerian Atomization Model ”. In: *Atomization and Sprays* 23.1 (2013), pp. 71–95. ISSN: 1044-5110. DOI: 10.1615/AtomizSpr.2013007198.

[3] Adrián Pandal Blanco. “ Implementation and Development of an Eulerian Spray Model for CFD simulations of diesel Sprays ”. PhD thesis. Valencia (Spain): Universitat Politècnica de València, July 2016. DOI: 10.4995/Thesis/10251/68490. URL: https://riunet.upv.es/handle/10251/68490.

[4] Ariane Vallet, A. A. Burluka and R. Borghi. “Development of a Eulerian model for the atomization of a liquid jet”. In: *Atomization and Sprays* 11.6 (2001). ISSN: 1044-5110.

[5] P. K. Senecal et al. “Multi-dimensional modeling of direct-injection diesel spray liquid length and flame lift-off length using cfd and parallel detailed chemistry”. In: *SAE Technical Papers* 724 (2003). ISSN: 26883627. DOI: 10.4271/2003-01-1043.

[6] A.A. Amsden. *KIVA-3V: A block-structured KIVA program for engines with vertical or canted valves.* Tech. rep. LA-13313-MS. Los Alamos, NM: Los Alamos National Laboratory (LANL), July 1997. DOI: 10.2172/505339. URL: http://www.osti.gov/servlets/purl/505339-tlyFln/webviewable/.

[7] Kawaguchi. “Thermo-Swing Wall Insulation Technology; - A Novel Heat Loss Reduction Approach on Engine Combustion Chamber”. In: *SAE technical Paper 2016-01-2333,2016* (2016).

[8] Shimo. “The New Small Diesel Engine MAZDA SKYACTIV-D 1.5l, AACHEN COLLOQUIUM. “Automobile and Engine Technology” October 5th-7th”. In: *AACHEN COLLOQUIUM. “Automobile and Engine Technology” October 5th-7th.* 2015.

[9] F. Payri, V. Bermúdez, R. Payri and F. J. Salvador. “The influence of cavitation on the internal flow and the spray characteristics in diesel injection nozzles”. In: *Fuel* 83.4-5 (2004), pp. 419–431. ISSN: 00162361. DOI: 10.1016/j.fuel.2003.09.010.

[10] Francisco Javier Salvador, Marcos Carreres, David Jaramillo and Jorge Martínez-lópez. "Analysis of the combined effect of hydrogrinding process and inclination angle on hydraulic performance of diesel injection nozzles". In: *Energy Conversion and Management* 105 (2015), pp. 1352–1365. ISSN: 0196-8904. DOI: 10.1016/j.enconman.2015.08.035.

[11] Wilhelm Bosch. "The Fuel Rate Indicator: A New Measuring Instrument For Display of the Characteristics of Individual Injection". In: (1966), p. 660749. ISSN: 0148-7191. DOI: 10.4271/660749. URL: http://papers.sae.org/660749/.

[12] R. Payri, F. J. Salvador, J. Gimeno and G. Bracho. "A new methodology for correcting the signal cumulative phenomenon on injection rate measurements". In: *Experimental Techniques* 32.1 (2008), pp. 46–49. ISSN: 07328818. DOI: 10.1111/j.1747-1567.2007.00188.x.

[13] R. Payri, J. M. García, F. J. Salvador and J. Gimeno. "Using spray momentum flux measurements to understand the influence of diesel nozzle geometry on spray characteristics". In: *Fuel* 84.5 (2005), pp. 551–561. ISSN: 00162361. DOI: 10.1016/j.fuel.2004.10.009.

[14] R Payri, J Gimeno, G Bracho and D Vaquerizo. "Study of liquid and vapor phase behavior on Diesel sprays for heavy duty engine nozzles". In: *Applied Thermal Engineering* 107 (2016), pp. 365–378. ISSN: 1359-4311. DOI: https://doi.org/10.1016/j.applthermaleng.2016.06.159. URL: https://www.sciencedirect.com/science/article/pii/S1359431116310730.

[15] Dennis L. Siebers. "Liquid-Phase Fuel Penetration in Diesel Sprays". In: *International Congress & Exposition*. SAE International, Feb. 1998. DOI: https://doi.org/10.4271/980809. URL: https://doi.org/10.4271/980809.

[16] Jose V. Pastor, Raul Payri, Jose M. Garcia-Oliver and Jean Guillaume Nerva. "Schlieren measurements of the ECN-spray a penetration under inert and reacting conditions". In: *SAE Technical Papers* (2012). ISSN: 26883627. DOI: 10.4271/2012-01-0456.

[17] J. M. Desantes, J. M. García-Oliver, J. M. Pastor and A. Pandal. "A comparison of diesel sprays CFD modeling approaches: DDM versus σ-γ Eulerian atomization model". In: *Atomization and Sprays* 26.7 (2016), pp. 713–737. ISSN: 10445110. DOI: 10.1615/AtomizSpr.2015013285.

[18] David Jaramillo Císcar. "Estudio experimental y computacional del proceso de inyección diésel mediante un código CFD con malla adaptativa". PhD thesis. Universitat politècnica de València, 2017.

[19] Jennifer C. Beale and Rolf D. Reitz. “Modeling spray atomization with the Kelvin-Helmholtz/Rayleigh-Taylor hybrid model”. In: *Atomization and Sprays* 9.6 (1999), pp. 623–650. ISSN: 10445110. DOI: 10.1615/atomizspr.v9.i6.40.

[20] Victor Yakhot and Leslie M. Smith. “The renormalization group, the eps-expansion and derivation of turbulence models”. In: *Journal of Scientific Computing* 7.1 (1992), pp. 35–61. ISSN: 0885-7474. DOI: 10.1007/BF01060210.

[21] J.-S. Wu, K.-H. Hsu, P.-M. Kuo and H.-J. Sheen. “Evaporation model of a single hydrocarbon fuel droplet due to ambient turbulence at intermediate Reynolds numbers”. In: *International Journal of Heat and Mass Transfer* 46.24 (2003), pp. 4741–4745. ISSN: 0017-9310. DOI: https://doi.org/10.1016/S0017-9310(03)00297-7. URL: https://www.sciencedirect.com/science/article/pii/S0017931003002977.

[22] J M Desantes, F J Salvador, M Carreres and D Jaramillo. “ Experimental Characterization of the Thermodynamic Properties of Diesel Fuels Over a Wide Range of Pressures and Temperatures ”. In: *SAE International Journal of Fuels and Lubricants* 8.1 (2015), pp. 951–2015. ISSN: 1946-3960. DOI: 10.4271/2015-01-0951. URL: http://papers.sae.org/2015-01-0951/.

[23] V. Macian, V. Bermudez, R. Payri and J. Gimeno. “New Technique for Determination of Internal Geometry of a Diesel Nozzle With the Use of Silicone Methodology”. In: *Experimental Techniques* 27.2 (2003), pp. 39–43. ISSN: 0732-8818. DOI: 10.1111/j.1747-1567.2003.tb00107.x. URL: http://doi.wiley.com/10.1111/j.1747-1567.2003.tb00107.x.

[24] F. J. Salvador, J. M. Pastor, J. De la Morena and E. C. Martínez-Miracle. “Computational study on the influence of nozzle eccentricity in spray formation by means of Eulerian Σ - Y coupled simulations in diesel injection nozzles”. In: *International Journal of Multiphase Flow* 129 (2020), p. 103338. ISSN: 03019322. DOI: 10.1016/j.ijmultiphaseflow.2020.103338. URL: https://doi.org/10.1016/j.ijmultiphaseflow.2020.103338.

[25] Jessica Brakora and Rolf Reitz. “A comprehensive combustion model for biodiesel-fueled engine simulations”. In: *SAE Technical Papers* 2 (2013). ISSN: 26883627. DOI: 10.4271/2013-01-1099.

[26] F. Payri, P. Olmeda, J. Martín and A. García. “A complete 0D thermodynamic predictive model for direct injection diesel engines”. In: *Applied Energy* 88.12 (2011), pp. 4632–4641. ISSN: 03062619. DOI: 10.1016/j.apenergy.2011.06.005. URL: http://dx.doi.org/10.1016/j.apenergy.2011.06.005.

[27] Helmut Knauss et al. “Novel Sensor for Fast Heat-Flux Measurements”. In: *Journal of Spacecraft and Rockets* 46 (Mar. 2009), pp. 255–265. DOI: 10.2514/1.32011.

[28] Günter Hohenberg. “Experimentelle Erfassung der Wandwärme von Kolbenmotoren”. deutsch. PhD thesis. 1980.

[29] Thomas Emrich. “Beitrag zur Ermittlung der WÃ¤rmeÃ¼bergÃ¤nge in BrennrÃ¤umen von Verbrennungsmotoren mit homogener und teilhomogener Energieumsetzung”. PhD thesis. UniversitÃ¤t Stuttgart, 2010.

[30] David Lejsek et al. “Berechnung des Wandwärmeübergangs im Motorhochlauf von Di-Ottomotoren”. In: (4 2010), pp. 250–257. DOI: https://doi.org/10.1007/BF03225562.

[31] Christian Eiglmeier. “PhÃ¤nomenologische Modellbildung des gasseitigen WandwÃ¤rmeÃ¼berganges in Dieselmotoren”. PhD thesis. Hannover : UniversitÃ¤t, Diss., 2001, 112 S, 2001.

[32] Sebastian Hensel. “Modellierung der Verbrennung und des Wandwärmeübergangs in Ottomotoren mit homogen kompressionsgezündeter Verbrennung”. German. PhD thesis. 2009. 121 pp. ISBN: 978-3-8325-2235-3.

[33] Junseok Chang et al. “New Heat Transfer Correlation for an HCCI Engine Derived from Measurements of Instantaneous Surface Heat Flux”. In: (Oct. 2004). DOI: 10.4271/2004-01-2996.

[34] Michael Bargende. “Wärmeübergang und Wärmebelastung im Dieselmotor”. In: *Handbuch Dieselmotoren*. Ed. by Helmut Tschöke, Klaus Mollenhauer and Rudolf Maier. Wiesbaden: Springer Fachmedien Wiesbaden, 2016, pp. 1–26. ISBN: 978-3-658-07997-0. DOI: 10.1007/978-3-658-07997-0_41-1. URL: https://doi.org/10.1007/978-3-658-07997-0_41-1.

[35] Philipp Hügel. “Untersuchungen zum Wandwärmeübergang im Teillastbetrieb an einem Einzylinder-Forschungsmotor mit Benzin-Direkteinspritzung”. German. PhD thesis. Karlsruher Institut fÃ¼r Technologie (KIT), 2017. 139 pp. ISBN: 978-3-8325-4520-8.

[36] Jeffrey Naber and L. Dennis. “Effects of Gas Density and Vaporization on Penetration and Dispersion of Diesel Sprays”. In: (1996), p. 960034. ISSN: 0148-7191. DOI: 10.4271/960034. URL: http://papers.sae.org/960034/.

[37] Raul Payri, F.J. Salvador, Jaime Gimeno and V. Soare. “Determination of Diesel Sprays Characteristics in Real Engine In-Cylinder Air Density and Pressure Conditions”. In: *Journal of Mechanical Science and Technology - J MECH SCI TECHNOL* 19 (Nov. 2005), pp. 2040–2052. DOI: 10.1007/BF02916497.

Capítulo 4

Influencia de geometrías elípticas sobre la mezcla

How to get an engineer's attention: Say "There has to be a better way to do this."

Anonymous engineer

Resumen: La influencia de la geometría como herramienta para mejorar la mezcla se explora en este capítulo a través del análisis de geometrías innovadoras elípticas. El análisis computacional usando modelos de flujo interno-externo acoplado permite el estudio simultáneo de ambas mecánicas y vincular el comportamiento del flujo en el interior de la tobera con la mezcla. El modelo Σ-Y ESA es validado frente a una tobera mono-orificio de investigación y datos experimentales de flujo interno de una tobera comercial con carácter cavitante.

Computational study on the influence of nozzle eccentricity in spray formation by means of Eulerian Σ - Y coupled simulations in diesel injection nozzles

Referencia: F.J. Salvador, J.M. Pastor, J. De la Morena, E.C. Martínez-Miracle, Computational study on the influence of nozzle eccentricity in spray formation by means of Eulerian Σ - Y coupled simulations in diesel injection nozzles, International Journal of Multiphase Flow, Volume 129, 2020, 103338, ISSN 0301-9322, https://doi.org/10.1016/j.ijmultiphaseflow.2020.103338.

Abstract: *The present work analyses the effect of the eccentricity of diesel nozzle orifices over the spray behaviour by means of CFD simulations. Several orifice geometries with varying horizontal eccentricity (from 0.50 to 0.94) are selected. Their performance is assessed at a high injection pressure of 200 MPa, a 3 MPa back-pressure and non-evaporative conditions. The nozzle flow characteristics, including cavitation modelled by a Homogeneous Relaxation Model (HRM), are accounted for in the spray performance by means of a Σ - Y model. The code is validated via two reference nozzles, the so called "Spray A" of the Engine Combustion Network plus a second nozzle from a production injector, and then extended to the eccentric geometries. The results and discussions include spray angle and penetration, air entrainment and flow parameters of the nozzle inner conditions versus the eccentricity value.*

4.1. Introduction

As the standards applied to combustion engines emissions become more stringent, the need to produce cleaner combustion systems compatible with future climatic requirements is critical. Diesel engines have been widely used

thanks to their potential to reduce CO_2 emissions, one of the most significant contributors to global warming effect. However, concerns about their capability to meet future NO_x and particulate matter emissions regulations have arisen over the last years. Even if these pollutants can be substantially reduced by means of aftertreatment systems (such as Diesel Particulate Filters -DPF-, Lean-NOx Trap-LNT- or Selective Catalytic Reactors -SCR-), the origin of the emissions must be also controlled in order not only to reduce them, but also to keep under control the cost, size, durability and fuel consumption impact of the aforementioned elements. While Exhaust Gas Recirculation (EGR) can be used to mitigate NO_x emissions thanks to the lower combustion temperature, its usage is limited due to the subsequent increase of the particulate matter (mainly composed of soot). However, soot formation is controlled by the air-fuel mixing process, which is mainly a result of the injection pressure and the morphology of the injector and chamber geometry [1–3]. Additionally, the fuel-air mixing controls the combustion timing and duration, affecting the indicated efficiency, as well as the flame distance to the cylinder walls, impacting heat transfer losses.

Since the 1970's the study of the parameters that characterize the spray performance has been a constant research topic with the aim of increasing efficiency while reducing emissions. First works by Wakuri et al. [4], the extensive studies by Hiroyasu et al. [5–8] and several others like Reitz et al. [9–11] postulated the importance of the spray mechanics, specially the relationship between the tip penetration, the spray angle and the air entrainment. Different optical diagnostics have been developed to evaluate the primary atomization and initial spray formation process [12–14], the fuel-air mixing [15, 16] and the combustion development [17, 18]. The evolution of computational fluid dynamics in the recent years has made possible to study in further details the importance of the nozzle geometry in the atomization process [19–22]. In this sense, approaches such as the $\Sigma - Y$ model [23, 24] which allows a coupled flux between nozzle and spray through a Eulerian-Eulerian simulation [25–27]. In this model, flux phases are considered as a pseudo-fluid inside a single velocity field. This method introduces the possibility of simulate cavitation phenomena if the geometry is prone to cavitate. In this sense, several authors such as Zhao et al. [28] and Battistoni et al. [29] used an Homogeneous Relaxation Model to evaluate cavitation phenomena in nozzles.

Already decades ago, works by Sforza et al. [30] and Trentacoste and Sforza [31] made first approximations to the aspects of jets produced by elliptical nozzles. Hussain et al. [32, 33] and Ho et al. [34] analysed also these jets from a theoretical perspective. More recently, studies about elliptical nozzles applied to spray mechanics revealed that this particular shape was able to improve the general dispersion of the injected fluid [35]. Lee et al. [36] performed comparisons between elliptical and cylindrical single-hole nozzles and found an improved spreading angle, specially in the plane corresponding

to the minimum diameter. Similar results were reported by [37], showing a lower penetration in favour of a wider angle and then a greater atomization effect associated to elliptical single-hole nozzles. Hong et al. [38] studied cavitation phenomena inside transparent elliptical nozzles, concluding that longer cavitation fields (up to the orifice outlet) were appearing. Based on the work by Hong et al., [39] applied CFD techniques in order to verify the relationship between the internal flow and the behaviour of the spray. Their investigation showed how cavitation takes place in the major axis limits due to a greater contraction of the stream-lines in that zone for single-hole nozzles. The internal profiles of the CFD simulations related the turbulence subjected to cavitation to a greater spreading angle in the major axis plane. Finally, some approximations to real diesel engines were made by Matsson and Andersson [40], accounting the impact on emissions of elliptical geometries, with a general decrease of NO_x emissions and fuel consumption for elliptical geometries, but with varying smoke production depending on the aspect ratio value.

Despite the previous works describe some of the physics related to the impact of elliptical orifices on nozzle flow and spray formation, most of them may not be fully representative from a practical point of view. On the one hand, most of the studies are performed for single-hole axi-symmetric nozzles. However, diesel engines require multi-orifice nozzles, which are affected by the change of direction of the flow induced by the inclination of the orifices' axis compared to the injector. On the other hand, nozzle sizes within literature are usually larger than a representative diesel nozzle (< 0.2 mm). A first approach to this more complex problem was described by [41]. In their work, several detailed CFD simulations were carried out in order to clarify how the internal flow of a common rail diesel injector with elliptical orifices could affect the atomization, and an extrapolation to the effects in the spray characteristics was made based on a theoretical reasoning. The present paper intends to get a deeper view into the effects of elliptical nozzles over the spray by means of advanced coupled internal-external flow simulations. This will also allow to understand some of the effects described in the literature. On the basis of a cavitating cylindrical nozzle whose hydraulic behaviour is known, six elliptical geometries have been modelled. The horizontal radius has been gradually increased from an eccentricity of 0.5 to 0.94, maintaining a constant outlet section, while the rest of the geometrical morphology has been kept as in the original nozzle. The validation of the computational model has been carried out following two lines of action. First, a non-cavitating single-hole nozzle from the Engine Combustion Network [42], named Spray A, has been evaluated in terms of mass flow rate, momentum flux, spray angle and projected mass density. Then, Homogeneous Relaxation Model (HRM) used to predict cavitation performance has been assessed against hydraulic experimental data from a cylindrical multi-hole nozzle, which is the same used as baseline for the rest of the study. Once the models are validated, the performance of the

elliptical nozzles is analysed in terms of the flow conditions at the nozzle outlet (mass flow, momentum flux, liquid and vapour fractions, radial and axial velocity profiles, etc), as well as spray features (such as the spray angle, the air entrainment and the spray tip penetration). Several discussions over the information available in literature have been exposed and the behaviour of the simulations have been clarified.

The investigation has been divided into six sections. Section 4.2 introduces the computational model, while section 4.3 describes the employed methodology. It includes the description of the models, the geometries, fluid properties and the post-process and comparison techniques. Section 4.4 discusses the validation of the model, including the description of the nozzle geometries used for this purpose (Spray A and a production multi-hole injector), the characteristics of the meshes and model constants configuration used. Section number 4.5 shows the results for the six nozzles elliptical geometries considered. All the nozzles have been compared relating their spray characteristics with the previous literature findings, paying special attention to coherence between extracted properties at the nozzle outlet and the spray behaviour. The last section collects the main conclusions of the present work.

4.2. Model description

The coupling between the nozzle internal flow and the spray is made by means of a $\Sigma - Y$ atomization model. In this formulation, all the phases are treated as a pseudo-fluid with an unique velocity field for vapour fuel, liquid fuel and chamber gas [26, 43]. This approximation assumes that the exiting spray is characterised by large values of Reynolds and Webber numbers. From this point of view, bigger scales of turbulence can be transported, while small unresolved scales are computed using standard closure models. The dispersion of the liquid phase is then traced by means of a scalar function. This magnitude takes a value of 1 when only liquid exists, and 0 if there is only vapour phase. The transport equation for the liquid mass fraction on its Favre averaging form is:

$$\frac{\partial \bar{\rho}\tilde{Y}}{\partial t} + \frac{\partial \bar{\rho}\ \tilde{u}_i \tilde{Y}}{\partial x_i} = 0, \tag{4.1}$$

where $\bar{\rho}$ denotes the density, $\tilde{u}$, x the axial position and $\tilde{Y}$ is the mean mass-averaged volume fraction defined as:

$$\tilde{Y} = \frac{\overline{\rho_{liq} Y}}{\bar{\rho}}. \tag{4.2}$$

$\bar{Y}$ being the volume fraction.

If an immiscible mixture is assumed for the two phases, the relation between the mass-averaged value of the liquid volume fraction can be related to the density by:

$$\frac{1}{\bar{\rho}} = \frac{\tilde{Y}}{\rho_l} + \frac{1-\tilde{Y}}{\rho_g}. \tag{4.3}$$

An equation of state is then assigned to each phase:

$$\rho_g = \frac{P}{R_g T}, \tag{4.4}$$

$$\rho_l = f(p, T). \tag{4.5}$$

The energy transport equation only accounts the internal energy of the fluid, and stands as follows:

$$\frac{\partial \bar{\rho} e}{\partial t} + \frac{\partial \tilde{u_j} \bar{\rho} e}{\partial x_j} = -P\frac{\partial \tilde{u_j}}{\partial x_j} + \sigma_{ij}\frac{\partial \tilde{u_i}}{\partial x_j} + \frac{\partial}{\partial x_j}\left(K\frac{\partial T}{\partial x_j}\right) + \frac{\partial}{\partial x_j}\left(\bar{\rho} D \sum_m h_m \frac{\partial \tilde{Y_m}}{\partial x_j}\right), \tag{4.6}$$

Where Y_m and h_m are the mass fraction and enthalpy for each species respectively, D is a mass diffusion coefficient, P is the pressure,σ_{ij} the stress tensor, e is the specific energy and T is the temperature. The relation between the different species is given by:

$$h(T) = \tilde{Y} \cdot h_l(T) + (1-\tilde{Y}) \cdot h_g(T). \tag{4.7}$$

The turbulent term in the liquid mass transport is modelled as

$$\bar{\rho}\widetilde{u_i' Y'} = \frac{\mu_t}{Sc}\frac{\partial \tilde{Y}}{\partial x_i}. \tag{4.8}$$

Subsequently, the momentum conservation equation can be written as:

$$\frac{\partial \bar{\rho}\tilde{u_i}}{\partial t} + \frac{\bar{\rho}\tilde{u_i}\tilde{u_j}}{\partial x_j} = -\frac{\partial P}{\partial x_i} + \frac{\partial \sigma_{ij}}{\partial x_j} + S_i, \tag{4.9}$$

where σ_{ij} denotes the viscous stress tensor, equals to:

$$\sigma_{ij} = \mu\left(\frac{\partial \tilde{u_i}}{\partial x_j} + \frac{\partial \tilde{u_j}}{\partial x_i}\right) + \left(\frac{2}{3}\mu\frac{\partial \tilde{u_k}}{\partial x_k}\delta_{ij}\right), \tag{4.10}$$

μ is representing the viscosity and δ_{ij} is the Kronecker delta.

Finally, the interphase surface area density is defined as the quantity of spatial surface per unit volume [23, 44]. Hence, the transport equation associated to this scalar magnitude is:

$$\frac{\partial\tilde{\Sigma}}{\partial t}+\frac{\partial\tilde{u_j}}{\partial x_j}-\frac{\partial}{\partial x_j}\left(D_\Sigma\frac{\tilde{\Sigma}}{\partial x_j}\right)- C_\Sigma\tilde{\Sigma}\left(1-\frac{\tilde{\Sigma}}{\Sigma_{eq}}\right)-S_{\Sigma_{evap}}-S_{\Sigma_{init}}=0, \quad (4.11)$$

where

$$\overline{\Sigma_{eq}}=\frac{3\bar{\rho}Y}{\rho_l r_{eq}}, \quad (4.12)$$

$$S_{\Sigma_{evap}}=\frac{2\Sigma}{3\bar{Y}}S_{evap}, \quad (4.13)$$

$$C_\Sigma=\alpha_1\frac{\tilde{\varepsilon}}{\tilde{k'}}, \quad (4.14)$$

$$r_{eq}=\alpha_2\frac{\sigma^{3/5}}{\tilde{\varepsilon}^{2/3}}\frac{(\bar{\rho}\tilde{Y})^{2/15}}{\rho_l^{11/15}}, \quad (4.15)$$

$$D_\Sigma=\frac{\nu_T}{Sc_\Sigma}. \quad (4.16)$$

D_Σ is a diffusion coefficient, Y is the volume fraction of fuel, $S_{\Sigma_{evap}}$ is a source term related to vaporization, $S_{\Sigma_{init}}$ is the initialization value, r_{eq} is the equilibrium radius for virtual droplets. Finally, α_1 and α_2 are model parameters subjected to calibration. The terms above can be used to calculate equivalent droplet sizes as part of the transition chain to parcels in an hybrid Eulerian-Lagrangian model. Although this kind of comparison is beyond the limits of this paper, it is a good indication of the potential of the model.

$$S_{\Sigma_{init}}=\frac{\Sigma_{min}-\Sigma}{\Delta t}pos(\Sigma_{min}-\Sigma), \quad (4.17)$$

$$\Sigma_{min}=\sqrt{\alpha(1-\alpha)}V^{1/3}, \quad (4.18)$$

$$pos(\Psi)=\begin{cases}1 & \text{if } \Psi>0\\ 0 & \text{if } \Psi\leq 0.\end{cases} \quad (4.19)$$

In diesel engines, usual values for α_1 and α_2 are respectively 1 and 4 [24, 25]. For a deeper mathematical explanation of the model and coefficients, previous work by [43] can be consulted.

As stated during the introduction, the mass transfer between fuel vapour and liquid phase due to cavitation is modelled by a Homogeneous Relaxation Model (HRM) [45, 46]. The model assumes that the rate at which the instantaneous mass (x) approaches its equilibrium value ($\bar{x}$) depends on a time scale factor (θ_0) or relaxation factor. The linear relation is expressed as:

$$\frac{D_x}{Dt} = \frac{\bar{x} - x}{\theta}. \tag{4.20}$$

Two time scales are calculated, one for evaporation and another for condensation:

$$\theta_E = \theta_0 \alpha^{-0.54} \varphi^{-1.76}, \tag{4.21}$$

$$\theta_C = F\theta_0 \alpha^{-0.54} \varphi^{-1.76}. \tag{4.22}$$

Notice that α is the void fraction, equals to $(1 - \bar{Y})$. The value of θ_0 is set to $3.84e-7$ s and φ is the non-dimensional pressure ratio.

$$\varphi = \frac{P_{sat} - P}{P_c - P_{sat}}, \tag{4.23}$$

where P_c denotes the critical pressure of the fluid. In equation 4.22, F has a value of 5000 according to the conclussions from previous analysis by He et al. [47].

4.3. Methodology

The current study is divided in two steps. First, two existing injector nozzle geometries are used for the validation of the simulations in terms of the internal flow characteristics and the spray formation processes. The internal flow is validated based on hydraulic data from a multi-hole nozzle, characterized by cylindrical orifices so that cavitation is induced. For the validation of the spray models, the so called "Spray A" from the Engine Combustion Network ECN [42], which is a single-hole conical nozzle, is selected. The advantage of this nozzle is that it is widely characterised in terms of the spray evolution by different experimental techniques.

Later on, the impact of the eccentricity in the outlet section of the nozzle is analysed. For this purpose, six different 3D nozzle geometries with increasing levels of eccentricity have been explored for this study (Table 4.1), using as a basis the geometry from a production 6-hole diesel nozzle.

The initial dimensions of this injector were characterized using silicone moulds. This method was widely used in similar studies, providing a geometrical error about 2% in the main nozzle magnitudes [48–52]. The whole internal geometry of the real injector, including the needle seat, sac, the hydrogriding radius and the outlet section, has been replicated for all the six elliptical nozzles. Even though the outlet area of the orifice remains constant,

Radius [μm] and eccentricities		
R_{min} **(b)**	R_{max} **(a)**	e
80	90.31	0.50
75	96.33	0.62
70	103.21	0.73
65	111.15	0.81
55	131.36	0.90
50	144.5	0.94

Table 4.1: Geometries used for the study.

the nozzle shape varies as the minor radius (axial with respect to the injector axis) decreases and the mayor one (tangential to the injector) increases (see Figure 4.1a and 4.1b for further details). The outlet orifice has been defined taking into account the expressions below:

$$A_{ellipse} = \pi ab = D_{base}^2 \frac{\pi}{4} \mu m^2, \tag{4.24}$$

$$\text{being} \qquad a = \frac{A}{R_{min}\pi}, \tag{4.25}$$

$$\text{and} \qquad e = \frac{c}{a}. \tag{4.26}$$

Where is the minor radius, is the major radius and is the so-called linear eccentricity:

$$c = \sqrt{a^2 - b^2}. \tag{4.27}$$

(a) *eccentricity* = 0.50 (b) *eccentricity* = 0.94

Figure 4.1: 3D geometry models

In order to ensure the independence of the results from the computational boundaries, a 30 × 30 mm chamber domain has been chosen for the injec-

tion process (Figure 4.2). The symmetry of the problem allows to calculate a single 60° sector of the injector, corresponding to one nozzle orifice, reducing the computational effort. Turbulence is modelled by Unsteady Reynolds Averaged Navier-Stokes (U-RANS) methodology, employing a Favre-averaged formulation for compressible fluids. Given the high flow velocity and the expected appearance of cavitation, Reynolds values higher than 20000 have been estimated, so a turbulent flow is expected inside the nozzle. For this reason, a standard $k-\epsilon$ model [53, 54] has been selected as a turbulence model. Although this particular approach performance is known to be worse than others like the $k-\omega$ in recirculation zones (such as those generated in cavitation problems) and low-Reynolds-number flows [55], it has commonly produced better results in free stream flow conditions [55]. The Re-Normalisation Group (RNG) $k-\epsilon$ [56] model was also proposed since it helps to overcome some of the numerical problems induced by separated flows. However, several studies using the $\Sigma-Y$ model found in literature use the standard $k-\epsilon$ model for similar purposes as the current study, with a modified value for the $C_{\epsilon 1}$ coefficient equals to 1.6 instead of 1.44 [27, 43, 57–61]. Therefore, this last configuration has been taken to ensure consistency with previous works.

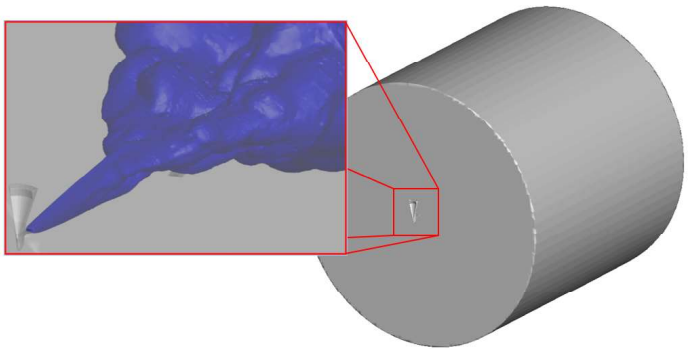

Figure 4.2: Simulated domain, $30 \times 30mm$

The energy equation has been solved in its internal form. As already introduced, a Homogeneous Relaxation Model (HRM) [45, 62–66] has been chosen in order to solve the cavitation generated at the nozzle inlet in the multi-hole geometries. In this zone, the accelerating fuel detaches from near walls and produces local pressure drops. This phenomenon depends on the injection pressure, the back-pressure and the nozzle geometry [67–74]. The geometries under study are expected to cavitate since none of them are conical. The effect of cavitation requires a small time step in order to reach convergence. This issue limits the total time of injection to 500 µs, performed at full needle lift conditions.

Regarding the boundary conditions, chamber outlet far boundaries (bottom circular plane and peripheral curved surface) are set as outflow conditions with zero normal gradient for the velocity. The inlet boundary at the nozzle

has been defined in terms of a static pressure. A wall function has been applied to all wall boundaries. For reference nozzles, the injection parameters match the ECN target conditions [42] in non-evaporative experiments. On the other hand, the elliptical nozzles have been simulated at 200 MPa injection pressure and 3 MPa back-pressure, with an initial temperature of 303 K. Table 4.2 summarizes all the applied conditions.

Boundary conditions, $P[MPa]$, $T[K]$				
Nozzles	P_{inj}	P_{back}	T_f	T_c
Spray A	150	2	343	303
Elliptical	200	3	303	303

Table 4.2: CFD boundary conditions.

A transverse mass criteria has been chosen in order to calculate the angle. As the results produced by the software are provided in an *OctreeMesh* [75], a Cartesian mesh with a 50 µm resolution is generated and adjusted to the domain for the first 20 mm (Figure 4.3a). Variables are then parallel interpolated for post-processing.

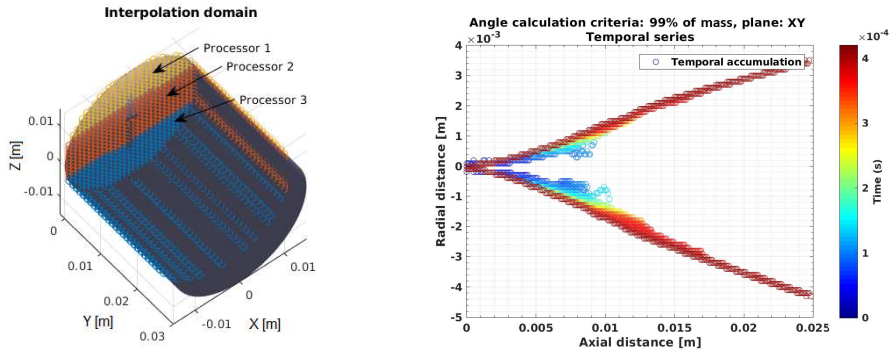

(a) Angle calculation, virtual mesh generation.(b) Points for CFD angle calculation, Spray A

Figure 4.3: CFD angle calculation methodology.

The transverse mass is then calculated according to the summation of the liquid mass in two planes projection XY (minor radius) and ZY (major radius), (see Figure 4.3b).

$$m_{liquid} = \sum_{n=1}^{n} \overline{\rho}_i \tilde{y}_{f_i} V_{mesh}. \tag{4.28}$$

Then, for each transverse integrated slice, the spray limits are calculated according to a certain percentage in mass (95 or 99%) of the total mass contained in each axial slice.

Following the normalized path suggested by the ECN, N-dodecane fluid and vapour tabulated properties have been used within the reference nozzle simulations. Vapour and nitrogen have been treated as ideal and compressible gases, while N-dodecane is set as dependent on temperature and pressure. With respect to the elliptical nozzles, a commercial diesel fuel has been chosen as working fluid and has also been characterized as a function of temperature and pressure. Temperature correlations have been implemented in a tabulated format while compressibility effect is taken into account by the compressibility modulus ($B = 1.49e9$ MPa). More details about how each of the main fuel properties is considered and the literature works from which the information was extracted can be seen in Table 4.3.

Propertiy	Value or function
Density	$825.5e^{\frac{P-P_{ref}}{B}}$ [76]
Viscosity	$f(T, P_{ref})$ [52, 76]
Vapour pressure	$f(T, P_{ref})$ [77]
Surface tension	0.029 $\mathrm{N\,m^{-1}}$ [78]
Specific heat (C_p)	$f(T, P_{ref})$ [77]

Table 4.3: Diesel fuel main properties ($P_{ref} = 0.1$ MPa).

4.4. Model validation

Two kinds of validation have been performed in this study. On the one hand, coupled nozzle-spray model (Σ - Y) has been compared to an extensive dataset available in the literature for Spray A (injector #210675) from the Engine Combustion Network group [42], which represents a conical (non-cavitating, HRM model not included) single-hole and almost axi-symmetric geometry. On the other hand, a partial validation of the injection process with cavitation has been performed based on nozzle internal flow experimental data for a cylindrical multi-hole nozzle, whose internal geometry and inner flow parameters have been previously characterised. All the models listed above have been configured within the software CONVERGE CFD [79].

- **Validation of single-hole Spray A**

  Figure 4.4a shows the geometry of the Spray A nozzle, which as previous said represents a single-hole quasi-axi-symmetric layout with a slight deviation of the nozzle from the main injector body axis. Since this deviation barely affects the spray performance, it is commonly considered axi-symmetric. The 3D geometry has been acquired from the

x-ray measurements provided in the ECN data base [80]. The nominal diameter is measured at 90 µm and the nozzle exhibits a *k-factor* of 1.5 [48].

The chosen mesh configuration (Table 4.4) provides a minimum of fifteen rows of cells inside the nozzle, representing an average of 6 µm. Some authors have established a minimum of ten cells as a good approach [27, 60, 81].

Cell size [μm]	
Mesh region	**Spray A**
Base size	384
Nozzle	6
Near nozzle spray	12 (up to 5 mm)
Needle	48
AMR u (nozzle)	Disabled
AMR α (nozzle)	Disabled
AMR u (spray)	24
Total cells	$\sim 9e6$

Table 4.4: Mesh configuration for Spray A

Figures 4.4b and 4.4c show the computational mass flow and momentum flux at the nozzle outlet together with the experimental ones, extracted from the literature [82, 83]. Despite the experimental data is obtained from a transient injection process, while the simulations are made at steady maximum needle lift, it can be noted that a good agreement between steady-state parts of the injection is reached for either mass flow rate (Figure 4.4b) or momentum flux (Figure 4.4c).

The spray angle calculation has been carried out following the methodology in Section 4.3, computing an average angle of 19.1° for the 99% of the projected radial mass and 14.6° for the 95% in mass (Figure 4.5b). The interpolation of the angle has been conducted over the first 20 mm of the simulation discharge chamber. Mean angle values were calculated over the stationay part of the simulation ($>$ 300 µm). The experimental angle data is available in previous works [82, 83] based on Diffused Back-Light (DBI) visualisation tests. Figure 4.5a shows the fitting lines for an experimental angle up to 20 mm axial distance from the nozzle. Taking into account the experimental data, an absolute error of 0.87° is found in the spray angle.

X-ray radiography technology applied to the study of the injection process [80, 84–86] allows a deeper look inside the spray microscopic behaviour. Comparisons in projected mass density PMD are provided be-

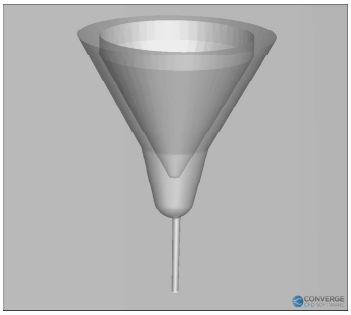

(a) Spray A, 3D geometry

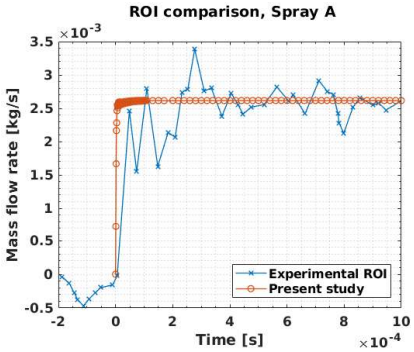

(b) Rate of injection

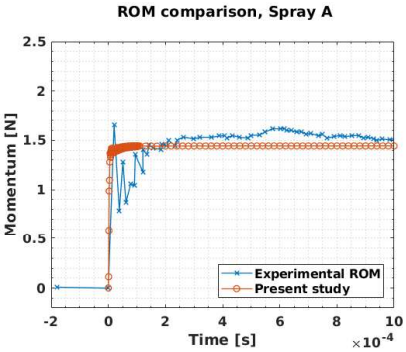

(c) Rate of momentum

Figure 4.4: Mass flow and momentum comparison for Spray A nozzle.

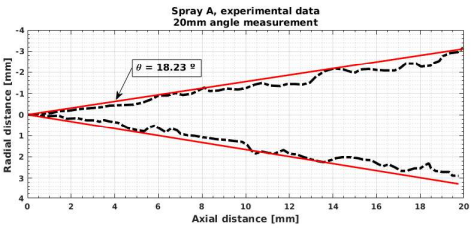

(a) Spray A, experimental angle [83] contour and fitting lines. A DBI technique was used for measuring the angle at 22.3 kg/m^3 of discharge density and 150 MPa injection pressure.

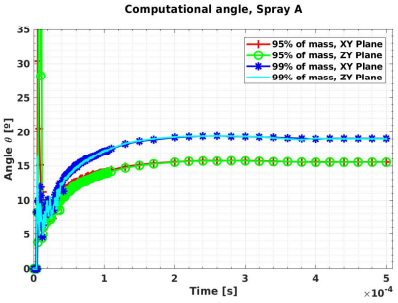

(b) Spray A, computational angle.

Figure 4.5: Spray A results.

low. Figure 4.6 shows several Gaussian profiles of projected mass density (PMD) along the spray axis (at 0.1 mm, 2 mm, 4 mm, 6 mm distance) on

the XY plane. Although the Spray A injector is considered to be quasi-axi-symmetric, the slight deviation of the nozzle from the main injector body axis [87] is captured by the deviation from 0 of the XY projection (Figure 4.6a, 4.6b, 4.6c, 4.6d). As reported in similar studies [27, 88], even if the PMD is well captured along first millimetres of the spray, the CFD case shows higher values far from the nozzle exit. Beyond 6 mm, the decay of the projected mass density is severe, and the difference between experiments and simulation significantly grows. Similar conclusions can be obtained looking at 2-dimensional PMD contours available in Figures 4.7a and 4.7b. As it can be seen, the simulation provides a faster axial decay and a wider radial evolution of PMD compared to the experimental reference data as the spray develops far from the nozzle exit. Advanced turbulence approaches such as Large Eddy Simulation (LES), coupled with capturing interface methods, have shown to better describe the evolution of the projected mass density in literature studies, as reported in the literature [22, 89]. However, since the main objective of the current study is to analyse the impact of the elliptical orifices on the nozzle flow behaviour and the primary atomization, the numerical setup used is deemed appropriate, since it has shown to be capable to properly capture the spray behaviour in the first millimetres of the nozzle outlet at a reduced computational cost.

Finally, a self similarity study for the velocity distribution has been performed. Figure 4.8 shows the evolution of the inverse of the velocity in the spray axis divided by the velocity at the nozzle orifice outlet. Additionally, the axial position has been made non-dimensional with respect to the nozzle equivalent diameter. As it can be seen, there is a linear increase after the so called intact length, as it would be predicted by gas jet theory. The results have an almost perfect match with the same information extracted from the work by Taub et al. [90] based on Direct Numerical Simulations. The slope of this increase has been computed by doing a linear fit to the data extracted from the simulations and compared with experimental data from Hussein et al. [91], showing a difference of approximately 4%. Both results can be seen as a further validation of the capability of the current model to properly capture the physics related with the momentum exchange between the fuel spray and the environment.

The previously mentioned result is complemented with the analysis of the radial distribution of the non-dimensional velocity, depicted in Figure 4.9. For axial positions equal or further than 24 times the equivalent diameter, all the radial profiles expressed in terms of the ratio between radial and axial positions collapse into a single curve. This corresponds to the disperse region of the spray, whose behaviour can be predicted according to gas jet theory. Instead, for closer positions to the nozzle

tip a slight variation of this profile can be observed.

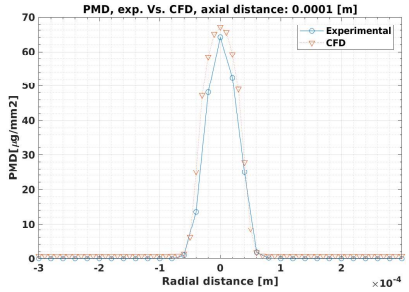

(a) Radial PMD, axial distance: 0.1 mm

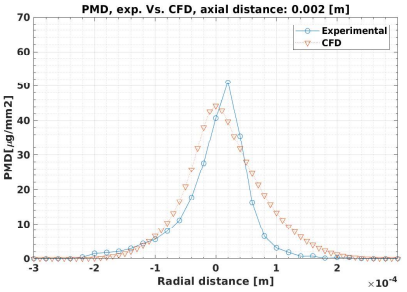

(b) Radial PMD, axial distance: 2 mm

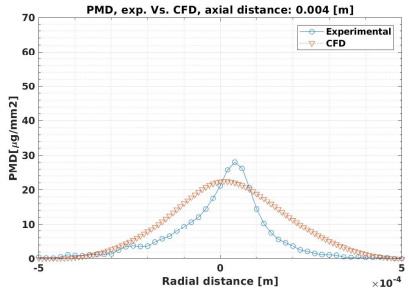

(c) Radial PMD, axial distance: 4 mm

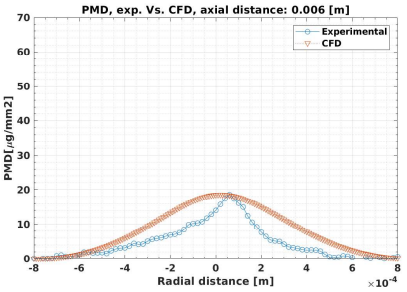

(d) Radial PMD, axial distance: 6 mm

Figure 4.6: Projected mass density profiles, Spray A.

- **Multi-hole reference cylindrical nozzle**

The second part of the model validation is focused on the analysis of the internal flow under cavitating conditions. Here, the mentioned 3D geometry of a commercial 6 holes injector with cylindrical orifices, previously characterised experimentally from an hydraulic standpoint [92], is used. All simulations are performed with the same physical models already described for the spray A case, and have been run until a steady state flow was reached. Since cavitation is expected, the HRM model has been incorporated to the model equations. In a preliminary step, a mesh independence study was completed using three different levels of refinement, with an increment of 2^n size ratio for the nozzle region, as established in Table 4.5. Additionally, the Adaptative Mesh Refinement (AMR) method is activated for subgrid velocity levels higher than 1 $\mathrm{m\,s^{-1}}$ and 0.1 of void fraction.

Mass flow rate and vapour mass at the outlet have been selected as the reference parameters for analysing the grid convergence. Once a

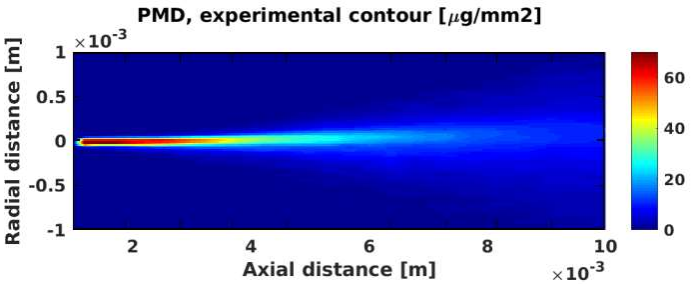

(a) Projected mass density in 2D view, X-Ray data from the Spray A [42].

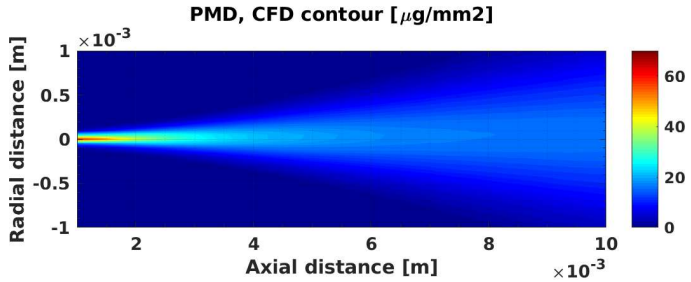

(b) Projected mass density in 2D view, CFD post-processed simulation from the Spray A.

Figure 4.7: Projected mass density contours, Spray A.

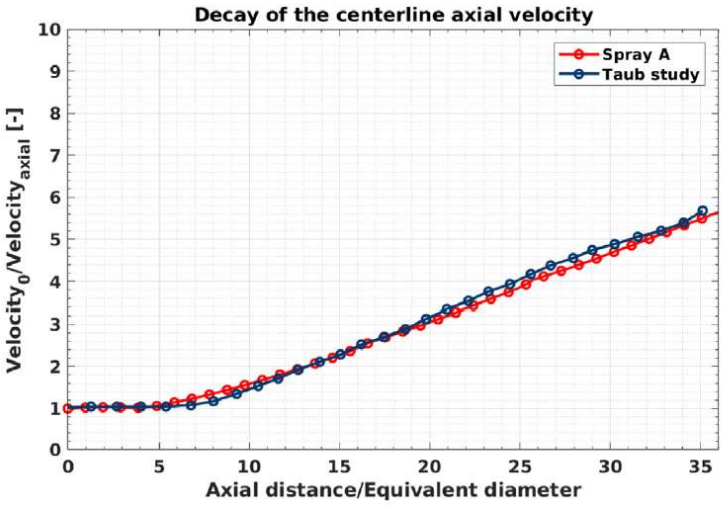

Figure 4.8: Axial evolution of the inverse of the non-dimensional velocity at the spray centerline.

steady state value of the selected variables has been reached, the convergence of the mesh was checked as described in [93] and [52]. The small

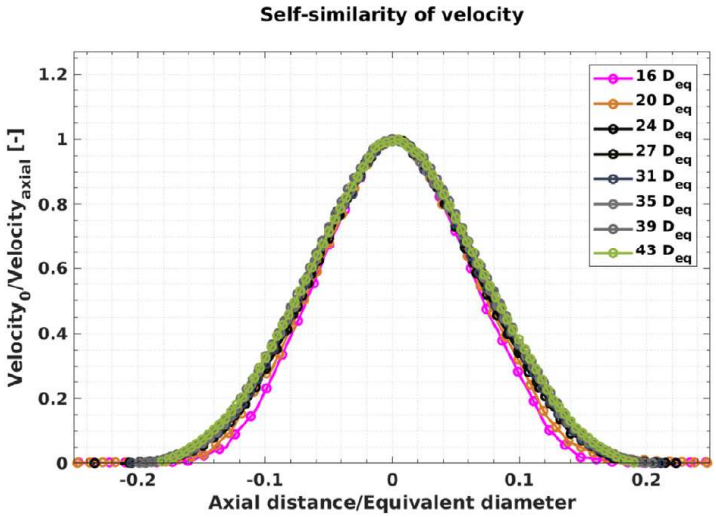

Figure 4.9: Radial distribution of the non-dimensional velocity.

Mesh independence study			
Base size = 384 μm	**Refinement level** n		
Region	**L**	**M**	**H**
Nozzle	2	3	4
Nozzle wall (3 levels)	5	6	7
AMR velocity	3	4	5
AMR void fraction	4	5	6
Needle	2	3	3
Total elements	18247	85687	389148

Table 4.5: Mesh configuration for the six orifices nozzle.

committed error between the results and the Richardson extrapolation ($P_{rh} < 0.47\%$), and the very low grid convergence index (GCI) leads to conclude that these variables are located into the asymptotic zone of its mesh dependent curves with a mesh convergence order of 2. The GCI slightly varies between the low and medium mesh resolution (0.0021 and 0.0058 for mass flow and vapour mass, respectively) and the medium to high resolution step (0.0086 and 0.0012 for mass flow and vapour mass, respectively). It was then deemed valid due to the low values achieved. However, for the simulations ahead the configuration with the highest mesh refinement has been chosen for the internal flow. The decision was based on the importance of not only reproduce the mean value of the flow, but also the particular distribution of the velocity and vapour

profiles at the nozzle outlet. Furthermore, the AMR performance can be greatly conditioned by the initial grid size as studied in [94]. A superior surface refinement ensures the stability of the calculations when cavitation appears, and the correct generation of a initial gradient for the AMR void fraction subgrid. It has to be noticed that for the nozzle with the highest eccentricity the resultant minor radius has 50 µm length. The cell size must take into account this reduction of the aspect ratio and provide a suitable number of elements inside the orifice.

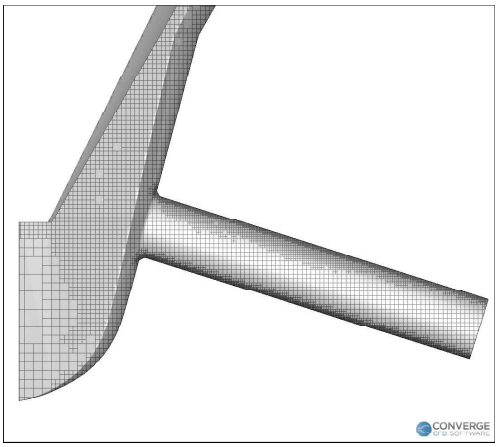

Figure 4.10: Detail of mesh configuration.

The experimental validation of the flow was carried out by means of several mass flow rate measurements at three injection pressures and six back-pressures [92]. Figure 4.11 depicts the values for the CFD and experimental results. As appreciated, the code is able to properly reproduce the mass flow choking conditions (the point at which mass flow rate reaches a critical limit value). An error of 5.4% is found for the maximum injection pressure of 160 MPa. The error is expected to progressively decrease as the injection pressure magnitude increases.

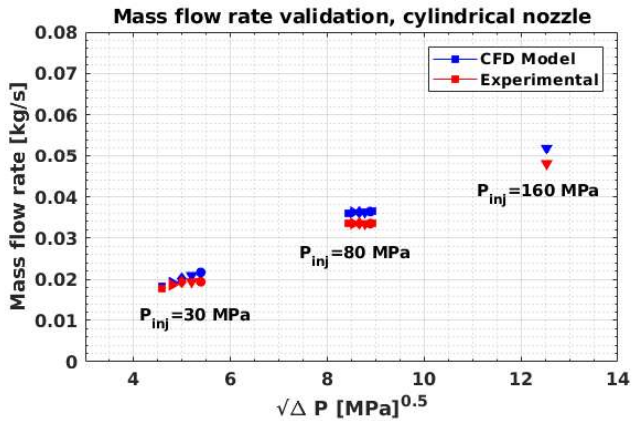

Figure 4.11: Experimental Vs. Computational mass flow. Each symbol represents a back pressure from 0.1 to 9 MPa.

4.5. Results and discussion

A first sight to the effect of the eccentricity in the injection nozzle is carried out by the study of the inner flow. For this purpose, the main non-dimensional flow coefficients of the nozzle, mainly including the discharge coefficient C_d, the velocity coefficient C_v and the area coefficient C_a, have been obtained [72]. The discharge coefficient, C_d, has been calculated according to the ideal mass flow value based on Bernoulli's equation:

$$C_d = \frac{\dot{m}_f}{\rho_l A_0 u_{th}} = \frac{\dot{m}_f}{A_o \sqrt{2\rho_l \Delta P}} \quad , \tag{4.29}$$

where mass flow is the mass flow, ρ_l is the liquid density, A_o is the geometric outlet orifice area and ΔP is the pressure drop.

From the comparison of the nozzle effective vs. theoretical velocities, the velocity coefficient is calculated as:

$$C_v = \frac{u_{eff}}{u_{th}}. \tag{4.30}$$

Finally, the area coefficient can be calculated taking into account that the relationship $C_d = C_v C_a$.

Figure 4.12 shows the flow parameters from the elliptical nozzles calculations. As it can be seen, mass flow rate slightly rises its value as the eccentricity increases, while the momentum value remains almost unchanged. In the studies by [36] and [39], a similar behaviour was observed for the mass flow. It is also in agreement with a previous publication by the authors [41]. The higher mass flow and similar outlet momentum are a consequence of a decreasing trend in the effective outlet velocity with increasing eccentricity, which can

be explained by the interaction between the eccentricity and the intensity of cavitation. The internal flow parameters (Figure 4.12) show that cavitation is reduced as the eccentricity increases. Less cavitation produces a greater area coefficient, as it can be seen from the figure, but a lower velocity coefficient [69]. In terms of mass flow, an increase would be foreseen when increasing the eccentricity, since the higher C_a would induce an also higher C_d if the velocity remained constant. However, since the velocity is also reduced when eccentricity diminishes, two opposing effects are found, preventing the mass flow rate and momentum from suffering major changes.

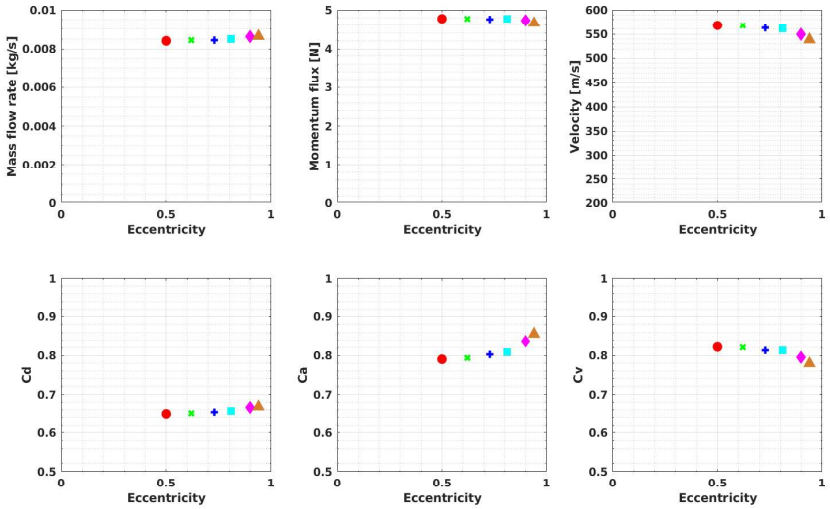

Figure 4.12: Hydraulic charaterization of the elliptical nozzles. The principal coefficients and variables have been calculated at the outlet for each nozzle. It includes the mass flow and momentum flux, effective velocity and non-dimensional parameters: the discharge coefficient, C_d, area coefficient, C_a, and velocity coefficient, C_v.

According to the literature, more intense cavitation field induces a slightly higher momentum (similar mass flow, higher velocity), which would enforce the spread angle and mixing process [95–97]. Additionally, many previous works available in the literature [8, 98] show the spray penetration can be mostly linked to the spray momentum and spreading angle. Therefore, slightly larger spray penetration could be anticipated for the cylindrical nozzles, which are characterized by slightly larger momentum. However, the following paragraphs will demonstrate that the sole study of the average flow parameters at the nozzle outlet is not enough to account the influence of eccentricity in the spray performance.

First of all, not only the cavitation intensity but its distribution along the nozzle section needs to be considered. As it can be seen from Figure

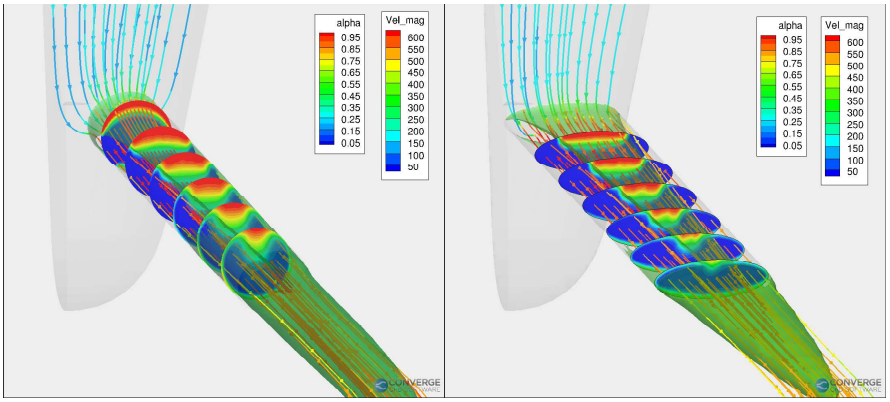

(a) Eccentricity = 0.50 (b) Eccentricity = 0.94

Figure 4.13: Flow conditions along the nozzle: the coloured stream-lines represent the variation of the velocity magnitude along the nozzle, while the radial slices show the void fraction evolution in six equally spaced sections. The iso-volume in green represents the void fraction for a value of 0.5. Notice how the vapour spreads further away from the orifice for the nozzle with lower eccentricity.

4.13, although the intensity of the void fraction is higher in the nozzle with $e = 0.50e$ (left side), the distribution of vapour in the most elliptical nozzle is wider over the whole section (right side). Even if the generation of vapour inside the nozzle is well known to improve the atomization from the literature, the low amount of experimental measurements from inside the nozzle hardens the complete understanding of how the vapour distribution itself affects the phenomena involved. As it could be anticipated, the aspect ratio of the elliptical nozzles (i.e. the ratio between major and minor radii) affects the vapour distribution field, in particular the interaction between the bottom and top side vapour in the nozzle outlet. Figures 4.13a and 4.13b show how the stream-lines are then approaching each other along the nozzle as eccentricity increases, which supports this effect. [38] suggested that the cavitation should be improved in the cross sectional area of the elliptical nozzles because of a severe contraction of the stream-lines. However, this statement may not be applied to multi-hole configurations, since the stream-lines are not symmetric. Unlike single-hole nozzles, in the proposed geometries the vapour is generated mainly in the top-part of the cross-section. This section, where the fluid accelerates, is wider for the nozzles with higher aspect ratio, and allows a larger path for the most critical stream-lines. A larger local curvature distributes the stream flow and reduces the pressure drop, so the vapour peak is lower. Additionally, it enforces the distribution of the vapour over the whole section, as it was already seen in Figure 4.13. Furthermore, the higher perimeter of the ellipse provides a more significant interaction of the spray section with the

chamber gas. With respect to the thermodynamic properties of the fluid, no major differences have been identified.

One important parameter that can be evaluated to start analysing the impact of the eccentricity in spray development is the evolution of the mixing field. This information is depicted in terms of the axial distribution of the fuel mass fraction (Figure 4.14), as well as the radial distribution of the fuel mass fraction at four axial positions and for two different planes (XY and ZY) in Figures 4.15a-4.15h. The axial distribution is defined in terms of the axial location divided by the equivalent diameter, defined as:

$$D_{eq} = D_o \sqrt{\frac{\rho_f}{\rho_a}} \tag{4.31}$$

where D_o is the diameter of a circle that would produce the same section as the outlet orifice of the eccentric nozzles, ρ_f the liquid fuel density and ρ_a the air density in the discharge chamber.

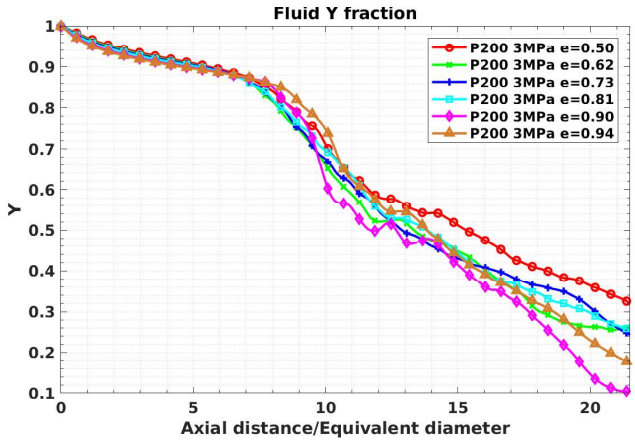

Figure 4.14: Axial liquid mass fraction

In the near nozzle region (up to 3 mm or 3.5 equivalent diameters), the axial evolution is very similar for all nozzles, while the radial distribution results are directly influenced by the nozzle morphology (Figure 4.15a and 4.15b). As the spray penetrates inside the chamber (3-8 mm, 3.5-9 equivalent diameters), the axial evolution is still similar, and the radial limits for the mass fraction start to become also more similar for both planes (Figure 4.15c and 4.15d). Beyond 8 mm (approximately 9 equivalent diameters), the axial evolution starts to be affected by the nozzle eccentricity, which can be also seen in the fact that the radial profiles associated to the more elliptical nozzles seem to reduce their

fraction peak in favour of a wider curve (Figure 4.15e and 4.15f). A decreasing value of the liquid mass fraction peak can only take place if the equivalent quantity of liquid is radially scattered, that is, the angle of the spray is also bigger. An inversion of width between both XY and ZY planes (corresponding to the minor and major axis, respectively) appears before reaching the 12 mm (approximately 14 equivalent diameters) position. This phenomenon becomes more severe as the aspect ratio increases (Figures 4.15g and 4.15h). Similar behaviour has been found by Yu et al. [37] in cavitating single-hole nozzles. In that case, where the flow enters symmetrically (in the direction of the nozzle axis), the initial perturbation starts on the sides of the major axis due to a greater contraction of the stream-lines. This produces an initial larger dispersion in the ZY (major axis) plane [38]. In the case of the present study, cavitation is generated in the top and bottom sections of the minor axis as a result of the inclination angle of the nozzle orifice with respect to the injector axis [72]. Hence, a wider spreading angle would be expected for the XY plane.

The radial and axial velocity profiles have also been extracted. The tendencies are similar to those of the liquid fuel mass fraction. A primary influence of the outlet geometry is followed by an almost perfect matching in the maximum value and shape of the velocity profiles as the spray develops in axial direction (Figures 4.16a, 4.16b, 4.16c, 4.16d). For an intermediate point (8 mm, 9 equivalent diameters), the velocity starts to decrease faster for higher eccentricity values (Figures 4.16e, 4.16f, 4.16g 4.16h). A faster dispersion of the fuel over the chamber is consistent with an earlier velocity fall. The mass exchange between the injected liquid and the inert gas (because of turbulent friction) results in kinetic energy losses which are, in fact, velocity losses. A similar trend can be seen in Figure 4.17 looking at the evolution of the inverse of the centerline velocity divided by the outlet velocity. While in the case of a circular nozzle (i.e. symmetric jet) a linear trend would be seen, as it was already analyzed for Spray A data in Figure 4.8 , for the elliptical geometries this linear trend can only be perceived for an axial distance up to 10 times the equivalent diameter. From that point on, inverse of the velocity clearly increases with a faster rate than a linear trend, actually more intense as the nozzle eccentricity increases.

Figure 4.18 represents the air entrainment for each nozzle spray. As it can be seen, there is a general trend of increasing entrainment as the eccentricity rises. A smooth growing trend is observed for the first four nozzles ($e = 0.50 \div 0.81)e$ while the two last cases are characterised by a bigger initial entrainment. In line with the discussion above, the enhanced air entrainment is consistent with a wider divergence of the angle and a slightly bigger mass flow rate (Figure 4.12) [99, 100]. Both liquid fuel mass fraction and velocity profiles indicate that the spreading angle in ZY plane is enhanced as the eccentricity of the nozzle increases. Taking this into account, its impact on the spray penetration can be evaluated. In this sense, if the spray momentum

is defined as:

$$\dot{M}(x) = \dot{M}_0 = \dot{m}_f U_0 = \int_A \rho_f U^2(x) dA. \tag{4.32}$$

The relationship between the spreading angle and the penetration can be established as follows [101]:

$$S(t) \propto M_f^{0.25} \rho_a^{-0.25} tan^{-0.5}(\theta/2) t^{0.5}. \tag{4.33}$$

The penetration is then proportional to the momentum and inversely proportional to the tangent of the spreading angle. From Figure 4.14, it can be observed how beyond a medium distance from the nozzle outlet, the elliptical nozzles diminish the liquid fraction faster along the injection axis, which must be supported by an increment of the spreading angle. Given that the momentum (4.12) does not change significantly, an angle reduction will cause a slower penetration slope. From a qualitative view, Figure 4.19 shows how the 0.01 mass fraction iso-volume regions for the most extreme nozzles (almost cylindrical and very elliptical), highlighting the wider dispersion from the most eccentric nozzle as the spray develops.

Even if the momentum value is nearly the same for all nozzles, the interaction of this momentum with the ambient gas is not. On the one hand, the surface of elliptical nozzles adds an extra perimeter of contact with the air for a same geometric area value. On the other hand, the momentum thickness [102] varies across the section in different ways for all cases so a lineal behaviour is not necessarily expected between the sprays. This surface interaction gain between the discharge gas and the diesel jet is exponentially increasing with eccentricity. From Figure 4.20, the numerical breach in the shape area interaction between the first four nozzles ($e = 0.50 \div 0.81$)e and the two last nozzles ($e = 0.90$ and 0.94) can provide some explanation to the leap in entrainment. The resulting jet shape at the outlet for the maximum accounted eccentricity originates a value of 21.27% over the initial cylindrical nozzle perimeter for the same geometric area. This fact makes the rise in surface interaction compatible in general terms with the results for the entrainment and angle.

Finally, Figures 4.21a and 4.21b show the average computed angle (section 4.3) for all the elliptical nozzles. The angle projected on XY plane (4.21a) oscillates around 14° with no clear trend. The deviation from the mean value (dotted grey line) does not exceed 1.5°. From what was exposed in the internal flow parameters, the more cylindrical nozzle should develop a higher XY angle due to a more intense cavitation. However, the decreasing thickness in that plane for the elliptical nozzles also favours the increment of the angle due to instabilities. These effects oppose each other and may be the cause of an almost constant XY angle. This behaviour can be also connected to the fluctuations produced by cavitation, given that it takes place in the top and bottom parts of the nozzle section (minor axis view, XY plane).

The pulsatile and unsteady instabilities of vapour could lead to a still transient deposition of liquid in the XY plane for the simulated time. Nev-

ertheless, this result is in agreement with the mass fraction profiles in the radial XY plane (Figure 4.15e, 4.15g), where the limit threshold value of the mass fraction appears in almost the same radial coordinate. Differently, the angle on ZY projection depicted in Figure 4.21b shows a clear tendency also according to the right column of picture 4.15, indicating that the divergence of the angle in ZY is proportional to the eccentricity value. Continuing with the pattern previously suggested in the entrainment discussion, a smooth jump in the angle is found until a eccentricity value of 0.81 while the last two nozzles shows a wider but closer angle. Regarding the angle proximity between nozzles 5 and 6, the proposed simulations may have reached the eccentricity threshold value at which the spray angle no longer increases. An increment about 10° is detected for the maximum eccentricity nozzle with respect to the lower one. Hong et al. [38] showed in its experiments with transparent nozzles how the angle increases in both major and minor axis planes when elliptical single-hole nozzles are subjected to cavitation. However, in those proposed geometries, the cavitation and hence the source of instabilities were located in the major axis extremes, the opposite to that of the diesel nozzle of the present paper (Figure 4.13). As exposed by [39], this fact produces a greater spreading angle in the major axis (ZY plane).

Figure 4.22a depicts the temporal evolution of the angle for the nozzle simulation with highest aspect ratio ($e = 0.94$)e. A first view on the right side of Figure 4.5 shows an almost constant angle for the first millimetres of the spray up to 8 mm. At this point, the angle starts to grow and the trend is more significant. It is coherent with the absence of higher disturbances at the nozzle outlet on the extremes of the major axis, unlike Kun et al. Image 4.22a traces a complete different behaviour from the computational angle. The minor axis plane (XY) angle strongly grows first millimetres of the spray. This issue is explained by the high disturbances at the outlet in the XY plane according to the existence of cavitation. Beyond 8 mm the XY angle suddenly reduces its growth. It can be seen how both XY and ZY angles share the inflexion point at which its width trends switch. As previously commented, the XY plane is expected to have a wider angle. For cylindrical nozzles, the spreading of fuel is enforced by cavitation generating a almost axi-symmetric and wider spray that non cavitating cylindrical nozzles. In related studies [32–34, 102], a switching axes behaviour has been repeatedly detected. In these works, the anomaly in the spray behaviour compared to cylindrical nozzles was attributed to a self-induced vortex of the elliptical spray. One similar behaviour was described by [37] in experiments with single-hole nozzles. Although the bibliography above has only exposed single-hole nozzles, and it can not be directly compare to those of this study, several of its physical phenomena can be extrapolated to the performance of multi-hole nozzles. Figure 4.24 depicts the switching axis behaviour, first frames 4.24a, 4.24b, 4.24c and 4.24c shows the initial greater opening of the angle in the minor axis due to the effect of cavitation, the minor

axis becomes the major axis. From frames 4.24d to 4.24i the instabilities start to rise in the new minor axis and it breaks in an inflexion point. The switching axis occurs between 4.24j and 4.24l. In picture 4.24m to 4.24s the greater dispersion in the ZY plane (geometrical major axis) starts to form a new and more defined elliptical shape. Summarizing, the general angle grows as the eccentricity rises being this fact more noticeable in the ZY angle (major axis) while in the minor XY axis the angle is at least as much bigger as the more cylindrical one.

A final outline over the problem commands the exam of penetration. Even if the simulations have been accomplished with a full needle lift, differences supporting the earlier discussion can be observed. Figure 4.23 provides the temporal evolution of penetration for all cases. As expected, a wider angle (high eccentricity values) generates a slower penetration curve [101, 103]. However, it is true that in terms of penetration, the difference between the nozzle 4 and 6 is not as big as it could be suggested by previous data. The evolution of the jet further from this point is an interesting topic, specially for big engines. Unfortunately, computational resources have limited the simulation space and the injection duration. For future works, larger time injections in order to clarify both angles behaviours must be carried out for a better understanding of this kind of nozzles. Even so, it has been demonstrated that the general influence of eccentricity enforces the spray atomization by means of a wider angle. Also, it has been discussed how the internal parameters such as momentum and mass flow, are not enough for fully describing the spray atomization potential and how the entrainment and fluid fraction along the spray are in resonance with the angle and entrainment. The increment of the surface area of jet-air interaction and the momentum thickness must be considered along with the self behaviour of the generated spray for the correct understanding of elliptical jets. A more complex model such as LES or near field DNS simulations could provide more specific data to measure these parameters.

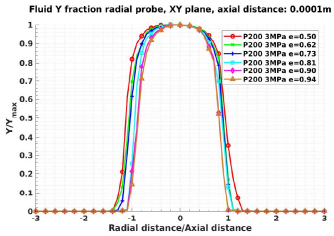

(a) XY, 0.1mm (0.12 D_{eq})

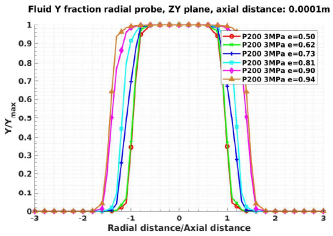

(b) ZY, 0.1mm (0.12 D_{eq})

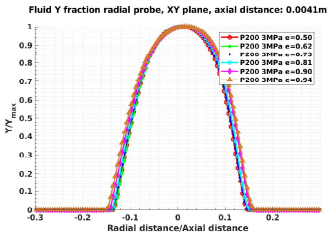

(c) XY, 4.1mm (4.86 D_{eq})

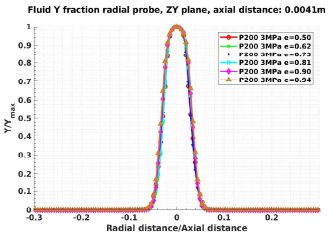

(d) ZY, 4.1mm (4.86 D_{eq})

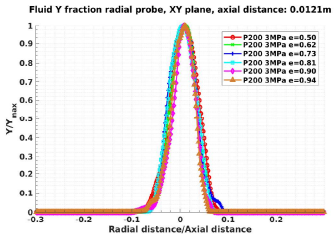

(e) XY, 12.1mm (14.37 D_{eq})

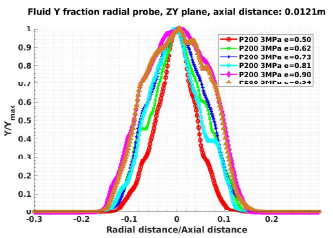

(f) ZY, 12.1mm (14.37 D_{eq})

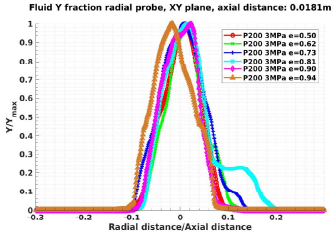

(g) XY, 18.1mm (21.5 D_{eq})

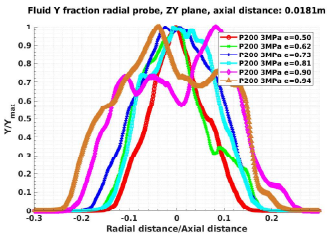

(h) ZY, 18.1mm (21.5 D_{eq})

Figure 4.15: Radial liquid mass fraction profiles for the elliptical nozzles.

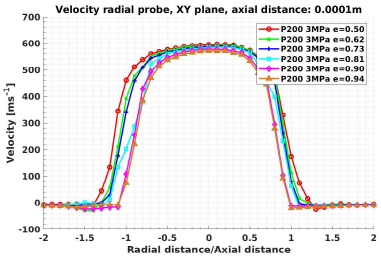

(a) XY, 0.1 mm (0.12 D_{eq})

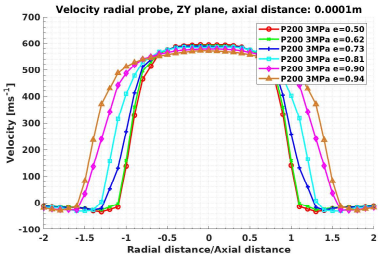

(b) ZY, 0.1 mm (0.12 D_{eq})

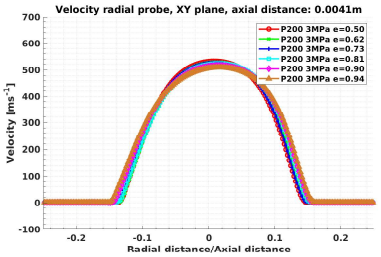

(c) XY, 4.1 mm (4.86 D_{eq})

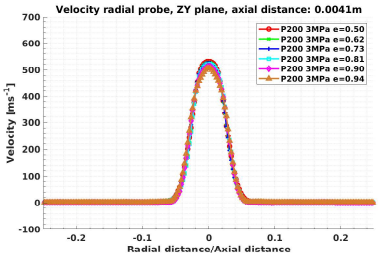

(d) ZY, 4.1 mm (4.86 D_{eq})

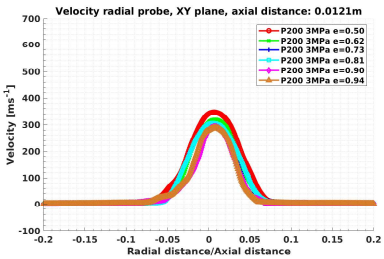

(e) XY, 12.1 mm (14.37 D_{eq})

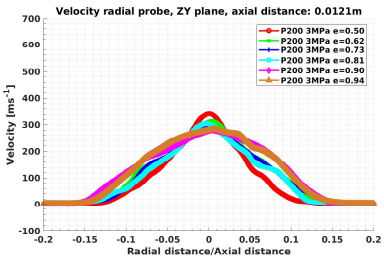

(f) ZY, 12.1 mm (14.37 D_{eq})

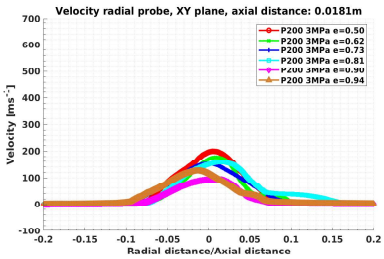

(g) XY, 18.1 (21.5 D_{eq}) mm

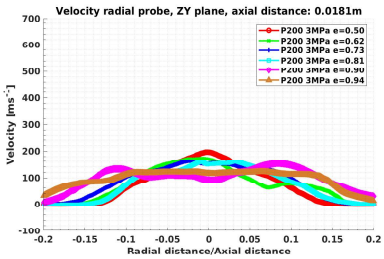

(h) ZY, 18.1 (21.5 D_{eq}) mm

Figure 4.16: Radial velocity profiles for the elliptical nozzles.

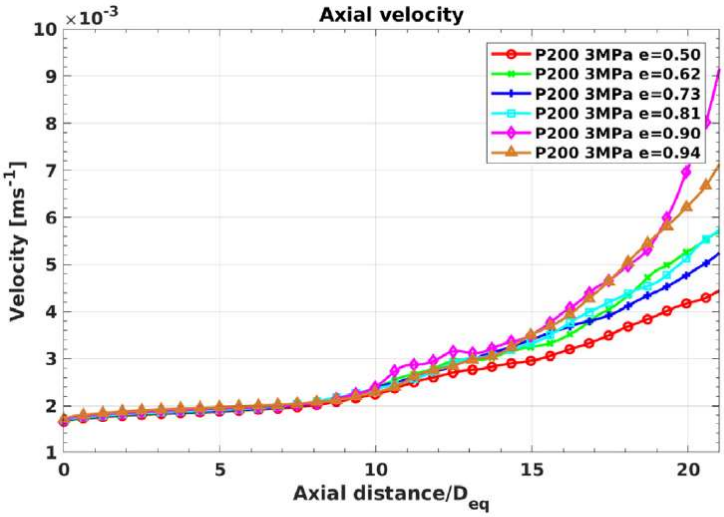

Figure 4.17: Axial liquid inverse velocity

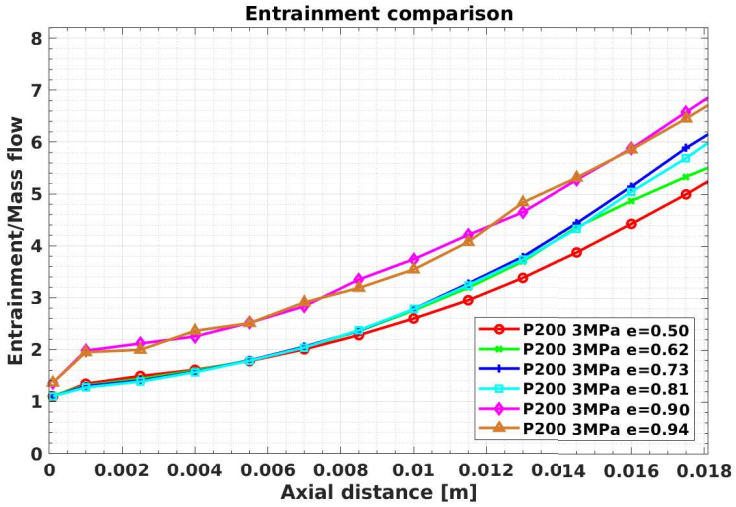

Figure 4.18: Jet entrainment.

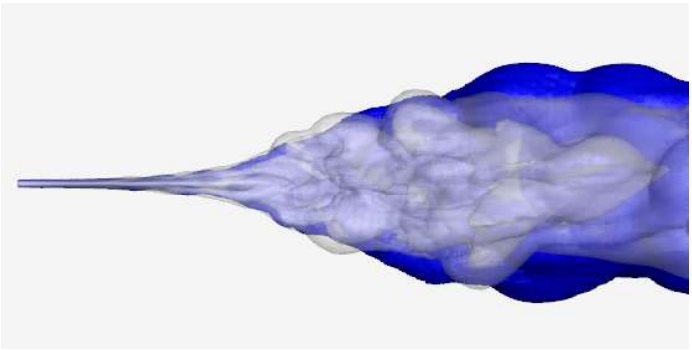

Figure 4.19: Iso-volume for a liquid mass fraction value of 0.01, ZY visualization plane. The nozzle of 0.50 eccentricity is depicted in white, the nozzle of 0.94 in blue.

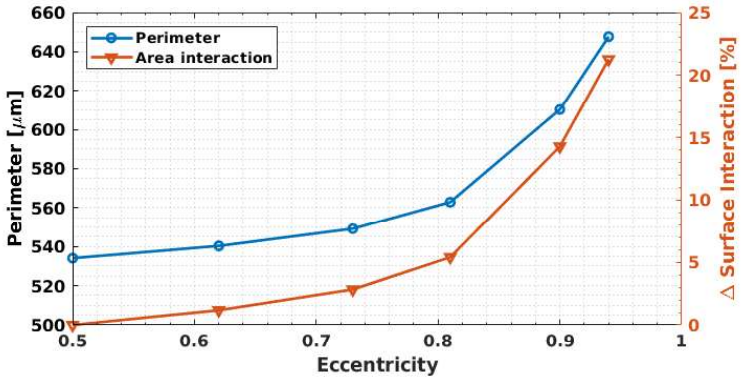

Figure 4.20: Geometrical effects of eccentricity over the spray interaction.

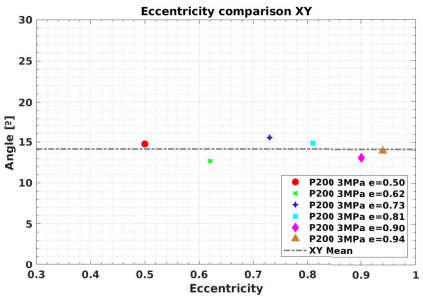

(a) Mean angle comparison in the minor axis plane (XY).

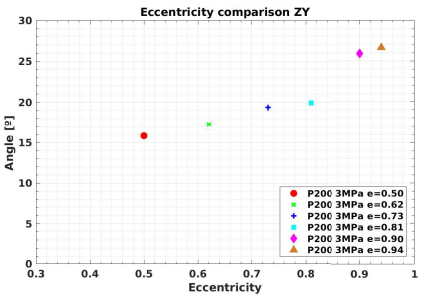

(b) Mean angle comparison in the major axis plane (ZY).

Figure 4.21: Angle comparison, elliptical nozzles.

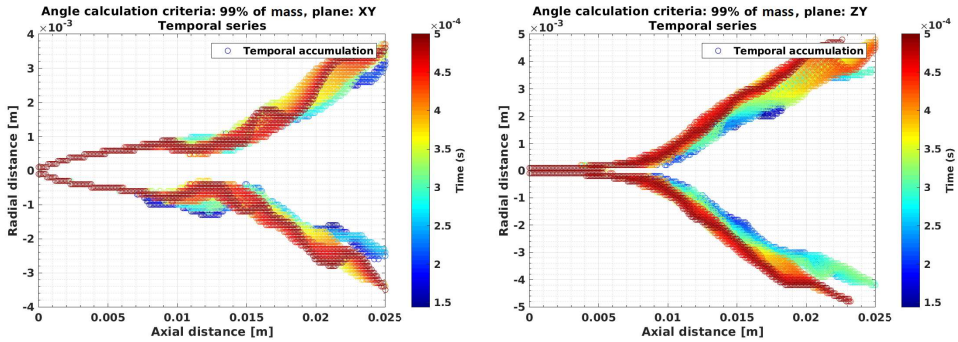

(a) Plane XY, minor axis (b) Plane ZY, major axis

Figure 4.22: Temporal variation of angle, eccentricity = 0.94.

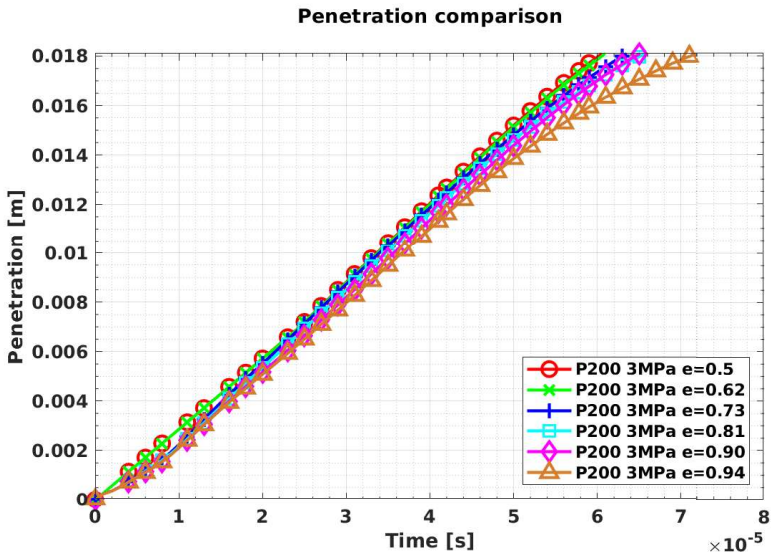

Figure 4.23: Penetration curves for the elliptical nozzles at full needle lift.

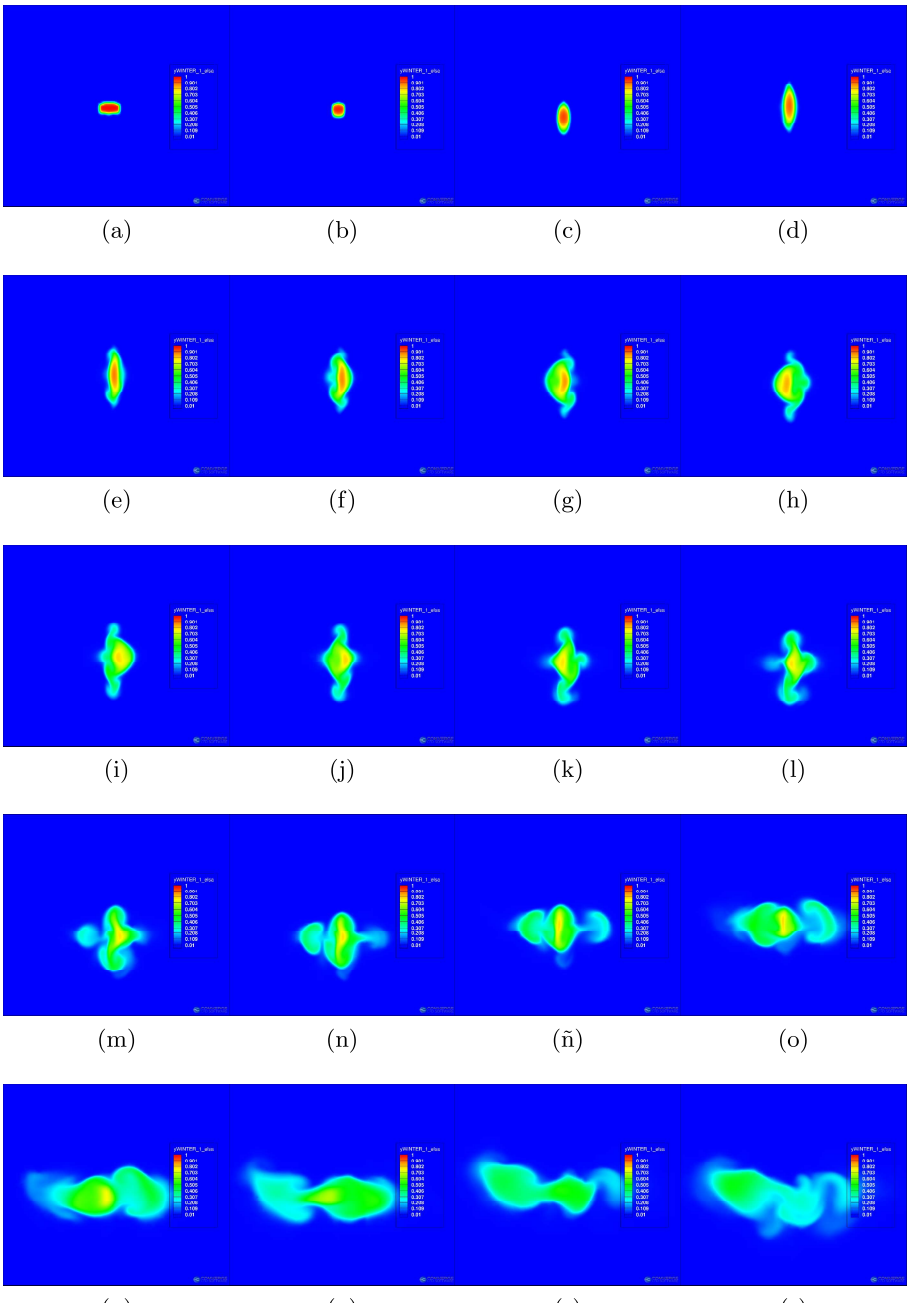

(a) (b) (c) (d)

(e) (f) (g) (h)

(i) (j) (k) (l)

(m) (n) (ñ) (o)

(p) (q) (r) (s)

Figure 4.24: Main injection axis rotation due to self-induced vorticity of the jet, CFD.

4.6. Conclusions

Several elliptical nozzles with the same outlet area and different eccentricity have been simulated coupling the inner nozzle flow and spray formation by means of an advanced CFD code. The code has been previously validated in terms of internal flow and spray formation for both a single-hole conical nozzle as well as a multi-hole cylindrical one. In the case of the latest, the simulation included the activation of a HRM model which accurately predicted the mass flow collapse induced by cavitation. This multi-hole geometry has been taking as a reference to produce the elliptical geometries.

The main conclusions of the study are summarized below:

1. A new study showing in depth the capabilities of elliptical nozzles in order to improve the atomization and mixing processes has been carried out by means of a numerical CFD model coupling the internal nozzle morphology and the external spray performance.

2. The $\Sigma - Y$ model is able to capture the internal geometric morphology of the nozzle and translate its characteristics to the spray.

3. For an equal area and boundary conditions, increasing the eccentricity for horizontal elliptical nozzles improves the discharge and area coefficients due to lower cavitation. The velocity coefficient is slightly decreased, producing very similar outlet momentum. In terms of cavitation, such geometries induce a vapour field with lower intensity but more dispersed across the outlet section of the orifice.

4. The spray behaviour has shown to be sensitive to the nozzle flow characteristics. In this sense, the spray cannot be fully understood only by simple average parameters at the nozzle outlet, which are the ones normally achievable with experimental tools. The way the nozzle shape interacts with the discharge chamber is critical.

5. In terms of spray characteristics, more elliptical nozzles produce an improvement of air entrainment, with the minor angle showing small variations, while the major angle increases significantly. Consequently, spray penetration tends to be reduced.

6. A significant increment of the angle and jet entrainment as the eccentricity rises are an indication that elliptical nozzles can help to improve the spray atomization processes.

Some of the aforementioned features found have been also confronted with previous literature works, providing consistent trends.

Declaration of conflicting interests

The author(s) declared no potential conflicts of interest with respect to the research, authorship, and/or publication of this article.

Acknowledgements

The authors would like to thank the computer resources, technical expertise and assistance provided by Universitat Politècnica de València in the use of the super-computer "Rigel". The authors want to express their gratitude to CONVERGENT SCIENCE Inc. and Convergent Science GmbH for their kind support for the CFD calculations with the CONVERGE software.

Funding

The author(s) disclosed receipt of the following financial support for the research, authorship, and/or publication of this article: This work was supported by the Ministerio de Ciencia, Innovación y Universidades of the Spanish Government. The PhD studies by Enrique C. Martínez-Miracle have been funded by the Agencia Estatal de Investigación of the Spanish Government and the ESF (European Social Fund), project "Desarrollo de modelos de combustión y emisiones HPC para el análisis de plantas propulsivas de transporte sostenibles" (TRA2017-89139-C2-1-R) by means of the "Subprograma Estatal de Formación del Programa Estatal de Promoción del Talento y su Empleabilidad en I+D+i".

References

[1] John B. Heywood. *Internal combustion engine fundamentals*. McGraw-Hill, 1988. ISBN: 007028637X.

[2] Masataka Arai. "Physics behind Diesel Sprays". In: *ICLASS 2012, 12th Triennial International Conference on Liquid Atomization and Spray Systems, Heidelberg, Germany, September 2-6, 2012 Physics* (2012), pp. 1–18. URL: http://scholar.google.com/scholar?hl=en%7B%5C&%7DbtnG=Search%7B%5C&%7Dq=intitle:Physics+behind+Diesel+Sprays%7B%5C#%7D0.

[3] A. H. Lefebvre and V. G. McDonell. *Atomization and Sprays, Second Edition.* 2017, p. 300. ISBN: 9781498736268. DOI: 10.1016/0009-2509(90)87140-N.

[4] Yutaro Wakuri, Masaru Fujii, Tatsuo Amitani and Reijiro Tsuneya. " Studies on the Penetration of Fuel Spray in a Diesel Engine ". In: *Bulletin of JSME* 3.9 (1960), pp. 123–130. ISSN: 1881-1426. DOI: 10.1299/jsme1958.3.123. URL: http://www.mendeley.com/research/geology-volcanic-history-eruptive-style-yakedake-volcano-group-central-japan/%20http://joi.jlc.jst.go.jp/JST.Journalarchive/jsme1958/3.123?from=CrossRef.

[5] H. Hiroyasu and T. Kadota. "Fuel droplet size distribution in diesel combustion chamber". In: *SAE International* (1974). DOI: https://doi.org/10.4271/740715.

[6] Hiro Hiroyasu and Masataka Arai. "Structures of Fuel Sprays in Diesel Engines". In: 2002.724 (Feb. 1990). DOI: 10.4271/900475. URL: https://www.sae.org/content/900475/.

[7] Hiroyuki Hiroyasu. "Spray Breakup Mechanism from the Hole-type Nozzle and its Applications". In: *Automization and Sprays: Journal of the International Institutions for Liquid Atomization and Spray Systems* 10 (May 2000), pp. 511–527. DOI: 10.1615/AtomizSpr.v10.i3-5.130.

[8] Hiro Hiroyasu and Haiyan Miao. "Measurement and Calculation of Diesel Spray Penetration". In: *Proceedings of ICLASS Conference* October (2003). URL: http://www.ilasseurope.org/ICLASS/iclass2003/fullpapers/1413.pdf.

[9] R. D. Reitz and F. V. Bracco. "Mechanism of atomization of a liquid jet". In: *Physics of Fluids* 25.10 (1982), pp. 1730–1742. ISSN: 10706631. DOI: 10.1063/1.863650.

[10] Rolf D. Reitz and R. Diwakar. "Structure of High-Pressure Fuel Sprays". In: (Feb. 1987). DOI: 10.4271/870598. URL: https://www.sae.org/content/870598/.

[11] Rolf Reitz. "Modeling atomization processes in high-pressure vaporizing sprays". In: *Atomisation Spray Technology* 3 (Jan. 1987), pp. 309–337.

[12] C. Dumouchel. "On the experimental investigation on primary atomization of liquid streams". In: *Experiments in Fluids* 45 (Sept. 2008), pp. 371–422. DOI: 10.1007/s00348-008-0526-0.

[13] Jose Maria Desantes, Francisco Javier Salvador, Jose Javier Lopez and Joaquin De la Morena. "Study of mass and momentum transfer in diesel sprays based on X-ray mass distribution measurements and on a theoretical derivation". In: *Experiments in Fluids* 50.2 (2011), pp. 233–246. ISSN: 07234864. DOI: 10.1007/s00348-010-0919-8. URL: http://link.springer.com/article/10.1007/s00348-010-0919-8.

[14] J. Manin et al. "Microscopic investigation of the atomization and mixing processes of diesel sprays injected into high pressure and temperature environments". In: *Fuel* 134 (2014), pp. 531–543. ISSN: 0016-2361. DOI: https://doi.org/10.1016/j.fuel.2014.05.060. URL: https://www.sciencedirect.com/science/article/pii/S0016236114005225.

[15] Christoph Espey, John E Dec, Thomas A. Litzinger and Domenic A. Santavicca. "Planar laser rayleigh scattering for quantitative vapor-fuel imaging in a diesel jet". In: *Combustion and Flame* 109.1-2 (1997), pp. 65–86. ISSN: 00102180. DOI: 10.1016/S0010-2180(96)00126-5. URL: http://www.sciencedirect.com/science/article/pii/S0010218096001265.

[16] Christof Schulz and Volker Sick. "Tracer-LIF diagnostics: quantitative measurement of fuel concentration, temperature and fuel/air ratio in practical combustion systems". In: *Progress in Energy and Combustion Science* 31.1 (2005), pp. 75–121. ISSN: 03601285. DOI: 10.1016/j.pecs.2004.08.002. URL: http://linkinghub.elsevier.com/retrieve/pii/S0360128504000619.

[17] Cherian A Idicheria and Lyle M Pickett. "Ignition , soot formation , and end-of-combustion transients in diesel combustion under high-EGR conditions". In: *International Journal of Engine Research* 12 (2011), pp. 1–17. DOI: 10.1177/1468087411399505.

[18] Jose Maria Desantes, José Maria García-Oliver, Antonio García and Tiemin Xuan. "Optical study on characteristics of non-reacting and reacting diesel spray with different strategies of split injection". In: *International Journal of Engine Research* 301 (May 2018). ISSN: 20413149. DOI: 10.1177/1468087418773012. URL: http://journals.sagepub.com/doi/10.1177/1468087418773012.

[19] Olivier Desjardins and Heinz Pitsch. “Detailed Numerical Investigation of Turbulent Atomization of Liquid Jets”. In: *Atomization and Sprays* 20.4 (2010), pp. 311–336. ISSN: 1044-5110. DOI: 10.1615/AtomizSpr.v20.i4.40.

[20] F. J. Salvador, J. Martínez-López, J.-V. Romero and M.-D. Roselló. “Study of the influence of the needle eccentricity on the internal flow in diesel injector nozzles by computational fluid dynamics calculations”. In: *International Journal of Computer Mathematics* 91.1 (2014), pp. 24–31. DOI: 10.1080/00207160.2013.770483.

[21] Francisco Javier Salvador, David Jaramillo, J. V. Romero and M. D. Roselló. “Using a homogeneous equilibrium model for the study of the inner nozzle flow and cavitation pattern in convergent-divergent nozzles of diesel injectors”. In: *Journal of Computational and Applied Mathematics* 309 (2015), pp. 630–641. ISSN: 03770427. DOI: 10.1016/j.cam.2016.04.010. URL: http://dx.doi.org/10.1016/j.cam.2016.04.010.

[22] J. Anez et al. “Eulerian-Lagrangian spray atomization model coupled with interface capturing method for diesel injectors”. In: *International Journal of Multiphase Flow* 113 (2018), pp. 325–342. ISSN: 03019322. DOI: 10.1016/j.ijmultiphaseflow.2018.10.009. URL: https://doi.org/10.1016/j.ijmultiphaseflow.2018.10.009.

[23] Ariane Vallet and Roland Borghi. “ Modelisation eulerienne de l’atomisation d’un jet liquide ”. In: *Comptes Rendus de l’Academie de Sciences - Serie IIb: Mecanique, Physique, Chimie, Astronomie* 327.10 (1999), pp. 1015–1020. ISSN: 12874620. DOI: 10.1016/S1287-4620(00)87013-1.

[24] Ariane Vallet, A. A. Burluka and R. Borghi. “Development of a Eulerian model for the atomization of a liquid jet”. In: *Atomization and Sprays* 11.6 (2001). ISSN: 1044-5110.

[25] Yue Wang, Won Geun Lee, Rolf Reitz and Ramachandra Diwakar. “Numerical simulation of diesel sprays using an Eulerian-Lagrangian Spray and Atomization (ELSA) model coupled with nozzle flow”. In: *SAE 2011 World Congress and Exhibition*. Apr. 2011. DOI: 10.4271/2011-01-0386. URL: https://www.sae.org/content/2011-01-0386/.

[26] Jose Maria Desantes et al. “Coupled/decoupled spray simulation comparison of the ECN spray a condition with the Σ-Y Eulerian atomization model”. In: *International Journal of Multiphase Flow* 80 (2016), pp. 89–99. ISSN: 03019322. DOI: 10.1016/j.ijmultiphaseflow.2015.12.002.

[27] Q. Xue et al. "An Eulerian CFD model and X-ray radiography for coupled nozzle flow and spray in internal combustion engines". In: *International Journal of Multiphase Flow* 70.December (2015), pp. 77–88. ISSN: 03019322. DOI: 10.1016/j.ijmultiphaseflow.2014.11.012.

[28] Hongwu Zhao et al. "Validation of a Three-Dimensional Internal Nozzle Flow Model Including Automatic Mesh Generation and Cavitation Effects". In: *Journal of Engineering for Gas Turbines and Power* 136 (Sept. 2014). DOI: 10.1115/1.4027193.

[29] Michele Battistoni et al. "EFFECTS OF NONCONDENSABLE GAS ON CAVITATING NOZZLES". In: *Atomization and Sprays* 25.6 (2015), pp. 453–483. ISSN: 1044-5110.

[30] P. M. Sforza, M. H. Steiger and N. Trentacoste. "Studies on three-dimensional viscous jets". In: *AIAA Journal* 4.5 (1966), pp. 800–806. ISSN: 00011452. DOI: 10.2514/3.3549.

[31] Nicholas Trentacoste and Pasquale Sforza. "Further experimental results for threedimensional free jets". In: *AIAA Journal* 5.5 (1967), pp. 885–891. ISSN: 00011452. DOI: 10.2514/3.4096.

[32] Fazle Hussain and Hyder S Husain. "Elliptic jets. Part 1. Characteristics of unexcited and excited jets". In: *Journal of Fluid Mechanics* 208 (Nov. 1989), pp. 257–320. ISSN: 0022-1120. DOI: 10.1017/S0022112089002843. URL: https://www.cambridge.org/core/product/identifier/S0022112089002843/type/journal%7B%5C_%7Darticle.

[33] Hyder S. Husain and Fazle Hussain. "Elliptic jets. part 2. dynamics of coherent structures: Pairing". In: *Journal of Fluid Mechanics* 233.439 (1991), pp. 439–482. ISSN: 14697645. DOI: 10.1017/S0022112091000551.

[34] Chih-Ming Ho and Ephraim Gutmark. "Vortex induction and mass entrainment in a small-aspect-ratio elliptic jet". In: *Journal of Fluid Mechanics* 179 (June 1987), p. 383. ISSN: 0022-1120. DOI: 10.1017/S0022112087001587. URL: http://www.journals.cambridge.org/abstract%7B%5C_%7DS0022112087001587.

[35] Gong Yunyi, Liu Changwen, Huang Yezhou and Peng Zhijun. "An experimental study on droplet size characteristics and air entrainment of elliptic sprays". In: *SAE Technical Papers* 724 (1998). ISSN: 26883627. DOI: 10.4271/982546.

[36] Choong-won Lee et al. "Experimental study of the effects of nozzle hole geometry for a DI diesel engine". In: *ICLASS 2006*. Kyoto, 2006.

[37] Shenghao Yu et al. "Experimental study on the spray characteristics discharging from elliptical diesel nozzle at typical diesel engine conditions". In: *Fuel* 221.February (2018), pp. 28–34. ISSN: 00162361. DOI: 10.1016/j.fuel.2018.02.090.

[38] Jung Goo Hong, Kun Woo Ku, Sung Ryoul Kim and Choong Won Lee. "Effect of cavitation in circular nozzle and elliptical nozzles on the spray characteristic". In: *Atomization and Sprays* 20.10 (2010), pp. 877–886. ISSN: 10445110. DOI: 10.1615/AtomizSpr.v20.i10.40. URL: http://www.scopus.com/inward/record.url?eid=2-s2.0-79955791257&partnerID=tZOtx3y1.

[39] Kun Woo Ku, Jung Goo Hong and Choong Won Lee. "Effect of internal flow structure in circular and elliptical nozzles on spray characteristics". In: *Atomization and Sprays* 21.8 (2011), pp. 655–672. ISSN: 10445110. DOI: 10.1615/AtomizSpr.2012004192.

[40] Andreas Matsson and Sven Andersson. "The effect of non-circular nozzle holes on combustion and emission formation in a heavy duty diesel engine". In: *SAE Technical Papers* 724 (2002). ISSN: 26883627. DOI: 10.4271/2002-01-2671.

[41] S. Molina, F. J. Salvador, M. Carreres and D. Jaramillo. " A computational investigation on the influence of the use of elliptical orifices on the inner nozzle flow and cavitation development in diesel injector nozzles ". In: *Energy Conversion and Management* 79 (2014), pp. 114–127. ISSN: 01968904. DOI: 10.1016/j.enconman.2013.12.015. URL: http://dx.doi.org/10.1016/j.enconman.2013.12.015.

[42] Engine Combustion Department of Sandia National Laboratories. *Engine Combustion Network Data search*. URL: https://ecn.sandia.gov/ecn-data-search/.

[43] Adrián Pandal Blanco. " Implementation and Development of an Eulerian Spray Model for CFD simulations of diesel Sprays ". PhD thesis. Valencia (Spain): Universitat Politècnica de València, July 2016. DOI: 10.4995/Thesis/10251/68490. URL: https://riunet.upv.es/handle/10251/68490.

[44] Mamoru Ishii and Takashi Hibiki. "Thermo-fluid dynamics of two-phase flow". In: *Thermo-Fluid Dynamics of Two-Phase Flow* (2006), pp. 1–462. DOI: 10.1007/978-0-387-29187-1.

[45] Z. Bilicki and J. Kestin. "Physical Aspects of the Relaxation Model in Two-Phase Flow". In: *Proceedings of the Royal Society A: Mathematical, Physical and Engineering Sciences* 428.1875 (Apr. 1990), pp. 379–397. ISSN: 1364-5021. DOI: 10.1098/rspa.1990.0040. URL: http://dx.doi.org/10.1098/rspa.1990.0040%20http://rspa.royalsocietypublishing.org/cgi/doi/10.1098/rspa.1990.0040.

[46] B. Shields, K. Neroorkar and D.P. Schmidt. "Cavitation as Rapid Flash Boiling". In: ILASS-Americas 23rd Annual Conference on Liquid Atomization and Spray Systems. 2011.

[47] Zhixia He et al. "Investigations of effect of phase change mass transfer rate on cavitation process with homogeneous relaxation model". In: *International Communications in Heat and Mass Transfer* 89 (2017), pp. 98–107. ISSN: 0735-1933. DOI: https://doi.org/10.1016/j.icheatmasstransfer.2017.09.021.

[48] V. Macian, V. Bermudez, R. Payri and J. Gimeno. "New Technique for Determination of Internal Geometry of a Diesel Nozzle With the Use of Silicone Methodology". In: *Experimental Techniques* 27.2 (2003), pp. 39–43. ISSN: 0732-8818. DOI: 10.1111/j.1747-1567.2003.tb00107.x. URL: http://doi.wiley.com/10.1111/j.1747-1567.2003.tb00107.x.

[49] R. Payri, F. J. Salvador, M. Carreres and J. De La Morena. " Fuel temperature influence on the performance of a last generation common-rail diesel ballistic injector. Part II: 1D model development, validation and analysis ". In: *Energy Conversion and Management* 114.May (2016), pp. 376–391. ISSN: 01968904. DOI: 10.1016/j.enconman.2016.02.043.

[50] Francisco Javier Salvador, Joaquin De la Morena, Gabriela Bracho and David Jaramillo. "Computational investigation of diesel nozzle internal flow during the complete injection event". In: *Journal of the Brazilian Society of Mechanical Sciences and Engineering* 40.3 (2018). ISSN: 18063691. DOI: 10.1007/s40430-018-1074-z.

[51] R. Payri, F.J. Salvador, J. Gimeno and R. Novella. "Flow regime effects on non-cavitating injection nozzles over spray behavior". In: *International Journal of Heat and Fluid Flow* 32.1 (2011), pp. 273–284. ISSN: 0142-727X. DOI: https://doi.org/10.1016/j.ijheatfluidflow.2010.10.001. URL: https://www.sciencedirect.com/science/article/pii/S0142727X10001633.

[52] Francisco Javier Salvador, Marcos Carreres, Joaquin De la Morena and E Martínez-Miracle. " Computational assessment of temperature variations through calibrated orifices subjected to high pressure drops: Application to diesel injection nozzles ". In: *Energy Conversion and Management* 171 (Sept. 2018), pp. 438–451. ISSN: 01968904. DOI: 10.1016/j.enconman.2018.05.102. URL: https://linkinghub.elsevier.com/retrieve/pii/S0196890418305867.

[53] B. E. Launder and D. B. Spalding. "The numerical computation of turbulent flows". In: *Computer Methods in Applied Mechanics and Engineering* 3.2 (1974), pp. 269–289. ISSN: 00457825. DOI: 10.1016/0045-7825(74)90029-2. arXiv: 1204.1280v1.

[54] B.E. Launder and B.I. Sharma. "Application of the energy-dissipation model of turbulence to the calculation of flow near a spinning disc". In: *Letters in Heat and Mass Transfer* 1.2 (Nov. 1974), pp. 131–137.

ISSN: 00944548. DOI: 10.1016/0094-4548(74)90150-7. URL: https://linkinghub.elsevier.com/retrieve/pii/0094454874901507.

[55] David C.Wilcox. *Turbulence Modelling CFD Wilcox*. 1994, p. 460. ISBN: 0-9636051-0-0.

[56] Victor Yakhot and Leslie M. Smith. "The renormalization group, the eps-expansion and derivation of turbulence models". In: *Journal of Scientific Computing* 7.1 (1992), pp. 35–61. ISSN: 0885-7474. DOI: 10.1007/BF01060210.

[57] Sergio Hoyas et al. "Evaluation of the Eulerian-Lagrangian Spray Atomization (ELSA) model in spray simulations: 2D cases". In: *Mathematical and Computer Modelling* (2013). DOI: 10.1016/j.mcm.2011.11.006.

[58] J. Janicka and N. Peters. "Prediction of turbulent jet diffusion flame lift-off using a pdf transport equation". In: *Symposium (International) on Combustion* 19.1 (1982), pp. 367–374. ISSN: 00820784. DOI: 10.1016/S0082-0784(82)80208-7.

[59] B. B. Dally, D. F. Fletcher and A. R. Masri. "Flow and mixing fields of turbulent bluff-body jets and flames". In: *Combustion Theory and Modelling* 2.2 (1998), pp. 193–219. ISSN: 17413559. DOI: 10.1088/1364-7830/2/2/006.

[60] Jose Maria Garcia-Oliver et al. " Diesel Spray Cfd Simulations Based on the Σ-Υ Eulerian Atomization Model ". In: *Atomization and Sprays* 23.1 (2013), pp. 71–95. ISSN: 1044-5110. DOI: 10.1615/AtomizSpr.2013007198.

[61] S. B. Pope. "An explanation of the turbulent round-jet/plane-jet anomaly". In: *AIAA Journal* 16.3 (1978), pp. 279–281. ISSN: 00011452. DOI: 10.2514/3.7521.

[62] E W Bilicki, Salim Ali, Fluid Flow Machinery and Polish Academy. "Evaluation of the relaxation time of heat and mass exchange in the liquid-vapour bubble flow". In: 39.4 (1996).

[63] P. Downar-Zapolski, Z. Bilicki, L. Bolle and J. Franco. "The non-equilibrium relaxation model for one-dimensional flashing liquid flow". In: *International Journal of Multiphase Flow* 22.3 (1996), pp. 473–483. ISSN: 03019322. DOI: 10.1016/0301-9322(95)00078-X.

[64] David P. Schmidt, Christopher J. Rutland and M. L. Corradini. "A numerical study of cavitating flow through various nozzle shapes". In: *SAE Technical Papers* 412 (1997). ISSN: 26883627. DOI: 10.4271/971597.

[65] David P. Schmidt, Suresh Gopalakrishnan and H. Jasak. "Multi-dimensional simulation of thermal non-equilibrium channel flow". In: *International Journal of Multiphase Flow* 36.4 (Apr. 2010), pp. 284–292. ISSN: 03019322. DOI: 10.1016/j.ijmultiphaseflow.2009.11.012. URL: http://linkinghub.elsevier.com/retrieve/pii/S030193220900192X.

[66] Federico Brusiani et al. "Comparison of the Homogeneous Relaxation Model and a Rayleigh Plesset Cavitation Model in Predicting the Cavitating Flow Through Various Injector Hole Shapes". In: *SAE International* (2013). DOI: 10.4271/2013-01-1613. URL: http://papers.sae.org/2013-01-1613/.

[67] C. Arcoumanis, H. Flora, M. Gavaises and M. Badami. "Cavitation in Real-Size Multi-Hole Diesel Injector Nozzles". In: *SAE International* (Mar. 2000). ISSN: 0148-7191. DOI: https://doi.org/10.4271/2000-01-1249. URL: https://doi.org/10.4271/2000-01-1249.

[68] R. Payri, C. Guardiola, F.J. Salvador and J. Gimeno. "Critical Cavitation Number Determination in Diesel Injection Nozzles". In: *Experimental Techniques* 28.3 (2004), pp. 49–52. ISSN: 0732-8818. DOI: 10.1111/j.1747-1567.2004.tb00164.x. URL: http://doi.wiley.com/10.1111/j.1747-1567.2004.tb00164.x.

[69] R. Payri, J. M. García, F. J. Salvador and J. Gimeno. "Using spray momentum flux measurements to understand the influence of diesel nozzle geometry on spray characteristics". In: *Fuel* 84.5 (2005), pp. 551–561. ISSN: 00162361. DOI: 10.1016/j.fuel.2004.10.009.

[70] Celia Soteriou, Richard Andrews and Mark Smith. "Direct Injection Diesel Sprays and the Effect of Cavitation and Hydraulic Flip on Atomization". In: *SAE Technical Paper Series* 1.412 (2010). DOI: 10.4271/950080.

[71] Zuo Yu Sun et al. " Numerical investigation on effects of nozzle's geometric parameters on the flow and the cavitation characteristics within injector's nozzle for a high-pressure common-rail di diesel engine ". In: *Energy Conversion and Management* 89 (2015), pp. 843–861. ISSN: 01968904. DOI: 10.1016/j.enconman.2014.10.047. URL: http://dx.doi.org/10.1016/j.enconman.2014.10.047.

[72] Francisco Javier Salvador, Marcos Carreres, David Jaramillo and Jorge Martínez-lópez. "Analysis of the combined effect of hydrogrinding process and inclination angle on hydraulic performance of diesel injection nozzles". In: *Energy Conversion and Management* 105 (2015), pp. 1352–1365. ISSN: 0196-8904. DOI: 10.1016/j.enconman.2015.08.035.

[73] Francisco J. Salvador, Joaquin de la Morena, Marcos Carreres and David Jaramillo. "Numerical analysis of flow characteristics in diesel injector nozzles with convergent-divergent orifices". In: *Proceedings of the Institution of Mechanical Engineers, Part D: Journal of Automobile Engineering* 231.14 (2017), pp. 1935–1944. ISSN: 09544070. DOI: 10.1177/0954407017692220.

[74] J. Javier López, Oscar A. De La Garza, Joaquin De La Morena and S. Martínez-Martínez. "Effects of cavitation in common-rail diesel nozzles on the mixing process". In: *International Journal of Engine Research* 18.10 (2017), pp. 1017–1034. DOI: 10.1177/1468087417697759.

[75] Kelly Senecal et al. *Method and apparatus for automated grid formation in multi-cell system dynamics models*. 2011.

[76] J M Desantes, F J Salvador, M Carreres and D Jaramillo. " Experimental Characterization of the Thermodynamic Properties of Diesel Fuels Over a Wide Range of Pressures and Temperatures ". In: *SAE International Journal of Fuels and Lubricants* 8.1 (2015), pp. 951–2015. ISSN: 1946-3960. DOI: 10.4271/2015-01-0951. URL: http://papers.sae.org/2015-01-0951/.

[77] Nikolay Ivanov Kolev. "Thermodynamic and transport properties of diesel fuel". In: *Multiphase Flow Dynamics 4: Turbulence, Gas Adsorption and Release, Diesel Fuel Properties*. Berlin, Heidelberg: Springer Berlin Heidelberg, 2012, pp. 293–327. ISBN: 978-3-642-20749-5. DOI: 10.1007/978-3-642-20749-5_13. URL: https://doi.org/10.1007/978-3-642-20749-5_13.

[78] Jérôme Dechoz and Claude Rozé. "Surface tension measurement of fuels and alkanes at high pressure under different atmospheres". In: *Applied Surface Science* 229.1 (2004), pp. 175–182. ISSN: 0169-4332. DOI: https://doi.org/10.1016/j.apsusc.2004.01.057. URL: https://www.sciencedirect.com/science/article/pii/S016943320400090X.

[79] K.J. Richards, P.K. Senecal and E. Pomraning. "CONVERGE 2.4.*, Convergent Science, Madison, WI (2021)". In: ().

[80] Alan L Kastengren et al. "Engine Combustion Network (ECN): Measurements of Nozzle Geometry and Hydraulic Behavior". In: *Atomization and Sprays* 22.12 (2012), pp. 1011–1052. ISSN: 1044-5110. DOI: 10.1615/AtomizSpr.2013006309.

[81] R. Lebas et al. "Numerical simulation of primary break-up and atomization: DNS and modelling study". In: 35.3 (), pp. 247–260. ISSN: 03019322. DOI: 10.1016/j.ijmultiphaseflow.2008.11.005.

[82] Lyle M. Pickett et al. "Relationship Between Diesel Fuel Spray Vapor Penetration/Dispersion and Local Fuel Mixture Fraction". In: *SAE International Journal of Engines* 4.1 (2011), pp. 764–799. ISSN: 19463936. DOI: 10.4271/2011-01-0686.

[83] Lyle M. Pickett et al. "Transient rate of injection effects on spray development". In: *SAE Technical Papers* 6 (2013), pp. 15–16. DOI: 10.4271/2013-24-0001.

[84] Alan Kastengren, Christopher F. Powell, Zunping Liu and Jin Wang. "Time resolved, three dimensional mass distribution of diesel sprays measured with X-ray radiography". In: *SAE Technical Papers* (2009). ISSN: 26883627. DOI: 10.4271/2009-01-0840.

[85] A. L. Kastengren et al. "Time-resolved X-ray radiography of sprays from Engine Combustion Network spray a diesel injectors". In: *Atomization and Sprays* 24.3 (2014), pp. 251–272. ISSN: 10445110. DOI: 10.1615/AtomizSpr.2013008642.

[86] Daniel J. Duke et al. "X-ray radiography of cavitation in a beryllium alloy nozzle". In: *International Journal of Engine Research* 18.1-2 (2017), pp. 39–50. ISSN: 20413149. DOI: 10.1177/1468087416685965.

[87] Lyle M. Pickett, Julien Manin, Alan Kastengren and Christopher Powell. "Comparison of Near-Field Structure and Growth of a Diesel Spray Using Light-Based Optical Microscopy and X-Ray Radiography". In: *SAE International Journal of Engines* 7.2 (Apr. 2014), pp. 1044–1053. ISSN: 1946-3936. DOI: https://doi.org/10.4271/2014-01-1412. URL: https://doi.org/10.4271/2014-01-1412.

[88] Jose Maria Desantes et al. "Coupled/decoupled spray simulation comparison of the ECN spray a condition with the Σ-Y Eulerian atomization model". In: *International Journal of Multiphase Flow* 80 (2016), pp. 89–99. ISSN: 03019322. DOI: 10.1016/j.ijmultiphaseflow.2015.12.002.

[89] Jose Maria Desantes et al. "Modelling and validation of near-field Diesel spray CFD simulations based on the Σ -Y model". In: *ILASS 2017*. 2017. DOI: 10.4995/ILASS2017.2017.4715. URL: https://www.cmt.upv.es/ILASS2017/Default.aspx.

[90] G. N. Taub, Hyungoo Lee, S. Balachandar and S. A. Sherif. "A direct numerical simulation study of higher order statistics in a turbulent round jet". In: *Physics of Fluids* 25.11 (Nov. 2013), p. 115102. ISSN: 1070-6631. DOI: 10.1063/1.4829045. eprint: https://pubs.aip.org/aip/pof/article-pdf/doi/10.1063/1.4829045/13383171/115102_1_online.pdf. URL: https://doi.org/10.1063/1.4829045.

[91] Hussein J. Hussein, Steven P. Capp and William K. George. "Velocity measurements in a high Reynolds number, momentum conserving, axisymmetric, turbulent jet". In: *Journal of Fluid Mechanics* 258 (1994), pp. 31–75. DOI: 10.1017/S002211209400323X.

[92] F. J. Salvador, S. Hoyas, R. Novella and J. Martinez-Lopez. "Numerical simulation and extended validation of two-phase compressible flow in diesel injector nozzles". In: *Proceedings of the Institution of Mechanical Engineers, Part D: Journal of Automobile Engineering* 225.4 (2011), pp. 545–563. ISSN: 09544070. DOI: 10.1177/0954407OJAUTO1569.

[93] P J Roache. " Perspective: A Method for Uniform Reporting of Grid Refinement Studies ". In: *Journal of Fluids Engineering* 116.3 (1994), p. 405. ISSN: 00982202. DOI: 10.1115/1.2910291. URL: http://fluidsengineering.asmedigitalcollection.asme.org/article.aspx?articleid=1427780.

[94] Raúl Payri, Ricardo Novella, Marcos Carreres and Mario Belmar-Gil. "Study about the influence of an automatic meshing algorithm on numerical simulations of a gaseous-fueled Lean Direct Injection (LDI) gas turbine combustor in non-reactive conditions". In: 2019. URL: https://ilass19.sciencesconf.org/247299.

[95] H. Chaves et al. "Experimental study of cavitation in the nozzle hole of diesel injectors using transparent nozzles". In: *SAE Technical Papers* 412 (1995). ISSN: 2688-3627. DOI: 10.4271/950290.

[96] N. Tamaki, M. Shimizu and Hiroyuki Hiroyasu. "Enhancement of the atomization of a liquid jet by cavitation in a nozzle hole". In: *Atomization and Sprays* 11.2 (2001). ISSN: 1044-5110.

[97] F. Payri, V. Bermúdez, R. Payri and F. J. Salvador. "The influence of cavitation on the internal flow and the spray characteristics in diesel injection nozzles". In: *Fuel* 83.4-5 (2004), pp. 419–431. ISSN: 00162361. DOI: 10.1016/j.fuel.2003.09.010.

[98] Jeffrey Naber and L. Dennis. "Effects of Gas Density and Vaporization on Penetration and Dispersion of Diesel Sprays". In: (1996), p. 960034. ISSN: 0148-7191. DOI: 10.4271/960034. URL: http://papers.sae.org/960034/.

[99] S. A. MacGregor. "Air entrainment in spray jets". In: *International Journal of Heat and Fluid Flow* 12.3 (1991), pp. 279–283. ISSN: 0142727X. DOI: 10.1016/0142-727X(91)90064-3.

[100] L. Araneo, A. Coghe, G. Brunello and G. E. Cossali. "Experimental investigation of gas density effects on diesel spray penetration and entrainment". In: *SAE Technical Papers* 724 (1999). ISSN: 26883627. DOI: 10.4271/1999-01-0525.

[101] Jose Maria Desantes, Raul Payri, Francisco Javier Salvador and Jaime Gimeno. "Different Measurement Techniques To Determine Hole To Hole dispersion in a real diesel injector". In: *Proceedings of the FEDSM2006* February 2015 (2006), pp. 1–8. DOI: 10.1115/FEDSM2006-98212.

[102] A. Krothapalli, D. Baganoff and K. Karamcheti. "On the mixing of a rectangular jet". In: *Journal of Fluid Mechanics* 107 (1981), pp. 201–220. ISSN: 14697645. DOI: 10.1017/S0022112081001730.

[103] Jaime Gimeno, Gabriela Bracho, Pedro Martí-Aldaraví and Jesús E. Peraza. "Experimental study of the injection conditions influence over n-dodecane and diesel sprays with two ECN single-hole nozzles. Part I: Inert atmosphere". In: *Energy Conversion and Management* 126 (2016), pp. 1146–1156. ISSN: 01968904. DOI: 10.1016/j.enconman.2016.07.077. URL: http://dx.doi.org/10.1016/j.enconman.2016.07.077.

Capítulo 5

Influencia de la convergencia de la sección en toberas elípticas sobre la mezcla

"The engineer's first problem in any design situation is to discover what the problem really is.´´

Anonymous engineer

Resumen: Este capítulo describe la influencia de secciones convergentes y constantes sobre toberas de perfil elíptico. Los modelos previamente validados sobre toberas calibradas mono-orificio son aplicados posteriormente a toberas multi-orificio incluyendo en ambos casos los efectos de cavitación. Los resultados son analizados en términos de flujo interno y chorro.

Performance of elliptical nozzles on the spray dynamics of convergent and constant section nozzles by means of a $\Sigma - Y$ coupled model

Referencia: F.J. Salvador, J.M. Pastor, J. Gomez-Soriano, E. C. Martínez-Miracle, Performance of elliptical nozzles on the spray dynamics of convergent and constant section nozzles by means of a Σ-Y coupled model, Fuel, Volume 346, 2023, 128259, ISSN 0016-2361, https://doi.org/10.1016/j.fuel.2023.128259.

Abstract: *In this paper, a computational study on the differences between a convergent and a constant section elliptical nozzle is performed. Coupled internal-external flow simulations were carried out by means of a Σ-Y model experimentally validated. The differences reported in terms of internal flow and spray parameters present the cavitation as an important effect in the elliptical nozzle geometries. The conclusions suggest a mixture improvement potential for the cavitating elliptical nozzles.*

5.1. Introduction

In the past few years, the growing impact of fossil fuels over the environment and society has led to the adoption of a lot of different measures from governments. The increasing electrification of the automobile segment combines with other solutions like hybridization, fuel cells, hydrogen direct combustion or e-fuels. The combination of internal combustion engines and other propulsion systems seems to be a realistic picture of the future power-plant. Emissions of an internal combustion engine are generated in the combustion process, the later residual gasses and particles are conducted through a post-treatment system and finally released with a suitable concentration. However, the efficiency of combustion highly affects the quantity of those emissions, a complete combustion, a minimum use of fuel and restrained heat-losses through the cylinder among other issues conform a quite complex objective. For the design of modern power plants, a combination of experimental and computational techniques is applied to optimize the whole process from the piston bowl geometry to the spray characteristics. From this point of

view and since experimental access inside the engine is most of the time prohibitive, Computational Fluid Dynamics (CFD) techniques have shown their great potential to help improving those processes. From the extensive work of Hiroyasu et al. [1, 2] and Naber et al. [3] on the spray analysis, the penetration, angle and other structures were linked to the chamber conditions. Here, the atomization capacity of the injection system in order to spread the fuel across the chamber the more uniform and faster as possible was found to be critical. A step forward was made by some other authors like Payri et al. [4–6] and Salvador et al. [7, 8] where the internal geometry of the injector was experimental and computationally studied to clarify if the characteristics of the nozzle affect the spray characteristics. Common computational models for studying the atomization and combustion make use of a Droplet Discrete phase Modeling (DDM) that requires the calibration of several mathematical constants with some experimental and previously available data. There is no input information from the nozzle geometry and the predictive capacities of the model are limited. More recently, researchers have successfully coupled the internal and external flow using Eulerian models [9–13] and in depth demonstrated the correlation between nozzle and spray performance. The improvement of the nozzle geometry with the help of CFD techniques has become an interesting point of study. Salvador et al. [14] exposed the potential of innovative convergent-divergent nozzles where cavitation played an important role to enhance atomization. Molina et al. [15] explored the elliptic shape in orifices also from the internal flow perspective. They concluded that the horizontal-oriented elliptical nozzles could have better performance than cylindrical ones. Ku et al. [16] and Hong et al. [17] corroborate this conclusions through transparent nozzles showing that the cavitanting elliptical nozzles have better atomization. Lee et al. [18] also studied the influence of elliptical shapes on the spray penetration and angle using scaled orifices. Their results were also in consonance, elliptical nozzles can increase the spray angle leading to a jet with bigger air entrainment [19–21]. More recently, Yu et al. [22] investigated on the effect of elliptical orifices under several injection and chamber pressures including the axis-switching effect for explaining the air-entrainment ratio increment. Salvador et al. [23] coupled the internal and external flow for several cavitating nozzles with different eccentricities and explored the direct effect of the elliptical shape over the spray. Jia et al. [24] used a one-way coupled method to firstly calculate the internal flow and then used a mass flow input to generate a DDM simulation for circular and elliptical nozzles. The elliptical nozzles showed a slower tip penetration while producing a wider spray. The present study represents a step forward on this investigation by analyzing the potential of a cavitating nozzle with constant elliptical cross-section versus a convergent elliptical non-cavitating nozzle. The influence of the higher momentum flux and velocity of the convergent nozzle will be put in contrast to the higher turbulence induced by cavitation. The problem will be faced by means of a full coupled model widely validated through a

reference nozzle. This study will be carried through a first model description section, a second section for validating the CFD approach, a third section describing the results and a final part for drawing the conclusions.

5.2. Model description

The model employed for all simulations was the $\Sigma - Y$ [25] atomization model implemented in the software CONVERGE. This approach considers that the two-phase flow can be modelled as a pseudo-fluid sharing the same velocity field [26]. The model relies on the assumption that the injected turbulent flow develops in the high Reynolds and Weber number conditions, and then, it is possible to separate the large-scale processes, such as liquid dispersion, from the atomization process at smaller scales of turbulence. The proposed Eulerian framework approach is more suitable for near-field atomization, and naturally accounts for nozzle flow effects. The extent of the atomization process is computed from an interface surface density equation, Σ, and then it is not required to presume any particular shape for liquid fragments. The mass dispersion is obtained by Equation 5.1 with the mass fraction, Y, on its Favre averaged form where $\tilde{Y} = \frac{\overline{\rho Y}}{\bar{\rho}}$,

$$\frac{\partial \bar{\rho}\tilde{Y_m}}{\partial t} + \frac{\partial \bar{\rho}\tilde{u_i}\tilde{Y_m}}{\partial x_i} = \frac{\partial}{\partial x_i}\left(\bar{\rho}D\frac{\partial \tilde{Y_m}}{\partial x_i}\right) + S_m \quad m = 1, ..., n \tag{5.1}$$

Here, the m subscript defines a certain specie and n is the total number of them. ρ is the mixture density, D is a diffusion coefficient and S_m is a source term. From now on and for simplicity, the Favre notation will be omitted. The pseudo-fluid is considered as a mixture of species where the relation between the liquid and gaseous phases is

$$\tilde{Y_l} = 1 - \sum_{m=1}^{n_g} \tilde{Y_m} \tag{5.2}$$

In this approach, all gaseous phases are treated as ideal gases

$$\rho_g = \frac{p}{R_g T} \tag{5.3}$$

and the equation of state for the liquid phase depends on both pressure and temperature. The employed characteristics of the fuel have been implemented in a tabulated form following the results of [23, 27, 28].

$$\rho_l = f(p, T) \tag{5.4}$$

where the gaseous phase is considered as ideal for simplicity. The void fraction is then calculated as

$$\alpha = \frac{\frac{m_g}{\rho_g}}{\frac{m_g}{\rho_g} + \frac{m_l}{\rho_l}} \tag{5.5}$$

being m_g and m_l the mass of gas and liquid respectively. The variable Σ is defined as the surface area density of the liquid phase or the ratio of liquid surface per unit of volume. The initial model was proposed by Vallet et al. [29], where the idea of a Lagrangian particle tracking approach is substituted by a Eulerian calculation of the liquid-gas interfacial surface area. The small scales of the atomization are represented by the transport equation of the Σ scalar and defined as follows

$$\frac{\partial \Sigma}{\partial t} + \frac{\partial u_i}{\partial x_i} - \frac{\partial}{\partial x_i}\left(D_\Sigma \frac{\Sigma}{\partial x_i}\right) - C_\Sigma \Sigma \left(1 - \frac{\Sigma}{\Sigma_{eq}}\right) - S_{\Sigma_{evap}} - S_{\Sigma_{init}} = 0, \quad (5.6)$$

The diffusion coefficient D_Σ is calculated through the kinematic viscosity, ν, and the Schmidt number, Sc_Σ:

$$D_\Sigma = \frac{\nu}{Sc_\Sigma}. \quad (5.7)$$

The Σ value for the radius of a droplet in equilibrium , Σ_{eq}, is reached set as

$$\Sigma_{eq} = \frac{3\rho\Upsilon}{\rho_l r_{eq}}. \quad (5.8)$$

where Υ is the liquid volume fraction and r_{eq} is the equilibrium radius of the droplet [25]

$$r_{eq} = \alpha_2 \frac{\sigma^{3/5}}{\varepsilon^{2/3}} \frac{(\rho\Upsilon)^{2/15}}{\rho_l^{11/15}}. \quad (5.9)$$

In the expression above, α_2 is a model constant. For Equation 5.6 C_Σ scales to the inverse of the turbulent time scale:

$$C_\Sigma = \alpha_1 \frac{\varepsilon}{k}. \quad (5.10)$$

$S_{\Sigma_{evap}}$ is the evaporation source term:

$$S_{\Sigma_{evap}} = \frac{2\Sigma}{3\gamma} S_{evap}. \quad (5.11)$$

$S_{\Sigma_{init}}$, last term within equation 5.6, accounts for the first initialization of the interface area density [30] magnitude.

$$S_{\Sigma_{init}} = \frac{\Sigma_{min} - \Sigma}{\Delta t} pos(\Sigma_{min} - \Sigma). \quad (5.12)$$

where

$$pos(\Sigma_{min} - \Sigma) = \begin{cases} 1 & \text{if } \Sigma_{min} - \Sigma > 0 \\ 0 & \text{if } \Sigma_{min} - \Sigma \leq 0 \end{cases} \quad (5.13)$$

and

$$\Sigma_{min} = \sqrt{\alpha(1-\alpha)} V^{-1/3} \quad (5.14)$$

Although α_1 and α_2 can be subjected to calibration [31], in this study they are set to 1. Further model description can be found in [25, 32, 33]. The momentum and energy transport equation solved by the model are shown below.

$$\frac{\partial \rho u_i}{\partial t} + \frac{\rho u_i u_j}{\partial x_j} = -\frac{\partial P}{\partial x_i} + \frac{\partial \sigma_{ij}}{\partial x_j} \tag{5.15}$$

being σ_{ij} the viscous stress tensor modeled as :

$$\sigma_{ij} = \mu \left(\frac{\partial u_i}{\partial x_j} + \frac{\partial u_j}{\partial x_i} \right) - \frac{2}{3} \mu \frac{\partial u_k}{\partial x_k} \delta_{ij}. \tag{5.16}$$

In the viscous stress tensor equation (eq: 5.16), the viscosity is calculated according the combination of the molecular viscosity, μ, and the turbulent viscosity, μ_t, being this one a function of the turbulent kinetic energy (k) and its dissipation rate (ϵ),

$$\mu_{total} = \mu_{molecular} + \mu_t = \mu_{molecular} + C_\mu \rho \frac{k^2}{\varepsilon} \tag{5.17}$$

The energy equation is solved as

$$\frac{\partial \rho e}{\partial t} + \frac{\partial u_j \rho e}{\partial x_j} = -P \frac{\partial u_j}{\partial x_j} + \sigma_{ij} \frac{\partial u_i}{\partial x_j} + \frac{\partial}{\partial x_j} \left(K_t \frac{\partial T}{\partial x_j} \right) + \frac{\partial}{\partial x_j} \left(\rho D_t \sum_m h_m \frac{\partial \mathrm{Y}_m}{\partial x_j} \right), \tag{5.18}$$

here, e is the specific internal energy, K is the thermal conductivity, h_m is the enthalpy of each specie, σ_{ij} is the stress tensor and T stands for the temperature. The thermal conductivity for a turbulent problem is approached by

$$K = K_{molecular} + K_t = K_{molecular} + C_p \frac{\mu_t}{Pr_t} \tag{5.19}$$

For model closure, a two equation $k - \epsilon$ model has been selected, described by the following equations:

$$\frac{\rho k}{\partial t} + \frac{\partial \rho u_i k}{\partial x_i} = \tau_{ij} \frac{\partial u_i}{\partial x_j} + \frac{\partial}{\partial x_j} \frac{\mu + \mu_t}{Pr_k} \frac{\partial k}{\partial x_j} - \rho \epsilon. \tag{5.20}$$

and

$$\frac{\rho \epsilon}{\partial t} + \frac{\partial \rho u_i \epsilon}{\partial x_i} = \frac{\partial}{\partial x_j} \frac{\mu + \mu_t}{Pr_\epsilon} \frac{\partial \epsilon}{\partial x_j} + C_{\epsilon 3} \rho \epsilon \frac{\partial u_i}{\partial x_i} + \left(C_{\epsilon 1} \frac{\partial u_i}{\partial x_j} \tau_{ij} - C_{\epsilon 2} \rho \epsilon \right) \frac{\epsilon}{k}. \tag{5.21}$$

Constants $C_{\epsilon 1}$, $C_{\epsilon 2}$ and $C_{\epsilon 3}$ are empirical values needed for the model.

Description of the HRM cavitation model

The cavitation is modeled according to a homogeneous relaxation model (HRM) [34, 35]. The evaporation is represented by a simply lineal approach where S_m in equation 5.1 is estimated by the transfer rate:

$$\frac{DY}{Dt} = \frac{\bar{Y} - Y}{\theta} \tag{5.22}$$

being Y the liquid mass fraction in a specific instant, $\bar{Y}$ the equilibrium mass fraction and θ_0 a relaxation time scale. This local time scale is calculated for evaporation as a monotonically decreasing function

$$\theta_E = \theta_0 \alpha^{-0.54} \varphi^{-1.76} \tag{5.23}$$

where α is the void fraction and φ the non-dimensional local pressure ratio

$$\varphi = \frac{P_{sat} - P}{P_c - P_{sat}} \tag{5.24}$$

θ_0 takes the value of $3.84e^{-7}$ s [36]. In the same way than evaporation, for condensation it is found

$$\theta_C = F\theta_0 \alpha^{-0.54} \varphi^{-1.76} \tag{5.25}$$

here, F is a time scale factor with a value of 5000 [37] meaning that the condensation process is 5000 times slower that the evaporation process.

5.3. Validation of the model

A extensive validation of the model has been done over two reference nozzles being the Spray A and Spray C of the Engine Combustion Network (ECN) [38]. The Spray A consist of a convergent 90 µm non-cavitating nozzle with a high k-factor, on the other hand, Spray C is a constant section 200 µm cavitating nozzle with a 0 k-factor value. The k-factor is a standard conicity measurement given by the difference between the entry and outlet diameters in the nozzle throat divided by 10,

$$\text{k-factor} = \frac{\phi_f - \phi_0}{10} \tag{5.26}$$

The point of study corresponds to the standard inert and non-evaporative conditions of the ECN, using nitrogen as ambient gas. Table 5.1 summarizes the configuration of experimental and simulated points. The turbulent inlet intensity was defined in a 5% and the length scale of the turbulent dissipation as a 10% of the nozzle diameters . Turbulent kinetic energy and its dissipation rate were initialized to 1 m^2/s^2 and 10 m^2/s^3 respectively. The nozzle was

Nozzle nominal parameters		
Reference nozzles	**Spray A**	**Spray C**
Fuel	Dodecane	
Outlet diameter	90 μm	200 μm
K-factor	2.5	0
Nozzle length	1 mm	1 mm
Injection pressure	150 MPa	150 MPa
Back Pressure	2 MPa	2 MPa
Chamber temperature	303 K	303 K
Fuel temperature	363 K	363 K
Injector temperature	343 K	343 K

Table 5.1: Simulation conditions and parameters.

fully initialized with Y=1 and Σ is set to zero across all the domain except for the initial interphase between the nozzle and the chamber where it varies accordingly.

The mesh and CFD configuration were first applied to the Spray A case and then scaled to the other cases. In all cases the meshes were proved to provide proper solutions in terms of convergence and consistency thanks to a convergence mesh study. In this way, several geometries under similar flow conditions can be fairly compared. The general configuration consists of a cartesian grid with a specific base size. In order to refine a specific zone, a geometrical form (embbeding), is created. For this cartesian mesh, the size of the smaller elements evolves according to the power of two (octree-mesh) as in,

$$cell\,size = \frac{base\,size}{2^n} \tag{5.27}$$

Each refinement level is then determined by the level, , set in the previous expression. After the initial Spray A mesh configuration, cell size for rest of the cases was scaled using the geometrical diameter. Mesh embedding sizes were scaled using the equivalent diameter, ϕ_{eq}, where

$$\phi_{eq} = \phi_{geom}\sqrt{\frac{\rho_f}{\rho_{chamber}}} \tag{5.28}$$

Given that the base size is scaled for Spray C taking spray A as the reference, the element sizes varies from one nozzle to another. However, the grid levels shown in Table 5.2 are constant for all simulated cases. For both internal and external flow, a mesh independence study was carried out in terms of mass flow, penetration and angle. Starting from literature data [10, 39], the base size was progressively increased trying to find an acceptable trade-off between data reliability and computational cost. A base size of 384 µm (850 µm for

Spray C after the scaling), with the refinements shown in Table 5.2, was found to ensure convergent results for both the internal and the spray flow. An adaptive mesh refinement routine (AMR) is also activated depending on the velocity gradients. An example of the mesh setup applied to Spray C is represented in Figure 5.1.

Mesh refinement, levels (n) and sizes				
Region	n	Spray A [μm]	Spray C [μm]	Elliptical [μm]
Injector	3	48	106.3	98.8*
Injector AMR	5	12	26.6	24.7
Nozzle	6	6	13.3	12.3*
Near 1 mm spray zone	6	6	13.3	12.3
Spray up to 6 mm	5	12	26.6	24.7
Spray 1 mm transition to base size	3	48	106.3	98.8
Spray AMR based on velocity	4	24	53.1	49.4

Table 5.2: Mesh configuration. $b_{size}(SprayA)$: $384\mu m$, $b_{size}(SprayC)$: $850\mu m$, $b_{size}(Elliptical)$: $790\mu m$. *See modifications in elliptical nozzles section.

Steady state internal flow CFD results for Spray A and Spray C using the configuration already explained are collected and compared in Table 5.3 with its experimental steady state [31, 40]. Both convergent and constant section nozzles offer a good agreement between simulations and experiments. CFD values of the internal flow were computed at the outlet section of the nozzle. Spray A shows a mass flow difference of $0.01\,\mathrm{g\,s^{-1}}$ which results in a relative error of -0.38%. In terms of momentum flux, the difference is quite similar with a relative error of -1.97%. Effective velocity is also in agreement with previous magnitudes showing a relative error of -1.86%. Dimensionless coefficients of the nozzles reproduce the previous behavior with minimum deviation of the experimental results. The discharge coefficient expressed as the ratio between the computed mass flow and the maximum theoretical one,

$$C_d = \frac{\dot{m}_f}{\dot{m}_{theo}} = \frac{\dot{m}_f}{A_o\sqrt{2\rho_f \Delta p}}, \tag{5.29}$$

is slightly under the experimental one (-3.33%) since the simulated mass flow is smaller. On the other hand, the velocity coefficient

$$C_v = \frac{u_{eff}}{u_{theo}} \tag{5.30}$$

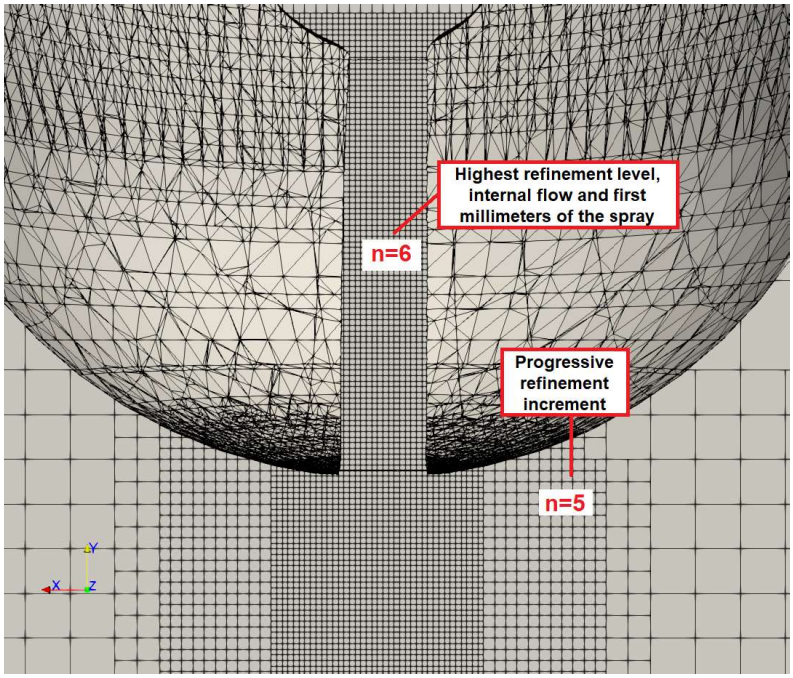

Figure 5.1: Spray C mesh configuration with main internal flow and first millimeters n levels of refinement.

returns the same value. The difference in the discharge coefficient is then balanced by the area coefficient which is reduced (-4%) for the CFD simulation since

$$C_d = C_a \mathring{u} C_v \tag{5.31}$$

The hydraulic characterization of the Spray C shows a similar behavior with a small error in mass flow, momentum, effective velocity and rest of hydraulic coefficients. In this case, the mass flow increases its relative error up to -6.48%, however, the absolute deviation of $0.7\,\mathrm{g\,s^{-1}}$ can be considered within a normal range taking into account the cavitating phenomena [7]. This issue also applies to a momentum value close to the empirical one, the data generates a -5.3% relative error. On the other hand, the effective velocity is very well reproduced by a -0.34% error. With the same effective velocity and a minor mass flow and momentum, the computational discharge coefficient is again under the experimental one (-1.54%). The difference between velocity coefficients is negligible and the effective area and so the area coefficient are responsible for the divergence in the discharge coefficient.

It has to be noticed that results of both simulations and experiments are sensitive to the differences and uncertainties between 3D geometries and their real geometries. For Spray A, the nominal diameter is reduced up to 89 µm for both 3D and real nozzle and, for Spray C, the deviation is more noticeable being 208 µm in the computational case and 212 µm for the experimental one.

Nozzle	Spray A		Spray C	
	CFD	EXP	CFD	EXP
$\dot{m}_f[g/s]$	2.56	2.57	10.1	10.72
$M_f[N]$	1.49	1.52	5.53	5.89
$V_{eff}[m/s]$	582	593	548	549.89
Cd	0.87	0.9	0.64	0.65
Ca	0.94	0.98	0.74	0.75
Cv	0.92	0.92	0.87	0.87

Table 5.3: Hydraulic results for validation nozzles, Spray A and Spray C.

On the simulation side, a certain over-prediction of the mass transfer process from the liquid to the vapor phase can increase the velocity coefficient due to a reduction of the friction effect. The vapor phase acts as a isolating layer with small viscosity located between the liquid phase and the nozzle wall. The effective area and the mass flow also decrease because of the greater amount of the vapor fraction. Nevertheless, the CFD code can predict with small errors the hydraulic behavior of both nozzles cavitating and non-cavitating one. At this point, the authors want to highlight that there are other turbulence approaches whose formulation is more suitable for fluids where cavitation, detached flow and re-circulation zones have an important role. The RNG $k-\epsilon$ [41] or the SST $k-\omega$SST [42] are some of these examples. However, the behavior of such models seems to not provide a good performance in terms of spray simulations for locations far from the nozzle [31]. Also, the deployment of distinct models for each nozzle would have included some unwanted uncertainty hindering a fair comparison. In general, related literature uses the $k-\epsilon$ equations with the rounding jet correction $C_{\epsilon 1} = 1.6$ as the standard base model [31, 43].

A priori, the visual comparison of the CFD flow and the experimental one [44] in Figure 5.2 would suggest that a good approach is reached for the internal flow. Cavitation starts at the inlet section of the nozzle, vapor phase is represented by a white zone in the experimental view (Figure 5.2a and 5.2c) and by a red to green color gradient standing for the void fraction in the computational slices of Figure 5.2b and 5.2d. The cavitation occurs in the sharpest edge zone of the inlet rounding radius and spreads close to the wall. The maximum intensity is generated in the middle of this zone, represented for the XY plane section view, and decreases as the inlet rounding radius becomes more soft along the inlet perimeter of the nozzle. This fact can be seen from the thickness comparison between the vapor film in the XY plane and ZY plane section of Figure 5.2 [45].

The internal flow directly affects the first millimeters of the atomization process, as the computational model showed before, the nozzle geometry pro-

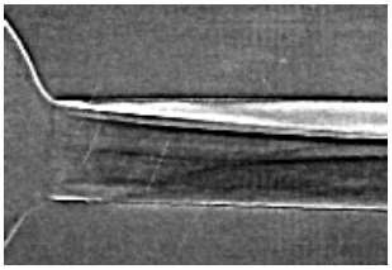

(a) Spray C experimental internal view, XY plane or plane of cavitation symmetry.

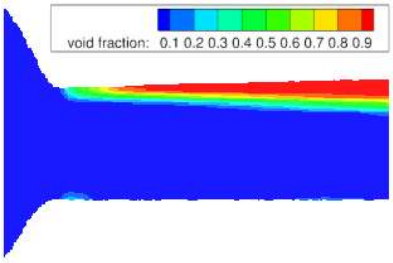

(b) Spray C CFD void fraction slice, XY plane or plane of cavitation symmetry.

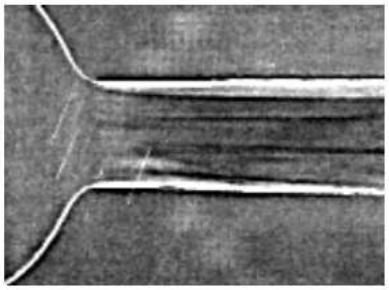

(c) Spray C experimental internal view, ZY plane or plane of non-symmetric cavitation.

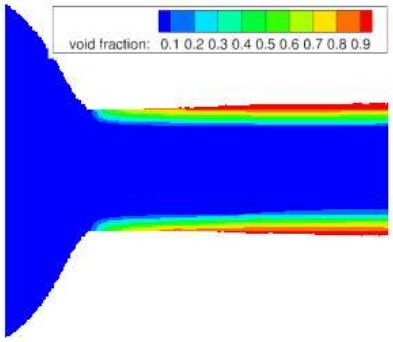

(d) Spray C CFD void fraction slice, ZY plane or plane of non-symmetric cavitation.

Figure 5.2: Visual comparison of computational void fraction slices and experimental x-ray views of the internal flow [45] for the XY and ZY plane of the Spray C nozzle.

duces very different velocity gradients and turbulence. However, this comparison often only relies on macroscopic magnitudes of the flow, such as mass flow rates, discharge coefficients or momentum measurements. The microscopic study of the fluid could be done in a qualitative way like has been done above, comparing computational results with experimental views in Figure 5.2. In general, this is because the access to the nozzle internal morphology is limited by the available technical resources. Nevertheless, in this case it is possible to quantitatively validate the internal flow by looking at the first millimeters of the jet, close to the nozzle orifice. This further comparison has been done employing the data available in [44]. By means of an x-ray beam it is possible to study the core of the spray in the middle of a injection event [46–48]. The variable of study, the projected mass density at 2 mm is shown for the symmetry plane of cavitation and the frontal view in pictures 5.3a and 5.3b respectively. It can be seen how CFD curves (continuous line) follow the experimental trends (dash line) and are properly reproduced. A lower projec-

ted density is found in the positive section of the jet due to the lower liquid phase fraction in that zone, the maximum experimental value peak is close to the computational one and the lateral slopes of the quasi-gaussian functions are almost overlapped. In the second projection view, the two characteristic hills are also captured, the curve peak within the positive section of the graph is over the x-ray measurement, the peak value in the negative zone of the horizontal axis is well reproduced. The valley of the projected mass of Figure 5.3b is generated by the inheritance of the biggest vapor fraction zone over the center of the spray making the fluid density decrease. More quantitatively, the accumulated point to point error of the difference between experimental and computational curves gives an 8% for the 5.3a projection and a 6.9% for the second 5.3b projection. The Spray A was also analysed in terms of projected mass density in a previous authors work [23], results are not replicated here for simplicity purposes.

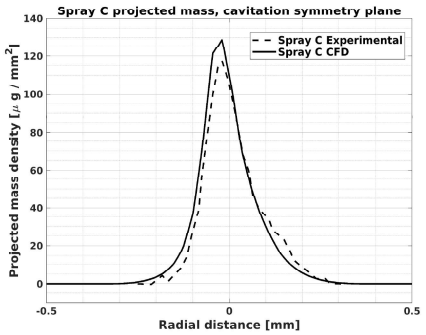

(a) Spray C projected mass density, view perpendicular to the symmetry plane of cavitation (XY).

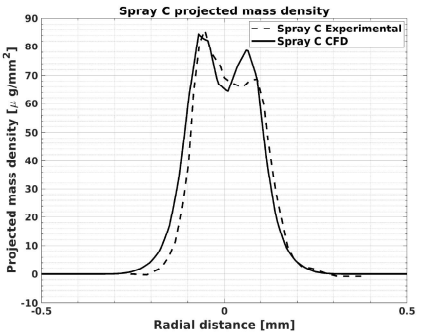

(b) Spray C projected mass density, view perpendicular to the non-symmetric plane of cavitation (ZY).

Figure 5.3: Projected mass density at 2 mm of the nozzle outlet, Spray C. This study versus experimental [44].

It has to be noticed that this error, even though it can be useful to numerically quantify the deviation of the projected mass, is dependent on the relative coordinates between the computational and experimental spray, which can slightly vary. The good behavior of projected mass density variable that directly depends on the previous internal flow, can be considered as a proof of the validation of the near nozzle spray zone and so, of the primary atomization process. In summary, the analysis of the internal flow in the most complex nozzle, the Spray C, yields to a solid validation of the hydraulic response of the nozzle and the first millimeters of the spray. After the validation of the internal flow, the spray dispersion along the chamber is explored in terms of spray tip penetration and cone angle. The needle of both nozzles includes a lift law according to the experimental data base available in [38, 44, 45]

for the specific working condition (Table 5.1). The possible wobble effect has been neglected for simplification. The evolution of the injection event only embraces the aperture and the steady state up to 1 ms in order to validate the initial penetration slope and the main spray angle for both nozzles. Other aspects such as closing needle events or higher detailed analysis of the initial transient lift are beyond the scope of this paper, however, they will be taken into account in future works. Penetration curves for both cases can be seen in Figure 5.4. The needle lift movement is able to reproduce the slope penetration, the higher error is produced in the first millimeters of penetration where the relative difference between experimental and CFD curves is larger. However, as the fluid penetrates into the chamber, the relative point to point error rapidly decreases. The spray penetration and resulting angle of Spray

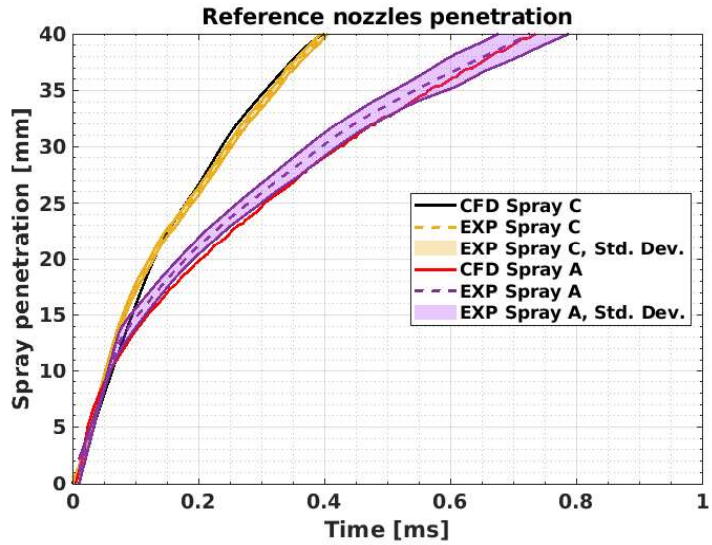

Figure 5.4: Spray A and Spray C penetration curves .

C were measured at the CMT-Motores Térmicos Research Institute by means of a Diffuse Backlight Illumination (DBI) technique. With this method, the spray plume is illuminated from behind with a uniform diffuse light. The shape of the shadow of the spray is then captured with a high speed camera and post-processed. An example of the technique is depicted in Figure 5.5, here the angle is calculated taking the 60% of the spray contour penetration starting from the injector. Two lines are then forced to fit the upper and lower part of the contour plume. The experimental fit lines of the DBI contour are compared with their equivalents for the projection of a 99% of the mass of the CFD simulation. It provides a temporal evolution of the angle as can be seen in Figure 5.6. This figure denotes the ability of the model to reproduce not only penetration but also the radial dispersion of the fuel across the chamber for a complex nozzle (Spray C). The measurement of the spreading angle

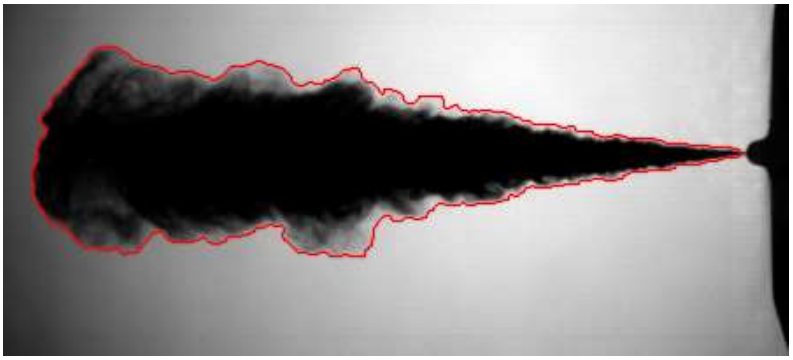

Figure 5.5: Spray C, DBI visualization and shape capture.

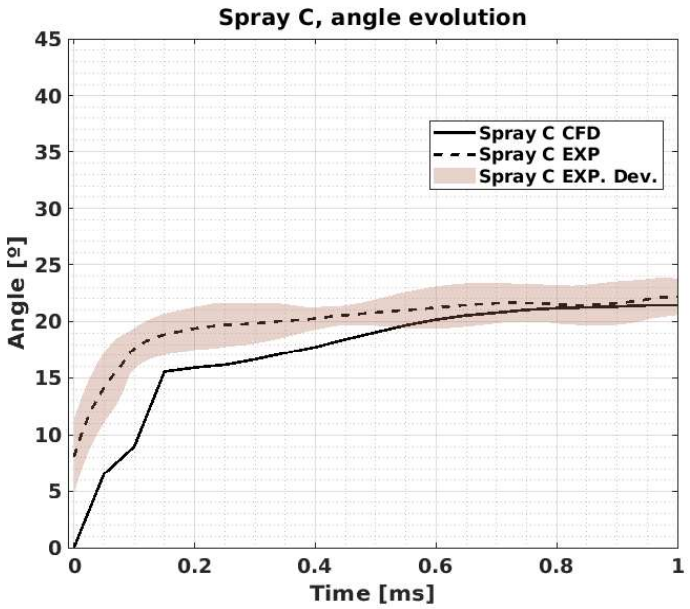

Figure 5.6: Spray C experimental vs. computational angle comparison, temporal evolution.

commonly carries a larger uncertainty than penetration, specially at the first moments of the injection where the behavior is less repetitive. Although at first milliseconds the computational angle falls below the experimental one, the mean value is reached fast with a minimum steady state error. The Spray A angle also returns a similar behavior with the same computational methodology as explained in [23]. Although a sensitivity study of the simulations to the initial experimental conditions has not been performed yet, the reported deviation of the experimental pressure is small (10 bar), so no major changes would be expected. According to the presented data, it can be said that this model is suitable to be applied to new exploratory studies such as the one

presented below.

5.4. Application to elliptical nozzles

Setup

The previous section of the current study has demonstrated the capability of the $\Sigma - Y$ model of being applied in two completely different nozzles. Starting from a validated model, in this section, this study tries to understand the effect of an elliptical shaped orifice applied to a high convergent (and so non-cavitating) and to a constant section nozzle (and so with high level of cavitation), employing coupled internal-external simulations. The geometrical characteristics of the nozzles selected for this analysis are summarized in Table 5.4, whereas Figure 5.7 displays the geometrical parameters and boundaries of the 3D domain. An eccentricity of 0.90 has been applied to a 170 µm five circular orifice nozzle that serves as base for the geometry. Both eccentric nozzles share the same geometrical area at the outlet, equivalent to a circular orifice of 170 µm. The convergent nozzle introduces a rounding radius, R_r, of 30 µm and a final area reduction (AR) of a 30 %. In the constant section nozzle (cavitating), the rounding radius has been replaced by a small chamfer entrance and there is no area reduction along the throat. As mentioned, both orifices have an eccentricity, e, of 0.90 at the outlet and the major diameter, ϕ_h, is perpendicular to the injector axis. This orientation (see Figure 5.8) was selected taking into account recommendations from literature. Molina et al. [15] found that the greater benefits of the elliptical shape are achieved in the mentioned orientation, for which the effect of cavitation is reinforced. The

Parameter	**Convergent**	**Constant section**
ϕ_{minor} $[\mu m]$	110	110
ϕ_{major} $[\mu m]$	263	263
e	0.9	0.9
AR [%]	30	0
R_r $[\mu m]$	30	0
L/D	5.6	5.6

Table 5.4: Geometrical parameters for the convergent and the constant section elliptical nozzles.

nozzle orifice ends onto a cylindrical chamber whose domain extends up to 35 mm long and 30 mm width. The mesh configuration follows the methodology explained in the previous section. Cell base size has been scaled using the mean geometrical diameter of the ellipse ($\phi_{mean} =$ 186 µm) giving a value of 790 μm. However, this reduces the relative resolution since the proximity

between the different points that form the elliptical shape are not the same, the number of cells along the minor diameter of the ellipse decreases. Each refinement level was kept the same as for Table 5.2 with the additional level of 7 and 3 layers in the nozzle wall to counter this higher proximity in the ellipse minor axis. The resolution inside the sac and needle has also to be increased because of the dimensional relation between the sac volume and number of orifices. The AMR level of refinement in the needle and sac zone was substituted for a permanent refinement of level 6, leading to the same cell size as for the Spray A inside the body injector. Representation of the mesh configuration can be appreciated in Figure 5.8.

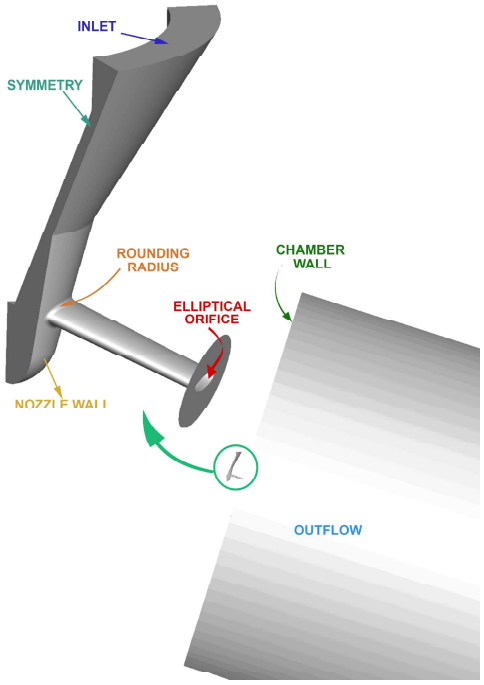

Figure 5.7: 3D Domain of the elliptical nozzles.

Results

A hydraulic characterization of both nozzles was performed. A comparison between both geometries in terms of mass flow rate, momentum, and dimensionless coefficients has been done in order to study the internal flow. No needle lift law motion has been defined for these simulations, the needle lift is positioned at 170 µm of its seat for the whole simulation. Simulated conditions are summarized in Table 5.5.

The chosen fluid for this simulation has been deeply described in previous studies [27, 28], it consists of a commercial diesel fuel which properties density, viscosity, enthalpy, etc. were experimentally characterized and have been

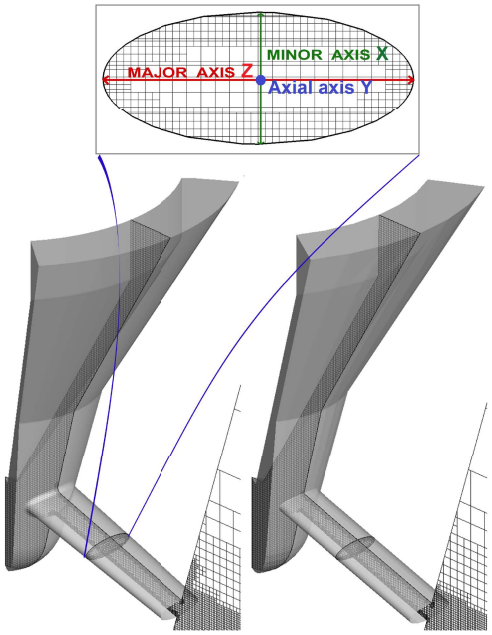

Figure 5.8: Geometry and mesh configuration for convergent (left) and constant section (right) elliptical nozzles, with axis nomenclature.

Condition	**Value**
$\boldsymbol{P_{inj}[MPa]}$	200
$\boldsymbol{P_{back}[MPa]}$	3
Chamber temperature $[K]$	303
Fuel temperature $[K]$	363
Fuel	Diesel

Table 5.5: Simulated conditions for the eccentrical nozzles.

implemented in the software. Vapor phase properties have been approached by tetradecane. The internal flow results are shown in Table 5.6.

As expected for a same outlet area, the constant section nozzle provides a smaller mass flow rate since its effective area is reduced because of the vapor fuel generated by cavitation. As a result, the area coefficients of both differ: the tapered nozzle shows a unity value while the constant section elliptical one shows an area coefficient of 0.87. The vapor phase inside the nozzle also derives in a increased velocity. First, the vapor phase makes the viscous friction smaller and second, due to the area reduction the fluid is accelerated. Consequently, this effect makes the difference between the velocity coefficients smaller than the difference between the discharge coefficients. However, the

Results	Convergent	Constant section
$\dot{m}_f[g/s]$	11.1	8.7
$M_f[N]$	6.53	4.65
$V_{eff}[m/s]$	591	532
Cd	0.85	0.67
Ca	1	0.87
Cv	0.85	0.77

Table 5.6: Hydraulic characterization results for elliptical nozzles.

resulting effective velocity of the constant section nozzle is lower than that of the convergent one and so it is also its velocity coefficient. Finally, the increment in velocity is not enough to compensate the loss of area and, for that, the mass flow rate is larger for the elliptical convergent nozzle. As the discharge coefficient is directly proportional to the mass flow, the convergent nozzle computes a higher value of 0.85 for this dimensionless parameter versus a corresponding value of 0.67 for the cavitating nozzle. The momentum flux is affected by the mass flow and also for the effective velocity, as both of them are lower for the constant section nozzle, so is the resulting momentum flux. At this moment, as it was done for the validation nozzles, a closer view into some different variable gradients within the nozzle reveals some interesting facts. Figure 5.9 shows the void fraction gradient in the nozzle throat of both nozzles, here the cylindrical nozzle starts to generate the vapor phase in the detachment zone of the flow. Since there is no rounding inlet radius, the inertial forces of the fluid produce a low pressure zone because of the fast and abrupt curvature. This strong decrease in pressure is what makes the fluid to cavitate.

In the convergent nozzle, as Figure 5.9a demonstrates, the flow is smoothly redirected thanks to the high rounding radius inside the convergent nozzle. A high L/D ratio together with the area reduction derived in a high uniform flow at the nozzle outlet. In contrast, the flow inside the elliptical nozzle with constant section only manages to reattach because of the high L/D ratio (see Figure 5.9b). The constriction experimented by the flow on its way through the section occupied by the vapor phase generates an increment in its velocity [49] but not enough to catch the convergent one. The smaller viscosity value of the vapor phase also contributes to this fact.

Velocity profiles at the outlet section are shown in Figure 5.10 for both nozzles. According with the discharge coefficient values, the convergent elliptical nozzle presents a general higher velocity profile where the rounding radius and the area reduction improve the flow velocity at the extremes of the major axis. The constant section nozzle suffers from the absence of this geometrical features and carries an important velocity loss. For both nozzles, highest peak

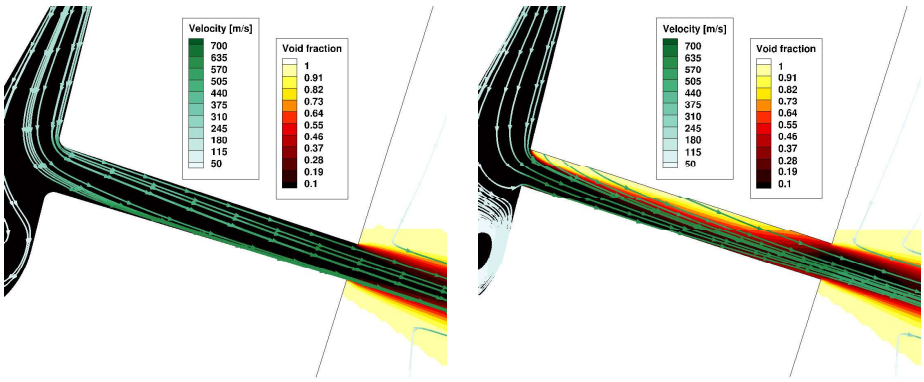

(a) Convergent elliptical nozzle, velocity streamlines over the void fraction contour.

(b) Constant section elliptical nozzle, velocity streamlines over the void fraction contour.

Figure 5.9: Void fraction and velocity streamlines of elliptical nozzles.

velocity values are found in the upper and lower section of the ellipse, these zones of higher velocity are connected because of a minor distance between points of the perimeter which produces the flow path generated in the upper and lower part of the throat entrance to have a greater interaction than inside a circular nozzle. On the other side, extremes of the ellipse major axis have a lower velocity compared to a circular orifice since the flattening of the entrance obstructs the lateral flow [23].

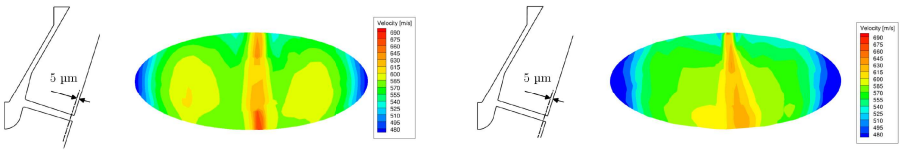

(a) Convergent nozzle.

(b) Constant section nozzle.

Figure 5.10: Velocity contour at 5 µm before the outlet nozzle orifice, elliptical nozzles.

Figure 5.11 shows the vorticity gradients of the nozzles displayed by its streamlines colored by vorticity magnitude over the void fraction contour. Here, the convergent nozzle (Figure 5.11a) shows a unique vorticity core that progressively ends in three minor cores, two laterals and one that connects the upper side and the lower side of the highest velocity zones. With respect to vorticity in the elliptical nozzle of constant section (Figure 5.11b), a high non-uniform field is found at the outlet section of its orifice. The upper and lower part are deeply connected, zones where vapor is produced and where the velocity is large. This larger vorticity and turbulence generated by the vapor

are expected to derive in core and surface instabilities which would later help the atomization process counteracting the minor momentum value of this flow.

The ideas formulated during the study of the internal flow are now carried to the analysis of the spray behavior.

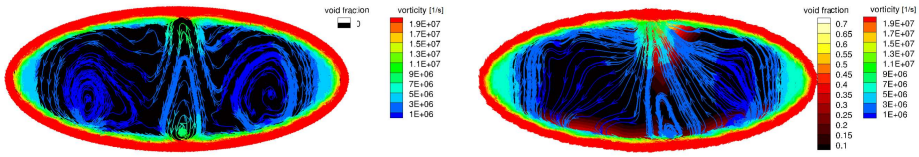

(a) Convergent nozzle. (b) Constant section nozzle.

Figure 5.11: Vorticity streamlines colored in magnitude over the void fraction contour at 5 µm before the outlet nozzle orifice, elliptical nozzles.

Figure 5.12a of Figure 5.12 shows the evolution of the fuel penetration in the chamber. For the first millimeters of both simulations, their curves are almost overlapped. However, as the internal flow velocity increases and cavitation takes place, the trends start to diverge and the constant section nozzle falls. The penetration is correlated with the spreading angle and momentum [49, 50] by the expression

$$S(t) \propto M_f^{1/4} \rho_a^{-1/4} tan^{-1/2}(\theta/2) t^{1/2} \tag{5.32}$$

where $S(t)$ is the time dependent penetration, M_f is the momentum flux, ρ_a is the ambient density and θ is the spray angle. The momentum conservation implies that for a lower penetration the behavior of the spray must be translated to a wider angle. In this case, the momentum value for the constant section elliptical nozzle is lower than the convergent one, which indeed contributes to this lower penetration. However, subtracting the influence of the momentum flux value of the spray penetration curve leads to Figure 5.12b where, according to equation 5.32, the angle must be responsible for the differences between both curves. As the constant section nozzles still presents in this state a lower penetration, at least beyond the first moments of the injection, a higher value of the spreading angle is expected for this nozzle.

Figure 5.13 shows the angle contour for the elliptical nozzles at 800 µm in two planes of study, XY and ZY, according to axis represented in Figure 5.8. Here, starting from the origin of the injection, both nozzles present a similarly evolution of the angle for the first millimeters of penetration with the convergent nozzle slightly above the constant section one. For the major axis projection (XY plane of Figure 5.8), a divergence is found at 20 mm where the fuel spreading across the discharge chamber becomes more intense and the angle rapidly increases. In the minor axis projection of the ellipse (ZY plane

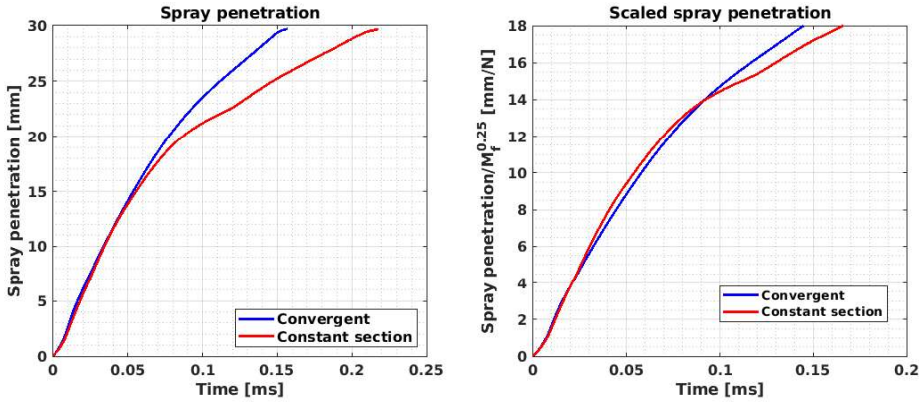

(a) Spray penetration. (b) Scaled spray penetration.

Figure 5.12: Spray penetration and scaled with momentum flux spray penetration for the elliptical nozzles.

of Figure 5.8), this increment of the angle occurs earlier, at 13 mm. This behavior could lead to a mayor discussion, the switching axis phenomenon reported for elliptical nozzles [19, 20] can affect the point at which the jets cross. In this process, the mayor axis turns into the minor axis and vice-versa in a periodically way [51]. For moderate Reynolds numbers, the switching point is said to depend on the ellipse aspect ratio [52]. However, for high Reynolds number it is not a clear issue. This, coupled with the presence of cavitation, means that the moment at which the constant section nozzle overtakes the convergent nozzle requires further and more detailed analysis in future work.

Temporal evolution of the mean angle value is displayed in Figure 5.14. Here, the differences between both nozzles become more obvious. Even if the convergent orifice produces a wider angle for the first moments of the injection (up to 150 µs), the mean angle of the constant section elliptical nozzle significantly improves after 150 µs. Note that the peak value located between 0 and 10 µs should be considered as non-representative since the entity of the spray is not sufficient to offer a good estimation of the spray angle. For the convergent nozzle, the averaged angle for the last 100 µs of simulation returns a value of 9.67 degrees for the minor axis projection and 14.11 for the major axis projection while the constant section nozzle shows 15.56 and 19 respectively in the range of study. This involves an increment of 60% and 31% in individual measures. The angle of the spray in this study is defined as the mean of both XY and ZY giving a value of 11.89 degrees for the convergent nozzle and 17.28 degrees for the constant section nozzle (steady-state averaged). It is noticed the variations from one angle plane of study to the other for the same nozzle. This effect is the addition of two parameters, the non-symmetrical

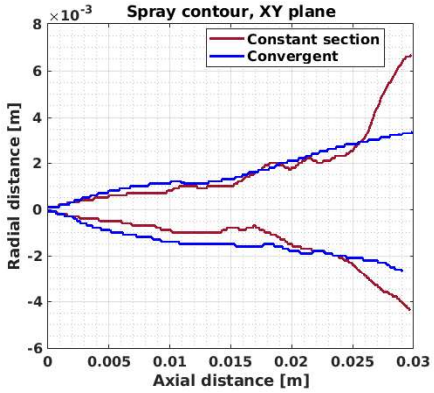

(a) Major axis projection.

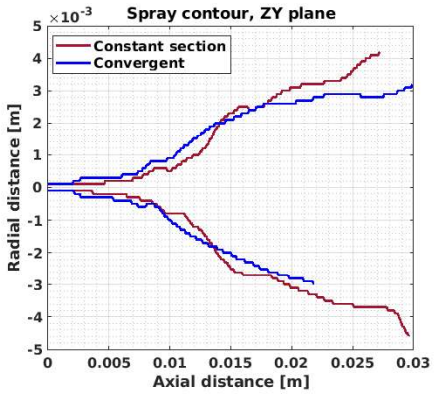

(b) Minor axis projection.

Figure 5.13: Spray angle contour at 800 µs ASOI.

streamlines of the flow due to the orifice inclination and the self elliptical shape of the orifice that enforces the divergence between both planes of study. However, the study of the balance between both parameters is left for future works.

The behavior inside the spray plume can be also analyzed by the mass fraction and velocity profiles. Figure 5.16 and Figure 5.16 depict the evolution of the mass fraction along the spray axis and several radial positions averaged over the last 100 µs of simulation. Taking first the axial evolution of Figure 5.15 and in the same line as previous variables, both nozzles start from a similar point of mass fraction value. However, the convergent nozzle faster increases the dispersion of fuel for the first millimeters of penetration, probably due to a higher momentum flux.

At a certain distance (∼12.5 mm), the constant section elliptical nozzle decreases its slope and passes under the convergent one. It can be noticed the more irregular shape of the constant section nozzle line, the variations are

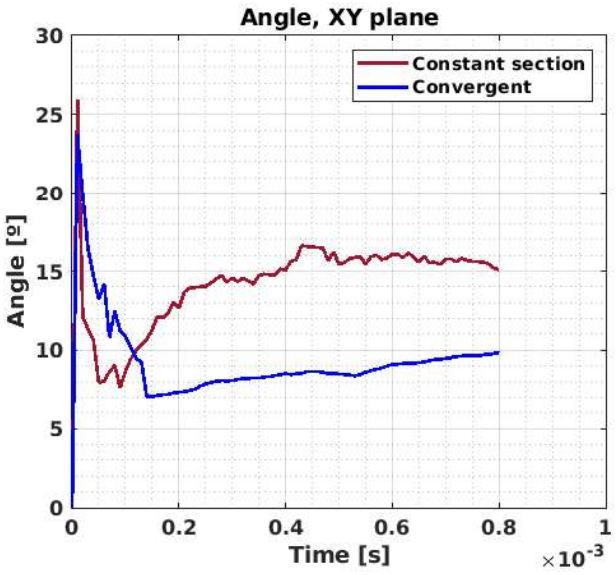

(a) Major axis projection.

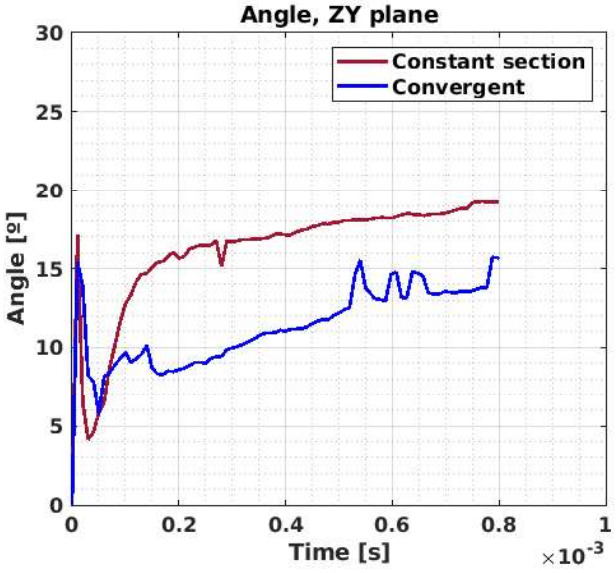

(b) Minor axis projection.

Figure 5.14: Spray angle mean value, temporal evolution.

associated to the transient nature of cavitation. The axial mass fraction of the constant section nozzle faster decreases in the last millimeters of the spray. Radial profiles are also in line with the axial findings, in Figures 5.16a and 5.16c, radial profiles in the minor axis direction show a smaller dispersion for the constant section nozzle in the first millimeters. This trend is inverted for the last axial positions of Figure 5.16e. For the major axis, the mass fraction

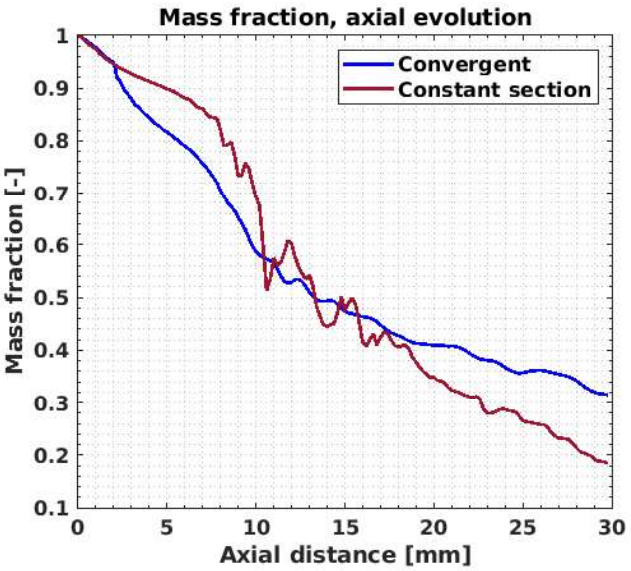

Figure 5.15: Axial mass fraction, time averaged from 700 to 800 µs.

of both curves has not a clear separation in the range between 1 and 16 mm, this zone is represented by the lines in yellow and purple of Figures 5.16b and 5.16d. After this neutral section and according to the axial values, the radial diffusion of the fuel is higher for the constant section nozzle for both in the minor (Figure 5.16e) and major axis (Figure 5.16f) direction of the ellipse and the maximum mass fraction peak is reduced.

For a more illustrative perspective, Figure 5.17 shows the contour map for planes of Figure 5.16 at 800 μs for the convergent (Figure 5.17a) and the constant section nozzle 5.17b.

Axial velocity profiles of Figure 5.18 and Figure 5.19 also offer an important view of the spray dynamics. With respect to the axial velocity in the spray axis (Figure 5.18), both nozzles follow a parallel slope up to 15 mm where a divergence point is found.

As it can be seen in Figure 5.19a and 5.19b for both minor and major axis, radial profiles show similar maximum peaks for the convergent and constant section elliptical nozzles in the first points of study. However, the limits of the Gaussians are more concentrated for the constant section orifice. This trend disappears for points far away from the origin (Figure 5.19c and 5.19d) where the Gaussian width seems to reach the convergent one. This fact is more visible for probes in the minor axis direction as Figure 5.19e and 5.19f show for points at 21 and 26 mm.

The faster decrease of axial velocity supports the slower penetration of Figure 5.12. This decrease is also in line with the faster radial momentum transfer shown in Figure 5.13a and 5.14b by a higher spreading angle. Al-

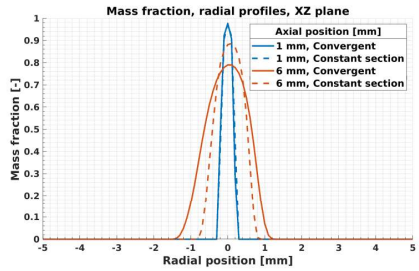

(a) Radial probes, minor axis direction.

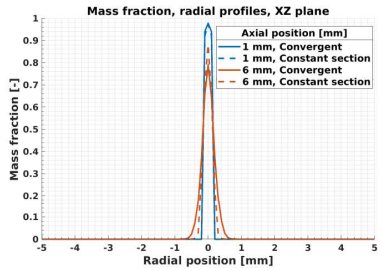

(b) Radial probes, major axis direction.

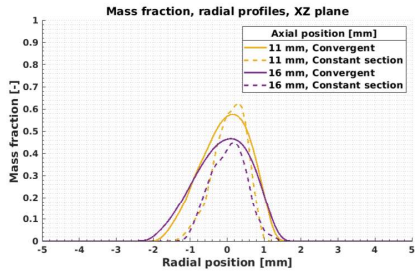

(c) Radial probes, minor axis direction.

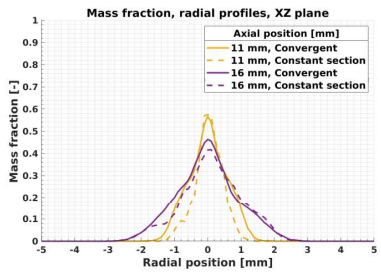

(d) Radial probes, major axis direction.

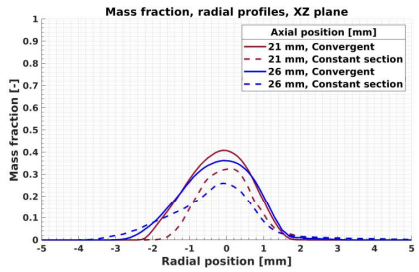

(e) Radial probes, minor axis direction.

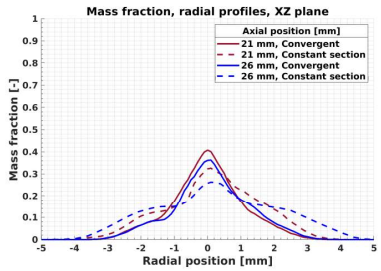

(f) Radial probes, major axis direction.

Figure 5.16: Mass fraction profiles for different axial positions, time averaged from 700 to 800 µs, XZ plane (see Figure 5.8).

though it is difficult to perform a balance between the contribution of the cavitation induced flow instabilities, and the liquid dispersion dominated by other flow structures, cavitation has demonstrated to play an important role in the improvement of the mixture. This effect has been widely reported in the literature [53] for circular nozzles. For elliptical nozzles, the importance of this phenomenon is still under study since it is even more difficult to evaluate the weights of the initial conditions of the flow and the downstream flow

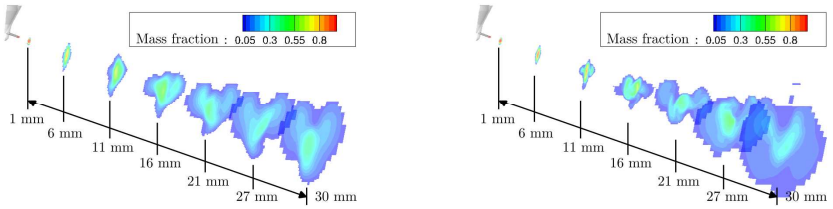

(a) Convergent section nozzle. (b) Constant section nozzle.

Figure 5.17: Mass fraction contour for several perpendicular planes from nozzle orifice at 800 µm.

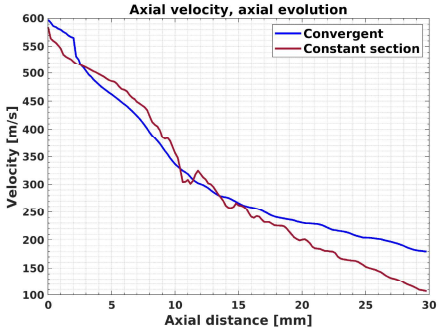

Figure 5.18: Axial velocity, time averaged from 700 to 800 µs.

structures over the mixture process. Initial disturbances of the flow can exert a greater influence on the later jet than in circular nozzles due to its auto-induced self-similarity [19]. Also, some studies have shown that cavitation applied to elliptical nozzles improves the atomization [17]. In this study and with the shown evidences without further validation, it seems fair to affirm that cavitation has also a noticeable influence in elliptical nozzles. The mixing process of the spray can be seen from a qualitative point of view in Figure 5.20, where the instantaneous void fraction iso-surface at 800 µs is plotted for both nozzles. Here, the spatial distribution of the constant section nozzle presents a wider and more irregular spatial distribution.

Spray entrainment summarizes all trends observed in the previous parameters. Figure 5.21 depicts the axial evolution of the normalized jet entrainment averaged for the last 100 µs of the simulations. The graph shows how both nozzles proportionally capture a similar quantity of mass in the first up to a middle section of the jet. Beyond 12 mm, the constant section elliptical nozzle faster improves over the convergent one. As expected, this variable presents a similar behavior to the velocity profiles, mass fraction profiles and angle.

In summary, the cavitation in elliptical nozzles seems to clearly improve

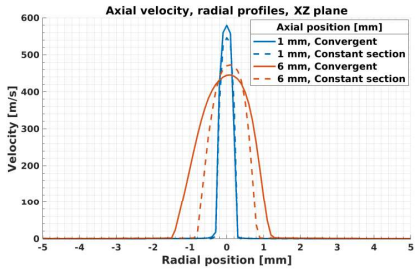

(a) Radial probes, minor axis direction.

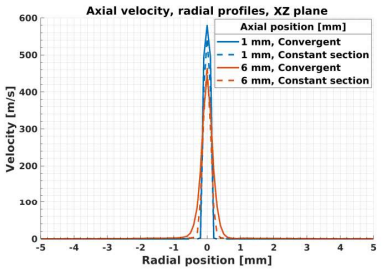

(b) Radial probes, major axis direction.

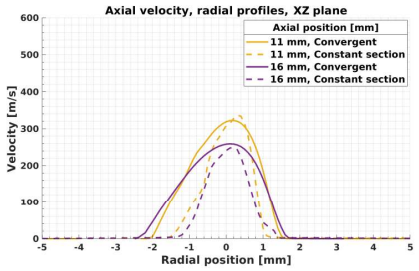

(c) Radial probes, minor axis direction.

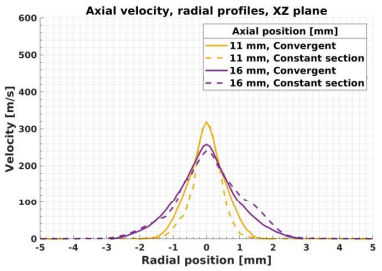

(d) Radial probes, major axis direction.

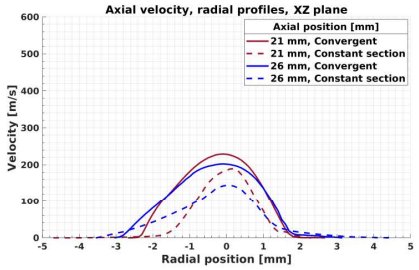

(e) Radial probes, minor axis direction.

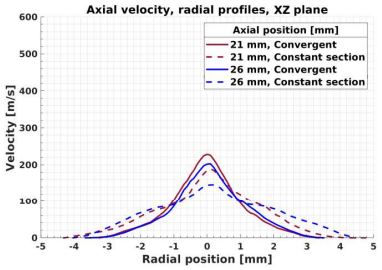

(f) Radial probes, major axis direction.

Figure 5.19: Axial velocity profiles for different axial positions, time averaged from 700 to 800 µs, XZ plane (see Figure 5.8).

the mixture process for points beyond a middle section of the spray. On the contrary, this improvement is more questionable for points near the nozzle.

(a) Convergent nozzle. (b) Constant section nozzle.

Figure 5.20: Void fraction iso-surface, $\alpha = 0.999$.

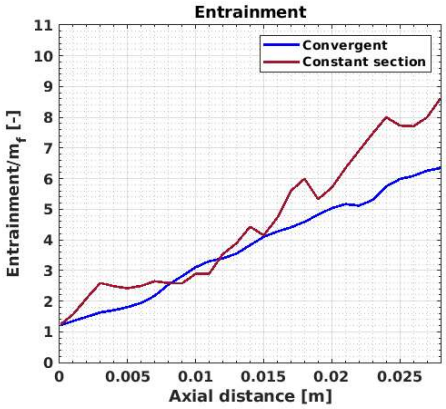

Figure 5.21: Normalized entrainment of the convergent and constant section elliptical nozzles, time averaged from 700 to 800 800 µs.

5.5. Conclusions

A CFD approach based on the $\Sigma - Y$ Eulerian model has been validated for two calibrated nozzles, Spray A (non-cavitating) and Spray C (cavitating), in terms of mass flow rate, momentum, effective velocity, and characteristic coefficients for the internal flow and also in terms of penetration, spreading angle and other properties. Based on the two reference nozzles results, the code has been employed over two elliptical nozzles, non-cavitating and cavitating. The convergent and constant section elliptical nozzles have been compared in terms of internal mass flow and spray dynamics with quantitative and qualitative data. The results of the comparative can be summarized as follows:

- The suggested CFD model is able to reproduce the behavior of both the

internal and external flow with an acceptable error under the conditions presented in this work.

- Results show that cavitation is still a quite noticeable effect applied to elliptical nozzles.
- In the cases of this study, cavitation has the potential to improve the mixture process.
- This effect seems to be more important from a middle region of the spray which can affect the practical applications of this kind of nozzle. However, for points beyond a middle range, the constant section elliptical nozzle seems to be over the convergent elliptical in mixture effectiveness.
- In future works, the conclusions above must be extended to different conditions. First, it is necessary to study the behavior of the elliptical nozzles for evaporative cases in order to see how the liquid length and vapor generation is affected and then, for real operating conditions.

Declaration of conflicting interests

The author(s) declared no potential conflicts of interest with respect to the research, authorship, and/or publication of this article.

Acknowledgements

The authors would like to thank the computer resources, technical expertise and assistance provided by Universitat Politècnica de València in the use of the "Rigel" computation cluster. The authors want to express their gratitude to CONVERGENT SCIENCE Inc. and Convergent Science GmbH for their kind support for the CFD calculations with the CONVERGE software.

Funding

The author(s) disclosed receipt of the following financial support for the research, authorship, and/or publication of this article: This work was supported by the Ministerio de Ciencia, Innovación y Universidades of the Spanish Government. The PhD studies by Enrique C. Martínez-Miracle have been funded by the Agencia Estatal de Investigación of the Spanish Government and the ESF (European Social Fund), project "Desarrollo de modelos de combustión y emisiones HPC para el análisis de plantas propulsivas de transporte sostenibles" (TRA2017-89139-C2-1-R) by means of the "Subprograma Estatal de Formación del Programa Estatal de Promoción del Talento y su Empleabilidad en I+D+i".

References

[1] Hiro Hiroyasu and Haiyan Miao. "Measurement and Calculation of Diesel Spray Penetration". In: *Proceedings of ICLASS Conference* October (2003). URL: http://www.ilasseurope.org/ICLASS/iclass2003/fullpapers/1413.pdf.

[2] Hiro Hiroyasu and Masataka Arai. "Structures of Fuel Sprays in Diesel Engines". In: 2002.724 (Feb. 1990). DOI: 10.4271/900475. URL: https://www.sae.org/content/900475/.

[3] Jeffrey Naber and L. Dennis. "Effects of Gas Density and Vaporization on Penetration and Dispersion of Diesel Sprays". In: (1996), p. 960034. ISSN: 0148-7191. DOI: 10.4271/960034. URL: http://papers.sae.org/960034/.

[4] F. Payri, V. Bermúdez, R. Payri and F. J. Salvador. "The influence of cavitation on the internal flow and the spray characteristics in diesel injection nozzles". In: *Fuel* 83.4-5 (2004), pp. 419–431. ISSN: 00162361. DOI: 10.1016/j.fuel.2003.09.010.

[5] R. Payri, F. J. Salvador, J. Gimeno and J. de la Morena. "Effects of nozzle geometry on direct injection diesel engine combustion process". In: *Applied Thermal Engineering* 29.10 (2009), pp. 2051–2060. ISSN: 13594311. DOI: 10.1016/j.applthermaleng.2008.10.009. URL: http://dx.doi.org/10.1016/j.applthermaleng.2008.10.009.

[6] Raul Payri, Francisco Javier Salvador, Jaime Gimeno and Juan P Viera. "Experimental Analysis on the Influence of Nozzle Geometry Over the Dispersion of Liquid N-Dodecane Sprays". In: *Frontiers in Mechanical Engineering* 1.October (2015). ISSN: 2297-3079. DOI: 10.3389/fmech.2015.00013. URL: http://journal.frontiersin.org/Article/10.3389/fmech.2015.00013/abstract.

[7] F. J. Salvador, S. Hoyas, R. Novella and J. Martinez-Lopez. "Numerical simulation and extended validation of two-phase compressible flow in diesel injector nozzles". In: *Proceedings of the Institution of Mechanical Engineers, Part D: Journal of Automobile Engineering* 225.4 (2011), pp. 545–563. ISSN: 09544070. DOI: 10.1177/09544070JAUTO1569.

[8] Francisco Javier Salvador, Joaquin De la Morena, Gabriela Bracho and David Jaramillo. "Computational investigation of diesel nozzle internal flow during the complete injection event". In: *Journal of the Brazilian Society of Mechanical Sciences and Engineering* 40.3 (2018). ISSN: 18063691. DOI: 10.1007/s40430-018-1074-z.

[9] Qingluan Xue et al. "Eulerian CFD Modeling of Coupled Nozzle Flow and Spray with Validation Against X-Ray Radiography Data". In: *SAE International Journal of Engines* 7.2 (2014), pp. 2014–01–1425. ISSN: 1946-3944. DOI: 10.4271/2014-01-1425. URL: http://papers.sae.org/2014-01-1425/.

[10] Michele Battistoni, Sibendu Som and Christopher F. Powell. "Highly resolved Eulerian simulations of fuel spray transients in single and multihole injectors: Nozzle flow and near-exit dynamics". In: *Fuel* 251.April (2019), pp. 709–729. ISSN: 00162361. DOI: 10.1016/j.fuel.2019.04.076. URL: https://doi.org/10.1016/j.fuel.2019.04.076.

[11] Kaushik Saha et al. "Coupled Eulerian Internal Nozzle Flow and Lagrangian Spray Simulations for GDI Systems". In: (2018). DOI: 10.4271/2017-01-0834.Abstract.

[12] J. Anez et al. "Eulerian-Lagrangian spray atomization model coupled with interface capturing method for diesel injectors". In: *International Journal of Multiphase Flow* 113 (2018), pp. 325–342. ISSN: 03019322. DOI: 10.1016/j.ijmultiphaseflow.2018.10.009. URL: https://doi.org/10.1016/j.ijmultiphaseflow.2018.10.009.

[13] Sampath Rachakonda et al. "A Computational Approach to Predict External Spray Characteristics for Flashing and Cavitating Nozzles". In: *International Journal of Multiphase Flow* 106 (May 2018). DOI: 10.1016/j.ijmultiphaseflow.2018.04.012.

[14] Francisco J. Salvador, Joaquin de la Morena, Marcos Carreres and David Jaramillo. "Numerical analysis of flow characteristics in diesel injector nozzles with convergent-divergent orifices". In: *Proceedings of the Institution of Mechanical Engineers, Part D: Journal of Automobile Engineering* 231.14 (2017), pp. 1935–1944. ISSN: 09544070. DOI: 10.1177/0954407017692220.

[15] S. Molina, F. J. Salvador, M. Carreres and D. Jaramillo. " A computational investigation on the influence of the use of elliptical orifices on the inner nozzle flow and cavitation development in diesel injector nozzles ". In: *Energy Conversion and Management* 79 (2014), pp. 114–127. ISSN: 01968904. DOI: 10.1016/j.enconman.2013.12.015. URL: http://dx.doi.org/10.1016/j.enconman.2013.12.015.

[16] Kun Woo Ku, Jung Goo Hong and Choong Won Lee. "Effect of internal flow structure in circular and elliptical nozzles on spray characteristics". In: *Atomization and Sprays* 21.8 (2011), pp. 655–672. ISSN: 10445110. DOI: 10.1615/AtomizSpr.2012004192.

[17] Jung Goo Hong, Kun Woo Ku, Sung Ryoul Kim and Choong Won Lee. "Effect of cavitation in circular nozzle and elliptical nozzles on the spray characteristic". In: *Atomization and Sprays* 20.10 (2010), pp. 877–886. ISSN: 10445110. DOI: 10.1615/AtomizSpr.v20.i10.40. URL: http://www.scopus.com/inward/record.url?eid=2-s2.0-79955791257&partnerID=tZOtx3y1.

[18] Choong-won Lee et al. "Experimental study of the effects of nozzle hole geometry for a DI diesel engine". In: *ICLASS 2006*. Kyoto, 2006.

[19] Fazle Hussain and Hyder S Husain. "Elliptic jets. Part 1. Characteristics of unexcited and excited jets". In: *Journal of Fluid Mechanics* 208 (Nov. 1989), pp. 257–320. ISSN: 0022-1120. DOI: 10.1017/S0022112089002843. URL: https://www.cambridge.org/core/product/identifier/S0022112089002843/type/journal%7B%5C_%7Darticle.

[20] Hyder S. Husain and Fazle Hussain. "Elliptic jets. part 2. dynamics of coherent structures: Pairing". In: *Journal of Fluid Mechanics* 233.439 (1991), pp. 439–482. ISSN: 14697645. DOI: 10.1017/S0022112091000551.

[21] Gong Yunyi, Liu Changwen, Huang Yezhou and Peng Zhijun. "An experimental study on droplet size characteristics and air entrainment of elliptic sprays". In: *SAE Technical Papers* 724 (1998). ISSN: 26883627. DOI: 10.4271/982546.

[22] Shenghao Yu et al. "Experimental study on the spray characteristics discharging from elliptical diesel nozzle at typical diesel engine conditions". In: *Fuel* 221.February (2018), pp. 28–34. ISSN: 00162361. DOI: 10.1016/j.fuel.2018.02.090.

[23] F. J. Salvador, J. M. Pastor, J. De la Morena and E. C. Martínez-Miracle. "Computational study on the influence of nozzle eccentricity in spray formation by means of Eulerian Σ - Y coupled simulations in diesel injection nozzles". In: *International Journal of Multiphase Flow* 129 (2020), p. 103338. ISSN: 03019322. DOI: 10.1016/j.ijmultiphaseflow.2020.103338. URL: https://doi.org/10.1016/j.ijmultiphaseflow.2020.103338.

[24] Hekun Jia, Zhuangbang Wei, Bifeng Yin and Zhiyuan Liu. "Analysis of elliptical diesel nozzle spray dynamics using a one-way coupled spray model". In: *International Journal of Engine Research* (2021), pp. 755–766. ISSN: 1468-0874. DOI: 10.1177/14680874211063352.

[25] Ariane Vallet, A. A. Burluka and R. Borghi. "Development of a Eulerian model for the atomization of a liquid jet". In: *Atomization and Sprays* 11.6 (2001). ISSN: 1044-5110.

[26] Jose Maria Desantes et al. “Coupled/decoupled spray simulation comparison of the ECN spray a condition with the Σ-Y Eulerian atomization model”. In: *International Journal of Multiphase Flow* 80 (2016), pp. 89–99. ISSN: 03019322. DOI: 10.1016/j.ijmultiphaseflow.2015.12.002.

[27] J M Desantes, F J Salvador, M Carreres and D Jaramillo. “ Experimental Characterization of the Thermodynamic Properties of Diesel Fuels Over a Wide Range of Pressures and Temperatures ”. In: *SAE International Journal of Fuels and Lubricants* 8.1 (2015), pp. 951–2015. ISSN: 1946-3960. DOI: 10.4271/2015-01-0951. URL: http://papers.sae.org/2015-01-0951/.

[28] Francisco Javier Salvador, Marcos Carreres, Joaquin De la Morena and E Martínez-Miracle. “ Computational assessment of temperature variations through calibrated orifices subjected to high pressure drops: Application to diesel injection nozzles ”. In: *Energy Conversion and Management* 171 (Sept. 2018), pp. 438–451. ISSN: 01968904. DOI: 10.1016/j.enconman.2018.05.102. URL: https://linkinghub.elsevier.com/retrieve/pii/S0196890418305867.

[29] Ariane Vallet and Roland Borghi. “ Modelisation eulerienne de l’atomisation d’un jet liquide ”. In: *Comptes Rendus de l’Academie de Sciences - Serie IIb: Mecanique, Physique, Chimie, Astronomie* 327.10 (1999), pp. 1015–1020. ISSN: 12874620. DOI: 10.1016/S1287-4620(00)87013-1.

[30] Y Wang et al. “Application of Interface Area Density Modeling to Define Spray Plume Boundary Department of Mechanical and Industrial Engineering University of Massachusetts-Amherst General Motors Global R & D”. In: May (2015).

[31] A. Pandal, R. Payri, J. M. García-Oliver and J. M. Pastor. “Optimization of spray break-up CFD simulations by combining Σ-Y Eulerian atomization model with a response surface methodology under diesel engine-like conditions (ECN Spray A)”. In: *Computers and Fluids* 156 (2017), pp. 9–20. ISSN: 00457930. DOI: 10.1016/j.compfluid.2017.06.022.

[32] Adrián Pandal Blanco. “ Implementation and Development of an Eulerian Spray Model for CFD simulations of diesel Sprays ”. PhD thesis. Valencia (Spain): Universitat Politècnica de València, July 2016. DOI: 10.4995/Thesis/10251/68490. URL: https://riunet.upv.es/handle/10251/68490.

[33] K.J. Richards, P.K. Senecal and E. Pomraning. “CONVERGE 2.4.*, Convergent Science, Madison, WI (2021)”. In: ().

[34] Z. Bilicki and J. Kestin. “Physical Aspects of the Relaxation Model in Two-Phase Flow”. In: *Proceedings of the Royal Society A: Mathematical, Physical and Engineering Sciences* 428.1875 (Apr. 1990), pp. 379–397. ISSN: 1364-5021. DOI: 10.1098/rspa.1990.0040. URL: http://dx.doi.org/10.1098/rspa.1990.0040%20http://rspa.royalsocietypublishing.org/cgi/doi/10.1098/rspa.1990.0040.

[35] E W Bilicki, Salim Ali, Fluid Flow Machinery and Polish Academy. “Evaluation of the relaxation time of heat and mass exchange in the liquid-vapour bubble flow”. In: 39.4 (1996).

[36] P. Downar-Zapolski, Z. Bilicki, L. Bolle and J. Franco. “The non-equilibrium relaxation model for one-dimensional flashing liquid flow”. In: *International Journal of Multiphase Flow* 22.3 (1996), pp. 473–483. ISSN: 03019322. DOI: 10.1016/0301-9322(95)00078-X.

[37] Zhixia He et al. “Investigations of effect of phase change mass transfer rate on cavitation process with homogeneous relaxation model”. In: *International Communications in Heat and Mass Transfer* 89 (2017), pp. 98–107. ISSN: 0735-1933. DOI: https://doi.org/10.1016/j.icheatmasstransfer.2017.09.021.

[38] Engine Combustion Department of Sandia National Laboratories. *Engine Combustion Network Data search*. URL: https://ecn.sandia.gov/ecn-data-search/.

[39] Q. Xue et al. “An Eulerian CFD model and X-ray radiography for coupled nozzle flow and spray in internal combustion engines”. In: *International Journal of Multiphase Flow* 70.December (2015), pp. 77–88. ISSN: 03019322. DOI: 10.1016/j.ijmultiphaseflow.2014.11.012.

[40] R. Payri, J. Gimeno, J. Cuisano and J. Arco. “ Hydraulic characterization of diesel engine single-hole injectors ”. In: *Fuel* 180.April (2016), pp. 357–366. ISSN: 00162361. DOI: 10.1016/j.fuel.2016.03.083.

[41] Victor Yakhot and Leslie M. Smith. “The renormalization group, the eps-expansion and derivation of turbulence models”. In: *Journal of Scientific Computing* 7.1 (1992), pp. 35–61. ISSN: 0885-7474. DOI: 10.1007/BF01060210.

[42] David C. Wilcox. “Reassessment of the scale-determining equation for advanced turbulence models”. In: *AIAA Journal* 26.11 (1988), pp. 1299–1310. ISSN: 00011452. DOI: 10.2514/3.10041.

[43] J. M. Desantes, J. M. García-Oliver, J. M. Pastor and A. Pandal. “A comparison of diesel sprays CFD modeling approaches: DDM versus σ-γ Eulerian atomization model”. In: *Atomization and Sprays* 26.7 (2016), pp. 713–737. ISSN: 10445110. DOI: 10.1615/AtomizSpr.2015013285.

[44] Brandon A Sforzo et al. "Fuel Nozzle Geometry Effects on Cavitation and Spray Behavior at Diesel Engine Conditions". In: *Proceedings of the 10th International Symposium on Cavitation (CAV2018)* (2019), pp. 474–480. DOI: 10.1115/1.861851_ch90.

[45] Katarzyna E Matusik et al. "High-resolution X-ray tomography of Engine Combustion Network diesel injectors". In: *International Journal of Engine Research* 19.9 (2018), pp. 963–976. DOI: 10.1177/1468087417736985.

[46] Alan L Kastengren and Christopher F Powell. "Spray density measurements using X-ray radiography". In: *Proceedings of the Institution of Mechanical Engineers, Part D: Journal of Automobile Engineering* 221.6 (Jan. 2007), pp. 653–662. ISSN: 0954-4070. DOI: 10.1243/09544070JAUTO392. URL: http://sdj.sagepub.com/lookup/10.1243/09544070JAUTO392.

[47] A. L. Kastengren et al. "Time-resolved X-ray radiography of sprays from Engine Combustion Network spray a diesel injectors". In: *Atomization and Sprays* 24.3 (2014), pp. 251–272. ISSN: 10445110. DOI: 10.1615/AtomizSpr.2013008642.

[48] Daniel J. Duke et al. "X-ray radiography of cavitation in a beryllium alloy nozzle". In: *International Journal of Engine Research* 18.1-2 (2017), pp. 39–50. ISSN: 20413149. DOI: 10.1177/1468087416685965.

[49] R. Payri, J. M. García, F. J. Salvador and J. Gimeno. "Using spray momentum flux measurements to understand the influence of diesel nozzle geometry on spray characteristics". In: *Fuel* 84.5 (2005), pp. 551–561. ISSN: 00162361. DOI: 10.1016/j.fuel.2004.10.009.

[50] Jose Maria Desantes, Raul Payri, Francisco Javier Salvador and Jaime Gimeno. "Different Measurement Techniques To Determine Hole To Hole dispersion in a real diesel injector". In: *Proceedings of the FEDSM2006* February 2015 (2006), pp. 1–8. DOI: 10.1115/FEDSM2006-98212.

[51] Chih-Ming Ho and Ephraim Gutmark. "Vortex induction and mass entrainment in a small-aspect-ratio elliptic jet". In: *Journal of Fluid Mechanics* 179 (June 1987), p. 383. ISSN: 0022-1120. DOI: 10.1017/S0022112087001587. URL: http://www.journals.cambridge.org/abstract%7B%5C_%7DS0022112087001587.

[52] Philip J. Morris. "Instability of elliptic jets". In: *AIAA Journal* 26.2 (1988), pp. 172–178. ISSN: 00011452. DOI: 10.2514/3.9869.

[53] Francisco Javier Salvador, Jorge Martínez-López, J. V. Romero and M. D. Roselló. "Computational study of the cavitation phenomenon and its interaction with the turbulence developed in diesel injector nozzles by Large Eddy Simulation (LES)". In: *Mathematical and Computer Modelling* 57.7-8 (2013), pp. 1656–1662. ISSN: 08957177. DOI: 10.1016/

j.mcm.2011.10.050. URL: http://dx.doi.org/10.1016/j.mcm.2011.10.050.

Capítulo 6

Discusión de los resultados

You want a valve that doesn't leak and you try everything possible to develop one. But the real world provides you with a leaky valve. You have to determine how much leakiness you can tolerate.

Arthur Rudolph

Resumen: Este capítulo resume y realiza un comentario final a los resultados encontrados a través de las investigaciones anteriores.

6.1. Comentarios finales a los resultados

A través de los capítulos anteriores se han ido desarrollando una serie de investigaciones alrededor del flujo interno, desarrollo de la mezcla y combustión tomando como eje central de las mismas los efectos de la geometría sobre dichos procesos. Procediendo de un forma natural desde el flujo interno, las variaciones que la geometría produce sobre éste se han tratado con más o menos detalle a lo largo de todos lo capítulos. Si bien el Capítulo 2, ha focalizado en el flujo del interior de los orificios de inyección, a través de la introducción de una caracterización en detalle de los combustibles, y de la resolución de las ecuaciones de energía teniendo en cuenta efectos de compresibilidad, el resto de capítulos arrastran algunos de los puntos más importantes de éste, como son las propiedades tabuladas del combustible diesel empleado. La obtención de una correcta metodología en el modelado del flujo interno, esto es, unos modelos adecuados de turbulencia, transmisión de calor y una apropiada caracterización del combustible todo ello aplicado sobre un representación fiel de la geometría, es crítica a la hora de obtener resultados numéricos fiables y se revela como la conclusión más importante de este estudio. La hipótesis

base para el flujo interno en esta primera investigación es decir, la ausencia de intercambio de calor con el exterior, o flujo adiabático, a lo largo de la geometría de inyección, también supone una condición de contorno importante, especialmente en términos de simplificación del problema. A partir de algunos de los resultados de este primer capítulo, en los Capítulos 3, 4 y 5 se ha profundizado en la relación de la geometría interna sobre la mezcla. Empezando por el estudio de geometrías con un carácter más convencional, el Capítulo 3 ha estudiado dos geometrías cónicas una de ellas con un factor longitud diámetro (L/D) reducido que se han comparado tanto experimental como numéricamente. En esta sección, se han empleado dos modelos numéricos diferentes, un modelo discreto Lagrangiano y el modelo Σ-Y Euleriano. El modelo Σ-Y empleado en este capítulo ha sido validado extensamente según distintas geometrías y sus correspondientes medidas experimentales. Por un lado, frente a toberas calibradas de estudio, las denominadas Spray A y C del ECN, y por otro, frente a las propias toberas de carácter convencional o comercial. La validación respecto a las primeras se ha detallado ampliamente en los Capítulos 4 y 5 no solo en los términos experimentales más convencionales, como el flujo interno, penetración o ángulo, sino en otros como la densidad proyectada. El buen comportamiento del modelo en estas dos geometrías se hace patente en una primera instancia bajo los resultados obtenidos del flujo interno. La posibilidad de disponer de unos modelos 3D provenientes del escaneado por tomografía electrónica junto con las leyes de levantamiento de aguja llevan al modelo a reproducir fielmente tanto comportamientos transitorios como valores estacionarios. Los errores son bajos en todos los parámetros de estudio, como se ha mostrado en la Tabla 5.3, pese a incluir la cavitación, cuyo modelado suele incurrir en desviaciones mayores, en el caso del Spray C. La dispersión del fluido en cámara bajo unos términos macroscópicos también es correctamente capturada como se desprende de la Figura 5.4, donde se muestra la evolución de la penetración del Spray A y C, y de las comparaciones del ángulo según la Figura 4.5 y la Figura 5.6 para el Spray A y C respectivamente. Los análisis de densidad proyectada acompañan al resto de medidas con resultados razonables, más precisos en zonas cercanas a la tobera y con algo más de desviación en zonas alejadas y, en todo caso, en consonancia con otras simulaciones similares disponibles en la literatura. Los buenos resultados encontrados para este tipo de toberas de investigación han permitido estudiar trasladar con confianza el cálculo hacia geometrías multiorificio. Siguiendo esta línea, en el Capítulo 3 se han estudiado variaciones de la geometría a través de dos toberas cónicas con diferentes ratios l/d y diferencias en los radios de la zona de entrada de la tobera (Figura 3.5). Para analizar los efectos sobre el chorro y la combustión se ha empleado una metodología que combina los modelos DDM y ELSA (Σ-Y con transición de gotas Euleriana-Lagrangiana) anteriormente mencionados. Los modelos DDM se han configurado utilizando las curvas de tasa y valores de ángulo procedentes de los estudios de caracterización hidráulica y la visualización del chorro respectivamente. La calibración

se ha realizado en función de las constantes de tiempo y de tamaño del modelo KH-RT consiguiendo un buen ajuste a las curvas de penetración de vapor y de longitud líquida, como se puede apreciar en la Figura 3.29. Las simulaciones ELSA fueron validadas en una primera parte respecto al flujo interno y a la caracterización hidráulica experimental. Al no disponer de las leyes de levantamiento como condición de contorno en las simulaciones ELSA de chorro, éstas se sustituyeron por los perfiles de velocidad y resto de variables del flujo interno derivadas de la adaptación del flujo másico numérico instantáneo a su homólogo en las curvas de tasa experimentales. La campaña experimental realizada en en este capítulo también ha servido para validar los resultados de flujo interno y chorro provenientes del modelo ELSA. En el flujo interno (Figura 3.21), las desviaciones conseguidas han oscilado alrededor del 3 %, valores similares a los obtenidos en las toberas calibradas, y se han capturado las diferencias en velocidad y momento derivadas de la geometría (Figura 3.27). El chorro en las simulaciones ELSA también ha sido capaz de reflejar las tendencias observadas en las medidas experimentales, con una penetración de vapor menor para la tobera SN (de menor ratio longitud diámetro), una menor longitud líquida y un ángulo algo mayor, según se muestra en la Figura 3.30. En lo que respecta a la combustión, el estudio de la misma se ha basado principalmente en el uso de los modelos DDM dado su menor coste computacional y la limitada ventana temporal disponible para realizar las simulaciones. Utilizando la tobera BN como referencia para las validaciones, se puede afirmar que la reproducción de los comportamientos experimentales del chorro a través de una correcta calibración ha permitido trasladar sus diferencias a los resultados en combustión. Estas diferencias, derivadas de los distintos parámetros geométricos de las toberas se han traducido en diferencias también en los balances de energía del ciclo. Donde la tobera SN, según lo esperado de acuerdo a su mayor ángulo experimental y una menor longitud líquida (Figura 3.28), ha conducido a un mejor proceso de mezcla y, por tanto, a una combustión más eficiente. El acercamiento de la combustión a la tobera detectado para esta mismo tobera ha conseguido reducir las pérdidas por calor a través de las paredes del sistema. Esto, junto con el incremento de la eficiencia de la combustión, ha llevado a un incremento del trabajo del ciclo. La aproximación híbrida ELSA, debido a su elevado coste computacional, solo ha podido ser ejecutada en condiciones de combustión de forma limitada y más orientada a validar las tendencias observadas tanto en el modelo discreto como en las medidas experimentales. En este sentido, sus resultados acompañan a los resultados del DDM (Figura 3.32). Se puede afirmar que la influencia de la geometría como forma de alterar el proceso de mezcla y combustión ha quedado demostrada en este capítulo a través del análisis de dos toberas cuyas geometrías han sido estudiadas numérica y experimentalmente en términos de flujo interno, chorro y combustión.

Con el fin de profundizar aún más en métodos de mejorar la mezcla a

través de la modificación de la morfología de las toberas, el Capítulo 4 y el Capítulo 5 han introducido en el estudio toberas de sección elíptica a través del modelo Σ-Y (ESA) de flujo interno-externo acoplado. En el Capítulo 4, el estudio de este tipo de perfiles se ha realizado en condiciones de cavitación a través de secciones constantes a lo largo de toda la tobera. A la validación del código otorgada por las toberas calibradas mencionadas anteriormente (Spray A y Spray C del ECN) se ha añadido un estudio de flujo interno sobre la geometría de una tobera multiorificio también cavitante. El error máximo encontrado en este caso ronda el 5.4 %, acorde con lo encontrado en la literatura para toberas de estas características, pudiendo observarse el colapso característico del flujo másico en la Figura 4.11. Una vez discutido ampliamente el potencial del modelo acoplado, se ha utilizado para explorar el efecto de distintos grados de excentricidad partiendo de una tobera circular de referencia. Generando geometrías con igual área geométrica de salida, la excentricidad se ha incrementado hasta un valor de 0.94 simulando un total de 6 toberas. Bajo condiciones de alta presión (2000 bar) y media contrapresión (30 bar) que favoreciesen la aparición de cavitación, las toberas se han caracterizado hidráulicamente obteniendo los parámetros adimensionales y valores estacionarios del flujo, incluyendo flujo másico, momento y velocidades efectivas a la salida. Al análisis de estos valores se ha unido la visualización de la distribución de vapor observada a la salida de las toberas, donde la dispersión de esta fase a lo largo de la sección del orificio ha sido mayor según se aumentaba el valor de la excentricidad. El estado del flujo en el orificio de salida se ha vinculado luego con la distribución de velocidades y fracciones másicas a lo largo del eje del chorro y en varias secciones transversales del mismo. De los resultados obtenidos se desprende que una mayor excentricidad produce una mayor interacción o un mayor intercambio de momento entre el chorro y el gas del volumen de descarga. Partiendo de unos valores similares en las variables del flujo interno según la Figura 4.12, el aumento de la excentricidad de la sección tiende ha reducir más rápidamente la velocidad axial y la concentración de combustible sobre el eje del chorro. Este efecto se puede ver sobre las curvas de la Figura 4.17 y la Figura 4.14 para la velocidad y la fracción másica de líquido respectivamente. La disminución de estas variables sobre el eje tiene su contrapartida en la visualización de los perfiles radiales también de la velocidad (Figura 4.16) y fracción másica (Figura4.15). Aquí, la disminución observada sobre el eje se traduce en una mejor distribución en dirección radial de estas variables según avanza el chorro en el volumen de descarga. En consonancia con el estudio de los perfiles, la penetración (Figura 4.23) se reduce en favor de una mayor apertura del ángulo (Figura 4.21). El cálculo del englobamiento en la Figura 4.18 actúa como variable síntesis de esta mecánica, reflejando una mayor cantidad de aire abarcada por el chorro a medida que aumenta la excentricidad de las toberas. Tras observar los resultados obtenidos, se puede afirmar que las geometrías de toberas elípticas de sección constante pueden influenciar positivamente los procesos de mezcla produciendo ángulos de cho-

rro y englobamientos mayores. En esta situación convergen distintos factores, por un lado y como se ha mencionado anteriormente, la fase vapor se encuentra más distribuida a lo largo de las secciones elípticas pudiendo favorecer la desintegración del de chorro. Por otro lado, aunque el área de salida es un parámetro mantenido constante en este estudio, el aumento de la excentricidad de la sección tiene como efecto paralelo un aumento del perímetro de la misma. Al aumentar la superficie de interacción entre el fluido y el gas de los alrededores se favorece el intercambio de masa y energía. A estos fenómenos se une el comportamiento particular de los chorros elípticos donde la asimetría del chorro genera cierto efecto de vorticidad, observable a través de la alternancia de los ejes mayor y menor del chorro (Figura 4.24), y que puede contribuir a la mezcla. Aunque el potencial de estas toberas ha quedado establecido, aún es necesario intentar descomponer estos efectos para comprender completamente el desarrollo de la mezcla. En el Capítulo 5 se ha estudiado el efecto del tipo de sección en este tipo de toberas, distinguiendo entre secciones convergente y constantes. Utilizando la misma metodología de flujo interno-externo acoplado a través de un modelo Σ-Y sin transición (ESA), se han analizado dos geometrías de excentricidad 0.9, con misma área de sección de salida, bajo condiciones de alta presión de inyección. Siguiendo un camino similar al del estudio anterior, inicialmente se ha analizado el flujo interno a través de sus principales variables integrales y coeficientes adimensionales. Acorde con los parámetros geométricos, en ausencia de conicidad y de radio de hidroerosión a la entrada, la tobera de sección constante produce una caída de velocidad mucho más importante que la tobera convergente, reduciendo el valor del coeficiente de velocidad. La presencia de la fase vapor también reduce el coeficiente de área llevando a un valor menor final del coeficiente de descarga y de flujo másico. Esto, junto con la pérdida de velocidad a la salida provoca un flujo con una menor cantidad de movimiento. Para evaluar correctamente el efecto del momento sobre la penetración, la Figura 5.12 presenta la penetración con y sin normalizar respecto a esta variable. Tras eliminar la influencia del momento sobre la curva, se observa como, tras un cierto tiempo, la curva de la tobera de sección constante cae por debajo de la convergente. Considerando que las diferencias en momento han sido suprimidas por la normalización, la divergencia entre ambas curvas es absorbida por una mayor penetración radial del chorro en la tobera de sección constante. Esta mayor dispersión transversal del líquido queda evidenciada por el análisis del ángulo en ambos ejes, donde la tobera de sección constante devuelve valores mayores en las dos proyecciones. El análisis de los perfiles de fracción de líquido y velocidad también respaldan esta mayor apertura del chorro como muestran la Figura 5.16 y la Figura 5.19 respectivamente. Para resumir el efecto sobre la mezcla, la Figura 5.21 devuelve el englobamiento generado por cada una de las toberas. En esta comparativa, la curva de la tobera de sección constante (normalizada por su flujo másico) se eleva por encima de la tobera convergente. Las discusiones conducidas a lo largo de este capítulo indican como el efecto de la cavitación

es un factor a tener en cuenta en las toberas de sección elíptica como método de mejorar la mezcla sobre sus equivalentes convergentes.

El debate desarrollado a lo largo de estos capítulos pone de manifiesto no solo la influencia de la geometría de la tobera sobre el chorro y la combustión sino también el margen de mejora aún disponible a través de la exploración de nuevas geometrías. Aunque es cierto que su viabilidad queda sujeta a la tecnología de manufactura, siempre que las propuestas no sean irreales, se abre un gran abanico de posibilidades y aún más si se combinan con otros avances como nuevas estrategias de inyección, nuevos combustibles, etc. De esta forma, el motor de combustión puede aspirar a un mejor aprovechamiento de la energía en la fuente de su generación.

Capítulo 7

Conclusiones y trabajos futuros

Todos los modelos son erróneos,
pero algunos de ellos son útiles

George P. E. Box

Resumen: En los capítulos anteriores se han planteado diferentes estudios sobre la influencia de la geometría. Primero, desde una perspectiva eminentemente del flujo interno y luego, observando también su efecto en el chorro y la mezcla. Empezando con toberas de morfologías convencionales, se ha finalizado incluyendo en los análisis toberas Diesel elípticas con un carácter innovador. Este capítulo resume las principales conclusiones derivadas de dichos estudios.

7.1. Conclusiones

Durante los capítulos anteriores se han analizado los diferentes efectos que las geometrías de las toberas de inyección producen sobre el flujo interno, la mezcla y la combustión. En las conclusiones mostradas a continuación quedan sintetizados.

- Sobre las bases de flujo adiabático, y una detallada caracterización de las propiedades físicas del combustible, se han estudiado los efectos termohidráulicos de la geometría en el flujo interno. Las propiedades físicas del fluido se han definido en función de la temperatura y presión y han sido trasladas al cálculo bajo el supuesto de fluido compresible. La metodología planteada ha permitido obtener desviaciones menores al 0.9 % en temperatura a la salida de una geometría calibrada, realzando la importancia de la correcta inclusión tanto de las propiedades físicas del combustible como de los parámetros morfológicos ésta en el cálculo numérico.

Estas condiciones han mostrado el efecto contrapuesto del incremento de temperatura por efectos de fricción en las paredes de las toberas, y del enfriamiento originado en el flujo debido a la descompresión del fluido. Cuando se introducen dichos efectos en toberas convergentes Diesel sometidas a grandes caídas de presión y velocidades, la diferencia local de temperatura en el orificio de salida puede llegar a ser muy notable, en el caso planteado: 80 K. Estas diferencias pueden derivar en variaciones importantes de las propiedades del combustible y ser relevantes en los mecanismos de atomización posteriores. Por tanto, la geometría define el estado termo-hidráulico del flujo afectando también a las condiciones térmicas con la consiguiente variación de las propiedades físicas del combustible debidas a la presión y a la temperatura.

- Se ha demostrado como una geometría con un ratio l/d reducido manteniendo un permeabilidad, o flujo másico similar, es capaz de mejorar el proceso de mezcla obteniendo unos desempeños en ciclo cerrado mayores gracias al mejor rendimiento de la combustión y unas pérdidas en pared reducidas. Los modelos empleados han servido para definir una metodología robusta, capaz de trasladar la influencia de la geometría al comportamiento del chorro. Por un lado, utilizando modelos tradicionales DDM y por otro, con modelos ELSA (Σ-Y) más avanzados. El error obtenido en los modelos numéricos ha sido más que aceptable en términos de flujo interno y chorro. En los parámetros del ciclo de combustión propuesto, las simulaciones también han producido un buen rendimiento aunque con desviaciones menores. La mejora de la eficiencia obtenida al emplear la tobera de ratio reducido se ha calculado del orden de un significativo 1 % en simulación, con una reducción importante de las pérdidas por calor a través de la pared un mejor aprovechamiento del combustible. En contraposición, la optimización propuesta para esta misma geometría ha dado resultados poco reseñables, requiriendo probablemente más iteraciones en este aspecto. Se puede concluir, que no solo el uso de geometrías con l/d reducido puede contribuir al mejor desempeño del evento de inyección-combustión, sino que el uso de los modelos propuestos en el estudio de la geometría ha demostrado ser una forma eficaz de ayudar en el diseño de los sistemas de inyección.

- Utilizando el modelo Σ-Y (ESA), se han explorado geometrías de sección elíptica como forma de mejorar el proceso de atomización y mezcla en sistemas de inyección Diesel. Simulando el flujo interno y externo de forma acoplada se ha capturado y trasladado el efecto de la geometría sobre el chorro. El código se ha validado frente a dos toberas calibradas mono-orificio, Spray A y C, obteniendo excelentes resultados en los principales parámetros del flujo interno, con errores máximos alrededor de 5.4 % en condiciones de cavitación, y chorro, también con desviaciones

muy reducidas, entorno a 1° para los valores de ángulo y siempre dentro de la desviación experimental para la evolución del líquido en cámara. Los resultados obtenido tras la aplicación de este modelo sobre geometrías elípticas cavitantes muestran una mayor interacción del chorro de estos perfiles con el gas ambiente. El incremento del ángulo alcanzado, derivado de un mayor valor de excentricidad, puede llegar a superar en 10° grados al equivalente circular con el consiguiente aumento, también significativo, de la cantidad de aire englobado.

- La importancia de la variación de la sección a lo largo de la tobera queda demostrada en las toberas de perfil elíptico. Utilizando el código ya validado, se han analizado dos toberas elípticas, una de ellas de sección convergente y otra de sección constante, siendo esta última de carácter cavitante. De acuerdo a los resultados, la presencia de cavitación es un factor determinante en el comportamiento del chorro de las toberas elípticas en cámara. En este sentido, las diferencias encontradas se han analizado tomando como punto de partida las características, parámetros macroscópicos y variables locales del flujo interno originadas por las geometrías. La mejora de los parámetros del chorro demuestra que se favorece la mezcla en distancias medias a la tobera siendo menos notable en zonas cercanas a ésta en las condiciones de contorno propuestas.

7.2. Trabajos futuros

Los trabajos realizados en este documento han tenido como objetivo el estudio del efecto de la geometría sobre el evento de inyección y sobre la combustión. Las metodologías presentadas, en especial las relativas a los modelos de flujo acoplado Σ-Y (ELSA, ESA) han sido validadas como forma de profundizar no solo en el estudio de estos sistemas sino también en el diseño de los mismos. Aunque los puntos de vista incorporados a través de los distintos capítulos han sido amplios, las limitaciones usuales de este tipo de desarrollos impiden muchas veces abarcar todas las posibilidades, aplicar todas las mejoras, o profundizar en determinados temas. Algunos de estos desarrollos quedan entonces para trabajos futuros y son reflejados a continuación.

- Aunque los modelos han respondido satisfactoriamente en las aplicaciones planteadas. Existen combinaciones susceptibles de mejorar los resultados obtenidos. Queda pendiente la inclusión de modelos de turbulencia más complejos, como las aproximaciones LES, donde la literatura han conseguido mejores resultados sobre toberas mono-orificio.

- Es necesario extender las simulaciones acopladas a condiciones motor más extensas donde poder seguir estudiando el efecto de la geometría, utilizando además toberas de diferentes rasgos. Se incluyen aquí toberas

innovadoras como las elípticas. Por otro lado, los estudios presentados quedan acotados al balance energético del ciclo cerrado del motor, no habiendo considerado por falta de tiempo y otras limitaciones la generación de contaminantes o procesos de renovación de la carga. Es mandatorio abordar también estos temas en trabajos futuros.

- Aunque se ha estudiado el efecto de las morfologías elípticas, aún falta por analizar su comportamiento en situaciones reales. Para ello será necesario responder primero a las preguntas inconclusas sobre las mecánicas particulares del chorro elíptico en condiciones inertes y luego, replicar estos estudios en condiciones evaporativas. Previamente a dar el salto a condiciones motor, la manufactura de toberas prototipo cuyas medidas experimentales puedan validar los modelos también debe ser considerado un objetivo.

- Finalmente, es necesario extender estas metodologías a nuevas geometrías de toberas susceptibles de ser fabricadas y con potencial de mejorar el proceso de mezcla.